Universidade de Aveiro Departamento de Física
2014

NUNO MIGUEL FREITAS FERREIRA

MATERIAIS E CONCEITOS PARA PRODUÇÃO DE FERRO POR PIROELETRÓLISE COM BAIXA EMISSÃO DE CO_2

MATERIALS AND CONCEPTS FOR CO_2 LEAN IRONMAKING BY PYROELECTROLYSIS

Universidade de Aveiro Departamento de Física
Ano 2014

Nuno Miguel Freitas Ferreira

MATERIAIS E CONCEITOS PARA PRODUÇÃO DE FERRO POR PIROELETRÓLISE COM BAIXA EMISSÃO DE CO_2

MATERIALS AND CONCEPTS FOR CO_2 LEAN IRONMAKING BY PYROELECTROLYSIS

Tese apresentada à Universidade de Aveiro para cumprimento dos requisitos necessários à obtenção do grau de Doutor em Engenharia Física, realizada sob a orientação científica do Prof. Doutor Jorge Frade, Professor Catedrático do Departamento de Engenharia dos Materiais e Cerâmica da Universidade de Aveiro, coorientação científica da Prof. Doutora Florinda Costa, Professora Associada do Departamento de Física da Universidade de Aveiro, e coorientação científica do Doutor Andrei Kavaleuski, Investigador Principal do Departamento de Engenharia dos Materiais e Cerâmica da Universidade de Aveiro.

This work was supported by the European Unions Research Fund for Coal and Steel (RFCS) research program, under grant agreement RFSR-CT-2010-00002

Dedico este trabalho à minha esposa e filho.

À memória do meu pai. ;)

o júri

presidente

Prof. Doutor Anibal Manuel de Oliveira Duarte
professor catedrático do Departamento de Eletrónica, Telecomunicações e Informática da Universidade de Aveiro

Prof. Doutor Luís Filipe Malheiro de Freitas Ferreira
professor catedrático da Faculdade de Engenharia da Universidade do Porto

Prof. Doutor Andrés Emilio Sotelo Mieg
professor titular do Instituto de Ciencia de Materiales de Aragón da Universidade de Zaragoza

Prof. Doutora Regina da Conceição Corredeira Monteiro
professora associada da Faculdade de Ciências e Tecnologia da Universidade Nova de Lisboa

Prof. Doutora Florinda Mendes da Costa
professora associada do Departamento de Física da Universidade de Aveiro

Prof. Doutor João Carlos de Castro Abrantes
professor adjunto da Escola Superior de Tecnologia e Gestão do Instituto Politécnico de Viana do Castelo

Doutor Andrei Kavaleuski
investigador principal do Departamento de Engenharia de Materiais e Cerâmica da Universidade de Aveiro

Doutor Duncan Paul Fagg
investigador auxiliar do Departamento de Engenharia Mecânica da Universidade de Aveiro

agradecimentos

A realização e elaboração desta tese não teria sido possível sem a colaboração de algumas pessoas e instituições, a quem eu deixo aqui expresso o meu sincero agradecimento.

Aos meus orientadores Prof. Doutor Jorge Frade, Prof. Doutora Florinda Costa e Doutor Andrei Kavaleuski, um agradecimento pela orientação, dedicação, confiança, paciência, discussão e partilha de conhecimentos ao longo desta minha jornada, e que sem eles, à sua maneira, não era possível.

Quero também agradecer ao programa European Unions Research Fund for Coal and Steel (RFCS) pelo apoio financeiro para a realização deste trabalho através do contracto: RFSR-CT-2010-00002.

A todos os técnicos do Departamento de Física e do Departamento de Engenharia de Materiais e Cerâmica da Universidade de Aveiro pela prontidão, apoio, conselhos e partilha de conhecimentos.

Aos meus colegas e amigos de laboratório do Departamento de Física da Universidade de Aveiro pelo apoio e momentos de convívio.

Aos meus amigos e colegas de laboratório do Departamento de Engenharia de Materiais e Cerâmica da Universidade de Aveiro pelo apoio, boa disposição e excelentes momentos de convívio dentro e fora do laboratório, foi muito bom, espero que continuem assim :=).

À minha família pelo apoio incondicional, enorme compreensão, carinho e acima de tudo paciência.

palavras-chave

Piroeletrólise do ferro, fusão de zona, ânodos consumiveis, eletrólitos fundidos, espinelas

resumo

Esta tese de doutoramento pretendeu demonstrar o conceito de piroeletrólise de ferro à escala laboratorial. Visou-se a deteção de objeções fundamentais e/ou restrições críticas, de modo a propor conceitos exequíveis para o método global e para elétrodos adequados, e identificar mais claramente os principais requisitos. O principal esforço foi dedicado ao estudo de materiais de ânodo adequados para o desenvolvimento de unidades industriais de larga escala, com eletrólito fundido à base de silicatos. O conceito compreende ânodos consumíveis à base de óxidos de ferro e um elétrodo de Fe fundido, com uma camada intermédia de Fe sólido entre o metal fundido e os refratários. Adicionalmente, foi testado um conceito alternativo de piroeletrólise com membrana bloqueadora eletrónica, e foram desenvolvidos protótipos com base neste conceito.

O eletrólito fundido baseou-se numa composição de aluminosilicato de magnésio com um mínimo de temperatura *liquidus*, com diferentes teores de óxido de ferro. Foram realizados estudos de desvitrificação, cristalização de óxidos de ferro ou outras fases e alterações redox da razão Fe^{2+}/Fe^{3+}, recorrendo à fusão de zona por laser, a diferentes velocidades. Estes estudos visaram a obtenção de critérios fundamentais para a dissolução de matérias-primas (óxidos de ferro) no eletrólito fundido, para avaliar a compatibilidade de espinelas à base de magnetite com potenciais ânodos e para prever as implicações de gradientes térmicos e/ou deficiente regulação térmica.

Foram preparados e testados diversos protótipos laboratoriais, para demonstrar o conceito de piroeletrólise com bloqueamento eletrónico e para identificar as questões mais críticas e desafios deste conceito. O comportamento destas células em condições de operação com e sem bloqueamento eletrónico originou informações muito pertinentes sobre as propriedades de transporte do eletrólito fundido (i.e., condutividades iónica e eletrónica), a sua variação sob polarização anódica e catódica, as limitações de eficiência faradaica e a ocorrência de reações eletroquímicas parasitas ou secundárias.

O conceito de ânodos consumíveis baseou-se em espinelas com composições derivadas da magnetite, em virtude da esperada estabilidade redox a altas temperaturas, mesmo em condições oxidantes. A composição destas espinelas foi ajustada para melhorar a sua refrataridade e a estabilidade em condições redox mais alargadas (T, pO_2 e sobretensão anódica), sem excessivo prejuízo para a condutividade elétrica, estabilidade termomecânica e outros requisitos. As alterações de composição dos materiais de ânodo consumíveis também foram determinadas pelos constituintes do eletrólito fundido, de modo a prevenir contaminações inaceitáveis e para minimizar a velocidade de dissolução dos ânodos consumíveis. Outras alterações de composição tiveram o propósito de incluir componentes de aços ou ligas de ferro (Cr, Mn, Ni, Ti).

keywords

Iron pyroelectrolysis, zone melting, consumable anodes, molten electrolytes, spinels

abstract

The main purpose of this PhD thesis was to provide convincing demonstration for a breakthrough concept of pyroelectrolysis at laboratory scale. One attempted to identify fundamental objections and/or the most critical constraints, to propose workable concepts for the overall process and for feasible electrodes, and to establish the main requirements on a clearer basis. The main effort was dedicated to studying suitable anode materials to be developed for large scale industrial units with molten silicate electrolyte. This concept relies on consumable anodes based on iron oxides, and a liquid Fe cathode, separated from the refractory materials by a freeze lining (solid) layer. In addition, one assessed an alternative concept of pyroelectrolysis with electron blocking membranes, and developed a prototype at small laboratory scale.

The main composition of the molten electrolyte was based on a magnesium aluminosilicate composition, with minimum *liquidus* temperature, and with different additions of iron oxide. One studied the dynamics of devitrification of these melts, crystallization of iron oxides or other phases, and Fe^{2+}/Fe^{3+} redox changes under laser zone melting, at different pulling rates. These studies were intended to provide guidelines for dissolution of raw materials (iron oxides) in the molten electrolyte, to assess compatibility with magnetite based consumable anodes, and to account for thermal gradients or insufficient thermal management in large scale cells.

Several laboratory scale prototype cells were used to demonstrate the concept of pyroelectrolysis with electron blocking, and to identify the most critical issues and challenges. Operation with and without electron blocking provided useful information on transport properties of the molten electrolyte (i.e., ionic and electronic conductivities), their expected dependence on anodic and cathodic overpotentials, limitations in faradaic efficiency, and onset of side electrochemical reactions.

The concept of consumable anodes was based on magnetite and derived spinel compositions, for their expected redox stability at high temperatures, even under oxidising conditions. Spinel compositions were designed for prospective gains in refractoriness and redox stability in wider ranges of conditions (T, pO_2 and anodic overpotentials), without excessive penalty for electrical conductivity, thermomechanical stability or other requirements. Composition changes were also mainly based on components of the molten aluminosilicate melt, to avoid undue contamination and to minimize the dissolution rate of consumable anodes. Additional changes in composition were intended for prospective pyroelectrolysis of Fe alloys, with additions of different elements (Cr, Mn, Ni, Ti).

Foreword

Overwhelming evidence of global warming and its undisputable risks for the human societies are rising the urgency to implement policies to suppress greenhouse gas emissions (CO_2, CH_4, …), with specific initiatives for industrial sectors, transportation, agriculture, domestic and office energy needs, etc. Iron/steelmaking is one of industrial sectors with highest energy consumption, relying mainly on consumption of coal as a reducing agent and other fossil fuels to sustain very high temperatures. These specific conditions imply much higher environmental impact compared to other energy intensive industries, such as aluminium production. The main difference is the ability to develop electrolytic technologies, with prospects to rely on renewable energy sources such as hydroelectric. Thus, steel industry has also been urged to seek alternative technologies to reduce its CO_2 emissions, including breakthrough electrolytic concepts such as direct electrochemical reduction of iron oxides in alkaline conditions, electrolysis in molten halides at intermediate temperatures, and pyroelectrolysis in molten oxide electrolytes at very high temperatures. The pyroelectrolysis concept is still very far from industrial implementation and it even lacks convincing academic demonstration. Thus, this was taken as the main scope of this PhD thesis.

Key requirements for conclusive demonstration of pyroelectrolysis in oxide melts include development of suitable electrodes and molten oxide compositions with good transport properties (high ionic conductivity and nearly unit transport number) and other suitable requirements to assist electrode kinetics (wettability of electrodes, low viscosity to facilitate elimination of oxygen bubbles, etc.). Though development of suitable molten oxide electrolytes is not trivial, this is probably the less critical issue. This task can rely on detailed information on properties of glass melts, as well as on those relevant for volcanic melts, corresponding frozen-in conditions in basaltic rocks, and useful information on redox changes of iron oxides in a variety of aluminosilicate melts. The author contributed to this development mainly in Chapters 3 and 6. The experimental studies in Chapter 3 were mostly based on Laser floating zone (LFZ) method, taking advantage of the author´s previous experience.

Chapter 6 is dedicated to demonstration of a novel concept of pyroelectrolysis with electron blocking, to demonstrate prospects that will allows reduction to metallic Fe, with high faradaic yields, except on reaching excessive depletion of iron oxide in the aluminosilicate melt. Experimental cells operated without electron blocking demonstrate that direct electrolysis mode fails to deliver acceptable faradaic yields and is, thus, still very arguable.

A plausible concept for the cathode may rely on a liquid Fe layer with a freeze lining layer to avoid direct contact with refractories. This requires temperatures above melting of metallic Fe, and other major difficulties, mainly if one seeks implementation at laboratory scale, without undue costs. Thus, one readily recognized that noble metals would be the only choices as cathode material to perform experimental studies of pyroelectrolysis, as described in Chapter 6. One important conclusion of this work also refers to drastic disintegration of Pt cathodes in pyroelectrolysis, showing that noble metals may be ill-suited for such application.

Still, the greatest uncertainties concern the development of workable anodes, taking into account the extremely aggressive nature of oxide melts at very high temperature under anodic polarization, which exclude any prospects to use common metallic electrodes and even raises doubts about the inertness of noble metals, independently of their prohibitive costs. Thus, one proposed a rather unique concept of consumable anode, based on magnetite and related multicomponent spinels. The composition of these spinels were selected mainly in the system Fe-Al-Mg-O, with other additions corresponding to the components of special steels (Ni, Cr, Nb, Ti, Mn, Si, Zr,…). The compositions were designed to meet suitable requirements (refractoriness, electrical conductivity, redox stability under the expected redox conditions, tolerance to thermal gradients and thermal shock,…), and also to be compatible with the intended metallic product (Fe or its alloys) and with the molten electrolyte, to retain sufficiently slow dissolution and to avoid undue contamination. These studies are reported mainly in Chapter 4, and include guidelines for relevant composition-structure-properties, which may also be used for other spinels, intended for applications at different temperatures, from room temperature up to very high temperatures. Additional contributions are presented in Chapter 5, taking advantage of the uniqueness of LFZ technique to attain much higher temperatures and to facilitate specific heat treatments.

Index

List of abbreviations & symbols

ΔE_{ox} – Energy of oxidative decomposition

ΔV_{ohmic} – Overall ohmic drop

E_i^{cell} – Energy of formation of the individual oxide

φ_d – Diffusion potential

<Bhf> – Average magnetic hyperfine field

$a_{FeO}^{sil.m.}$ – Activity of divalent iron in the silicate melt

a.u. – Arbitrary Units

a_{Mg} – Impact of the substitution with Mg,

Ar – Argon gas

arb.units – Arbitrary Units

a_{Si} – Activity of Si in the metallic liquid

a_{SiO2} – Activity of silica

BF – Blast Furnace

b_{Fe} – Impact of the spinel inversion

Bhf – Magnetic hyperfine field

b_{Mg} – Impact of magnesium in octahedral positions

BOF – Basic Oxygen Furnace

CPE – Constant phase element

C_{tr} – Capacitor corresponding to blocking of the electronic transport

CV – Current-Voltage

DRI – Direct Reduced Iron

e' – Free electron

E_0 – Lattice energy for undoped and not inverted magnetite

Ea – Activation energy

EAF – Electric Arc Furnace

EALFZ – Electrically Assisted Laser Floating Zone

E_{cell} – Cell reaction potential

EDS – Energy dispersive spectroscopy

Eh-pH diagrams – Pourbaix diagrams

E_{MF} – Electromotive force

EPR – Electron paramagnetic resonance

F – Faraday constant

FC – Field cooled

Fe_2O_3 – Hematite

Fe_3O_4 – Magnetite

Fe^{nx} – Valence states of iron

f_{O2} – Oxygen fugacity

G – Gibbs free energy

GS – Galvanostatic

Hc – Coercivity

i – Electrical current

p(O2) – Oxygen partial pressure

PDV – Potentiodynamic voltammometry

p_{H2O} – Water vapour partial pressure

$P_{O2,i}$ – Pure oxygen ion conductor

PS – Potentiostatic

PVA – *PolyVinyl Alcohol*

Q – Total charge

QS – Quadrupole splitting

R – Gas constant

r – Radial distance

$R_{I,m}$ and $R_{e,m}$ – Contribution of ionic and electronic transport in the molten

$R_{I,s}$ and $R_{e,s}$ – Contribution of ionic and electronic transport in the YSZ solid electrolyte

r_i/d_i – Inner radii/diameter of the YSZ cell

r_o/d_o – Outer radii/diameter of the YSZ cell

R_{YSZ} – Ohmic losses in the YSZ electrolyte

SEM – Scanning electron microscopy

SOM – Solid oxide membranes

SSR – Solid state route

T – Temperature

t - Time

TEC – Thermal expansion coefficient

tet – Tetrahedral sites

TG – Thermogravimetric

TGRBF –Top Gas Recycling Blast Furnace

ULCOS – Ultra Low CO2 Steelmaking

V_0 – Potential

V_{appl} – Applied potential

VSM – Vibrating Sample Magnetometer

$X_{FeO\ (s.m.)}$ – Solubility of divalent oxides in silicate melts

$X_{FeO1.5-\delta\ (s.m.)}$ – Solubility of trivalent oxides in natural silicate melts

X_i – contents of basic components

XRD – X-ray diffraction

YSZ - Ytria Stabilized Zirconia

ΔG^o – Free energy of reaction

ΔH – Enthalpies

$\Delta\mu_i$ – Chemical potential contributions

γ – Cation nonstoichiometry

η_3 – Overpotential of the outer electrode

η_1 – Overpotential of the interfacial losses at the melt/YSZ interface.

η_a – Overpotential of the anode

η_c – Overpotential of the cathode

$\rho_{I,m}$ – ionic resistivity of the molten electrolyte

$\sigma_{e,av}$ – average of electronic conductivity

σ_I – ionic conductivity

σ_n – n-type conductivity

σ_p – p-type conductivity

1 Introduction

A state of art and surround areas of steelmaking industry will be described in this chapter, together with actual problematic issues and proposed solutions. The chapter will present the description of relevant processes and methods for iron production, from fundamental viewpoint. It will also introduce the approaches, proposed in this thesis, and briefly describe the related limitations and possible ways to overcome them. Special attention will be given to structural, physical and chemical properties of spinel-type materials, as alternative electrode materials, and the Laser Floating Zone (LFZ) method, as a tool to access relevant process mechanisms in harsh and experimentally difficult conditions. The index of the chapter follows below:

1.1 Steelmaking industry nowadays

Iron production is one of the technological pillars of our civilization. The modern human deals with iron and steel everywhere. It can be found in transport, housing, energy, agriculture, water supply and infrastructures due its unique combination of strength, formability and versatility [Worrell2010, WSA2013].

Considering the wide application of iron and steel alloys, it is not surprising that the last year (2013), the world steel industry produced 1.6 billion tonnes of steel from iron ore and recycled steel.

Production of steel is usually a combined process that begins with production of pig iron. The resulting "hot metal" (liquid iron) is immediately afterwards processed into steel [Kim2002, Schinko2014]. Further processing of iron into steel is an exothermic process, as excess of carbon in the pig iron is burned with oxygen, being one of the CO_2 source emissions [EWC2014, Schinko2014, STEP2014]. In fact, 90 to 97 % of CO_2 emissions result from the coke preparation for iron production and, hence, any improvements in the iron production would greatly affect the CO2 emissions in steel production [Schinko2014].

Once produced steel becomes almost permanent resource, since it is 100 % recyclable and has a very long life cycle without loss of properties, making the steel unique and valuable [Worrell2010, WSA2013]. The steel industry believes that sustainable development must meet the needs of the present, without compromising the ability of future generations to get their own needs. It is for this reason that life cycle assessment is of vital importance [Worrell2010, WSA2013].

It is known that after steel discovery its use has overtaken the iron due its durability and malleability. In industrial and commercial matters steel is more spoken, while in research is given more importance to iron production. The present work focuses on iron making process, as an important part of steel production.

The main worldwide producers of steel and their evolution in the last eleven years are presented in Figure 1.1. One should notice the evolution of China as a main producer, while others countries decrease its production.

Although Chinese output also fell at the onset of the global crisis, China was the first to recover and, after 2009, producing crude steel at new monthly records until nowadays [UKS2009]. Portugal, as curiosity, occupied the 43 world rank position with 1.9 Mt (mega Tons) of steel production in 2012 [WSA2013].

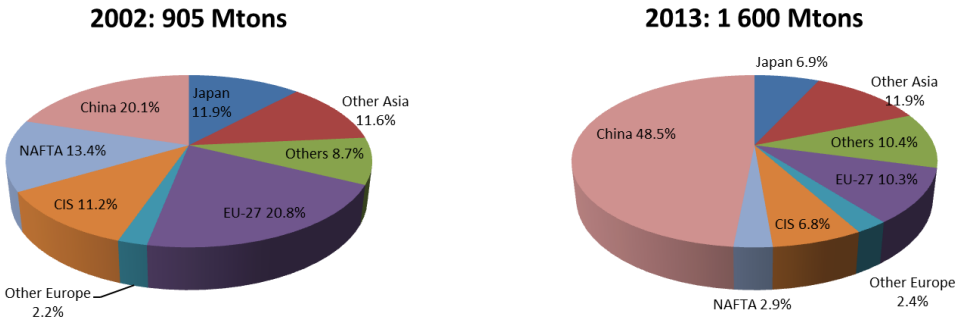

Figure 1.1 – Evolution of main steel producing countries. [WSA2013, Worrell2010], CIS = Byelorussia, Kazakhstan, Moldova, Russia, Ukraine, Uzbekistan; NAFTA = Canada, Mexico, United States; Others Asia: India, South Korea, Taiwan, Australia and New Zealand.

Table 1.1 presents the major steelmaking producers worldwide and their contribution, related to the worldwide steel production in 2013. From the average percentages of the steelmaking producer we can imagine the numbers of existence companies in this industry. It's also noteworthy the gap between the production of first position and others.

Table 1.1 – Steelmaking producers worldwide ranking [WSA2013].

Rank	Company	% Production	Rank	Company	% Production
1	ArcelorMittal	5.85%	10	Ansteel Group	1.89%
2	Nippon Steel & Sumitomo Metal Corporation	2.99%	11	Shandong Group	1.44%
3	Hebei Group	2.68%		Tata Steel	1.44%
4	Baosteel Group	2.67%	12	U.S. Steel	1.34%
5	POSCO	2.49%	13	Nucor	1.26%
6	Wuhan Group	2.28%	14	Gerdau	1.24%
7	Shagang Group	2.02%	15	Maanshan	1.08%
8	Shougang Group	1.96%	16	Hyndai Steel	1.07%
9	JFE	1.90%	17	RIVA Group	1.00%

1.1.1 Conventional iron and steelmaking

Iron ores rocks and minerals from which metallic iron can be economically extracted are found in diverse worldwide locations (Figure 1.2). The iron found in the content ranges from 25 to 65 % and itself is either found in the form of hematite (Fe_2O_3) or magnetite (Fe_3O_4). The treatment of ore starts with the removal of earth and the sizing of the ore into pieces that range from 15 to 40 mm [Worrell2010, Muwanguzi2010, Mohanty2012, Nadoll2014].

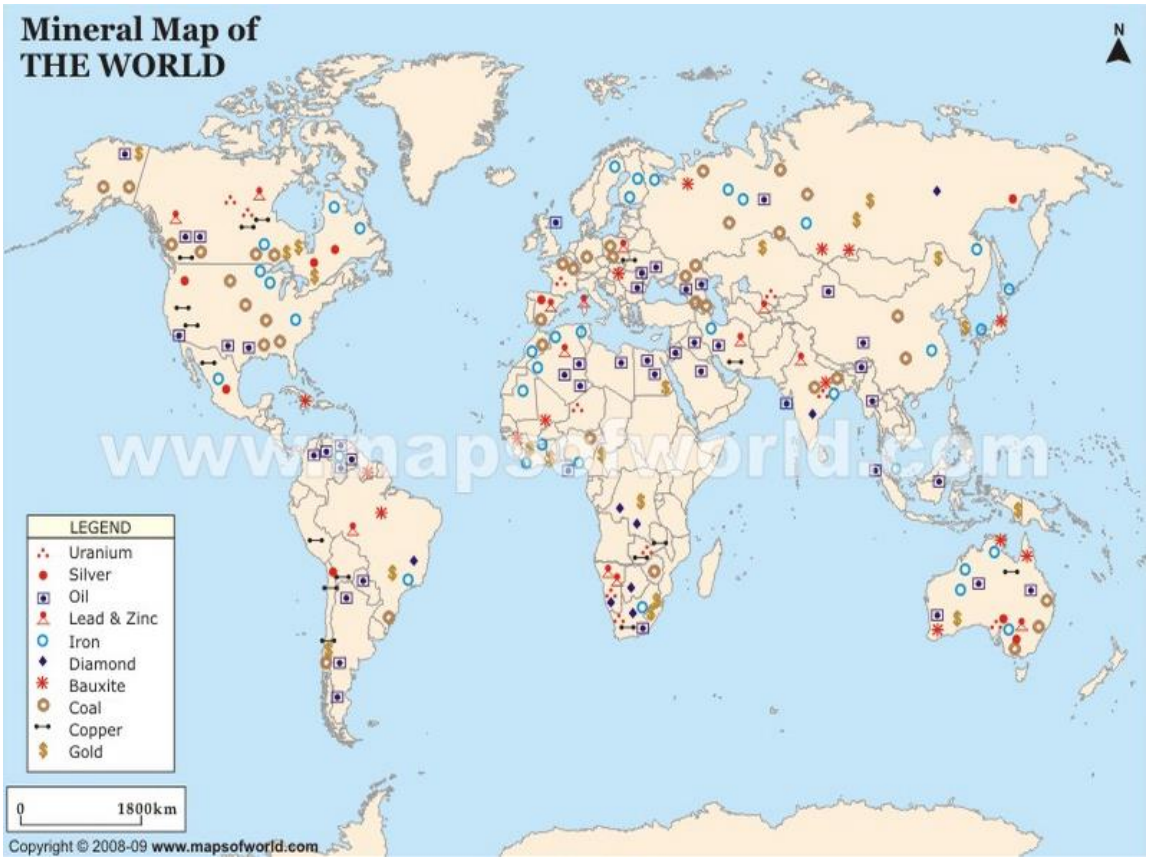

Figure 1.2 – Mineral map of the world [Mapworld2014].

The major compounds found in the iron ore are: SiO_2, Al_2O_3, Fe_2O_3, MnO, MgO, CaO, Na_2O, K_2O, TiO_2, P_2O_5. Other elements can be present in very trace amount, being its percentage dependent on mine site and raw materials available [Santos1965, Mohanty2012, Muwanguzi2010]. However, each source of iron has its own peculiar mineralogical characteristics and requires specific beneficiation and metallurgical treatment to get the best product out of it [Santos1965, Muwanguzi2010, Mohanty2012].

Steel production involves numerous processes/steps that can be laid out in various combinations depending on the products mix, available raw materials, energy supply and investment capital. The iron and steel industry produces a variety of products from slabs, ingots to thin sheets, depending of the production routes (Figure 1.3) [Kim2002, Hu2006, Worrell2010, Pardo2012, EWC2014, IS2014, Nadoll2014].

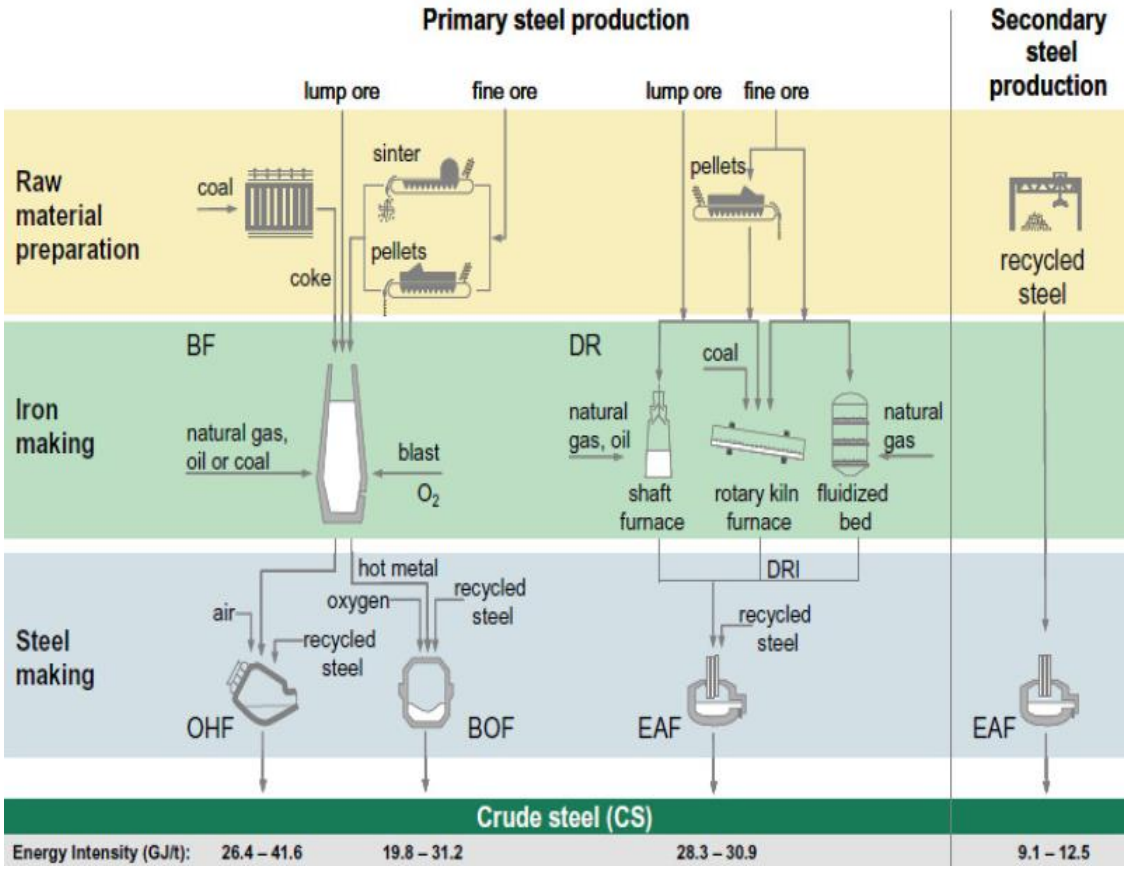

Figure 1.3 – Simplified scheme of iron and steel production routes [Pardo2012].

Key characteristics of the main processing routes used in the production of crude steel, are the following [Kim2002, Hu2006, Worrell2010, Pardo2012, EWC2014, IS2014]:

- In Blast Furnace (BF)/Basic Oxygen Furnace (BOF) route, pig iron is produced using mainly iron ore (70 to 100%) and coke in a blast furnace, and then turned into steel in a basic oxygen furnace. Due to the inclusion of coke making and sintering operations, this route is highly energy intensive;
- Electric Arc Furnace (EAF) route is primarily based on scrap for the iron input and has significantly lower energy intensity compared to the BF/BOF route due to the omission of coke making and iron making processes;

- Direct Reduced Iron (DRI)/EAF route, based on iron ore and often scrap for the iron input. Energy intensity of DRI production can be lower than BF route, depending on the size, and fuel and ore characteristics.

These production routes are expected to remain the mainstay of steel production for years to come [Hu2006, Worrell2010, Pardo2012, EWC2014, IS2014].

1.1.2 Alternative processes for iron and steelmaking production

The processes of iron and steelmaking are not only high-energy consumptive, but also the major source of air pollution, also requiring an intensive use of fossil fuels [Wang2007, Hiu2013, EWC2014]. The iron and steel industry require much raw material, since more than half of the mass input becomes outputs in the form of off-gases and solid wastes/by-products [IPPC2001].

For these reasons over the past 40 years, the European steel industry has more than halved its energy intensity and, therefore, reduced corresponding CO_2 emissions [IPPC2001, UKS2009, Hiu2013, EWC2014, IS2014]. This is one of the highest levels of energy conservation achieved by any industrial sector. This means that steelmaking processes are now so optimised that they are close to theoretical thermodynamic limits realised [UKS2009, Hiu2013, IS2014]. No simple process is available off-the-shelf that will help make further reductions. As a result, hot metal produced via the blast furnace route must be placed on a completely new technological path if one desires a significant advance [UKS2009, Hiu2013, IS2014].

Even the big efforts, made in the past, to reduce emissions by reuse and recycling solid metallic wastes, yielding to a considerable amounts of material to recycle disposed in landfills, without possibilities to expedite and convert as new material (by recycling) due how the process it's made. [IPPC2001, Hu2006]. Iron has been made in blast furnaces for more than 500 years. Blast furnaces require coke, and coke plants are expensive and have many environmental problems associated with their operation. Thus, it would be beneficial from an economical and environmental point of view to produce iron ore without the use of coke [IPPC2001, EWC2014].

Nowadays, nearly all blast furnaces reduce their coke consumption significantly by means of reductant injection at tuyeres [IPPC2001]. However, coke cannot be fully replaced in a blast furnace because of its burden supporting function. The minimum blast furnace coke rate is approximately 200 kg/t pig iron [IPPC2001].

The blast furnaces have evolved into highly efficient reactors. However, other techniques are now available which present a challenge to the blast furnace route for pig iron production [IPPC2001].

Pressure for improvements exerted on steel producers lead to creation of a European consortium in a R&D programme, seeking to develop radical new iron ore based steelmaking technologies called ULCOS (Ultra Low CO_2 Steelmaking) [UKS2009]. This consortium is composed by all major EU steel companies, of energy and engineering partners, research institutes and universities and is supported by the European commission, started in 2005 with a financial support of 60 million €, for cooperative research & development initiative with the aims deliver a 50% reduction in CO_2 emissions from steel production in 2050 [UKS2009, IS2014].

Until now ULCOS program has investigated over 80 different options for these new concept routes, using modelling and laboratory approaches to evaluate their potential, in terms of CO_2 emissions, energy consumption, operating cost and sustainability. From the various technological options, four broad families of process routes have been selected within the ULCOS programme (Table 1.2), for further investigation and eventual scale up [UKS2009, ETP2010, Pardo2012, IS2014].

These technologies can be divided into two types [Pardo2012]:

- Industrial innovative technologies, which have been demonstrated already on an industrial scale, but whose use are not widespread in the European Iron & Steel sector;
- Promising technologies for the medium term, which are currently under development.

The driving force for developing new processes for steelmaking usually involves around one of three major cost factors [Welch1999, Pardo2012]:

- Electrical energy reduction demands, because of the so-called inefficiency;
- Capital cost reduction of the reactor per annual production tonne;
- Environmental considerations (compliance with existing greenhouse gas regulations).

Table 1.2 – Four breakthrough technologies for the iron and steel industry [Sadoway95, Wang2007, US2007, Allanore2008, UKS2009, ETP2010, Kim2011, Wang2011, Pardo2012, IS2014, STEP2014].

Technology	R&D needs
Blast furnace	The top gas of the blast furnace goes through CO_2 capture and the remaining reducing gas is re-injected at the base of the reactor, which also operates with pure oxygen rather than hot blast (air). This has been called the Top Gas Recycling Blast Furnace (TGRBF). The CO_2-rich gas stream is sent to storage.
Smelting reduction process	Based on the combination of a hot cyclone and of a bath smelter called HIsarna and incorporating some of the technology of the HIsmelt process. (The raw materials for the process, which are coal and iron ore, remove the need for coke ovens and sinter plants in the integrated steel route). The process also uses pure oxygen and generates an off-gas which is virtually ready for storage.
Direct reduction process	Produces Direct Reduced Iron (DRI) in a shaft furnace, either from natural gas or from coal gasification (ULCORED). Off-gas from the shaft is recycled into the process after CO_2 has been removed and captured, which leaves the DR plant in a concentrated stream for storage.
Two electrolysis concepts (are at the early stages of research)	In an early stage of research, produce metal either from a water alkaline solution at around 100 °C (electrowinning process - ULCOWIN).
	Steelmaking temperature with a molten salt electrolyte made of slag (pyroelectrolysis - ULCOLYSIS).

The electrolysis concept, which leads directly to final products, is to be compared to a whole raw material preparation step, which has an energy consumption of 15 to 20 $\times 10^9$ J / t liquid steel, with a similar order of magnitude. The technology might be attractive in terms of CO_2 emissions, if it is low the carbon emission during electricity production [Hu2006]. The next section will discuss the advantages and disadvantages of the molten oxide electrolysis (MOE) process.

1.2 Molten oxide pyroelectrolysis: concept & challenges

As described above, the electrolysis is being investigated for steel industry application as a carbon-clean route that scopes with the potential environmental constraints on emissions. Among all methods under consideration, only MOE produces liquid metal from oxide feedstock (Figure 1.4), and compared with traditional methods of extractive metallurgy offers both a substantial simplification of the process and a significant reduction in energy consumption [Hu2006, Kim2011, Allanore2013, EWC2014].

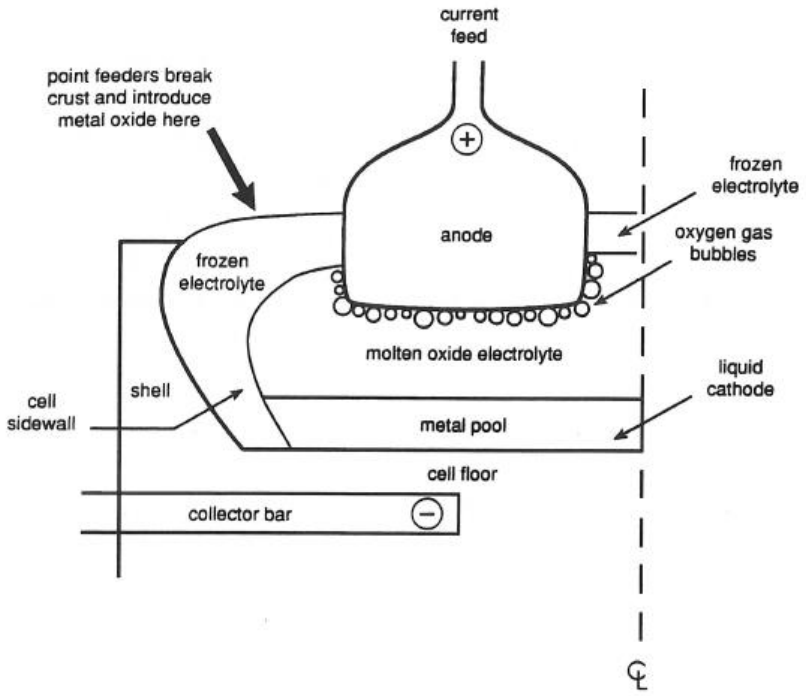

Figure 1.4 – Concept for iron pyroelectrolysis [Sadoway95].

The earliest attempt of electrowinning iron (the formation of iron by electrolysis) from carbonates appears to have been in 1944, as an unsuccessful attempt of iron electrodeposition from sodium carbonate, peroxide, metabore mix at ~ 500 ºC. The process resulted in sodium and magnetite (iron oxide) deposition, rather than iron extraction [STEP2014]. Other attempts have focused on iron electrodeposition from molten mixed halide electrolytes, which has not provided a successful route to form iron, or aqueous iron electrowinning that is hindered by thermodynamic limitations and slow kinetics at low temperature [STEP2014].

Electrolysis with molten electrolyte is a well-known method used for commercial production of aluminium, magnesium, sodium, potassium, lithium, beryllium, titanium, [Cooper2006], silicon [Barron2010], among others. The electrolysis in molten salts was proved to be a techno-economically feasible for these elements [Chen2000, Mishra2005, Tan2009, Arriesgado2011].

Several other reactive metals, such as lanthanides and actinides, also make use of molten salt processing for extraction and refining [Mishra2005]. The high temperature associated with the generation of significant quantity of waste, needs to develop alternative processes that have low waste or ideally a 'zero-waste' generation. Low temperature multicomponent molten salts, as well as room temperature ionic liquids have been developed for materials processing [Mishra2005].

The reduction mechanism in MOE is similar to Hall-Héroult process for aluminium production, which consists of the electrolytic decomposition of aluminium oxide, dissolved in a molten fluoride solvent, comprising cryolite: Na_3AlF_6, (Fig. 1.5).

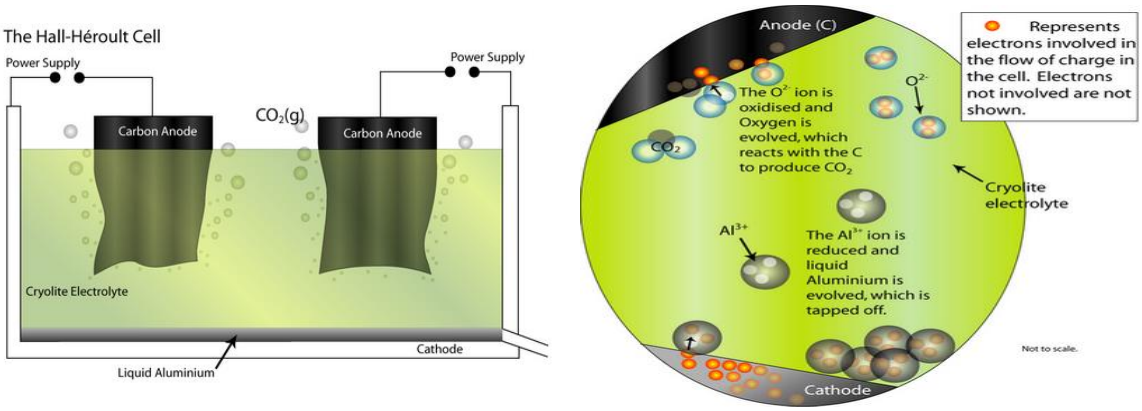

Figure 1.5 – The Bayer-Hall-Héroult process produces primary aluminium from bauxite ore [DoITPoMS2014].

However, these two processes are fundamentally different in relation to the compensating oxidation reaction at the anode. In the Hall-Héroult cell, oxidation requires the attendant consumption of the carbon anode resulting in the generation of carbon dioxide [Kim2011].

In the case of titanium oxide, the solid TiO_2 dissolves into electrolyte (liquid of BaO or cryolite) as Ti^{4+} and O^{2-}. By introducing electrodes to the system and running a current from the positively charged anode to the negatively charged cathode, the ionic species

will migrate to the oppositely charged electrode and donate or receive electrons to neutralize to an uncharged valence structure [Cooper2006].

As example the titanium reduces at the cathode as:

$$Ti^{4+} + 4e^- \rightarrow Ti\ (s) \qquad (1.1)$$

while the oxygen is oxidized to gas at the anode as:

$$O^{2-} \rightarrow \frac{1}{2} O_2\ (g) + 2e^- \qquad (1.2)$$

complete the ionic current [Cooper2006].

In order to successfully harvest the liquid titanium, the molten oxide must have less density, so the titanium can sink to the bottom [Cooper2006]. Also, the process would use a conductive crucible as the cathode, so that the titanium forms at the bottom of the cell [Cooper2006]. Typically, if solid metal is drawn out of the solution at temperatures below the melting point of the metal, it will electroplate the cathode as a solid, which will continue to conduct and grow layers of the deposited metal [Cooper2006].

The ideal process should produce ‘zero’ waste and the metals can be recovered from inexpensive oxides/chlorides without the need for an expensive reductant. Operational costs include graphite anode, electric power and recyclable salt only. The process is also amenable to allow production directly by incorporating co-reduction of respective oxides [Mishra2005].

In the case of iron, to meet the production requirements of an industrial process, the anode must sustain high current densities, potentially exceeding 1 A/cm^2. Under these conditions most of metals are poor candidates for anode materials, due to the effects from strongly oxidizing anodic conditions [Kim2011].

Anodic oxidation can be a strong constraint on the metal-producing efficiency of the electrolytic system. Therefore, the identification of optimal materials for the cell anode is critical for the success of the electrolytic system [Cooper2006, EWC2014]. As a consumable alternative, the graphite anode produces just as much CO_2 as the conventional process, which is environment unfriendly and gives an opposite direction for the CO_2 greenhouse evolution of the intent of MOE for iron [Kim 2011, Wang2012, Lantelme2013, EWC2014].

Preliminary studies of iron pyroelectrolysis in glass slags melts at high temperature have shown the complexity of the process and demonstrated that it is quite far away from pilot scale or industrial application [Sadoway94, Sadoway95, US2007, Kim2011, Wang2011].

In addition, big challenges still exist for iron production by MOE due the process conditions, such as [Mishra2005, kim2011, Allanore2013, EWC2014]:

- Extremely high temperatures (the melting point of iron is ~ 1575 ºC);
- High solubilizing power of a multicomponent oxide melt;
- Under anodic polarization most metals inevitably corrode in such conditions;
- Iron oxide undergoes spontaneous reduction on contact with most refractory metals and even carbon;
- Development of the anodes, tolerant to the extreme conditions imposed by high temperature of the melt;
- Evolution of pure oxygen gas at atmospheric pressure;
- Assessing the efficiency impact of ionic and/or electronic conductivity of salts and glass melts, containing dissolved iron oxide;

Next sections will discuss the work done until now and the challenges in terms of materials choice for cell elements.

1.2.1 Electrochemical cell

An electrochemical cell is defined as a device capable of either obtaining electrical energy from the chemical reactions or facilitating the chemical reactions by the electrical energy.

An electrochemical cell contains two electrodes, the anode and the cathode. The anode is an electrode where oxidation occurs, while the cathode is where reduction occurs [Tilquin95]. In general, a liquid (electrolyte) separates the two electrodes and serves as a galvanic contact between the electrodes. The electrolyte solution form an interface at which the electrolysis process takes place [Tilquin95].

A common example of an electrochemical cell is a standard 12 V battery. A galvanic cell (battery) contains two electrodes which are separated by a liquid (electrolyte), therefore the electrode reactions are also separated.

As an example, the experiment performed by Keller et al. for aluminium production with a tin oxide anode in a cell are shown schematically in Fig. 1.6a [Keller1997], while for MOE of iron is presented in Fig. 1.6b with an atmosphere control [Kim2011]. The position of the cathode and anode will determine the deposited iron and oxygen.

In a galvanic cell the electrochemical reaction proceeds spontaneously, that can be used as energy sources. The Gibbs free energy of cell reaction depends who made the work:

- **by** the battery: $\Delta_r G \leq 0$;
- **on** the battery: $\Delta_r G \geq 0$.

In the electrolysis cell, a non-spontaneous reaction is driven by an external source of current, e.g. a battery is charged (the work is done on the battery).

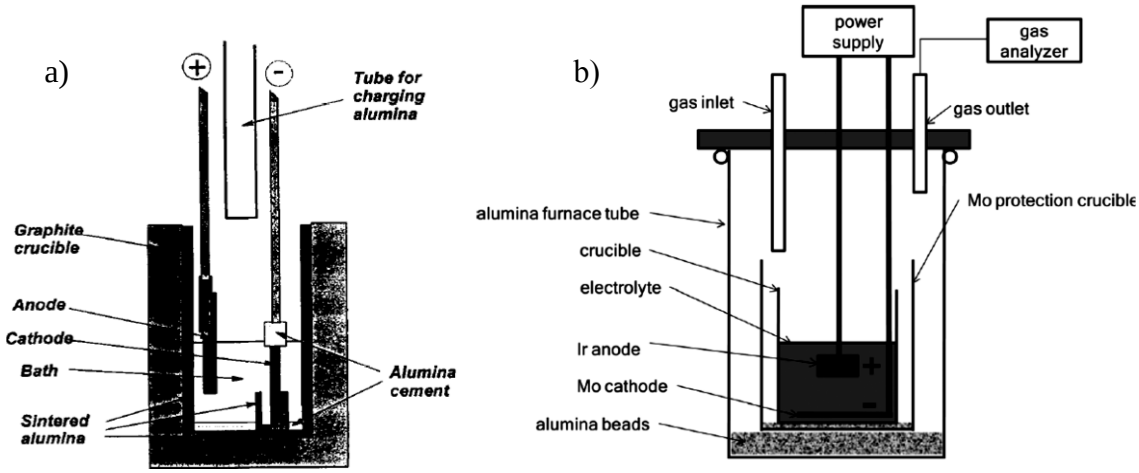

Figure 1.6 – Schematic of experimental set-up: a) testing tin oxide electrodes [Keller1997], b) Molten iron oxide electrolysis [Kim2011].

This way, the cell reaction potential, should be:

$$- z F E_{cell} = \Delta_r G \qquad (1.3)$$

where E_{cell}, the cell reaction potential is the potential difference between electrodes, z the number of moles of electron transferred in the cell reaction, F the Faraday constant and $z F E_{cell}$ is the maximum work that can be done by the cell. The thermodynamic sign convention for spontaneous (natural) processes is:

$$\Delta_r G \leq 0 \text{ thus } E_{cell} \geq 0 \qquad (1.4)$$

E_{cell} is measured.

At the conditions given, E_{cell} is a measure of maximum work the cell could do. From the measured E_{cell}, knowing the cell reaction itself, the reaction Gibbs free energy can be calculated. If diffusion current should be taken into account the φ_d (diffusion potential):

$$E_{MF} = E_{cell} + \varphi_d \tag{1.5}$$

the electromotive force E_{MF} is measured instead of E_{cell}. In this case a non-thermodynamic quantity is added to E_{cell}. In many case φ_d can be minimized down to several mV by the application of a salt bridge, and E_{cell} and E_{MF} can be taken equal.

When the cell reaction is in chemical equilibrium (at $\Delta T = 0$, $\Delta p = 0$)

$$\Delta_r G = 0 \text{ and } E_{cell} = 0 \tag{1.6}$$

the system is incapable to do any work.

A single liquid phase contains both the oxidized and reduced forms of electrode reaction. A noble metal electrode, e.g. Pt senses the potential difference between the bulk of solution and the metal. The electron exchange occurs in the liquid phase.

The electrochemical process which determines the electrode potential of redox electrode is given by:

$$\text{Pt(s)} \mid \text{Fe}^{2+}\text{(aq)}, \text{Fe}^{3+}\text{(aq)}$$

$$\text{Fe}^{3+} + \text{e}^- \rightarrow \text{Fe}^{2+}$$

$$\varepsilon_{\text{Fe}^{2+}/\text{Fe}^{3+}} = \varepsilon^0_{\text{Fe}^{2+}/\text{Fe}^{3+}} - \frac{RT}{zF}\ln\frac{a_{\text{Fe}^{2+}}}{a_{a_{\text{Fe}^{3+}}}} \tag{1.7}$$

$$\frac{a_{Fe^{3+}}}{a_{Fe^{2+}}} = 1 \rightarrow \frac{RT}{zF}\ln(\frac{a_{Fe^{3+}}}{a_{Fe^{2+}}}) = 0$$

where $a_{Fe^{2+}}$ and $a_{Fe^{3+}}$ is the activity of Fe^{2+} and Fe^{3+} in the cell. The electrode potential is identical to the standard potential.

$$\varepsilon_{\text{Fe}^{2+}/\text{Fe}^{3+}} = \varepsilon^0_{\text{Fe}^{2+}/\text{Fe}^{3+}}$$

$$\varepsilon^0_{\text{Fe}^{2+}/\text{Fe}^{3+}} = +0.771 \text{ V at T} = 293 \text{ K.} \tag{1.8}$$

$$\frac{a_{Fe^{3+}}}{a_{Fe^{2+}}} < 1 \rightarrow \frac{RT}{zF}\ln(\frac{a_{Fe^{3+}}}{a_{Fe^{2+}}}) < 0$$

The electrode potential is less than the standard potential:

$$\mathcal{E}_{Fe^{2+}/Fe^{3+}} \leq \mathcal{E}^{0}_{Fe^{2+}/Fe^{3+}} \tag{1.9}$$

In our case, since we want study the sample and its conductivity at high temperature, was necessary the development of another kind of cell based in this method. As will be shown and described in chapter 2, we plan to use an electrochemical cell of YSZ (Ytria Stabilized Zirconia). This material has exceptional thermochemical stability, allows using with melted metals [Fergus1998] or melted glass [Yamashita2008]. This solid electrolyte allows the implementation of unique and innovate electrochemical systems [Inoishi2012].

In MOE, the decomposition of iron oxide, dissolved in electrolyte melt, occurs as following:

$$\begin{aligned} Fe_3O_4 \rightarrow Fe^{2+} + O^{2-} + Fe_2O_3 \rightarrow Fe\ (l) + O_2\ (g) + Fe_2O_3 \\ Fe_2O_3 \rightarrow 2\ Fe^{3+} + 3\ O^{2-} \rightarrow Fe\ (l) + O_2\ (g) \end{aligned} \tag{1.10}$$

Electrochemically-produced ions can turn into different species depending of the pH of reactive media. More significant changes occur for iron, as it is further oxidized in solution once produced, even by oxygen. In this respect, it is known that Fe^{2+} oxidizes very slowly in contact with dissolved oxygen to Fe^{3+} in acidic media, according with Eq. 1.10 [Jiménez2012].

In each electrode the following reactions can occur:

$$\begin{aligned} \text{Cathode: } Fe^{2+} + 2e^{-} \rightarrow Fe\ (aq) \\ \text{Anode: } O^{2-} \rightarrow \tfrac{1}{2}\ O_2\ (g) + 2e^{-} \end{aligned} \tag{1.11}$$

In order to measure the efficiency of the electrolysis process, we can apply the Faraday's law, which allow to calculate the weight of the metal produced (m):

$$\boldsymbol{m = \frac{1}{F}\frac{Q\,M}{n}} \tag{1.12}$$

where F is the Faraday constant, Q is the total charge passed through the system, M is the molar mass of the metal, and n is the valence number of the metal ions in solution [Cooper2006]. The charge can be obtained by:

$$Q = i\,t \tag{1.13}$$

where, i is the current passing through the cell and t the time that current was held (coulombs = amperes x second) [Cooper2006].

Faraday theory is not equipped to handle systems where multivalent states are as abundant and unpredictable, as titanium or iron [Cooper2006, Jiménez2012]. Still, the positive relationship between charge and metal production remains, so higher operating current densities would lead to higher throughput of metals production [Cooper2006].

The electrolysis process can be studied by the Current-Voltage (CV) measurements, which is useful for picking out electrical and kinetic properties as they relate to metal reactivity and oxide formation, they do not represent the steady-state conduction properties that would govern an always-on electrolytic cell. However, feedstock the electrolysis of metal oxides, the cell maintains a consistent setting over a long time-frame. The electrochemical cell can be treated as an electrical device described by voltage and current characteristics. [Cooper2006].

The relevant properties can be also measured through cycles, including:

- ✓ potentiostatic (PS), constant voltage is maintained
- ✓ galvanostatic (GS), constant current is maintained
- ✓ potentiodynamic voltammometry (PDV)[Cooper2006]

The main difference between these techniques is the voltage/current scan speed [Cooper2006]. CV scans return the current densities that a voltage is capable of producing in the cell [Cooper2006].

The PDV scans it done with a slowly rate (~ 0.2 mV/s) to give a better idea of the long-term behaviour of the cell as a steady-state current [Cooper2006]. PS is even more long term as individual voltages are held for about 10 minutes and the average current is assessed based on that time-frame [Cooper2006].

This type of measurement can also be used to determine the corrosion layer thickness and the level of electrodeposition. The GS data should be consistent with the PS data, as both are merely holding one parameter constant and measuring the other, which is a direct function of the constrained parameter [Cooper2006].

The electrolytic voltagrams are non-linear is most cases, with critical potentials required to activate the electrolytic reaction and unlock current flow. The metal may reduce and deposit above a certain potential, with the molten oxide species (e.g. barium in the titanium system) actually reducing and depositing at the cathode at another higher potential [Cooper2006, EWC2014].

The same behaviour can be observed for oxygen evolution at the anode. However, while metal deposition at the cathode (according to Eq 1.11), still allows the conduction of electrons into the melt to continue the electrolysis, oxygen formation at the anode occurs as bubbles, which cover and insulate the anode, preventing electrical current flow (uptake of electrons from oxygen anions) [Tilquin95,Cooper2006, EWC2014]. It is noteworthy that MOE was also mentioned as a promising route for generation of oxygen for extra-terrestrial exploration [Wang2011, Allanore2013].

The efficiency of an electrochemical cell largely depends on the partial contribution of the electronic component into the ionic conductivity of electrolyte. Thus, assessment of this contribution is an important task. As an example, the Hebb-Wagner process is a technique based on the oxygen ions blocking movement, putting a membrane under a gradient of oxygen partial pressure [Pérez2011].

Somewhat similar approach was applied to the experimental electrolysis simulation performed in this work, in order to understand the impacts from electronic and ionic conduction.

1.2.2 Electrolyte materials

In the electrolysis process the electrolyte type used represents a process challenge, as shown in Table 1.3. The MOE becomes viable the mass production of aluminium and other metals by electrolysis in molten media [Sadoway94, Sadoway95, EWC2014], included metals with great technological importance like titanium [Sadoway94, Sadoway95, Fried2004, Mishra2005, Cooper2006, US2007, Kim2011].

Table 1.3 – Electrolyte-related challenges in electrolysis technology [Haarberg2005]

Possibilities	Problems/Challenges
Aqueous solutions	Low current efficiency Low current density Large space required
Molten Salts	Low Fe_2O_3 solubility No inert anode
Molten oxides	High temperature Corrosive electrolyte Electronic conduction No inert anode

The melt salts processing, possibilities to perform electrolysis by melts due to its capabilities to dissolve materials with high concentrations when compared to the presented by aqueous solutions [Mishra2005].

One of the problems in the process with aqueous solutions and molten salts include the use of various salt mixtures of chlorides, with additions of fluorides, that generate a considerable amount of contaminated waste that has to be processed before recycling or disposal [Mishra2005]. Beyond the high solubility, high temperature operation during molten oxide electrolysis also increases the ionic conductivity and promotes the reaction at the electrode, leading to higher current densities [Sadoway94, Mishra2005]. Further, high temperature can contribute for partial endothermic reduction, converting hematite into magnetite, for instance. The electrolysis with molten glass can also allow the use of slags with lower quality, without previous separation of harmful impurities [Sadoway95, Mishra2005, US2007, Kim2011, Wang2011], as will be discussed later. At the same time, the electrolyte composition should be optimized to meet a plurality of requirements. For example, the melting point of the slag must be less than 1450 ºC [Kim2011].

The literature data suggest a correlation between mixed transport properties of glasses or molten salts with the coexistance of different iron oxidation sates [Wang2011], which raise a risk of internal short-circuit, as a result of partial reduction at the cathode ($Fe^{3+} + e^{-} \rightarrow Fe^{2+}$) and reoxidation at the anode [Wang2011].

It is convenient to express the melt chemistry of this system in terms of its Lewis acid-base properties. In an oxide melt, silica polymerizes and acts as an electron-pair acceptor. Hence, melts high in silica are termed acidic [Kim2011]. Dissociating into alkaline-earth cations and oxide anions, magnesia and calcia act as electron-pair donors. Thus, melts high in magnesia or calcia are termed basic [Kim2011].

The valence of the iron in the electrolyte also depends on the pH of the electrolyte. This behaviour can be analysed through thermodynamic databases by means of Eh-pH diagrams also known as Pourbaix diagrams (Fig. 1.7) [Verink2000, Takeno2005]. An Eh-pH diagram depicts the dominant aqueous species and stable solid phases on a plane defined by the Eh and pH axes [Verink2000, Takeno2005].

The electrode potential for cathodic protection is represented by the equilibrium coexistence line between ferrous ion and iron in Fig. 1.7. The domain of potential and pH, in which anodic protection may be considered, is represented by the passive region (either Fe_3O_4 or Fe_2O_3), but care should be exercised to control the ratio Fe^{2+}:Fe^{3+} in order to allow the electric conduction in the electrolyte [Verink2000].

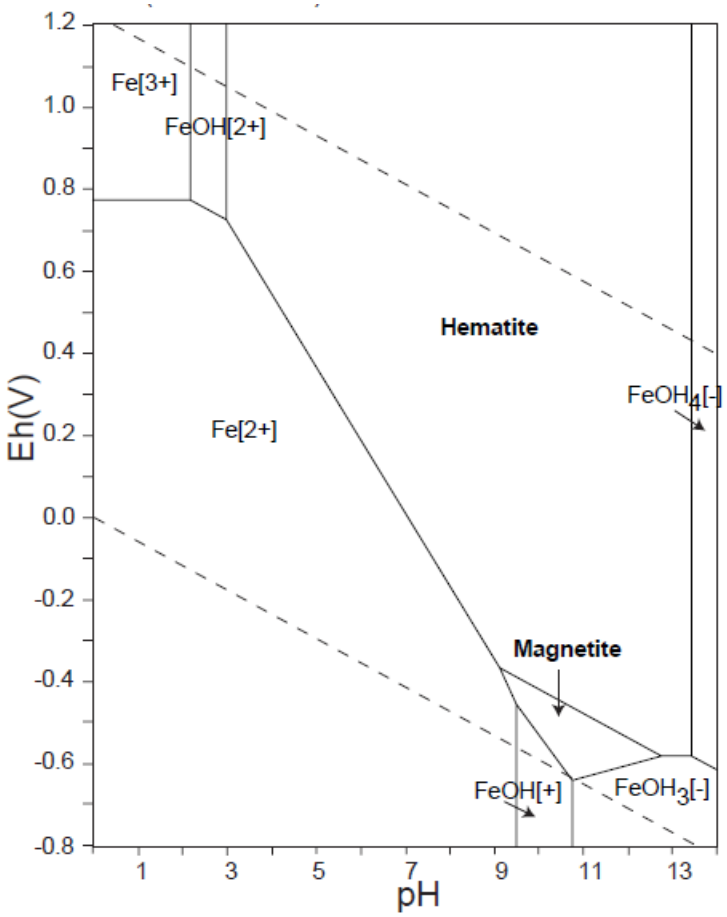

Figure 1.7 – Eh-pH diagrams of the system Fe-O-H, 25 ºC, 1 atm (considering as solid substances only Fe, Fe_3O_4, and Fe_2O_3) [Takeno2005].

If the electrode potential falls in a corrosion regime (e.g., in the region where ferrous ion is stable) it is possible to stop corrosion either by adding an oxidant that would bring the electrode potential into the region of Fe_2O_3 stability by raising the electrode potential, or by changing the pH in the alkaline direction, so as to move horizontally into the passive region, or by cathodic protection that has the effect of lowering the potential into the immunity region. It should be emphasized that the predictions made by using the Pourbaix diagram should be tested prior to actual use, since the formation of a reaction-product film does not necessarily mean that this film is protective [Verink2000].

The standard free energy of formation is directly related to the standard potential of an electrochemical reaction via the Nernst equation. Assuming activities that will not contribute to the applied potential at which metal oxide will be separated to metal and oxygen gas, any metal oxides lying below iron oxide will reside in the melt so long as sufficient iron ions are available for reduction. A metal with less electropositive than iron, will deposit at the cathode. The Ellingham diagram (Fig. 1.8) illustrates this concept. While potassium oxide and sodium oxide would have aided in lowering the melting temperature of the electrolyte and enhancing the ionic conductivity, they could not serve as fluxing agents in this system [Gmitter2008].

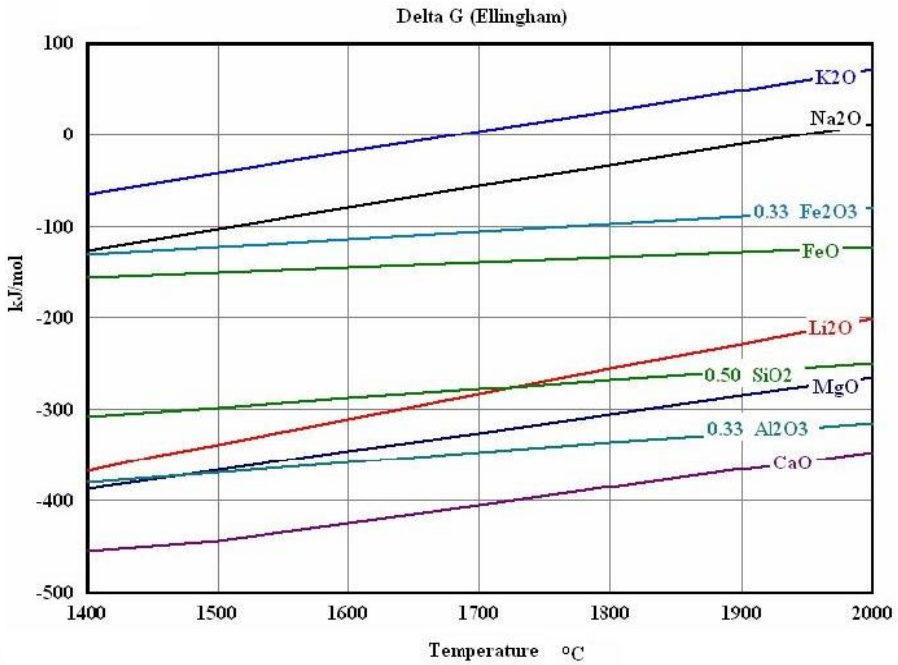

Figure 1.8 – Ellingham diagram at 1 atm p(O_2) illustrating metal oxides suitable for the electrolyte in a molten oxide electrolysis cell [Gmitter2008].

Therefore, the design of an electrolyte for MOE is an important task for optimizing the energetic efficiency of the process, as well as the stability of the refractory or the anode materials [Wang2012, Allanore2013].

The supporting electrolyte components are oxides, encompassing: silica (SiO_2), alumina (Al_2O_3), magnesia (MgO) and calcia (CaO) [Wang2012, Allanore2013]. These oxides are mainly present in iron ore (Fe_2O_3, SiO_2, Al_2O_3) and others constituents formers of slag (MgO, CaO) [Santos1965, Muwanguzi2010, Mohanty2012]. Principally they allow the use of consumable anodes based on magnetite, also taking into account the structural and redox stability issues [Jung2004, Guignard2008].

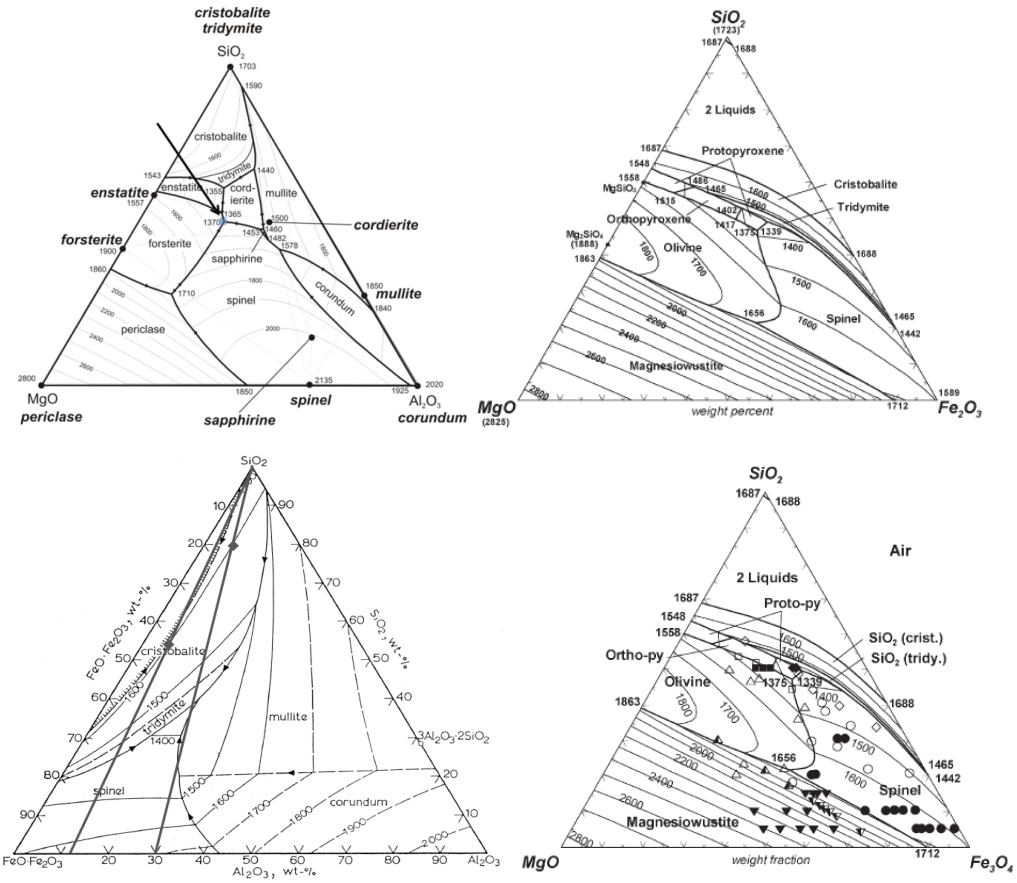

Figure 1.9 – Phase diagrams of vitreous systems to consider [Jung2004, Ana1997].

Previous results, obtained for magnesium aluminosilicate glass systems (MAS) doped with iron oxide [Smith2000, Wiedenroth2003], indicate good prospects for this glass system as a potential electrolyte material. Figure 1.9 presents some phase diagrams of the systems, which are considered to be promising in this sense. The selection of the composition should be performed in order to achieve the dissolution of iron in their midst, and also using the anodic/cathodic polarization.

1.2.3 Anode concepts & materials

One of the main challenges in this new approach is the selection of the optimal materials for the electrodes [Cooper2006]. The Table 1.4 shows examples of different types of the electrodes. However, one should consider the harsh conditions of the pyroelectrolysis process, which can facilitate a large number of reactions between the electrode and electrolyte, especially under condition of anodic polarization.

Table 1.4 – Conventional electrode types and applications [Kharkiv2012].

Electrode type	Example	Description	Electrode reaction (in reduction direction)
Metal metal-ion	$Cu(s) \mid Cu^{2+}(aq)$	Metal bathed in electrolyte containing its own ions.	$Cu^{2+}(aq)+2e \rightarrow Cu(s)$
Ion – ion (redox)	$Pt(s) \mid Fe^{3+},Fe^{2+}(aq)$	Noble metal in contact with solution of a redox couple	$Fe^{3+}(aq)+e \rightarrow Fe^{2+}(aq)$
Metal insoluble salt	$Hg(s) \mid Hg_2Cl_2(s) \mid KCl(aq)$	Metal in contact with its insoluble salt (i.s.) and a solution containing a soluble anion of the i.s.	$Hg_2Cl_2(s)+2e \rightarrow 2Hg+2Cl^-$
Gas	$Pt(s) \mid H_2(g) \mid H^+(aq)$	Noble metal in contact with a saturated solution for a gas and contains the reduced or oxidized form of the gas	$H^+(aq)+e \rightarrow 1/2H_2(g)$

Until now, MOE has been demonstrated using anode materials that are consumable (graphite for use with iron-alloys and titanium) or unaffordable for terrestrial applications (iridium for use with iron). To enable metal production without process carbon, MOE requires an anode material that resists to the depletion while sustaining oxygen evolution [Allanore2013].

Allanore et al. had shown that anodes comprising chromium-based alloys exhibit limited consumption during iron extraction and oxygen evolution by MOE [Allanore2013]. The anode stability is due to the formation of an electronically conductive solid solution of chromium(III) and aluminium oxides with corundum structure. These findings make more feasible larger-scale evaluation of MOE for the production of steel, and potentially provide a key material component enabling mitigation of greenhouse gas emissions while producing metal of superior metallurgical quality [Allanore2013].

The CV effects include the polarization of the IV curve due to mass transport kinetics [Cooper2006]. The three basic steps of electrolysis at the anode are [Cooper2006]:

- O^{2-} anion arrives at the anode surface;
- electrons transfer from the anion to the anode (oxidation);
- oxygen departs the anode surface as a gas.

If one of these steps is slower than the others, it will limit the electrolysis reaction and prevent the system from reaching equilibrium [Cooper2006].

However, while metal deposition at the cathode still allows the conduction of electrons into the melt to continue the electrolysis, oxygen formation at the anode (anode oxidation) can be a strong constraint on the metal-producing efficiency of the electrolytic system [Cooper2006]. Therefore, the identification of optimal materials for the cell anode is critical to the success of the electrolytic system [Cooper2006].

The candidate materials for anode electrode must be capable of [Cooper2006, Gmitter2008, wang2011, Vasudevan2013]:

- ✓ Enduring the high temperature hold-points (1575 ºC) that accompany the electrolysis process;
- ✓ Withstand as minimally reactive and have low solubility/consumable as possible to the melt (electrolyte) and the products;
- ✓ Maintain high current density to maximize the metal production throughput, where intermediate phases must not be soluble nor electronically insulating;
- ✓ Exhibit low volatility of metal and metal oxides;
- ✓ Match price and supply levels to be economically feasible;
- ✓ Withstand anodic polarization without becoming significantly oxidized;
- ✓ Possess sufficient wettability for intimate interfacial contact with electrolyte;
- ✓ Have robust mechanical properties including resistance to thermal shock and creep.

As mentioned before the noble metals such as platinum and iridium are extremely expensive, but are expected to be stable at high temperature and non-reactive [Cooper2006, Kim2011, Wang2012]. Molybdenum, tungsten, and carbon are cheap and have sufficiently high melting temperatures, but could form oxides too easily to serve as continually conductive or non-consumable anodes [Cooper2006].

The concept of an oxide-mediated inert anode should not be limited to iridium metal and molten oxide melts. In principle, the anodic behaviour of other noble metals including Pt, Rh, Au, and Ag may be explained to the extent that they form an intermediate compound by chemical combination with a constituent of the electrolyte [Wang2011]. Thus, one might possibly be able to obtain an inert anode by adjusting relative rates through control of temperature, electrolyte composition, and metal alloy composition [Wang2011].

The anodes used in electrochemical cells can be made of metallic, non-metallic or semiconducting materials. In recent years, the quest for the development of indestructible anodes either as a substitute for costlier anodes or to increase the life of the anodes in electrochemical industries, has grown very much and with the increasing interest in the scientific development of inert and insoluble anodes. A healthy competition is set up to carry out considerable amount of research both in the improvement of the existing anodes or in the development of new anodes. The complex nature and the problem evaluation stems from the number of variables involved such as electrode life, operating conditions or use cell and replacement costs [Vasudevan2013].

Carbon is generally regarded as a consumable anode for molten-salt electrolysis technologies [Lantelme2013]. However, the situation may change if the species discharged in the anode exhibits minor or no affinity with carbon [Lantelme2013]. In fact, carbon was used successfully as an inert anode for industrial Mg extraction where molten $MgCl_2$ was electroreduced with the evolution of chlorine gas in a carbon anode [Lantelme2013].

According to the results of previous works [Yaremchenko2011, Kovalevsky2012], $(Fe, Al, Mg)_3O_4$ spinels show the appropriate electrical and redox properties, to be considered as alternative anode materials for pyroelectrolysis process.

This type of anode combine adequate conductivity without prejudice the environment and compatibility with corresponding melts at temperatures above the melting iron (> 1550 °C), to allow the obtaining of iron in the liquid state. Chapter 1.3 will describe the structural and other relevant properties of magnetite-based spinels.

1.2.4 Experimental results and limitations of electrolysis process

For molten salts electrolysis there exist several studies, such as reported in [Keller1997, Haarberg2005, Wang2008, Gibilaro2011]. To MOE the number of reported studies is more restricted, however, will described some examples found in the literature.

Wang et al. studied the electrochemical decomposition of FeO dissolved in an alumino-silicate melt to produce oxygen gas and liquid metal at 1575 ºC [Wang2011]. They demonstrated that iridium can serve as an oxygen-evolving anode in an oxide melt at extremely high temperature.

Several proposed mechanisms explain the performance of iridium and provide guidance to future efforts aimed at development of inert anodes for other electrolytic systems [Wang2011].

The anodic behaviour of the $Ni_{0.94}Si_{0.04}Al_{0.02}$ metallic electrode in molten NaOH at 500 ºC was also investigated by Shubo Wang et al. [Wang2012]. The oxygen evolution at the interface of $Ni_{0.94}Si_{0.04}Al_{0.02}$ anode had proved to be environmentally friendly. Furthermore, the successful production of iron at the cathode revealed that the $Ni_{0.94}Si_{0.04}Al_{0.02}$ alloy could be a good candidate of inert anode in molten NaOH system to produce metals and alloys, whose corresponding oxides are less stable than Na_2O, without greenhouse gas emissions [Wang2012].

Other work performed by Kim et al. with an electrolyte containing multiple oxides (CaO, MgO, SiO2, Al_2O_3), in which iron oxide (Fe_2O_3) was added to the melt at a concentration of 9.1 wt% as feedstock for iron making by pyroelectrolysis [Kim2011]. In this experiment, yttria-stabilized zirconia crucibles were used as the electrolyte container. Chromium alloyed with 0 to 30 wt% of iron ($Cr_{1-x}Fe_x$ alloy, x ranging from 0 to 0.30), has been assessed for its suitability as an oxygen-evolving anode, while molybdenum was used as the cathode [Kim2011]. The experiment was continuously flowed with an inert atmosphere of high-purity helium. The monitoring of the oxygen level and the gas flow-rate at the reactor outlet allowed them to estimate the anodic faradaic efficiency, specific to this laboratory configuration [Kim2011]. However, the author also addressed the limitation of this method, because part of the oxygen is consumed by the oxidation of the metallic parts present into the tube furnace, in particular at the molybdenum current collectors [Kim2011].

The rate of anode consumption was shown to be dramatically different in a slag, rich in calcia, where the iridium consumption rate was ~ 20 times greater than in slag rich in silica, under similar experimental conditions [Kim2011]. Noteworthy is the fact that slag, rich in calcia, has a higher electrical conductivity and much lower viscosity than slag rich in silica. The author found that viscosity of the melt influenced mass transport, including the rate of delivery of oxygen bearing ions to the electrode and the rate of removal of oxygen gas, while electrical conductivity will influence the kinetics of corrosion [Kim2011].

The higher corrosion rate of iridium observed in the higher basic electrolyte may be related to iridium specification [Kim2011]. Basic melts attack iridium owing to the high concentration of free oxide ion coupled with the low viscosity, which results in unimpaired mass transport [Kim2011].

This result shows the problems of using a noble metal as electrode, due its corrosion during electrolysis process. Those experiments were conducted at currents ranging from 2 to 9 A during 1.5 and 6 h. After electrolysis, both electrodes were raised out of the melt to a cold zone in the furnace to assess the reaction products [Kim2011].

In the work, performed by Cooper et al., carbon, tungsten, platinum, and iridium were examined as candidate anode materials for an electrolytic cell [Cooper2006]. The materials were pre-selected to endure high process temperatures and were characterized for inertness and high current density during electrolysis using voltammometric techniques. Inertness is viewable through current discrepancies dependent on voltage scan direction at low voltage, consumption of current by metal oxide formation, and ease of surface oxide electro-stripping. During electrolytic oxidation is observable a current density maximization for high voltages [Cooper2006]. While carbon, tungsten, and platinum formed oxides surface, iridium remained quite inert. The voltage hold-time was found to affect the current density, the platinum presented a best performance during cyclic voltammometry, but iridium was for potentiostatic regime in the electrolysis process. The intermediate potentiodynamic scan-rate displays the transition from platinum to iridium dominated current density [Cooper2006].

The authors also observed a direct relation between voltages and electron transfer, where the voltage increases (more access to charge), and the current increases as well [Cooper2006]. For higher voltages (above 2.0 V), the electron transfer is sufficient, but the mass transport of oxygen to and from the surface is insufficient, so increasing the voltage does not increase the current significantly (only faster oxygen movement would increase current) [Cooper2006].

In general, these results show the inherent complexity of the processes, taking place in high-temperature electrolysis systems and related difficulties for experimental assessment and eventual scale-up to the industrial applications.

1.3 Relevant properties of spinel-type materials

Iron oxides exist in many forms in nature, with magnetite (Fe_3O_4), maghemite (γ-Fe_2O_3), and hematite (α-Fe_2O_3) being probably the most common. These three oxides are also very important technologically, and they are therefore the subject of many reviews [Allanore2008, Ovsyannikov2008, YamashitaASS2008, Teja2009] and ref. therein.

The magnetic properties of iron oxides have been exploited for a broad range of applications, including magnetic seals and inks, magnetic recording media, catalysts, ferrofluids, contrast agents for magnetic resonance imaging and therapeutic agents for cancer treatment [Teja2009], magnetic fluids, magnetic separation, magnetic resonance imaging as well as drug targeting [Hu2010], as pigments, magnetic materials, catalysts, magnetic recording medium [Hiremath2003, Cartaxo2007].

The shape and size of Fe_3O_4 significantly influence the properties, because of that, great efforts have been devoted to achieve controlled synthesis of Fe_3O_4 [O'Neill1983, Teja2009, Hu2010], since electrical and magnetic properties are strongly dependent on the chemical composition, cation distribution and preparation method [O'Neill1983, Hiremath2003].

1.3.1 Structural properties

From iron oxides, γ-Fe_2O_3 and magnetite Fe_3O_4 have inverse spinel structure, showing interesting electrical, thermal, magnetic and catalytic properties [Hiremath2003, Cartaxo2007, YamashitaASS2008, Skomurski2010]. In ambient conditions magnetite adopts a cubic spinel structure (space group Fd3m) with the inverse configuration. In terms of formal oxidation states the Fe^{3+}:Fe^{2+} ratio corresponds to 2:1, and the chemical composition can be expressed as $(Fe^{3+})^{tet}[Fe^{2+}, Fe^{3+}]^{oct}O_4$ [O'Neill1983, Harrison1999B, Hiremath2003, Ovsyannikov2008, Skomurski2010, Nadoll2014].

The inverse spinel structure can be also represented as AB_2O_4, where A represents a divalent cation such as Mg, Fe^{2+}, Ni, Mn, Co, or Zn, and B represents a trivalent cation such as Al, Fe^{3+}, Cr, V, Mn or Ga [Nadoll2014]. Titanium, with a 4+ charge, can also occupy the B site when substitution is coupled with a divalent cation [Nadoll2014].

Octahedral sites (oct) in the magnetite structure are randomly occupied by sub equal numbers of ferric (Fe^{3+}) and ferrous (Fe^{2+}) iron atoms, whereas tetrahedral sites (tet) are exclusively occupied by the smaller ferric iron atoms (Fig. 1.10A) [Skomurski2010, Nadoll2014].

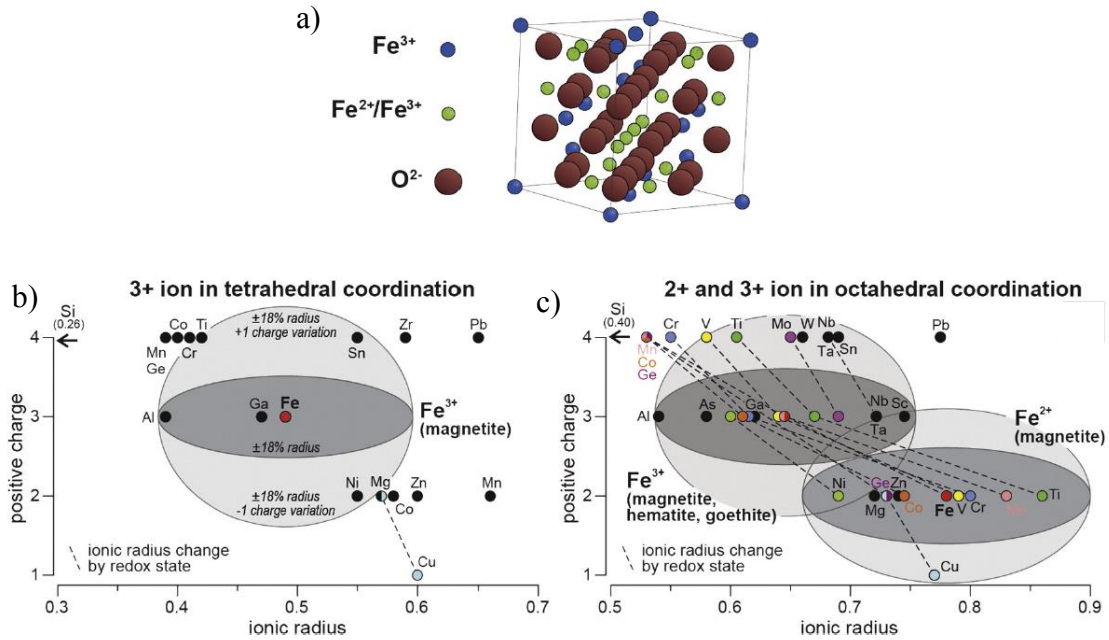

Figure 1.10 – Cubic inverse spinel structure of magnetite (a) and common cations that can substitute for Fe^{3+} in the tetrahedral sites (b) and Fe^{2+}/Fe^{3+} in the octahedral sites (c) [Nadoll2014].

Fig. 1.10 shows the cubic inverse spinel cell (a), and two diagrams illustrate the relationship between the ionic radius and cation charge for the tetrahedral site (b) and the octahedral site (c) [Nadoll2014]. The incorporation of foreign cations is more likely when the substituting cation has a similar charge and ionic radius [Nadoll2014].

The metal substitution (e.g., Cr, Co, Mn, Ni, Ti, Mg, Al, Ga, etc) in magnetite as $Fe_{3-x}M_xO_4$ (M = metal), had been reported to produce systematic variation in magnetic properties, e.g., saturation magnetization, the Curie temperature change, coercivity and electrical resistivity changes [O'Neill1983, Hiremath2003, Petric2007, Ovsyannikov2008, Varshney2012, Liang2013, Nadoll2014]. Other cations such as Nb, Ti, V, Cr, and Mn can occur in different oxidation states, and their incorporation is strongly dependent on the redox conditions. For example, V becomes incompatible in strongly oxidizing conditions, as it transforms to 5+ oxidation state [Nadoll2014].

1.3.2 Electrical properties & mechanisms

The electronic transport in magnetite and related iron-based spinels is assumed to occur via small polaron hopping between Fe^{2+} and Fe^{3+} cations (with Fe^{2+} ion representing localized n-type charge carrier) and is restricted to the octahedral cation sites in the spinel structure [Nell1991, Modi1996]. In agreement with this consideration, the highest conductivity is characteristic for undoped stoichiometric magnetite, which has the inverse spinel structure and, therefore, offers the maximum possible concentration of Fe^{3+} and Fe^{2+} cations in the octahedral sublattice [Park1999, Domingues2013]. Some works suggest that the substitution with magnesium decreases bivalent iron concentration and, consequently, electronic conductivity [Park1999, Domingues2013]. For that reason in the high-temperature range and oxygen partial pressure of 10 Pa, Domingues et al. had found an electrical conductivity of $Fe_{2.3}Mg_{0.7}O_{4\pm\delta}$ ceramics ~ 2.3 times lower than in Fe_3O_4 (fig 1.11) [Domingues2013].

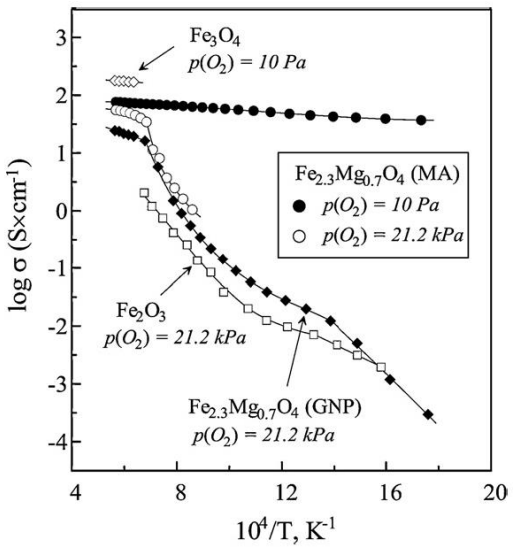

Figure 1.11 – Temperature dependence of electrical conductivity of $Fe_{2.3}Mg_{0.7}O_{4\pm\delta}$ ceramics measured in different atmospheres and preparation method (mechanical activation (MA), and a glycine–nitrate process (GNP)) [Domingues2013].

A similar result was obtained by Kovalevsky et al. for $Fe_{3-x}Al_xO_4$ spinel in the concentration range $0.1 \leq x \leq 0.4$, where the total conductivity at 1773 K and $p(O_2)$ ~ 10^{-5} to 10^{-4} atm was found to be only 1.1 to 1.5 times lower than for pure magnetite [Kovalevsky2012].

Oxidation mechanisms and thermal volume changes in magnetite is an important issue for anode application. Forsmo et al. had studied it in iron ore pellets (Fig. 1.12), being function of raw material particle size and porosity [Forsmo2008].

When a pellet starts to oxidize, a shell of hematite is formed around the pellet while the core still is magnetite. Expansion of about 0.52 % was measured during oxidation between 330 and 900 °C [Forsmo2008]. The extent of contraction was not influenced by raw material particle size or the original porosity in pellets. Simultaneously with the contraction in the hematite shell, linear expansion in the magnetite core took place. Sintering started earlier in the magnetite core (950 °C) compared to the hematite shell (1100 °C) [Forsmo2008]. The difference in sintering rates increased with particle size in the magnetite. A finer grind in the raw material would, therefore, promote the formation of hematite and magnetite [Forsmo2008].

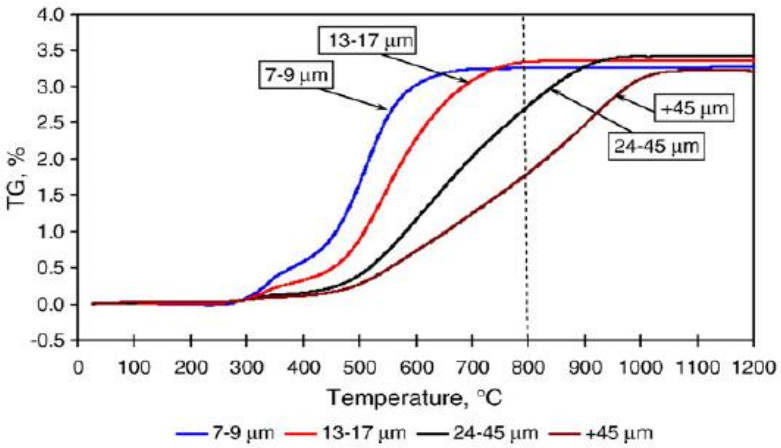

Figure 1.12 – Oxidation curves (TG) for different sized magnetite particles, heated at 5 °C/min in 16% O_2 [Forsmo2008].

The transition element doping as X = Ti, Cr, Mn, Co, Ni, Cu, and Zn in magnetite $(X_\delta\ Fe_{1-\delta})^{tet}\ [X_{1-\delta}\ Fe_{1+\delta}]^{oct}\ O_4$ with δ as the inversion parameter, has been reported by Varshney et al. [Varshney2012].

Doping with a transition element leads to a change in the electrical resistivity due to the cation distribution between tetrahedral (tet) and octahedral (oct) sites in Fe_3O_4 [Varshney2012]. The charge density changes with different dopants, such as with Zn, Ti, and Al. The nonmagnetic dopants enter at different lattice positions as Zn^{2+} at tetrahedral, Ti^{4+} at octahedral, and Al^{3+} both at tetrahedral as well as octahedral site [Varshney2012].

Zn as dopant enters at tetrahedral site in the Fe_3O_4, and the electrical resistivity for $x < 0.035$ show a first order Verwey transition. While $x = 0.035$, $Fe_{3-x}\,Zn_x\,O_4$ show the second order transformation and for above doping concentration ($0.13 \leq x \leq 0.29$) the electrical resistivity of $Fe_{3-x}\,Zn_x\,O_4$ show only a small variation in resistivity. Cu substitution occur in octahedral site of the spinel lattice in $Fe_{3-x}Cu_xO_4$, and no Verwey transition was observed in the range of $0.20 \leq x \leq 1.0$ [Varshney2012].

The substitution of Fe^{3+} ions by Ti^{4+} ions is evidenced from the changes in the electrical resistivity due to charge localization at the octahedral Fe sites. The electron hopping is the conduction mechanism between two adjacent octahedral sites in the spinel lattice and a transition between $Fe^{2+} \Leftrightarrow Fe^{3+}$ ions or $Ti^{4+} \Leftrightarrow Ti^{3+}$ might take place [Varshney2012]. The resistivity measurements clearly demonstrate that in $Fe_{3-x}Ti_x\,O_4$, as in magnetite, there only occurs one well-defined phase transition. Samples with $x \leq 0.03$ exhibit a phase transition of first order; while for $x \geq 0.10$ the transitions is of second or higher order and nature of the resistivity mechanism is related to small polaron conduction [Varshney2012].

The lattice expansion observed was due to the partial replacement of Fe^{3+} ions by Ti^{4+} ions, leading to a periodical ordering of Fe^{3+} and Fe^{2+} ions in the octahedral crystallographic site of Fe_3O_4. The samples show ferrimagnetic behaviour (Fe^{3+} oxidation states) of the Ti^{4+} based magnetites and suggest a preferential occupation of octahedral magnetite sites with spinel structure [Varshney2012]. This effect is also mentioned in the O'Neill et al. work, where they were able to predict accurately the unit cell parameters and oxygen parameters, using a set of ionic radii, observing lightly modifications on the properties of several spinels types [O'Neill1983].

1.3.3 Application as anodes

Oxide electrodes with spinel structure, have been extensively studied due to their promising catalytic activity as anodes for the oxygen evolution and reduction, namely those containing cobalt [Cartaxo2007]. During the last decades cobalt ferrite ($CoFe_2O_4$) was proposed as anode materials for lithium-ion batteries, as reported by Cartaxo et. al. [Cartaxo2007].

As described previously, the materials proposed for the anodes, should combine adequate electrical conductivity without loss of compatibility with molten base, and refractoriness at temperatures above melting point for iron (> 1550 ºC), to achieve iron in the liquid state, like in aluminium production by electrolysis process.

Magnetite combines a good refractoriness and electronic conduction for these operating conditions (temperature and oxygen activity), and its dissolution does not contaminate the process. However, the redox stability of the magnetite is limited, and the conditions for the anodic polarization can promote the oxidation of magnetite to hematite. This change will require increasing temperature in the electrolysis process, increasing the difficulties for implementing this technology.

Thus, the development of new spinels derived from magnetite with better redox stability refractoriness is required [Wang2011, Yaremchenko2011, Kovalevsky2012].

With this regard, an eutectic composition in the system based in Si – Mg – Fe – O allows the possibility of use magnetite or other spinels from the system (Fe, Al, Mg)$_3$ O$_4$ at a temperature higher than melting iron with suitable characteristics to use as consumable electrode concept [Jung2004, Guignard2008, Yaremchenko2011].

Other compositions could be used to ensure appropriate compromises between the redox stability at different temperatures and adequate electronic conduction in the extreme conditions, imposed by the pyroelectrolysis process. It is also noteworthy that the study of ferrites MFe_2O_4 (M = Ni, Co, Cu, etc.) can contribute highly to other technologies, such as for industrial electronic or magnetic components, in view of the versatility of the material properties, such as high anisotropy, high coercivity, mechanical strength, chemical stability, and moderate saturation magnetization magneto-resistance [Petric2007, Kumbhar2012].

Moderate additions of aluminium were found to be promising to improve the refractoriness of Fe_3O_4-based materials without significant reduction of the electrical performance [Kovalevsky2012]. Weak p(O_2)-dependence of the conductivity and phase stability at 1673 to 1773 K suggest a broad range of conditions where $Fe_{3-x}Al_xO_4$-based anodes can be successfully used in the pyroelectrolysis process.

However, insufficient redox stability at lower temperatures causes dimensional changes and loss of mechanical integrity in the course of thermal cycling, imposing certain restrictions on the applications of such electrodes. One promising strategy is to include co-doping of magnetite with Mg and Al in the concentration range where aluminium provides an improvement of refractoriness without significant deterioration of electric properties, whilst magnesium increases the tolerance against oxidative decomposition [Kovalevsky2012].

Similar study was performed by Yaremchenko et al. for $(Mg, Fe)_3 O_4$ based spinel, where the temperature dependencies of the electrical conductivity exhibit a complex behaviour associated with changes in the major defect-chemistry mechanism and kinetically frozen cation distribution in the spinel lattice below 800 K [Yaremchenko2011].

While the level of electronic transport increases with iron content above 1370 to 1470 K, the conductivity behaviour in the intermediate-temperature range is strongly affected by temperature variations of the cation nonstoichiometry and cation redistribution between the octahedral and tetrahedral sublattices. Within the phase stability domain, the electronic transport is essentially $p(O_2)$-independent [Yaremchenko2011].

These results highlight a promising type of material to be used as consumable anode in iron pyroelectrolysis. Still, further optimization of the relevant properties is obviously needed.

1.4 The laser floating zone method

In the present work the Laser Floating Zone (LFZ) technique, was used to study the material for electrolyte (molten) and electrode (spinels) application. The LFZ is a peculiar and matured technique that belongs to a non-conventional group of techniques used for crystals production, presenting the advantages of growth of high melting point materials. Moreover, being a crucible free process allows the production of high purity crystals and composite fibres, avoiding mechanical stress and contamination during the solidification process due to the crucible material. [Kirkpatrick1975, Ritzert1996, Costa2005].

1.4.1 Method development

In 1902 A. Verneuil started to grow crystals using the method of flame fusion growth (fig 1.13a, b). For the first time, it was achieved the control of nucleation and thus single crystal of ruby and sapphire with melting points above 2000 ºC were grown [Scheel2003]. In this method the fluid medium consists in a melted material obtained by a flame [Kirkpatrick1975, Scheel2003]. A. Verneuil can be regarded as the father of crystal growth technology as his principles of nucleation control and crystal-diameter control were adapted later in most growth methods from melt, like Tammann, Stober, Bridgman, Czochralki, Kyropoulos, Stockbarger, etc. The important crystal pulling from melts named after Czochralski was effectively developed by Teal, Little and Dash (fig 1.13b) [Scheel2003].

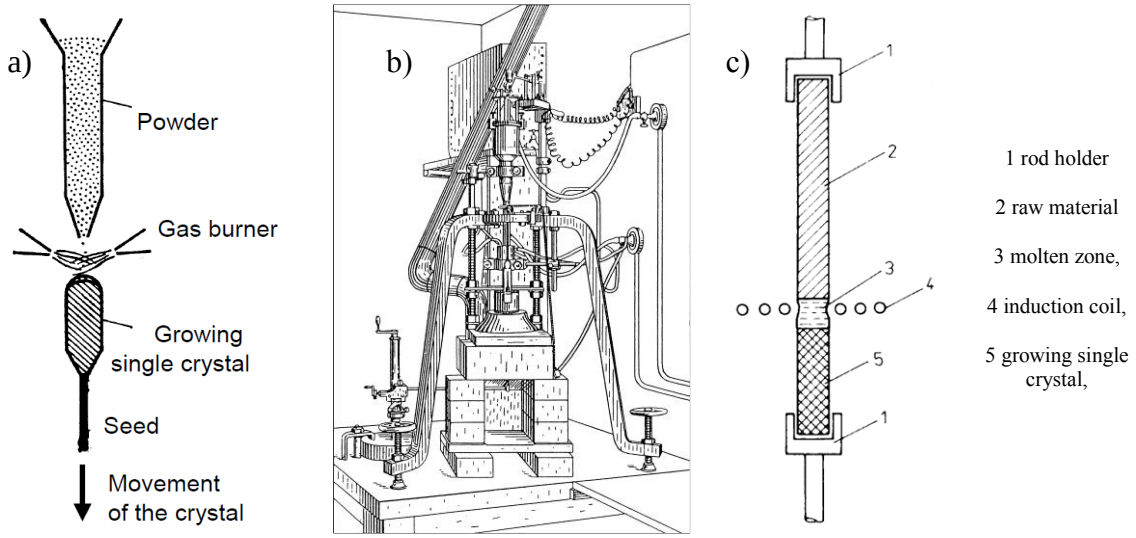

Figure 1.13 – Crystal growth from the melt, a and b) according to Verneuil method, c) improved system floating zone, adapted from [Leipner2014].

The discovery of the transistor at Bell Laboratories imposed the need to produce single crystals of semiconductor materials, being the first one germanium. Relatively large Ge crystal were produced in 1950 by Teal and Little using the process of crystal pulling from the melt [Scheel2003]. The multi-disciplinary nature of crystal growth technology and layer fabrication and the complex multi-parameter processes, where ten or more growth parameters have to be compromised and optimized, and also the scaling problem have blocked the scientific development of this important area. The deep understanding of the mechanism on experimental conditions allowed growing flat surfaces and interfaces of materials for important applications areas such as the case of optoelectronic and superconducting devices [Scheel2003].

The crystal growth process has suffered several improvements from its beginning. The power source to melt material started with a flame, which was improved by the employment of other power sources like induction coil (Fig. 1.13c), furnace, lamps and more recently laser systems as melting source [Ritzert1996, Scheel2003, Leipner2014]. The introduction of laser heating for the production of fibre shaped materials permits the development of high melting point materials almost impossible with conventional heating.

The equipment to grow single crystal fibres by the LFZ process (Fig. 1.14) has a workstation composed by systems that allow controlling and monitoring the growth process. Some systems obtain a uniform molten zone through a mirrors setup for shape manipulation of the laser beam (fig 1.14) [Ritzert1996, Costa2005, Carvalho2014] and also by rotational motion of the feed and seed rods [Costa2005, Carvalho2014].

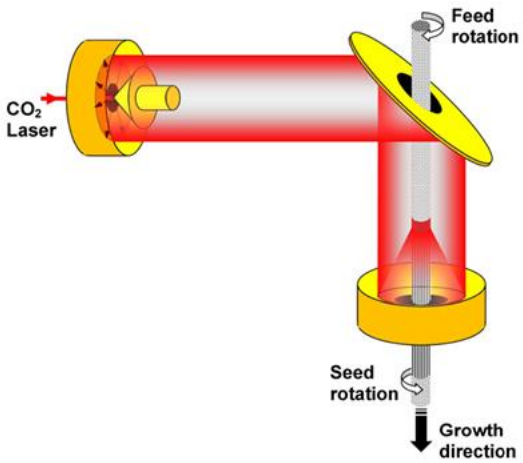

Figure 1.14 – Illustration of the laser floating zone apparatus [Carvalho2013].

The laser system must be sufficiently powerful to melt the material and maintain a stable condition of the molten zone [Ritzert1996]. Several types of laser systems here been used to grow materials, such as Nd:YAG [Costa2004, Diez2009], CO_2 [Costa1999, Costa2013, Ferreira2012] and more recently diode lasers [Ito2013].

The LFZ technique is basically a floating zone-like method where the heating element is a focused laser ring to create the molten zone. The growing process starts with basically four steps:

i) the alignment of the seed and pedestal rods, both centralized in the optical axis of the laser beam;
ii) the formation of a molten zone on the top of the rods increasing the laser power;
iii) the seed and feed rods are slowly and simultaneously brought together into laser beam until the molten tips and both touch each other to form a stable molten zone (Fig. 1.15);
iv) the motors start the pulling and rotation. This occurs after the equilibrium of molten zone, with its uniform temperature profile established.

To keep a constant volume, it is necessary to feed and pull at a fixed rate, since the crystal growth process is based in a mass conservation principle [Ritzert1996]. The ratio speeds between feed and seed rods determine the diameter of the as-grown fibre [Ritzert1996, Costa1999].

The main regions involved in LFZ process can be seen in Fig. 1.15: the feed rod, the molten zone and fibre single crystal. It is essential that the laser power remains stable and focused, so that the molten zone stays uniform during all growth process.

The growth speed and thermal conductivity of the material control the temperature gradient in the feed rod and crystal [Ritzert1996]. If the thermal gradient is high due to the lower thermal conductivity, the crystal is instantaneously “quenched” as it leaves the molten zone, causing higher residual stresses. A different effect occurs in the feed rod, as it decreases in temperature away from the melt, the powders change from highly sintered solids to loosely bonded powders, and eventually to loose powders that are hot enough to drive off the binder material but not hot enough to be sintered [Ritzert1996].

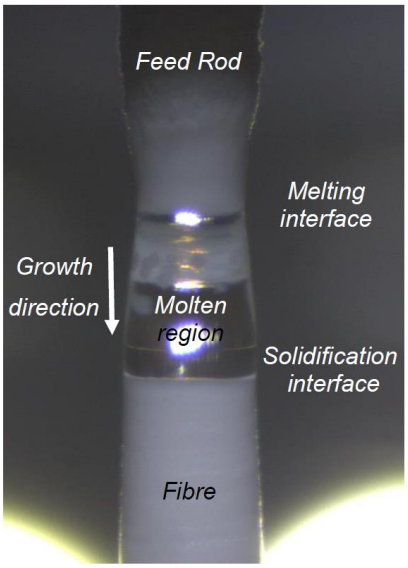

Figure 1.15 – Solid–liquid interface of a zirconia-mullite material growth by the LFZ method [Carvalho2014].

In the LFZ process the melt automatically adjusts to exactly the composition required to produce the appropriate steady state growth conditions [Costa2005]. Materials with high thermal conductivities tend to create internal stresses and become more difficult to grow than materials with low thermal conductivities. In some cases, fast growth can be advantageous due to the reduce time in the molten zone minimizing the vaporization process. However, in most cases, slow pulling rates originate crystals with superior crystallinity. Obviously, there are optimum experimental conditions that give the best results for each specific system [Ritzert1996].

The principal growth parameters that play a key role during growth of single crystals are feed rod characteristics, the growth rate, the growth atmosphere and its pressure, the temperature gradient, the molten zone temperature and the rotation rate. The effect of these parameters becomes even more acute in the growth of materials which may have intrinsic properties such as high density, low surface tension or a complicated phase diagram [Koohpayeh2008]. The growth parameters and their possible influences are summarized on Table 1.5.

Table 1.5 – Standard growth parameters and their possible influences during LFZ growth, adapted from [Koohpayeh2008].

Parameter	Influence
Feed rod characteristics	▪ A poorly compacted feed rod can lead to bubble formation in the molten zone or penetration of the melt into the feed rod, and also bubble formation in the growing crystal.
Crystallization rate	▪ Crystal growth at lower growth rates generally yields larger crystals; ▪ Slower growth rates give crystals with more homogeneous compositions and without second phases or inclusions. However, depending on the material and its phase stability, faster growth rates are sometimes needed to obtain crystals without inclusions; ▪ Crack formation is reduced when lower growth rates are used; ▪ Lower growth rates can lead to better crystal alignment and help to preserve the growth direction; ▪ Both higher and lower growth speeds can suppress the formation of low angle grain boundaries and twinning, depending upon the material in question; ▪ A lower growth rate is favourable for growing bubble-free crystals; ▪ In general, using a lower growth rate is more likely to give a planar growth front; ▪ The stability of a molten zone can be increased using either lower or higher growth speeds, depending upon the material in question.
Temperature gradient on molten zone	▪ Larger temperature gradients along the growth direction are more likely to cause cracking in the growing crystal due to thermal stresses; ▪ A sharper temperature gradient can lead to a concave solid/liquid interface towards the melt, while a reduction in the temperature gradient can give a convex interface; ▪ A steep temperature gradient helps to reduce the length of melting zone which can lead to a more stable molten zone; ▪ A lower molten zone temperature can help to prevent evaporation of components during growth and give a more homogeneous crystal.
Rotation rate	▪ Rotation is usually used to ensure efficient mixing in the molten zone; ▪ More homogeneous heating within the melt and around the sample can be achieved using rotation; ▪ Using a higher rotation rate can be a way of lowering the convexity of the interface, so giving a more stable molten zone; ▪ Rotation can lead to the formation of defects such as bubbles and low angle grain boundaries in the growing crystal.

1.4.2 Applications & improvements of LFZ technique

Crystal-growth technology including layer fabrication technology is of greatest importance for energy saving, for renewable energy, and for novel high technologies [Scheel2003]. In the last decades the growth of amorphous and crystalline materials (single and polycrystals), have been successfully reported in several material science area [Ritzert1996, LLorca2006, Costa 2004, Costa2005, Carrasco2009, Carvalho2010, Soares2011, Ferreira2012] and ref therein.

LFZ process has been developed into a quick extremely useful laboratory process to investigate amorphous, single-crystal and poly-crystals fibres that can be obtained by directional solidification from a melt induced by a beam laser incidence on the material [Ritzert1996]. This method was already used to study phase transformation kinetics, diffusion phenomena and crystallization path of different systems [Costa1999, Costa2001, Costa 2005].

The LFZ technique allows to produce oriented, small-diameter crystals that meet the requirements for high-temperature applications in today's advanced matrices [Ritzert1996], like high quality single crystals of a variety of oxides [Ritzert1996, Guptasarma2004, Carvalho2010, Soares2011], eutectic structures [LLorca2006, Carvalho2013] and highly oriented polycrystalline materials [Costa2005, Carrasco2009, Ferreira2012, Graça2013, Ramana2014].

Polycrystalline materials prepared by the LFZ method can achieve preferential crystals alignment due to the strong thermal gradient at the solidification interface [Ritzert1996, Costa 2005, Koohpayeh2008, Ferreira2012, Ramana2014]. Another advantage of the LFZ method is the high temperature reach due to the beam focus system. This technique allow the formation of high temperature metastable phases and the crystallization of incongruent phases due to high thermal gradients generated at the melt/fibre interface which can reach values of 10^3 to 10^4 ºC/cm [Ritzert1996, LLorca2006].

An improvement of the LFZ process can be made by the application of electrical stimulation during the growth process denominated as Electrically Assisted Laser Floating Zone (EALFZ). This technique was initially developed for superconductors materials processing, allowing to obtain an improvement on the crystals alignment, resulting in a very high electrical current density [Carrasco2009, Costa2004, Costa2005, Costa2013].

More recently, this technique has been applied to thermoelectrical materials, resulting in a power factor improvement [Ferreira2012, Madre2013]. In these works the current intensity and polarization revealed important influences on phase formation, morphology and grain alignment. This improvement can also be used to stimulate the pyroelectrolysis process in a quick way, due to the complexity of the pyroelectrolysis process and the extreme conditions that are necessary in conventional methods.

The LFZ method present some feasibility for the in situ, using the current or voltage appliance and the use of controlled atmospheres, allowing transformations or interactions between materials at very high temperatures [Ritzert1996, LLorca2006, Peña2007, Abell2008, Carrasco2009, Ferreira2012,]. The melting technique plus current appliance allow not only to stimulate the pyroelectrolysis process but also to study the interface reactions electrode/melted that occur at high temperature, in order to prepare materials to use as electrodes.

1.5 References

[Abell2008] – S.M. Koohpayeh, D. Fort, J.S. Abell, The optical floating zone technique: A review of experimental procedures with special reference to oxides, Progress in Crystal Growth and Characterization of Materials, 54 (2008) 121-137

[Allanore2008] – A. Allanore, H. Lavelaine, G. Valentin, J.P. Birat, F. Lapicque, Iron metal production by bulk electrolysis of iron ore particles in aqueous media; J. Electrochem. Soc.,155 (2008) E125-E129

[Allanore2013] – A. Allanore, L. Yin, D.R. Sadoway, A new nanodematerial for oxygen evolution in molten oxide electrolysis, Nature 497, 353–356 (16 May 2013), doi:10.1038/nature12134

[Ana1997] – A.M. Segadães, Refractários, Universidade de Aveiro, 1ª edição, Fundação João Jacinto Magalhães,1997

[Arriesgado2011] – R.F. Descallar-Arriesgado, N. Kobayashi, T. Kikuchi, R.O. Suzuki, Calciothermic reduction of NiO by molten salt electrolysis of CaO in CaCl2 melt Electrochimica Acta 56 (2011) 8422– 8429

[Barron2010] – A.R. Barron, Semiconductor Grade Silicon, Version 1.3: Jan 7, 2010 7:27 pm -06:00, http://cnx.org/content/m31994/1.3/ (last acess 3 January 2014)

[Carrasco2009] – M.F. Carrasco, R.F. Silva, J.M. Vieira, F.M. Costa, Pulling rate and current intensity competition in electrically assisted laser floating zone, Supercond. Sci. Tech. 22 (2009) 065016, http://dx.doi.org/10.1088/0953-2048/22/6/065016.

[Cartaxo2007] – M.A.M. Cartaxo, T.A.S. Ferreira, M.R. Nunes, M. Helena Mendonça, M.I. da Silva Pereira, F.M. Costa, Studies on FeeCo spinel electrodes, Solid State Sciences 9 (2007) 744e749, doi:10.1016/j.solidstatesciences.2007.05.001

[Carvalho2010] – R.G. Carvalho, A.J.S. Fernandes, F.J. Oliveira, E. Alves, N. Franco, C. Louro, R.F. Silva, F.M. Costa, Single and polycrystalline mullite fibres grown by laser floating zone technique, J. Eur. Ceram. Soc. 30 (2010) 3311–3318.

[Carvalho2013] – R.G. Carvalho, M.S. Pires, A.J.S. Fernandes, R.F. Silva, F.M. Costa, Directionally solidified eutectic and off-eutectic mullite–zirconia fibres, J. Eur. Ceram. Soc. 33 (2013) 953–963, http://dx.doi.org/10.1016/j.jeurceramsoc. 2012.09.032.

[Carvalho2014] – R.G. Carvalho, Laser assisted directional solidification of zirconia-based eutectics, PhD thesis, Physics Department, Aveiro University, 2014

[Chen2000] – G.Z. Chen, D.J. Fray, T.W. Farthing, Direct electrochemical reduction of titanium dioxide to titanium in molten calcium chloride, Nature 407 (2000) 361–364.

[Cooper2006] – B.D. Cooper, Electrode Materials for the Electrolysis of Metal Oxides, Bs Thesis, Department of Materials Science and Engineering, Massachusetts Institute of Technology, May 2006, http://dspace.mit.edu/bitstream/handle/1721.1/35072 /71231057.pdf?sequence=1 , last access Feb 2014

[Costa1999] – F.M. Costa, R.F. Silva, J.M, Vieira, Phase transformation kinetics during thermal annealing of LFZ Bi-Sr-Ca-Cu-O superconducting fibers in the range 800-870 ºC, Physica C, 323 (1999) 23-41

[Costa2001] – F.M. Costa, R.F. Silva, J.M. Vieira, Diffusion phenomena and crystallization path during the growth of LFZ Bi-Sr-Ca-Cu-O superconducting fibres, Supercond. Sci. Tech. 14 (2001) 910-920, http://dx.doi.org/10.1088/0953-2048/14/11/305

[Costa2004] – F.M. Costa, M.F. Carrasco, N. Ferreira, R.F. Silva, J.M. Vieira, LFZ fibre texture modification induced by electrical polarization, Physica C 408–410 (2004) 915–916, doi:10.1016/j.physc.2004.03.161

[Costa2005] – F.M. Costa, M.F. Carrasco, R.F. Silva, J.M. Vieira, High Tc superconducting fibers processed by conventional and electrical assisted laser floating zone, Chapter 4, In: Perspectives on Superconductivity Research ISBN 1-59454-523-5, Editor: P. S. Lewis, pp. 0-00 © 2005 Nova Science Publishers, Inc.

[Costa2013] – F.M. Costa, S. Rasekh, N.M. Ferreira, A. Sotelo, J.C. Diez · M.A. Madre, Effect of Current Polarity on BSCCO/Ag Ceramics Textured by Electrically Assisted Laser Floating Zone, J Supercond Nov Magn (2013) 26:943–946, DOI 10.1007/s10948-012-2029-8

[Diez2009] – J.C. Diez, E. Guilmeau, M.A. Madre, S. Marinel, S. Lemonnier, A. Sotelo, Improvement of Bi2Sr2Co1.8Ox thermoelectric properties by laser floating zone texturing Solid State Ionics, Volume 180, Issues 11–13, 22 June 2009, Pages 827–830, DOI: 10.1016/j.ssi.2009.02.004

[DoITPoMS2014] – DoITPoMS is funded by the UK Centre for Materials Education and the Department of Materials Science and Metallurgy, University of Cambridge, http://www.doitpoms.ac.uk/tlplib/recycling-metals/printall.php, last acess 2-04-2014

[Domingues2013] – E.M. Domingues, E.V. Tsipis, A.A. Yaremchenko, F.M. Figueiredo, J.C. Waerenborgh, A.V. Kovalevsky, J.R. Frade, Redox stability and electrical conductivity of $Fe_{2.3}Mg_{0.7}O_{4\pm\delta}$ spinel prepared by mechanochemical activation, Journal of the European Ceramic Society 33 (2013) 1307–1315, http://dx.doi.org/10.1016/j.jeurceramsoc.2012.12.014

[ETP2010] – Energy Technology Perspectives: Scenarios & Strategies to 2050, Internacional Energy Agency, France 2010, www.iea.org/Textbase/about/copyright.asp, Last acess Feb 2014

[EWC2014] – http://www.energy-without-carbon.org/IronAndSteel, last accessed April 2014

[Fergus1998] – J.W. Fergus, Chemical sensors for use in processing molten metals, Trans. Amer. Found. Soc., 106 (1998) 125-130

[Ferreira2012] – N.M. Ferreira, Sh. Rasekh, F.M. Costa, M.A. Madre, A. Sotelo, J.C. Diez, M.A. Torres, New method to improve the grain alignment and performance of thermoelectric ceramics, Mater. Lett. 83 (2012) 144–147, http://dx.doi.org/10.1016/j.matlet.2012.05.131

[Forsmo2008] – S.P.E. Forsmo, S.E. Forsmo, P.O. Samskog, B.M.T. Björkman, Mechanisms in oxidation and sintering of magnetite iron ore green pellets, Powder Technology 183 (2008) 247–259, doi:10.1016/j.powtec.2007.07.032

[Fried2004] – N.A. Fried, D.R. Sadoway, Titanium Extraction by Molten Oxide Electrolysis, TMS Meeting, Charlotte, NC, March 15, 2004, http://web.mit.edu/dsadoway/www/MOE_Ti.pdf

[Gibilaro2011] – M. Gibilaro, J. Pivato, L. Cassayre, L. Massot, P. Chamelot, P. Taxil, Direct electroreduction of oxides in molten fluoride salts, Electrochimica Acta 56 (2011) 5410–5415, doi:10.1016/j.electacta.2011.02.109

[Gmitter2008] – A.J. Gmitter, The influence of inert anode material and electrolyte composition on the electrochemical production of oxygen from molten oxides, Master Tesis at Massachusetts Institute of Technology , February 2008

[Goriparti2014] – S. Goriparti, E. Miele, F. De Angelis, E. Di Fabrizio, R.P. Zaccaria, C. Capiglia, Review on recent progress of nanostructured anode materials for Li-ion batteries, 257, July 2014, 421–443, http://dx.doi.org/10.1016/j.jpowsour.2013.11.103

[Graça2013] – M.P.F. Graça, M.V. Peixoto, N. Ferreira, J. Rodrigues, C. Nico, F.M. Costa, T. Monteiro, Optical and dielectric behavior of EuNbO4 crystals, J. Mater. Chem. C, 2013,1, 2913-2919, DOI: 10.1039/C3TC00793F

[Guignard2008] – M. Guignard, L. Cormier, Environments of Mg and Al in MgO–Al2O3–SiO2 glasses: A study coupling neutron and X-ray diffraction and Reverse Monte Carlo modeling, Chem. Geol. 256 (2008) 111–118

[Guptasarma2004] – P. Guptasarma, M.S. Williamsen, S.K. Ray, Floating Zone Growth of Bulk Single Crystals of Complex Oxides, MRS Proceedings 848 (2004), http://dx.doi.org/10.1557/PROC-848-FF10.3

[Haarberg2005] – G.M. Haarberg, Materials Technology Sustainable Electrolysis, NTNU, Trondheim, Norway, 2005, http://www.okabe.iis.u-tokyo.ac.jp/core-to-core/rmw/RMW3/slide/RMW3_03_Haarberg_C.pdf, last acess 9-Feb-2014

[Harrison1999] – R.J. Harrison, A. Putnis, The magnetic properties and crystal chemistry of oxide spinel solid solutions, Surveys in Geophysics 19: 461–520, 1999.

[Harrison1999B] – R.J. Harrison and A. Putnis, The magnetic properties and crystal chemistry of oxide spinel solid solutions, Surveys in Geophysics 19: 461–520, 1999, Kluwer Academic Publishers

[Hiremath2003] - Vijay A. Hiremath and A. Venkataraman, Dielectric, electrical and infrared studies of g-Fe2O3 prepared by combustion method, Bull. Mater. Sci., Vol. 26, No. 4, June 2003, pp. 391–396

[Hiu2013] – F. Xiao-hui , Y. Zhi-yuan, G. Min, Li Wen-qi , J.I. Zhi-yun, Influence of O2 Content in Circulating Flue Gas on Iron Ore Sintering, Journal of iron and steel research, international. 2013, 20(6), 01-06

[Hu2006] – HU Chang-qing, C. Li-yun , Z. Chun-xia, Q.I. Yuan-hong, Y. Rui-yu, Emission Mitigation of C02 in Steel Industry: Current Status and Future Scenarios, Journal of Iron and Steel Research International 2006, 13(6): 38-42, 52

[Hu2010] – M. Hu, R.P. Ji, J.S. Jiang, Hydrothermal synthesis of magnetite crystals: From sheet to pseudo-octahedron, Materials Research Bulletin 45 (2010) 1811–1815, doi:10.1016/j.materresbull.2010.09.023

[Inoishi2012] – A. Inoishi, S. Ida, S. Uratani, T. Okanoc, T. Ishihara, High capacity of an Fe–air rechargeable battery using LaGaO3-based oxide ion conductor as an electrolyte, Phys. Chem. Chem. Phys. (2012) 14, 12818–12822

[IPPC2001] – Integrated Pollution Prevention and Control (IPPC): Best Available Techniques Reference Document on the Production of Iron and Steel, European Comission, December 2001

[IS2014] – Iron and Steel: Technology and Resources, The Institute for Industrial Productivity, http://ietd.iipnetwork.org/ (last acess: January 2014)

[Ito2013] – T. Ito, T. Ushiyama, Y. Yanagisawa, Y. Tomioka, Isamu Shindo, A. Yanase, Laser-diode-heated floating zone (LDFZ) method appropriate to crystal growth of incongruently melting materials, Journal of Crystal Growth, Volume 363, 15 January 2013, Pages 264–269, DOI: 10.1016/j.jcrysgro.2012.10.059

[Jiménez2012] – C. Jiménez, C. Sáez, F. Martínez, P. Cañizares, M.A. Rodrigo, Electrochemical dosing of iron and aluminum in continuous processes: A key step to explain electro-coagulation processes, Separation and Purification Technology 98 (2012) 102–108, http://dx.doi.org/10.1016/j.seppur.2012.07.005

[Jung2004] – I.H. Jung, S.A. Decterov, A.D. Pelton, Critical thermodynamic evaluation and optimization of the FeO-Fe2O3-MgO-SiO2 system, Met. Mat. Trans. B, 35B (2004) 877

[Kharkiv2012] – Medical chemistry: module ii, physical and colloid chemistry, V. N. Karazin Kharkiv National University, Kharkiv – 2012

[Kim2002] – Y. Kim, E. Worrell, International comparison of CO2 emission trends in the iron and steel industry, Energy Policy 30 (2002) 827–838

[Kim2011] – H. Kim, J. Paramore, A. Allanore, D.R. Sadoway, Electrolysis of Molten Iron Oxide with an Iridium Anode: The Role of Electrolyte Basicity Journal of The Electrochemical Society, 158 (10) E101-E105 (2011) 0013-4651/2011/158(10)/E101/5/$28.00

[Kirkpatrick1975] – R.J. Kirkpatrick, Crystal Growth from the melt: a review, American Mineralogist, 1975, 60, 798-814

[Koohpayeh2008] – S.M. Koohpayeh, D. Fort, J.S. Abell, "The optical floating zone technique: A review of experimental procedures with special reference to oxides", Progress in Crystal Growth and Characterization of Materials, 54(2008)121-137.

[Kovalevsky2012] – A.V. Kovalevsky, E.N. Naumovich, A.A. Yaremchenko, J.R. Frade, High-temperature conductivity, stability and redox properties of Fe3-xAlxO4 spinel-type materials, J. Europ. Ceram. Soc. 32 (2012) 3255-3263.

[Kumbhar2012] – V.S. Kumbhar, A.D. Jagadale, N.M. Shinde, C.D. Lokhande, Chemical synthesis of spinel cobalt ferrite (CoFe2O4) nano-flakes for supercapacitor application, Applied Surface Science 259 (2012) 39– 43

[Lantelme2013] – F. Lantelme, H. Groult, Chapter 9 – Inert Anode Dvelopement for high-temperature molten salts, Molten Salts Chemistry: From Lab to Applications, First Edition 2013, Elsevier, ISBN:978 -0-12-398538-5

[Leipner2014] – H.S. Leipner, R. Krause-Rehberg, Defects in crystals, Part III: Role in technology, http://www.cmat.uni-halle.de/~hsl/Realstruktur/Technology%20I%20-%20Introduction.pdf, last acess 3-april-2014

[LLorca2006] – J. LLorca, V.M. Orera, Directionally solidified eutectic ceramic oxides, Prog. Mater. Sci. 51 (2006) 711–809, http://dx.doi.org/10.1016/j.pmatsci.2005.10.002

[Liang2013] – X. Liang, Y. Zhong, S. Zhu, H. He, P. Yuan, J. Zhu, Z. Jiang, The valence and site occupancy of substituting metals in magnetite spinel structure $Fe_{3-x}M_xO_4$ (M = Cr, Mn, Co and Ni) and their influence on thermal stability: An XANES and TG-DSC investigation, Solid State Sciences 15 (2013) 115 -122, http://dx.doi.org/10.1016/j.solidstatesciences.2012.10.005

[Madre2013] – M.A. Madre, F.M. Costa, N.M. Ferreira, A. Sotelo, M.A. Torres, G. Constantinescu, Sh. Rasekh, J.C. Diez, Preparation of high-performance Ca3Co4O9 thermoelectric ceramics produced by a new two-step method, Journal of the European Ceramic Society 33 (2013) 1747–1754, http://dx.doi.org/10.1016/j.jeurceramsoc.2013.01.029

[Mapworld2014] – http://www.mapsofworld.com/world-mineral-map.htm, last accessed Feb 2014

[Mishra2005] – B. Mishra, D.L. Olson, Molten salt applications in materials processing, Journal of Physics and Chemistry of Solids 66 (2005) 396–401

[Modi1996] – K.B. Modi, H.H. Joshi, R.G. Kulkarni, Magnetic and electrical properties of Al3+-substituted MgFe204, Journal of Materials Science 31 (1996) 1311-1317

[Mohanty2012] – J. K. Mohanty, M. S. Jena1, A. K. Paul, Integrated Mineralogical Characterisation of Banded Iron Ores of Orissa and Its Implications on Beneficiation, Journal of Minerals and Materials Characterization and Engineering, 2012, 11, 1133-1142, Published Online December 2012, http://www.SciRP.org/journal/jmmce

[Muwanguzi2010] – A.J.B. Muwanguzi, Characterisation of Muko Iron Ores (Uganda) for the different routes or iron production, Licentiate Thesis, Stockholm 2010, Department of Materials Science and Engineering, Division of Applied Process Metallurgy Royal Institute of Technology, SE-100 44 Stockholm, Sweden

[Nadoll2014] – P. Nadoll, T. Angerer, J.L. Mauk, D. Frenchd, J. Walshe, The chemistry of hydrothermal magnetite: A review, Ore Geology Reviews 61 (2014) 1–32, http://dx.doi.org/10.1016/j.oregeorev.2013.12.013

[Nell1991] – J. Nell, B.J. Wood, High-temperature electrical measurements and thermodynamic properties of Fe3O4-FeCr2O4-MgCr2O4-FeAl2O4 spinels, American Mineralogist, Volume 76, pages 405-426, 1991

[O'Neill1983] – H.Sr.C. O'Neill, A. Navrotsky, Simple spinels: crystallographic parameters, cation radii, lattice energies, and cation distribution, American Mineralogist, (1983) 68, 181-194

[Ovsyannikov2008] – S.V. Ovsyannikov, V.V. Shchennikov, S. Todo, Y. Uwatoko, A new crossover in Fe3O4 magnetite under pressure near 6 GPa: modification to 'ideal' inverse cubic spinel?, J. Phys.: Condens. Matter 20 (2008) 172201 (6pp), doi:10.1088/0953-8984/20/17/172201

[Pardo2012] – N. Pardo, J.A. Moya, K. Vatopoulos, Prospective Scenarios on Energy Efficiency and CO2 Emissions in the EU Iron & Steel Industry, JRC Scientific and Policy Reports, 2012, Joint Research Centre, Netherlands, doi:10.2790/64264

[Park1999] – J.C. Park, D. Kim, C. S. Lee and D. K. Kim, A New Synthetic Route to Wüstite, Bull. Korean Chem. Soc. 1999, Vol. 20, No. 9 1005

[Peña2007] – P.B. Oliete, J.I. Peña, Study of the gas inclusions in Al2O3/Y3Al5O12 and Al2O3/Y3Al5O12/ZrO2 eutectic fibers grown by laser floating zone, Journal of Crystal Growth 304 (2007) 514–519

[Pérez2011] – D. Pérez-Coll, P. Nuñez, J.R. Frade (2011), "Reducibility of ceria-based materials exposed to fuels and under fuel/air gradients" in Advances in Ceramics - Synthesis and Characterization, Processing and Specific Applications, C Sikalidis, New York, InTech, Chapt.15, pp. 337-362

[Petric2007] – A. Petric, H. Lingw, Electrical Conductivity and Thermal Expansion of Spinels at Elevated Temperatures, J. Am. Ceram. Soc., 90 [5] 1515–1520 (2007), DOI: 10.1111/j.1551-2916.2007.01522.x

[Ramana2014] – E.V. Ramana, N.M. Ferreira, M.P.F. Graça, M.A. Valente, Effect of Processing Parameters on Ferroelectric Properties of 0.5(Ba,Ca)TiO3-0.5Ba(Zr,Ti)O3:Bulk, Thin Films and Fibers, Ferroelectrics, 466:1, 36-41, DOI:10.1080/00150193.2014.894857

[Ritzert1996] – F. Ritzert, L. Westfall, Laser-heated floating zone production of single-crystal fibers, NASA Technical Memorandum, Vol 4732, N.A.S.A. Office of Management, Scientific and Technical Information Program, (1996).

[Sadoway94] – D.R. Sadoway, New opportunities for waste treatment by electrochemical processing in molten salts, Metals and Materials Waste Reduction, Recovery and Remediation, Edited by K.C. Liddel, R. G. Bautista, R. J. Orth, The Minerals, Metals & Materials Society, 1994 73-76

[Sadoway95] – D.R. Sadoway, New opportunities for metals extraction and waste treatment by electrochemical processing in molten salts, J. Mater Res. Vol 10 N 3 487-492, Mar 1995

[Santos1965] – J.L.G. dos Santos, Ensaios com o minério de ferro de Moncorvo na Lurgi Gesellschaft fur Chemie und Huttenwesen m.b.H. (FrankFurt-Main), Bol. Minas (Lisboa) 2(1): 3/17, Jan/Mar 1965

[Scheel2003] – H.J. Scheel, The development on crystal growth Technology, in Crystal Growth Technology, Edited by Hans J. Scheel, Tsuguo Fukuda, John Wiley & Sons, Ltd, ISBN: 0-471-49059-8, 2003

[Schinko2014] – T. Schinko, B. Bednar-Friedl, K.W. Steininger, W.D. Grossmann, Switching to carbon-free production processes: Implications for carbon leakage and border carbon adjustment, Energy Policy 67 (2014) 818–831, http://dx.doi.org/10.1016/j.enpol.2013.11.077

[Schrantz2013] – K. Gajda-Schrantz, S. Tymen, F. Boudoire, R. Toth, D.K. Bora, W. Calvet, M. Gratzel, E.C. Constabled and A. Braun, Formation of an electron hole doped film in the a-Fe2O3 photoanode upon electrochemical oxidation, Phys.Chem. Chem. Phys., 2013, 15, 1443, 10.1039/c2cp42597a

[Skomurski2010] – F.N. Skomurski, Sebastien Kerisit, Kevin M. Rosso, Structure, charge distribution, and electron hopping dynamics in magnetite (Fe3O4) (1 0 0) surfaces from first principles, Geochimica et Cosmochimica Acta 74 (2010) 4234–4248, doi:10.1016/j.gca.2010.04.063

[Smith2000] – D.R. Smith, R.F. Cooper, Dynamic oxidation of a Fe2+‡-bearing calcium-magnesium- aluminosilicate glass: the effect of molecular structure on chemical difusion and reaction morphology, Journal of Non-Crystalline Solids 278 (2000) 145±163

[Soares2011] – M.R.N. Soares, C. Nico, M. Peres, N. Ferreira, A.J.S. Fernandes, T. Monteiro, F.M. Costa, Structural and optical properties of europium doped zirconia single crystals fibers grown by laser floating zone technique, J. Appl. Phys. 109 (2011) 013516, http://dx.doi.org/10.1063/1.3527914

[STEP2014] – N. Enteria, A. Akbarzadeh, Solar Energy Sciences and Engineering Applications, Solar Thermal Electrochemical production: Chapter 8.3.3 - Step Iron CRC Press/Balkema, Taylor & Francis Group, London, pag 239-243 UK, 2014

[Takeno2005] – N. Takeno, Atlas of Eh-pH diagrams, Intercomparison of thermodynamic databases, Geological Survey of Japan Open File Report No.419, National Institute of Advanced Industrial Science and Technology, Research Center for Deep Geological Environments, May 2005

[Tan2009] – S. Tan, T. Örs, K. Aydınol, T. Öztürk, I. Karakaya, Synthesis of FeTi from mixed oxide precursors, J. Alloys & Comp., 475 (2009) 368–372

[Teja2009] – A.S. Teja and P.Y. Koh, Synthesis, properties, and applications of magnetic iron oxide nanoparticles, Progress in Crystal Growth and Characterization of Materials, 55 (2009) 22-45, doi:10.1016/j.pcrysgrow.2008.08.003

[Tilquin95] – J.Y. Tilquin, J. Glibert, P. Claes, Anodic polarization in molten silicates, Journal of Non-Crystalline Solids 188 (1995) 266-274

[UKS2009] – UK Steel Annual Review 2009, London Office Broadway House, Tothill Street, London, 2009, www.eef.org.uk/uksteel, last acess Feb 2014

[US2007] – Technical Feasibility Study of Steelmaking by Molten Oxide Electrolysis, U.S. Department of Energy, Energy Efficiency and Renewable Energy, September 2007

[Varshney2012] – D. Varshney, A. Yogi, Structural, transport and spectroscopic properties of Ti4+ substituted magnetite: Fe3−xTixO4, Materials Chemistry and Physics 133 (2012) 103– 109, doi:10.1016/j.matchemphys.2011.12.068

[Vasudevan2013] – S. Vasudevan, Anodes for Electrochemcial Processes (Part-I), Research Journal of Chemical Sciences, Vol. 3(5), 1-2, May (2013)

[Verink2000] – E.D. VERINK, JR., Simplified Procedure for Constructing Pourbaix Diagrams, pags 111 – 124, Uhlig's Corrosion Handbook, Second Edition, Edited by R. Winston Revie. ISBN 0-471-15777-5 © 2000 John Wiley & Sons, Inc

[Wang2007] – D. Wang, Molten Oxide Electrolysis: Towards “Green” Steelmaking & Lunar in situ Resource Utilization, 3rd Reactive Metals Workshop, MIT, Cambridge, Mar. 3, 2007

[Wang2008] – W. Shu-Ian, G.M. Haarberg, E. Kvalheim, Electrochemical Behavior of Dissolved FeZ03 in Molten CaClz-KF, Journal of Iron and Steel Research International. 2008, 15(6): 48-51

[wang2011] – D. Wang, A.J. Gmitter, D.R. Sadoway, Production of Oxygen Gas and Liquid Metal by Electrochemical Decomposition of Molten Iron Oxide, Journal of The Electrochemical Society, 158 (6) E51-E54 (2011)

[Wang2012] – S. Wang, J. Ge, Y. Hu, H. Zhu, S. Jiao, Electrochemical reduction of iron oxide in molten sodium hydroxide based on aNi0.94Si0.04Al0.02 metallic inert anode, Electrochimica Acta (2010), doi:10.1016/j.electacta.2012.09.044

[Welch1999] – B.J. Welch, Aluminum Production Paths in the New Millennium, JOM, 51 (5) (1999), pp. 24–28

[Wiedenroth2003] – A. Wiedenroth, C. Russel, The effect of MgO on the thermodynamics of the Fe2+/Fe3+-redox equilibrium and the incorporation of iron in soda-magnesia-aluminosilicate melts, Journal of Non-Crystalline Solids 320 (2003) 238–245, doi:10.1016/S0022-3093(03)00076-0

[Worrell2010] – E. Worrell, Paul Blinde, Maarten Neelis, Eliane Blomen, and Eric Masanet, Energy Efficiency Improvement and Cost Saving Opportunities for the U.S. Iron and Steel Industry: An ENERGY STAR® Guide for Energy and Plant Managers, Energy Analysis Department, Environmental Energy Technologies Division, Ernest Orlando Lawrence Berkeley National Laboratory, University of California, Berkeley, CA 94720, October 2010

[WSA2013] – World Steel Association 2013, ISBN 978-2-930069-73-9, http://www.worldsteel.org (last acess Jan 2014)

[Yamashita2008] – M. Yamashita, Studies on the redox state of metal ions in glass and the basic properties of glass melts, PhD thesis, Osaka University, 2008

[YamashitaASS2008] – T. Yamashita, P. Hayes, Analysis of XPS spectra of Fe2+ and Fe3+ ions in oxide materials, Applied Surface Science 254 (2008) 2441–2449, http://dx.doi.org/10.1016/j.apsusc.2007.09.063

[Yaremchenko2011] – A.A. Yaremchenko, A.V. Kovalevsky, E.N. Naumovich, V.V. Kharton, J.R. Frade, High-temperature electrical properties of magnesiowustite Mg1−xFexO and spinel Fe3−x−yMgxCryO4 ceramics, Solid State Ionics 192 (2011) 252–258

2 Experimental procedure

This chapter will briefly disclose the application of Laser Floating Zone method (LFZ) for preparation and studies of the electrolyte and spinel compositions. The electrochemical cell preparation to simulate the pyroelectrolysis process will be also described in detail, together with the techniques used for samples and cell characterization. More details of the equipment and experimental conditions used will be given in respective paper of each chapter. This chapter will have the following index:

2.1 Laser Floating Zone method

For electrolyte characterization was selected the Laser Floating Zone (LFZ) method. This technique allows growing materials with very high melting temperature, due to the narrow laser beam focus. Moreover, this method avoids the usual contaminations due to reactions of molten material with crucible walls. The as-grown material exhibits a fibre shape, as described in chapter 1.4. The LFZ equipment used in the present work includes a laser system; a growth chamber (with a controlled atmosphere); a homemade monitoring system (laser parameters, pulling rate and rotation speed) and an image capture system. Fig 2.1 shows photographs of this LFZ system, depicting the core elements of the system as well a zoom of the growth chamber, where the growing process occurs.

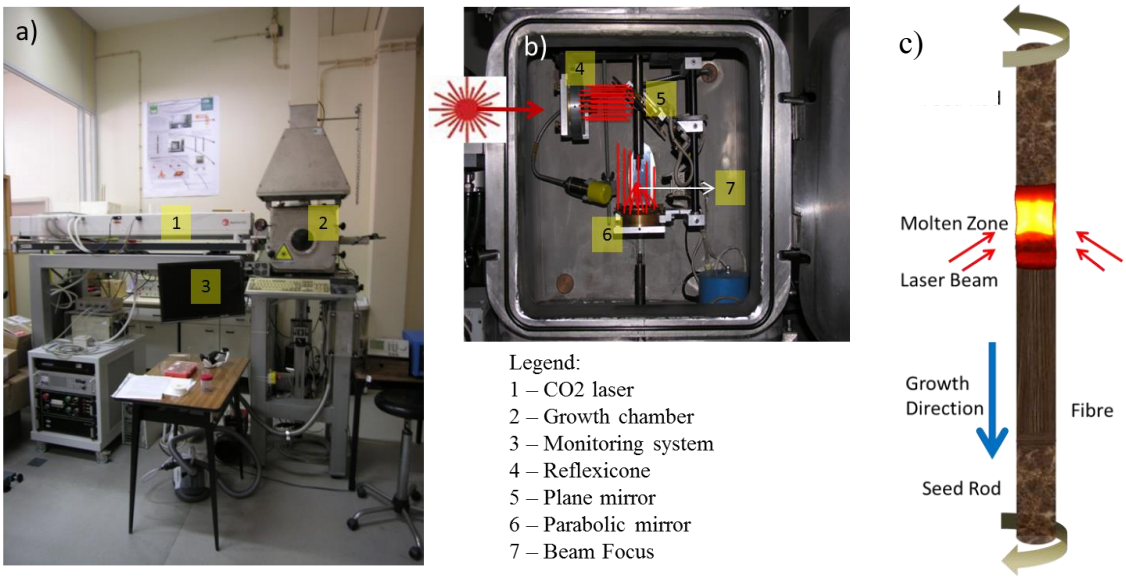

Figure 2.1 – a) LFZ system, b) Growth chamber, c) Identification of the several regions during the LFZ growth process.

The system comprises a continuous 200 W CO_2 laser (Spectron SLC, λ = 10.6 µm) with a beam spot size of 0.6 mm. A homemade program based in Labview® software (from National Instrument®), was used for monitoring and control of the LFZ growth system, including the following hardware:

- Laser: on/off emission; power value (melting temperature), open/closed internal and external shutters;

- Motors: growth speed and direction, as well as the homogeneity of the fibres by rotation of feed and seed rods;
- Image capture and its control parameters (zoom, contrast and brightness) allow us to get a better visualisation of the molten zone and mainly of the melt/solidification interfaces.

The growth chamber (Fig. 2.1b), where the growth occurs due to incidence of the CO_2 laser beam on precursor rods, can work at different atmospheres and pressure (1 – 2 atm) in air or other gases and in lower pressure (10^{-5} – 1 atm). In this work the growth was conducted in air under environmental conditions.

To melt uniformly the feed/seed rods precursor, the laser beam is transformed from a ring road into a circular crown-shape, using a reflexicone (4). Afterwards, it is reflected by a planar mirror (5) towards a parabolic mirror (6) that converges the beam to the top of the rod precursors, where all the beam laser power is located (7). Fig. 2.1c is a zoom of the molten zone and of the adjacent regions observed during the growth by the LFZ method.

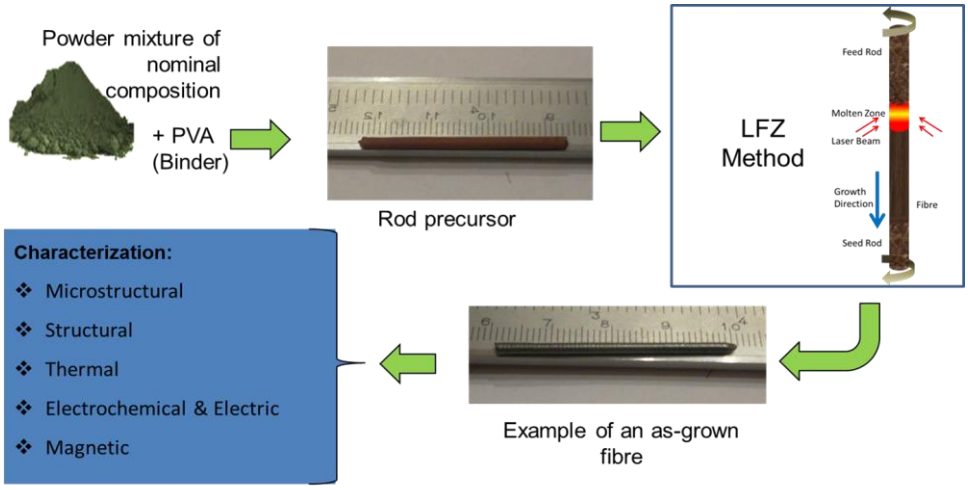

Figure 2.2 –Schematic procedure for preparation of fibres by the LFZ method.

The material to be used as precursors in the LFZ process should present a cylindrical shape to favour the chemical and thermal homogenization during the growth process. To start the growth process, the feed rod precursor is placed on laser beam focus to be melted. Afterwards, the seed rod precursor is immersed into the melt. The seed is pulled out while the feed is merged, allowing the fibre to grow through the cooling of the pulled material from the molten zone. The temperature of the pulled material decreases, leading to the change of the free energy and allowing the crystallization process.

The rod precursors were produced by cold extrusion of a paste made by adding the PVA (*PolyVinyl Alcohol*) to the powder. The extruded material presents a cylindrical shape that is dried at room temperature in atmospheric conditions, to get mechanical strength and allow to be used it as feed and seed bars for the LFZ process, as described in Fig. 2.2. The fibres with diameters of 1 to 3 mm and length up to 10 cm, were grown with a speed of 10 – 400 mm/h at 5 – 15 rpm. The as-grown fibres were characterized using the techniques described in chapter 2.3

2.2 Cells for studying pyroelectrolysis process

To simulate the electrolysis process in a laboratory scale, an electrochemical cell containing the electrolyte and electric electrodes was prepared (Fig. 2.3). This electrochemical cell was heated in a furnace from room temperature until the selected temperature to perform the pyroelectrolysis process. The cell was filled up with the electrolyte and electric contacts were made in order to study the iron electrolysis for different conditions: temperature, time, electrolyte composition, electrode configurations and applied voltage, as will presented in chapter 6.

Magnesium aluminium silicate ($MgO - Al_2O_3 - SiO_2$, MAS) glass-ceramic system was chosen to be used as electrolyte with different iron amount: $(100 - x)$ $(Mg_{0.203}\ Al_{0.374}\ Si_{0.423}\ O_{1.61}) \bullet$ Fex Oy, with x = 0, 2, 4 and 8 (mol%). The properties and the iron effects of this electrolyte (MAS_Fe), will be discussed hereafter in chapter 3.

2.2.1 Fabrication and assembling of the electrochemical cells

The electrochemical cell used in the present study consists of a yttria stabilized zirconia (YSZ) ceramic end tube with ~ 1 cm of diameter and ~ 5 – 10 cm of height, as shown in Figs. 2.3. The electrodes represented in Fig. 2.3a, were made using platinum ink and/or wire, allowing the electrolysis process to be performed and also impedance spectroscopy measurements. A picture of the cell after electrodes is shown in Fig. 2.3b.

The electrode position allows us to study the effect of conduction mechanisms:

- Electron blocking cell: between electrode 1 and 3;
- Direct electrolysis: between electrode 1 and 2.

The cathode position determinates the region where iron concentration occurs, the difference between these two processes will be shown in chapter 6. In all experiments of iron pyroelectrolysis, the electrolyte used was prepared by the LFZ process. The obtained fibres of the electrolyte (MAS_Fe) were crushed and ball-milled in ethanol to produce a fine glass powder to fill the inner of the cell (crucible) as electrolyte.

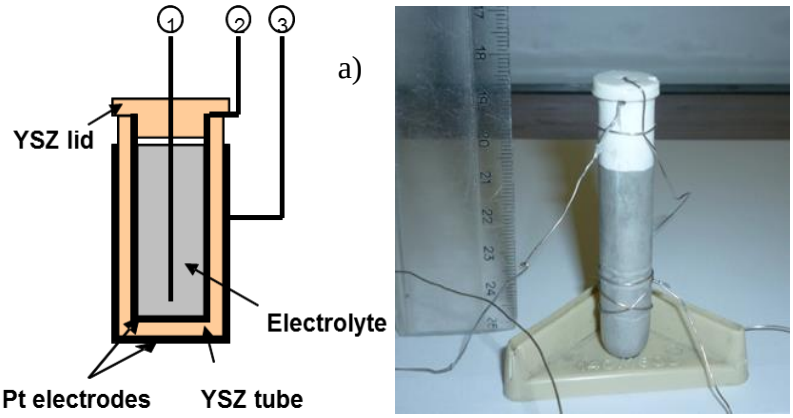

Figure 2.3 – Set-up of the electrochemical cell used: a) scheme, b) photo of the Pt wire as anode.

After filling with electrolyte, a platinum wire (~ 0.5 mm) is put in centre of the cell as an inner electrode (1). The cell is closed by an YSZ lid and this setup (alumina crucible, electrochemical cell, electrodes contact), was put on a conventional furnace in a vertical position and heated at 5 ºC/min, until reached the melting point of the electrolyte, which is near to the melting point of iron oxide (~ 1450 ºC). Several experiments of the electrolysis process were performed in various regimes and different configurations, in order to understand the iron deposition effect due to: iron concentration on the electrolyte, electrode configuration and the regime type, as will be present in respective chapter 6. Each experiment needs a new electrochemical cell preparation, since the cell must be destroyed for *post-mortem* analysis.

2.2.2 Operation regimes for performing pyroelectrolysis process

In order to understand the effects of temperature, electrolysis duration, iron concentration on electrolyte, applied voltage and polarization parameters under different experimental conditions were performed. The behaviour of the electrolyte on heating was monitored by electrochemical impedance spectroscopy.

After the desired temperature is reached and the electrolyte is molten, the electrolysis process is started. The resistance of the molten electrolyte and the electrochemical cell is measured by impedance spectroscopy using an Autolab equipment.

The electrolysis process was done in potentiostatic regime through a constant tension dc of 1.5 – 2 V, between cathode and anode during a defined time (15 – 120 min). After that period, the electrolysis process was stopped and the impedance of the molten in the electrochemical cell was measured to assess the iron deposition/concentration during the process.

The duration of process was estimated based on the Faraday Law (Eq. 1.12 and 1.13), taking into account the iron amount on the electrolyte and the average current that passing during the electrolysis process. When is reached the predetermined time to obtain iron, the experiment was stopped and the furnace cooled down to room temperature at 5 K/min. After cooled the cell is prepared for a *post-mortem* analysis.

2.2.3 Post-mortem analysis

After the pyroelectrolysis experiment the system was disassembled to perform detailed characterization of the sample at room temperature. Cross-sections of electrochemical cell crucible were obtained by cutting with a diamond saw, polished and mounting on a sample holder for analysis by optical microscopy, scanning electron microscopy (SEM) and energy dispersive spectroscopy (EDS).

2.3 Characterization techniques

The structural, morphological, electrical and magnetic properties of the samples, prepared by LFZ and solid state route (SSR) methods, were studied using the techniques presented in table 2.1.

Structural characterization was made mainly at room temperature. For fibres, obtained by the LFZ method, the cylindrical shape (bulk) was kept in order to allow the study of interfaces and morphology of different phases. An exception was made for X-ray diffraction (XRD) analysis, where the fibres were ground to exclude the influence of the preferential crystals orientation.

The samples of spinels based in magnetite, obtained by SSR were cut from bulk samples and ground for thermogravimetric (TG) and XRD analysis. For electric and magnetic characterization, the original shape of the sample was kept, to avoid defects that may appear due to the preparation techniques.

Table 2.1 – Characterization techniques used in the present work.

Characterization	Techniques	Parameters assessed	Sample shape
Microstructural	SEM/EDS	Morphology, Phase composition, Phase and elemental distribution	Bulk (SSR) Polished surface (LFZ and blocking cell)
Structural	XRD	Phase identification, Crystal size, Phases percentage	Powders
	Arquimedes Method Mass/volume ration	Density	Bulk sample
	Raman Spectroscopy	Vibration modes Phases identification	Polished surface
	Mossbauer Spectroscopy	Fe^{n+} valence and coordination	Powder
Thermal	TG	Weigh losses Phase transformations	Powder
	Thermal expansion	Thermal expansion coefficient	Bars 3 ×3 × 15 mm^3
Electrochemical and Electrical	dc conductivity: 100 – 360 K	Electrical conductivity	Bars; cylinders from fibres
	ac conductivity: 100 – 360 K, 40 – 2 x 10^6 Hz	Electrical conductivity	Pellets 3 × 3 × 15 mm^3, fibres ϕ 1.5 mm and length 5 mm
	Spectroscopic impedances 1000-1700 K (oxidant and reducing atmospheres)	Electrical conductivity at high temperature Activation energy	Bars 3x3x15 mm^3; fibres ϕ 1.5 mm and length 15 mm
	Permittivity/ loss factor: 100-360 K	Dielectric capacity	Bars 3x3x15 mm^3, fibres ϕ 1.5 mm and length 15 mm
	Electrochemical cell 300 – 1700 K	Mechanism of conduction (ionic, electronic or mixed)	Powder; fibres ϕ 1.5 mm and length 50 mm
Magnetic	EPR: 5 – 300 K	Resonance of magnetic ions	Bulk sample
	VSM: 5 – 300 K; - 10 to 10 Tesla	Magnetic moment and magnetic behaviour	Bulk sample

3 Potential electrolyte compositions assessed by LFZ method

3.1 Introductory notes

This chapter is based on recently published paper: 3.2 – Crystallization of iron-containing Si-Al-Mg-O glasses under laser floating zone conditions, and aims on detailed studies of the effects of iron oxide additions on relevant properties of the prospective electrolyte composition, based on MgO-Al_2O_3-SiO_2 (MAS) glass system. The proposed composition shows a reasonable melting point for using in high temperature pyroelectrolysis process, and includes the elements, which are abundant in iron ores (as described in chapter 1.1 and 1.2.3). The study focuses on the mechanisms of crystallization processes and related changes in structural and physico-chemical properties, with emphasis on conditions imposed by temperature gradients, as expected for freeze lining conditions in large scale industrial units. The work relies on the laser floating zone (LFZ) method as a tool to simulate the conditions occurring at extremely high temperatures and steep temperature gradients, at the same time avoiding uncertainties arising from the interactions with crucible material and other issues, characteristic of the conventional experimental approaches.

3.2 Crystallization of iron-containing Si-Al-Mg-O glasses under laser floating zone conditions

N.M. Ferreira, A.V. Kovalevsky, J.C. Waerenborgh, M. Quevedo-Reyes, A.A. Timopheev, F.M. Costa and J.R. Frade

(Journal of Alloys and Compounds 611 (2014) 57–64
http://dx.doi.org/10.1016/j.jallcom.2014.05.118)

3.2.1 Abstract

The glass system MgO-Al_2O_3-SiO_2-FeO_y has been mentioned as possible electrolyte for pyroelectrolysis of iron. This work was focused on the study of crystallization behaviour of the iron-containing Al-Mg-Si-O glass system under laser floating zone (LFZ) to identify expected changes occurring under freeze lining or other high temperature gradients at large industrial scale. Lower iron content and faster fibre growth were found favourable for the formation of isolated iron cations in the glass after cooling. The crystallization process, accompanied with separation of mullite and cordierite-type phases, is strongly affected by the formation of nanosized iron-containing clusters, confirmed by Mössbauer and EPR spectroscopies. LFZ method shows good prospects for studying crystallization/vitrification mechanisms in silicate-based glasses with additions of redox-active cations, by providing flexibility in tuning their oxidation state and attaining frozen-in conditions.

3.2.2 Introduction

The magnesium aluminosilicate system MgO-Al_2O_3-SiO_2 (MAS) is very relevant for potential applications as a refractory system [1]. It is also the basis of slag in high-temperature iron extractive metallurgy [2]. In this case, redox conditions and temperature are likely to determine the contents of iron oxides and onset of crystalline phases in the quaternary system MgO-Al_2O_3-SiO_2-FeO_y. In addition, this system has also been proposed as a basis for potential pyroelectrolysis process, to obtain molten Fe from its oxides [3 – 7]. Numerous publications have also addressed the impact of thermochemical processing conditions on structural changes of Fe oxides and related materials, with major impact on properties (magnetic, optical, catalytic, etc.) and prospective technological applications [1, 3 – 7].

Better understanding of the crystallization processes is, thus, important to establish the relationships between those microscopic and macroscopic changes and relevant physical-chemical and thermodynamic properties at very high temperatures [8,9], with emphasis on conditions imposed by temperature gradients, as expected for freeze lining conditions in large scale industrial units. Strong dependence of phase changes on thermochemical conditions thus require complicated and expensive experimental methodologies for harsh conditions imposed by very high temperatures, and inherent difficulties in adjusting other relevant conditions such as controlled temperature gradients, oxygen partial pressure, etc. Extreme conditions are also likely to cause interactions with crucibles or other supporting materials, with additional uncertainties about effects exerted by resulting composition changes.

Prospects for development of pyroelectrolysis of iron oxides as a breakthrough technology are, thus, still very inconclusive [3 – 7]. Few works had related the properties with the kinetics of glass-ceramic transition for this glass system doped with iron [10], and corresponding changes on cooling or under high temperature gradients. The present work relies on the laser floating zone (LFZ) method to study phase changes and structural effects occurring on cooling from very high temperatures of MgO-Al_2O_3-SiO_2 glasses with different FeO_y amounts, and corresponding changes in relevant properties. This method allows one to avoid uncertainties concerning high temperature interaction with crucibles or other materials, and offers unique conditions to obtain materials with specific features such as high quality single crystals of a variety of oxides [11 – 14], eutectic structures [15, 16] and highly oriented polycrystalline materials [17, 18]. Moreover, this method was already used to study phase transformation kinetics, diffusion phenomena and crystallization path [19, 20].

3.2.3 Experimental Procedure

Powders of MgO (Merck), Al_2O_3 (Merck), SiO_2 (Sigma-Aldrich) and Fe_2O_3 (Aldrich +99 %) were mixed in the required proportions to obtain samples with nominal compositions ($Mg_{0.203}\ Al_{0.374}\ Si_{0.423}O_{1.61}$), containing 0, 2, 4 and 8 mol% of iron cations. A binder (PVA - Polyvinyl alcohol) was then added to the powder mixture to allow extrusion of the precursor in the form of rods.

These rods were used as feed and seed in the LFZ setup [16], equipped with a continuous CO_2 Spectron SLC laser (λ = 10.6 μm; 200 W) to grow dense fibres.
The growth rates corresponded to 10 and 50 mm/h, and the seed and feed rod precursors rotated in opposite directions to enhance homogeneity of the fibres [17].

The phase composition and crystallinity of the fibres grown by LFZ method were investigated at room temperature by X-ray diffraction (XRD) analysis, using a Philips Panalytical X'Pert MPD system, and the obtained spectra were analysed using the JCPDS database. Phase distribution in the samples was examined by Raman spectroscopy (Horiba, Jobin Yvon HR 800 UV) at room temperature in backscattering configuration, using the 532 nm exciting line, from 100 to 1600 cm^{-1}. The relative intensity of a characteristic peak of a relevant crystalline phase was used to describe the impact of composition and processing condition in all samples. That relative intensity was determined by the followed equation:

$$I_r(\sim 1000\ cm^{-1}) = \frac{Ip_{sample}}{Ip_{0\%Fe}} \quad (1)$$

The microstructure of polished cross-section and transversal regions of the fibres was characterized by scanning electron microscopy (Hitachi SU 70), and the obtained data were analysed by ImageJ open source software [21].

Mössbauer spectra were collected at room temperature and 4 K in transmission mode using a conventional constant-acceleration spectrometer and a 25 mCi ^{57}Co source in a Rh matrix. The velocity scale was calibrated using α-Fe foil. The absorbers were obtained by pressing the powdered samples (5 mg of natural Fe/cm^2) into perspex holders. Spectra at 4 K were collected with the sample immersed in liquid He in a bath cryostat. Isomer shifts are given relative to metallic α-Fe at room temperature. The spectra were fitted to Lorentzian lines using a non-linear least-squares method [22]. The relative areas and widths of both peaks in a quadrupole doublet were kept equal during refinement. Distributions of quadrupole splittings or magnetic splittings were fitted according to the histogram method [23].

The electrical conductivity of the fibres was measured at room temperature using an Agilent 4292A Precision Impedance Analyser (at 100 kHz). To provide appropriate electrical connection, the Ag electrodes were applied on the both ends of the fibre. ERP spectra of bulk samples at room temperature were obtained using a Bruker model ESP300 E spectrometer working with X-band EPR spectra.

3.2.4 Results and discussion

XRD analysis (Fig. 1) of the samples with various iron concentrations reveals the presence of mullite ($Al_6Si_2O_{13}$ – JCPDS 00-015-0776) and/or cordierite ($Mg_2[Al_4Si_5O_{18}]$ – JCPDS 01-082-1884) phases in the glass matrix, the former corresponds to a broad hump at around 24 – 26 º. For the samples grown at 50 mm/h decreasing the iron content results in an increase of crystallites content, whilst low levels of crystallinity were observed for the sample with the highest iron concentration (x = 8 mol%). The crystallization process under LFZ conditions is controlled by cation diffusion kinetics rather than by thermodynamics of MAS-FeOy system, mainly at the highest LFZ pulling rates (cooling rate), according with work of Magnien et al. [24] on crystallization of iron in a silicate glass. In addition, sluggish reoxidation may hinder changes in relative fractions of Fe^{2+} and Fe^{3+} cations, coexisting in silicate-based glasses. Note that structural positions of these cations may differ significantly in the aluminosilicate melts. Namely, Fe^{2+} generally is a network modifier, while Fe^{3+} can act both as a network former and as a network modifier ([25] and Refs. therein).

Previously it was shown that, in SiO_2–Al_2O_3–MgO–CaO–FeO system, obtained by quenching from 1723 K and subsequent annealing at 993 K, higher total iron content ([Fe_{tot}]) and higher [Fe^{2+}] : [Fe_{tot}] ratio promote faster and more intensive crystallization [26]. These trends are opposite to those observed in the present work, apparently due to slower cooling of the sample in the above cited work, allowing crystal nucleation. Possible explanation for the obtained results may rely on the changes in configurational entropy of the melt during faster cooling under LFZ conditions, as explained in [27]. Namely, a more complex chemical composition of the melt provides a larger number of embryos that could evolve to nuclei; hence, as a result of mutual competition, crystal nucleation and growth may be hindered on sufficiently rapid cooling.

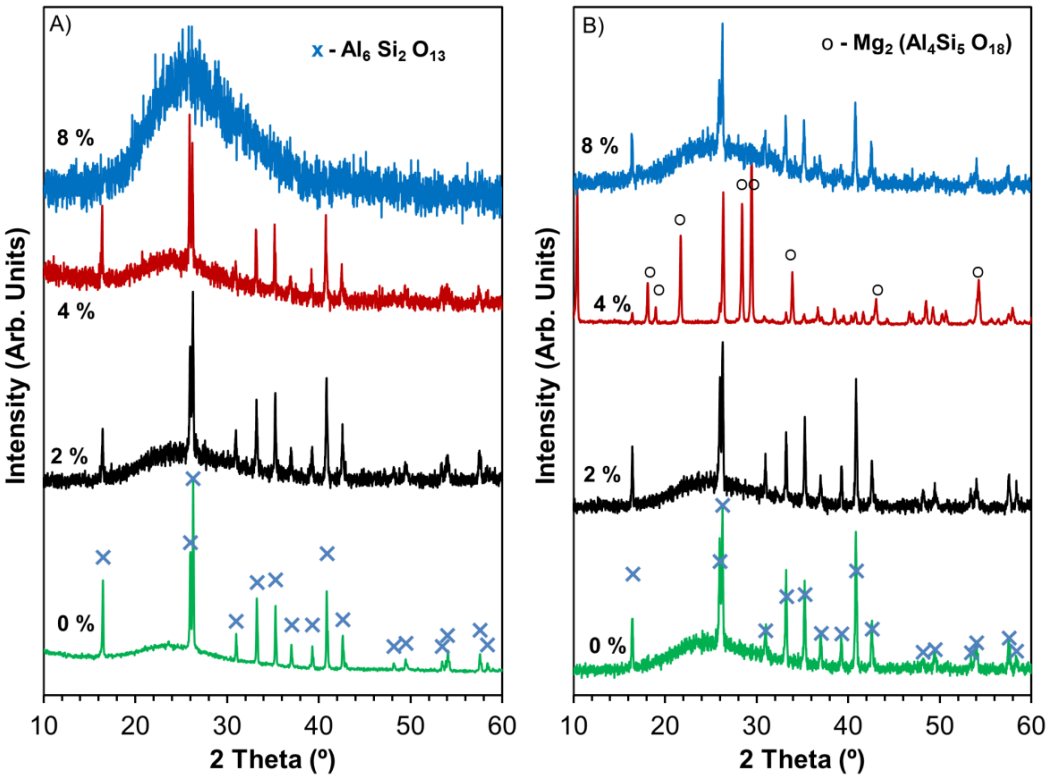

Figure 1 – XRD patterns of the fibres grown at 50 mm/h (A) and 10 mm/h (B), containing different amounts of iron.

The XRD patterns of the samples grown at 10 mm/h indicate even more complicated influence of the iron content on crystallization behaviour (Fig. 1): the maximum crystallinity was observed for 4 mol% iron-containing sample. Since the iron oxidation state and structural position are expected to affect crystallization process, Mössbauer spectroscopy was used to assist on the interpretation of the iron speciation impact on the crystallization mechanism.

The main feature of the observed Mössbauer spectra (Fig. 2) is an asymmetric broadened doublet frequently observed in silicate glasses [28, 29]. This doublet is due to the presence of Fe^{2+} located in environments which differ little from each other and which give rise to a distribution of unresolved quadrupole doublets with slightly different isomer shifts, IS, and quadrupole splittings, QS. However the spectra further reveal an additional contribution typical of Fe^{3+} in silicate glasses.

The analysis of the present spectra was therefore performed considering an Fe^{2+} distribution of quadrupole splittings and an Fe^{3+} symmetric Lorentzian doublet, as usually performed for similar spectra of silicate glasses [29].

A linear dependence of IS on QS was also refined for the Fe^{2+} distribution showing that IS increased with QS as commonly observed. This IS dependence on QS explains why the high velocity Fe^{2+} absorption peak is broader and has lower intensity than the low velocity one.

As explained in [30], the recoilless factor of Fe^{2+} decreases faster than the Fe^{3+} one with increasing temperature. As a consequence, the estimated relative areas of the Fe^{3+} subspectra at 295 K (Table 1) are higher than the relative Fe^{3+} fractions $[Fe^{3+}] : [Fe_{tot}]$ in the samples. Measurements at 4 K were therefore performed in order to suppress the recoil-free fraction effect [28, 31].

Except for the samples grown at 10 mm/h and containing 4 and 8 mol% of iron, the spectra obtained at 4 K (Fig. 3) were analysed in the same way as those obtained at room temperature.

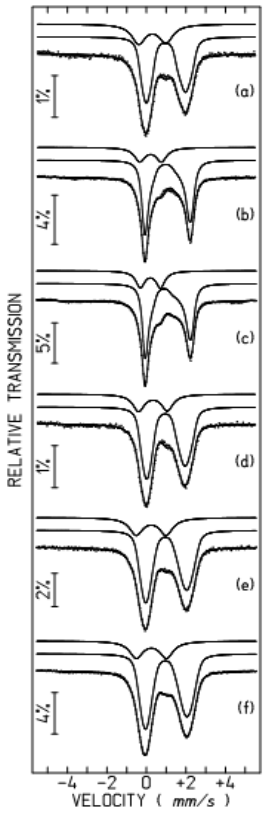

Figure 2 – Mössbauer spectra of glass samples taken at 295 K: (a) 2mol%. Fe, (b) 4mol%. Fe, (c) 8 mol% Fe, grown at 10 mm/h, and (d) 2mol%. Fe, (e) 4mol%. Fe, (f) 8mol%. Fe, grown at 50 mm/h.

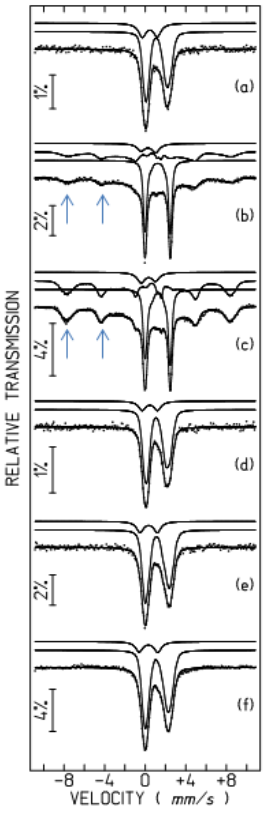

Figure 3 – Mössbauer spectra of the glass samples taken at 4 K: (a) 2 mol% Fe, (b) 4 mol% Fe, (c) 8 mol% Fe, grown at 10 mm/h (arrows indicate the sextets), and (d) 2 mol% Fe, (e) 4 mol% Fe, (f) 8 mol% Fe, grown at 50 mm/h.

As expected, the estimated Fe^{2+} relative areas at 4 K (Table 1) are higher than at 295 K (room temperature) and may be considered a good estimate of the actual Fe^{2+} fractions in the glass matrixes.

Table 1 - Estimated parameters from the Mössbauer spectra of the glass samples taken at different temperatures (T).

Fibre growth rate, mm/h	Iron content, mol%	T, K	Iron oxidation state	IS, mm/s	QS, 2ε, mm/s	$<B_{hf}>$, tesla	I (%)
10	2	295	Fe^{2+}	1.10	1.96	-	69
			Fe^{3+}	0.41	1.37	-	31
		4	Fe^{2+}	1.25	2.13	-	78
			Fe^{3+}	0.56	1.47	-	22
	4	295	Fe^{2+}	1.16	2.13	-	77
			Fe^{3+}	0.32	1.09	-	23
		4	Fe^{2+}	1.34	2.41	-	46
			Fe^{3+}	0.42	1.43	-	12
			$(Fe^{3+}\ Fe^{2+})^*$	0.63*	-0.21	36*	42
	8	295	Fe^{2+}	1.15	2.05	-	77
			Fe^{3+}	0.31	1.02	-	23
		4	Fe^{2+}	1.34	2.34	-	36
			Fe^{3+}	0.41	1.42	-	9
			$(Fe^{3+}\ Fe^{2+})^*$	0.56*	0.0	39*	55
50	2	295	Fe^{2+}	1.10	1.94	-	77
			Fe^{3+}	0.44	1.45	-	23
		4	Fe^{2+}	1.25	2.10	-	86
			Fe^{3+}	0.56	1.51	-	14
	4	295	Fe^{2+}	1.11	2.04	-	75
			Fe^{3+}	0.35	1.52	-	25
		4	Fe^{2+}	1.30	2.27	-	84
			Fe^{3+}	0.45	1.69	-	16
	8	295	Fe^{2+}	1.11	2.07	-	76
			Fe^{3+}	0.36	1.53	-	24
		4	Fe^{2+}	1.26	2.22	-	86
			Fe^{3+}	0.43	1.84	-	14

IS (mm/s) isomer shift relative to metallic α-Fe at 295 K; QS (mm/s) quadrupole splitting. $2\varepsilon = (e^2V_{zz}Q/4)(3\cos^2\theta - 1)$ [mm/s] quadrupole shift estimated for the sextets. $<B_{hf}>$ (tesla) average magnetic hyperfine field; I relative area. Estimated errors ≤ 0.02 mm/s for IS, QS, and <2 % for I.
* distribution of magnetic hyperfine fields. Average IS and B_{hf} are indicated.

The 4 K spectra of the samples grown at 10 mm/h and containing 4 and 8 mol% of iron, show sextets with broad peaks (two out of the six peaks of each sextet are indicated by arrows in Fig. 3). Sextets are commonly observed for diluted amorphous systems, such as silicate glasses containing trace amounts of Fe^{3+}. They result from slow spin-spin relaxation in systems where Fe^{3+} cations are too far apart to interact appreciably [29].

However, these effects are usually reported for glasses with less than 2 wt% FeO, whereas, in the present work, the sextets are observed for 4 and 8 mol% iron-containing glasses, and are absent in the 2 mol% iron-containing sample. Furthermore, the relative areas of the sextets increase with Fe content (Table 1). Therefore, these sextets cannot arise from slow spin-spin relaxation effects. Instead they can be explained by the formation of nanosized Fe clusters or nanosized Fe oxides in the samples containing 4 and 8 mol% of iron. Superparamagnetic relaxation of the magnetic moments of these clusters is fast at room temperature but, at least for most of them, becomes quenched at 4 K. As the sextet peaks are asymmetrically broadened suggesting a range of relaxation rates, their analysis was approached by a distribution of magnetic hyperfine fields, B_{hf}. The average magnetic hyperfine fields, $<B_{hf}> \sim 36$ and ~ 39 T, estimated for the samples grown at 10 mm/h and containing 4 and 8 mol% of iron, respectively, are lower than expected if the sextets would be only due to Fe^{3+}.

Moreover, the IS was found to decrease strongly with increasing B_{hf}, suggesting the contribution from Fe^{2+}. Most probably, both Fe^{2+} and Fe^{3+} are present in the nanoclusters, resembling magnetite-like clusters in nonstoichiometric wustite $Fe_{1-x}O$ [32].

However, the relative contributions to the spectra from Fe^{3+} and Fe^{2+} are not resolved in the observed sextets, and an estimate of the Fe^{3+} : Fe^{2+} ratios is, therefore, very difficult. In addition to the sextets, two doublets similar to those in the remaining glass samples are observed, suggesting the presence of isolated Fe^{2+} and Fe^{3+} within the glass structure, which do not belong to the nanosized clusters.

The assumption regarding possibility of iron nanoclustering in iron-containing magnesium silicate-based glasses, prepared by LFZ, is in agreement with the results for similar systems obtained in [33, 34]. In particular, Mössbauer data of CaO(MgO)-Al_2O_3-SiO_2-Fe-O samples quenched from melts with Ca/Al and Mg/Al ≥ 0.5, suggest that Fe^{2+} and Fe^{3+} cations may be associated within the glass melt [33], in such a way to produce local clusters, which compositionally resemble to a spinel structure [32]. EPR and Mössbauer studies of cenospheres from energy ashes with 3 – 4 wt% of iron revealed the presence of an iron-containing superparamagnetic phase with a spinel structure, having sizes of 30 – 50 Å, dispersed in aluminosilicate glass [34].

Although the MAS composition, studied in the present work is quite different, one may expect the formation of similar or even larger clusters in the samples with iron content above a critical value.

Note also that the condition Mg/Al>0.5 is observed in the actual compositions studied in the present work. These Fe-containing clusters, which are more likely to form at lower growth rates under LFZ conditions, may act as nucleation centers, providing separation of mullite and cordierite like phases and the highest crystallinity for the sample containing 4 mol% of iron and grown at 10 mm/h, in agreement with XRD results (Fig. 1B). The latter also explains the presence of crystalline phases in the sample containing 8 mol% of iron and grown at 10 mm/h, in contrast to the corresponding amorphous sample grown at 50 mm/h, while further decrease in the amount of crystalline phase on increasing iron content may originate from mutual competition between various nucleation pathways, as described above. The role of iron content on the crystallization of mullite in traditional ceramic compositions [35], and its dependence on firing conditions are also consistent with this prevailing effect for the highest concentrations of Fe.

For all samples grown at 50 mm/h Mössbauer data suggest similar Fe^{3+} fractions (Table 1), which are, however, lower than in the 2 mol% Fe-containing sample grown at 10 mm/h. Whatever the oxidation mechanism, a lower growth rate is expected to result in a higher oxidation level, considering that the average oxidation state tends to increase with decreasing temperature and corresponding effect on the fibres is more pronounced at a lower cooling rate. Higher Fe^{3+} content is also favourable for clustering, taking into account that, at least, part of the clusters may have Fe^{2+} $(Fe^{3+})_2O_4$ structure [32, 34]. Indeed, it is difficult to estimate the global Fe^{2+} : Fe^{3+} ratio in the samples containing 4 and 8 mol% of iron and grown at 10 mm/h, because of the strong overlap of the sextets due to Fe^{2+} and Fe^{3+} in the clusters, as discussed above.

Further evidences for the distinct nature of the local environments of iron ions in MAS structure follow from the results of EPR spectroscopy. The EPR spectra (Fig. 4) of the samples, containing iron, exhibit two well-known resonances at $g \approx 2$ (3400 Oe) and $g \approx 4.3$ (1700 Oe), which can be considered as a signature of the presence of Fe^{3+} ions in doped silicate glasses [36,37].

The resonances at g ≈ 4.3 (1700 Oe) refer to the usual isolated ions in the glass forming network, characteristic of the lowest iron contents, whereas the broad EPR signal at g ≈ 2.0 (3400 Oe) was ascribed to Fe^{3+} - containing clusters in silicate glasses [36, 37]. The latter is observed clearly for samples containing 4 and 8 mol%, grown at 10 mm/h (Fig. 4b), thus confirming the results of Mössbauer spectroscopy.

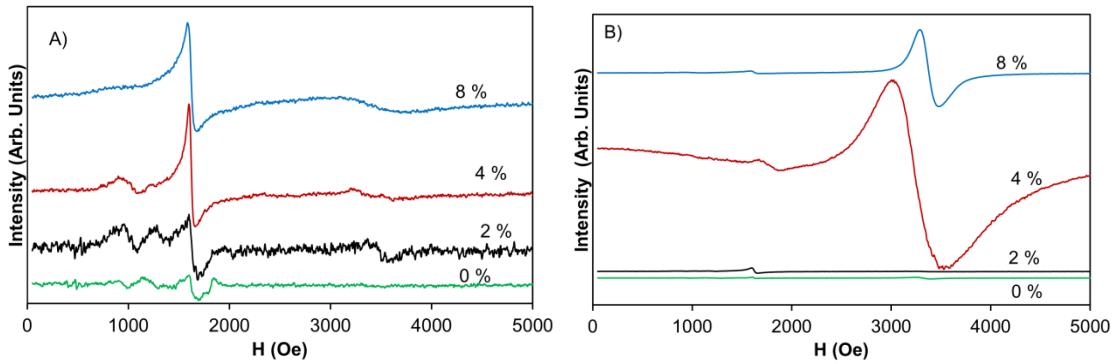

Figure 4 – EPR spectra for 50 mm/h (A) and 10 mm/h (B) –grown samples at 300 K for different iron content.

The increase of IS observed for all contributions to the spectra upon temperature drop from 295 to 4 K (Table 1) is explained by the second order Doppler shift. The values of IS of the different samples may be correlated with the Fe^{2+} and Fe^{3+} coordination. The estimated average IS at 295 K for most samples, <IS> ~ 1.10 – 1.11 mm/s, confirms that Fe^{2+} is a network modifier with preferential sixfold coordination [29, 31, 38]. The higher <IS> ~ 1.15 – 1.16 mm/s observed for the samples containing 4 and 8 mol% of iron and grown at 10 mm/h, may be related to the above referred inhomogeneities.

At 295 K, the values of 0.35 – 0.36 mm/s deduced for the IS of Fe^{3+} in the samples, containing 4 and 8 mol% of iron and grown at 50 mm/h, are at the upper limit of the tetrahedral Fe^{3+} IS range, according to [29] and already within the octahedral Fe^{3+} IS range according to [31, 38].

This may suggest that for these samples Fe^{3+} is present in both coordinations, which agrees well with the broader line widths observed for the doublets (Fig. 2). The IS ~ 0.41 – 0.44 mm/s estimated for fibres grown at 10 and 50 mm/h and containing 2 mol% of iron, suggest predominant octahedral coordination for Fe^{3+}.

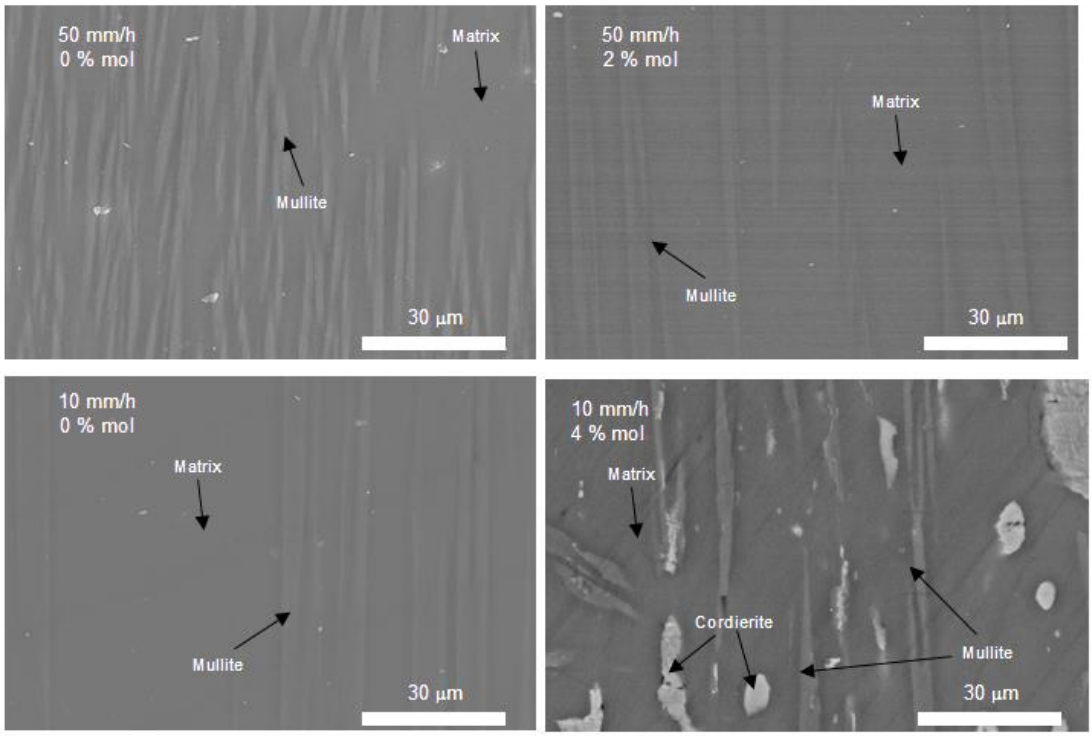

Figure 5 – SEM micrographs of longitudinal section of the fibres grown at 50 and 10 mm/h with 0, 2 and 4mol%. iron content.

SEM studies of the transversal sections of representative samples (Fig. 5) are consistent with the XRD results. The samples, where no clustering was detected by Mössbauer spectroscopy demonstrate similar morphology and crystal orientation. This type of crystals alignment was also observed by [14] for mullite fibres grown by LFZ at a higher rate (100 mm/h). Samples containing 4 mol% of iron and grown at 10 mm/h, show quite distinct microstructure, provided by more intensive crystallization and presence of cordierite phase coexisting with mullite (Fig. 1). The results on relative crystal area and crystal width for mullite phase, obtained by analysis of corresponding SEM micrographs of the samples grown at 50 mm/h, qualitatively confirm the observed general tendency for decrease in crystallinity while increasing iron content (Fig. 6).

Two distinct types of spectra are evidenced by Raman spectroscopy for the crystalline and amorphous regions of the samples grown at 50 mm/h. Fig. 7 gives an example of the Raman spectrum for the sample containing 2 mol% of iron. The results reveal the presence of vibration modes characteristic of mullite ($Al_6Si_2O_{13}$) phase, in accordance with the literature [13, 39]. The bands at ~ 500 and ~ 1000 cm^{-1} in all glass regions can be attributed to Si – O bond bending and stretching, that occur for SiO_4 tetrahedra in the glass state [39, 40].

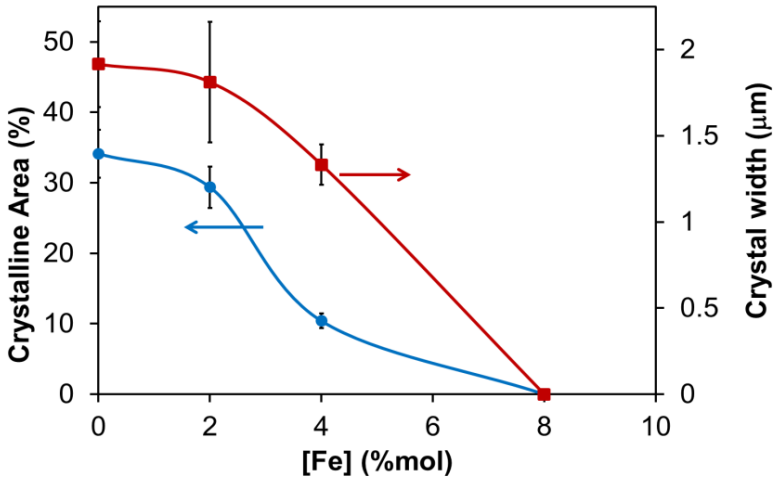

Figure 6 – Relative crystalline area (●) and crystal widths (■) for mullite phase, calculated from SEM images of fibres grown at 50 mm/h.

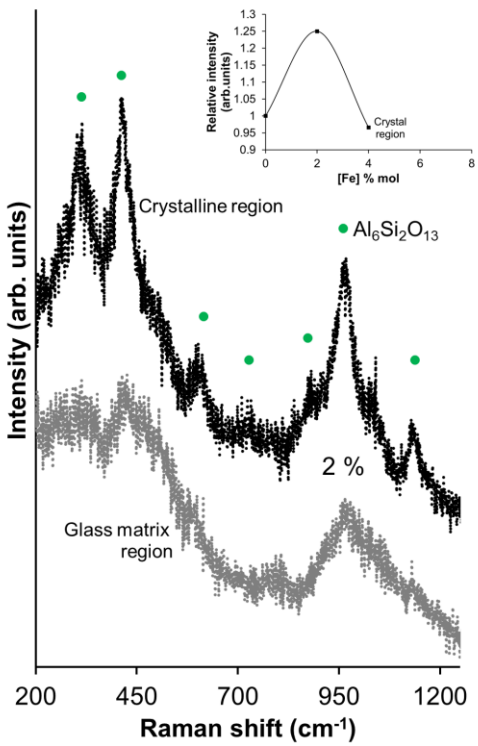

Figure 7 – Raman spectra for the sample, containing 2 mol% of iron and grown at 50 mm/h. The inset shows relative intensity of the peak near 1000 cm^{-1} within the crystalline region.

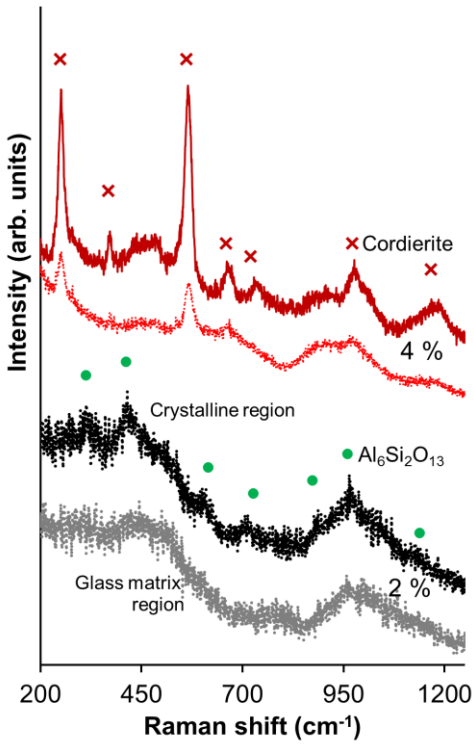

Figure 8 – Raman spectra for samples, containing 2 and 4 mol% of iron and grown at 10 mm/h in different sample regions.

The crystalline regions are characterized by sharper and stronger bands. The sample containing 2 mol% of iron, shows the maximum relative intensity of the mullite peak at ~1000 cm^{-1}, apparently indicating the highest crystallinity of this sample among those grown at 50 mm/h.

A similar trend was reported for the dependence of melt viscosity on Fe concentration in the CaO-SiO_2-Fe-O system, with a maximum at a certain concentration of Fe_2O_3 [25], suggesting that the impact of iron cations on crystallization/vitrification mechanisms in silicate glasses may be somewhat complex. It was shown that ferrous iron is commonly considered a glass-modifier [33]. Apparently the iron oxide in lower concentration can decrease the crystallization temperature and expanding the temperature range where crystallization may occur due to its coordination with glass elements [33]. Furthermore, this influence is more pronounced for the melt stage and playing a prevailing effect at higher iron concentrations [25, 33]. Onset of cordierite as a second crystalline phase at intermediate iron contents (Fig. 1) is also consistent with the transition from prevailing mechanisms; this is also supported by Raman spectroscopy for samples with 4mol% of iron content grown at 10 mm/h (Fig. 8) which show the characteristic vibration modes of cordierite [40, 41, 42, 43].

The values of electrical conductivity at 100 kHz, shown in Fig. 9, correspond to the typical range of silicate glass systems [44, 45]. Conductivity is strongly affected by thermal history, suggesting dependence on the fraction of crystalline phase (Fig. 1). However, the range of electrical conductivity values in Fig. 9 is still well above the room temperature electrical conductivity dc expected for pure mullite ($\approx 10^{-11}$ S/m) or iron-doped mullite ($\approx 10^{-9}$ S/m) [46]. Therefore, one should consider a prevailing conductivity contribution of the residual glass, and changes in conductivity may be a combination of increasing iron contents, its distribution between crystalline phases and residual glass [46]. A possible compositional change is expected by alumina depletion on the residual glass due its preferential crystallization in a rich mullite phase, with corresponding effects on conductivity [47]. One must also take into account changes in relative fractions of Fe^{2+} and Fe^{3+} cations and their structural environment, including prospective Fe^{2+}:Fe^{3+} clustering, as demonstrated by Mössbauer and Raman spectroscopy (Table 1). Evidence that the prevailing oxidation state in drawn fibres is Fe^{2+} (Table 1) also indicates preferential segregation of iron in the residual glassy phase because incorporation in the mullite phase should occur as trivalent Fe^{3+}, by substitution of Al^{3+} in octahedral or tetrahedral coordination [48]. Coexistence of both valence states thus suggests a polaron conduction mechanism in the glass, involving coexisting trivalent and divalent cations in the residual glass phase, or clusters (Table 1).

In fibres containing 4 and 8 mol% of iron and grown at 10 mm/h the conductivity increases significantly, probably due to precipitations of alumina-rich mullite, and corresponding decrease of its contents in the continuous residual amorphous phase, combined the redistribution of Fe^{n+} ions, which play a prevailing role on conductivity (e.g. [47]).

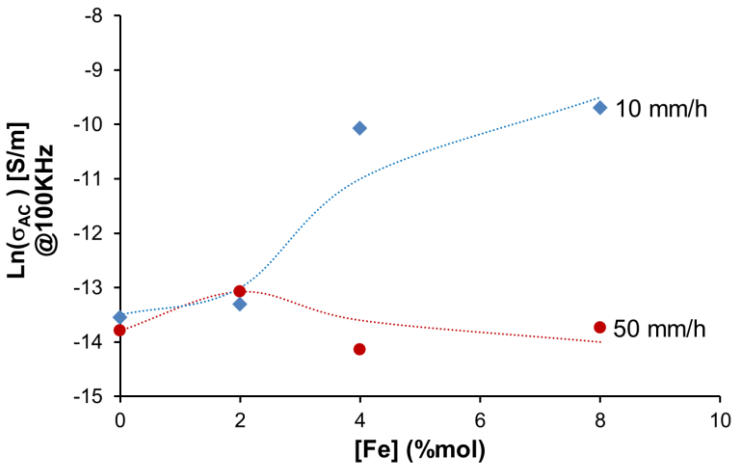

Figure 9 – Conductivity ac measured at 300k and 100 KHz, for samples grown at 10 (♦) and 50 (●) mm/h with different iron content.

3.2.5 Conclusions

Magnesium aluminosilicate-based glasses, containing various amounts of iron, were prepared by the laser floating zone technique at 10 and 50 mm/h growth rates. The structural and microstructural features of the prepared fibres were studied by XRD, SEM, Raman, EPR and Mössbauer spectroscopy. Iron oxidation state and local environment were found to be affected by the fibre growth rate, as a result of kinetic limitations imposed by specific conditions of the LFZ method. Formation of nanosized iron-containing clusters in the samples containing 4 and 8 mol% of iron, is closely related to massive crystallization and phase separation of mullite and cordierite-type phases, with significant impact on electrical conductivity. The observed effects of iron concentration in MAS glass on the phase composition suggest a complex nature of crystallization/vitrification mechanisms in these glasses, likely determined by the changes in configurational entropy of the melt upon cooling under LFZ conditions and network-forming capabilities of the Fe^{2+} and Fe^{3+} iron cations.

3.2.6 References

[1] – A. Prasad, A. Basu, Dielectric and impedance properties of sintered magnesium aluminum silicate glass-ceramic, Journal of Advanced Ceramics 2 (2013) 71–78, http://dx.doi.org/10.1007/s40145-013-0045-1.

[2] – A.J.B. Muwanguzi, A.V. Karasev, J.K. Byaruhanga, P.G. Jonsson, Characterization of Chemical Composition andMicrostructure of Natural Iron Ore from Muko Deposits, ISRN MATER SCI, Volume 2012, Article ID 174803, 9 pages, doi:10.5402/2012/174803.

[3] – D.R. Sadoway, New opportunities for waste treatment by electrochemical processing in molten salts, in K.C. Liddell, R. G. Bautista and R.J. Orth, Metals and Materials Waste Reduction, Recovery and Remediation, The Minerals, Metals & Materials Society, 1994, pp.73-76.

[4] – S.X. Wang, L.M. Wang, R.C. Ewing, R.H. Doremus, Ion beam-induced amorphization in MgO – Al_2O_3 – SiO_2. I. Experimental and theoretical basis, J. Non-Cryst. Solids 238 (1998) 198-213.

[5] – I.H. Jung, S.A. Decterov, A.D. Pelton, Critical Thermodynamic Evaluation and Optimization of the FeO – Fe_2O_3 – MgO – SiO_2 System, Metall. Mater. Trans. B 35B (2004) 877-889.

[6] – D. Wang, A.J. Gmitter, D.R. Sadoway, Production of oxygen gas and liquid metal by electrochemical decomposition of molten iron oxide, J. Electrochem. Soc. 158 (2011) E51-E54.

[7] – Z.H. Jiang, S.J. Li, Y. Li, Thermodynamic calculation of inclusion formation in Mg-Al-Si-O system of 430 stainless steel melts, Journal of Iron and Steel Research International 18 (2011) 14-17, http://dx.doi.org/10.1016/S1006-706X(11)60017-4.

[8] – M. Guignard, L. Cormier, Environments of Mg and Al in MgO – Al_2O_3 – SiO_2 glasses: A study coupling neutron and X-ray diffraction and Reverse Monte Carlo modelling, Chem. Geol. 256 (2008) 111–118, http://hal.archives-ouvertes.fr/hal-00346395.

[9] – V.C. Kress, M.S. Ghiorso, Multicomponent diffusion in $MgO - Al_2O_3 - SiO_2$ and $CaO - MgO - Al_2O_3 - SiO_2$ melts, Geochim. Cosmochim. Ac. 57 (1993) 4453-4466, http://dx.doi.org/10.1016/0016-7037(93)90495-I.

[10] – A. Mekki, Magnetic Properties of Fe ions in a silicate glass and ceramic, Phys. Status Solidi A 184 (2001) 327–333, http://dx.doi.org/10.1002/1521-396X(200104)184:2<327::AID-PSSA327>3.0.CO;2-O.

[11] – F. Ritzert, L. Westfall, Laser-heated floating zone production of single-crystal fibers, NASA Technical Memorandum, Vol 4732, N.A.S.A. Office of Management, Scientific and Technical Information Program, (1996).

[12] – P. Guptasarma, M.S. Williamsen, S.K. Ray, Floating Zone Growth of Bulk Single Crystals of Complex Oxides, MRS Proceedings 848 (2004), http://dx.doi.org/10.1557/PROC-848-FF10.3.

[13] – R.G. Carvalho, A.J.S. Fernandes, F.J. Oliveira, E. Alves, N. Franco, C. Louro, R.F. Silva, F.M. Costa, Single and polycrystalline mullite fibres grown by laser floating zone technique, J. Eur. Ceram. Soc. 30 (2010) 3311–3318.

[14] – M.R.N. Soares, C. Nico, M. Peres, N. Ferreira, A.J.S. Fernandes, T. Monteiro, F.M. Costa, Structural and optical properties of europium doped zirconia single crystals fibers grown by laser floating zone technique, J. Appl. Phys. 109 (2011) 013516, http://dx.doi.org/10.1063/1.3527914.

[15] – J.LLorca, V.M. Orera, Directionally solidified eutectic ceramic oxides, Prog. Mater. Sci. 51 (2006) 711–809, http://dx.doi.org/10.1016/j.pmatsci.2005.10.002.

[16] – R.G. Carvalho, M.S. Pires, A.J.S. Fernandes, R.F. Silva, F.M. Costa, Directionally solidified eutectic and off-eutectic mullite–zirconia fibres, J. Eur. Ceram. Soc. 33 (2013) 953–963, http://dx.doi.org/10.1016/j.jeurceramsoc. 2012.09.032.

[17] – N.M. Ferreira, Sh. Rasekh, F.M. Costa, M.A. Madre, A. Sotelo, J.C. Diez, M.A. Torres, New method to improve the grain alignment and performance of thermoelectric ceramics, Mater. Lett. 83 (2012) 144–147, http://dx.doi.org/10.1016/j.matlet.2012.05.131.

[18] – M.F. Carrasco, R.F. Silva, J.M. Vieira, F.M. Costa, Pulling rate and current intensity competition in electrically assisted laser floating zone, Supercond. Sci. Tech. 22 (2009) 065016, http://dx.doi.org/10.1088/0953-2048/22/6/065016.

[19] – F.M. Costa, R.F. Silva, J.M, Vieira, Phase transformation kinetics during thermal annealing of LFZ Bi-Sr-Ca-Cu-O superconducting fibers in the range 800-870 ºC, Physica C, 323 (1999) 23-41

[20] – F.M. Costa, R.F. Silva, J.M. Vieira, Diffusion phenomena and crystallization path during the growth of LFZ Bi-Sr-Ca-Cu-O superconducting fibres, Supercond. Sci. Tech. 14 (2001) 910-920, http://dx.doi.org/10.1088/0953-2048/14/11/305.

[21] – W. Rasband, ImageJ, Version 1.46r, Research Services Branch, National Institute of Mental Health, Bethesda, Maryland, USA, http://imagej.nih.gov/ij/index.html, (Acessed Nov 2013).

[22] – J.C. Waerenborgh, D.P. Rojas, N.P. Vyshatko, A.L. Shaula, V.V. Kharton, I.P. Marozau, E.N. Naumovich, Fe^{4+} formation in brownmillerite $CaAl_{0.5}Fe_{0.5}O_{2.5+\delta}$, Mater. Lett. 57 (2003) 4388-4393, http://dx.doi.org/10.1016/S0167-577X(03)00330-6.

[23] – J. Hesse, A. Rübartsch, Model independent evaluation of overlapped Mössbauer spectra, J. Phys. E Sci. Instrum. 7 (1974) 526-532.

[24] – V. Magnien, D.R. Neuville, L. Cormier, B.O. Mysen, V. Briois, S. Belin, O. Pinet, P. Richet, Kinetics of iron oxidation in silicate melts: a preliminary XANES study, Chem Geol 213 (2004) 253– 263.

[25] – B.O. Mysen, D. Virgo, C.M. Scarfe, D.J. Cronin, Viscosity and structure of iron- and aluminium-bearing calcium silicate melts at 1 atm, Am. Mineral. 70 (1985) 487-498.

[26] – P.M. Sørensen, M. Pind, Y.Z. Yue, R.D. Rawlings, A.R. Boccaccini, E.R. Nielsen, Effect of the redox state and concentration of iron on the crystallization behaviour of iron-rich aluminosilicate glasses, J. Non-Cryst. Solids 351 (2005) 1246-1253, http://dx.doi.org/10.1016/j.jnoncrysol.2005.03.015.

[27] – P. Richet, M. Roskosz, J. Roux, Glass formation in silicates: Insights from composition, Chem. Geol. 225 (2006) 388-401, http://dx.doi.org/10.1016/j.chemgeo.2005.08.030.

[28] – K.F.E. Williams, C.E. Johnson, M.F Thomas, Mössbauer spectroscopy measurement of iron oxidation states in float composition silica glasses, J. Non-Cryst. Solids 226 (1998) 19-23.

[29] – K.D. Jayasuriya, H.St.C. O'Neill, A.J. Berry, S.J. Campbell, A Mössbauer study of the oxidation state of Fe in silicate melts, Am. Mineral. 89 (2004) 1597-1609.

[30] – J.A. Johnson, C.E. Johnson, D. Holland, A. Mekki, P. Appleyard, M.F. Thomas, Transition metal ions in ternary sodium silicate glasses: a Mössbauer and neutron study, J. Non-Cryst. Solids 246 (1999) 104-114, http://wrap.warwick.ac.uk/id/eprint /14574.

[31] – J.A. Johnson, C.E. Johnson, Mössbauer spectroscopy as a probe of silicate glasses, J. Phys. – Condens. Mat. 17 (2005) R381-R412, http://dx.doi.org/ 10.1088/0953-8984/17/8/R01.

[32] – M.V. Tsodikov, T.N. Rostovshchikova, V.V. Smirnov, O.I. Kiseleva, Y.V. Maksimov, I.P. Suzdalev, V.N. Ikorskii, Structure and size effects in catalysis by immobilized nanoclusters of iron oxides, Catal Today 105 (2005) 634–640.

[33] – B.O. Mysen, D. Virgo, E.R. Neumann. F.A. Seifert, Redox equilibria and the structural states of ferric and ferrous iron in melts in the system CaO-MgO-Al_2O_3-SiO_2-Fe-O: relationships between redox equilibria, melt structure and liquid phase equilibria, Am. Mineral. 70 (1985) 317-331.

[34] – T.A. Vereshchagina, N.N. Anshits, N.G. Maksimov, S.N. Vereshchagin, O.A. Bayukov, A.G. Anshits, The nature and properties of iron-containing nanoparticles dispersed in an aluminosilicate matrix of cenospheres, Glass Phys. Chem. 30 (2004) 247-256.

[35] – G. Lecomte-Nana, J.P. Bonnet, N. Soro, Influence of iron on the occurrence of primary mullite in kaolin based materials: A semi-quantitative X-ray diffraction study, J. Eur. Ceram. Soc. 33 (2013) 669–677, http://dx.doi.org/10.1016/j.jeurceramsoc.2012.10.033.

[36] – S.T. Reis, W.M. Pontuschka, J.B. Yang, D.LA. Faria, Properties and structural features of iron doped BABAL glasses, Mater. Res. 6 (2003) 389-394, http://dx.doi.org/10.1590/S1516-14392003000300013.

[37] – E.S. Dunaeva, I.A. Uspenskaya, K.V. Pokholok, V.V. Minin, N.N. Efimov, E.A. Ugolkova, E. Brunet, Coordination and RedOx ratio of iron in sodium-silicate glasses, J. Non-Cryst. Solids 358 (2012) 3089–3095, http://dx.doi.org/10.1016/j.jnoncrysol.2012.08.004.

[38] – M. D. Dyar, A review of Mössbauer data on inorganic glasses: the effects of composition on iron valency and coordination, Am. Mineral. 70 (1985) 304-316.

[39] – P. Colomban, A. Tournie, L. Bellot-Gurlet; Raman identification of glassy silicates used in ceramics, glass and jewellery: a tentative differentiation guide; J. Raman Spectrosc. 37 (2006) 841-852.

[40] – H. Aguiar, J. Serra, P. González, B. León, Structural study of sol–gel silicate glasses by IR and Raman spectroscopies, J. Non-Cryst. Solids 355 (2009) 475–480.

[41] – A.I. Apopei, G. Damian, N. Buzgar, A Preliminary Raman and FT-IR Spectroscopic study of secondary hydrated sulfate minerals from the hondol open it (Metaliferi Mts., Romania), Journal of Mineral Deposits 85 (2012) 1-7.

[42] – T.I. Chuvaeva, O.S. Dymshits, V.I. Petrov, M.Y. Tsenter, A.V. Shashkin, A.A. Zhilin, V.V. Golubkov, Low-frequency Raman scattering of magnesium aluminosilicate glasses and glass-ceramics; J. Non-Cryst. Solids 282 (2001) 306-316, http://dx.doi.org/10.1016/S0022-3093(01)00314-3.

[43] – B.O. Mysen, D. Virgo, C.M. Scarfe, Relations between the anionic structure and viscosity of silicate melts – a Raman spectroscopic study, Am. Mineral. 65 (1980) 690-710.

[44] – C.H. Hsieh and H. Jain, Influence of network-forming cations on ionic conduction in sodium silicate glasses, J. Non-Cryst. Solids 183 (1995) 1-11, http://dx.doi.org/10.1016/0022-3093(94)00570-2.

[45] – M.D. Ingram, Superionic glasses: theories and applications, Curr. Opin. Solid St. M. 2 (1997) 399-404.

[46] – S.P. Chaudhuri, S.K. Patra, A.K. Chakraborty, Electrical resistivity of transition metal ion doped Mullite, J. Eur. Ceram. Soc. 19 (1999) 2941-2950, http://dx.doi.org/10.1016/S0955-2219(99)00058-8.

[47] – C.Y.SUN, X.M.GUO, Electrical conductivity of MO(MO=FeO, NiO)-containing CaO-MgO-SiO2-Al2O3 slag with low basicity, Trans. Nonferrous Met. Soc. China, 21 (2011) 1648-1654

[48] – S.P. Chaudhuri and S.K. Patra, Electron paramagnetic resonance and Mossbauer spectroscopy of transition metal ion doped mullite, J. Mater. Sci. 35 (2000) 4735– 4741, http://dx.doi.org/10.1023/A:1004863309464.

4 Spinels as consumable anode materials

4.1 Introductory notes

This chapter presents the results on processing and characterization of magnetite-based spinels, with emphasis on the properties relevant for prospective consumable anode materials for molten oxide electrolysis process. Chapter 4 includes two published papers. The first paper: 4.2 – Redox stability and high-temperature electrical conductivity of magnesium- and aluminium- substituted magnetite, demonstrates a co-substitutional approach using Mg and Al, for improving redox and electrical properties of ferrospinels. The second paper: 4.3 – Effects of transition metal additives on redox stability and high-temperature electrical conductivity of (Fe, $Mg)_3O_4$ spinels, aims at assessment of the relevant structural factors, which determine the electronic transport and tolerance against oxidative decomposition of magnetite, containing transition metals additives. The characterization include detailed structural and microstructural analysis, studies of thermochemical expansion, relative weight changes and electrical conductivity in relevant conditions, including high temperatures and wide range of oxygen partial pressures. The results suggest important guidelines for tuning the composition of magnetite-based spinels, if seeking prospective applications in harsh conditions.

4.2 Redox stability and high-temperature electrical conductivity of magnesium- and aluminium- substituted magnetite

A.V. Kovalevsky, A.A. Yaremchenko, E.N. Naumovich, N.M. Ferreira, S.M. Mikhalev, F.M. Costa and J.R. Frade

(Journal of the European Ceramic Society 33 (2013) 2751–2760
http://dx.doi.org/10.1016/j.jeurceramsoc.2013.04.008)

4.2.1 Abstract

Spinel-type magnetite-based oxides, possessing relatively high electrical conductivity, are considered as promising consumable anode materials for high temperature pyroelectrolysis, a breakthrough low-CO_2 steel technology to overcome environmental impact of classical extractive metallurgy. The present work focuses on the analysis of phase stability, thermal expansion and high-temperature electrical conductivity in (Fe, Mg, Al)$_3$ O_4 system under oxidizing and mildly reducing conditions. Metastable, nearly single-phase at room temperature (Fe, Mg ,Al)$_3O_4$ ceramics were obtained by sintering at 1753 – 1773 K for 10 h in argon atmosphere. Thermal expansion and redox induced dimensional changes were studied on heating, using TG, XRD and dilatometry. The results revealed that magnesium improves the tolerance against oxidative decomposition and minimizes unfavorable dimensional changes in ceramic samples upon thermal cycling. Co-substitution of iron with aluminium and magnesium was proved to be a promising strategy for improvement of refractoriness and phase stability of Fe_3O_4-based spinels at elevated temperatures, without significant reduction in the electrical conductivity.

4.2.2 Introduction

Steel production by molten oxide electrolysis promises environmental advantages over classic extractive metallurgy, by eliminating CO_2 emissions and reducing energy consumption [1-3]. Though theoretical simulations and predictions for the process are very optimistic [1], this concept is still far from being convincingly demonstrated even at laboratory scale. The inherent difficulties are largely associated with highly corrosive nature of high-temperature molten electrolytes, and finding suitable anode materials.

In particular, noble metals (e.g., Ir) were proposed for small scale demonstration [3], but they are still far from being truly inert in molten oxide electrodes, while their cost is not affordable for mass production. Similarly, although Mo showed good prospects for electric boosting in glass technology, one cannot consider anodic polarization of Mo electrodes in contact with molten oxide electrolytes. Thus, a major challenge is to seek alternative concepts of consumable electrodes, as currently used in aluminium production by electrolysis of melts.

Pure magnetite, Fe_3O_4, is known to show relatively good refractoriness and high temperature electronic conductivity [4-8]. It has been considered as a prospective candidate for consumable anodes in high temperature pyroelectrolysis [1,9], due to its compatibility with relevant molten oxide systems (e.g. SiO_2-MgO-FeO_x) and affordable cost for mass production,. An important advantage of magnetite also includes chemical composition itself, which does not lead to contamination of the system and may even account for a fraction of iron oxide raw materials. However, magnetite is thermodynamically unstable in air below 1667 K and even in inert gas ($p(O_2) \approx 10$ Pa) below 1300 – 1373 K [10]. Anodic polarization during electrolysis may also promote oxidation of magnetite to hematite, requiring higher operation temperatures to retain electrochemical stability magnetite phase, and, thus, sufficient refractoriness.

Redox stability of magnetite can be improved by substitution of iron with redox stable oxides, and, for that matter, magnesium and aluminium oxides look very attractive due to their low costs. Moreover, these oxides are also among the most important components of refractory materials for high temperature molten systems. As an example, substitution of iron with Al^{3+} or Mg^{2+} is known to shift the melting points from 1811 K for Fe_3O_4 to 2013 K for $FeAl_2O_4$ and 2023 K for $MgFe_2O_4$, i.e., well above the melting point of iron (1808 K) and the temperature range proposed for iron or steel production from iron ore by pyroelectrolysis. However, redox stability requirements are often in trade-off relation with electrical conductivity. In particular, although the phase diagrams [11, 12] predict substantially large compositional ranges for stable $Fe_{3-x}Mg_xO4$ spinels even in contact with pure oxygen atmosphere, partial iron substitution with magnesium significantly decreases the electrical conductivity at 1250 – 1773 K [8].

On the contrary, partial substitution with aluminium in magnetite has weaker negative impact on the conductivity but leads to a decrease in the redox stability [13]. Thus, a promising strategy may comprise co-substitution of magnetite with Mg and Al in the concentration range where aluminium may provide just an improvement of refractoriness without significant deterioration of the electric properties, whilst magnesium is expected to enhance the tolerance against oxidative decomposition. Earlier works on this ternary system [14-17] were mostly based on high magnesia or alumina contents and failed to attain the level of electrical conductivity, required for feasible consumable anodes in pyroelectrolysis. In addition, to our best knowledge, no systematic studies of the high-temperature redox stability for these materials were yet performed.

Thus, the present work focuses on studies of phase relationships, redox stability and high temperature electrical conductivity in the (Fe, Al, Mg)$_3$O$_4$ system under oxidizing and mildly reducing conditions. The selection of compositions was carried out assuming reasonably high electrical conductivity by extending the composition-property relations previously reported for binary systems $Fe_{3-x-y}Mg_xCr_yO_4$ [8] and $Fe_{3-z}Al_zO_4$ [13]. Particular attention is also given to the relevant properties in the intermediate temperature range, aiming on guidelines for electrode integrity, which may depend largely on the operation regime of the electrolysis cell.

4.2.3 Experimental

The powders of $Fe_{2.6}Al_{0.2}Mg_{0.2}O_4$, $Fe_{2.3}Al_{0.2}Mg_{0.5}O_4$, $Fe_{2.2}Al_{0.1}Mg_{0.7}O_4$, $Fe_{2.1}Al_{0.2}Mg_{0.7}O_4$ (further referred as moderately substituted), $Fe_{1.55}Al_{0.5}Mg_{0.95}O_4$ and $Fe_{1.55}Al_{0.95}Mg_{0.5}O_4$ (highly substituted) were prepared by solid state route from stoichiometric amounts of $FeC_2O_4{\cdot}2H_2O$ (99%, Sigma-Aldrich), Al_2O_3 (99.7%, Sigma-Aldrich) and $Mg(NO_3)_2{\cdot}6H_2O$ (99%, Avocado Research Chemicals). Solid state synthesis was performed in air at 1173 – 1473K for 15-20 hours, with multiple intermediate grindings. After subsequent ball-milling of thus prepared powders with ethanol, disk-shaped ceramic samples were compacted uniaxially at 300 – 400 MPa, sintered at 1753 – 1773 K for 10 h in argon atmosphere ($p(O_2) \sim 10^{-5} – 10^{-4}$ atm) and cooled down to room temperature at 3 K/min.

Hereafter, thus prepared ceramics are referred to as: as-prepared samples. Identical thermal cycle was used to prepare the ceramic samples in air atmosphere. For X-ray diffraction (XRD) and thermogravimetry (TG) studies, the ceramics were ground to powders in a mortar. For the measurements of total conductivity and thermal expansion, the obtained disk samples were cut into rectangular bars (~ $2 \times 3 \times 12$ mm^3). After polishing, experimental density of the ceramics was measured by Archimedes method.

X-ray diffraction patterns were recorded using a Rigaku D/Max-B diffractometer (CuKα, $2\Theta = 10 - 80$ º, step 0.02 º, exposition 2 s). Unit cell parameters were calculated from the diffraction data using profile matching method in Fullprof software [18]. High-temperature XRD analysis was made on Philips X´pert MPD equipment in vacuum (~ 10^{-7} atm). For SEM/EDS analysis (Hitachi SU-70 model equipped with Brucker silicon drift EDS detector), selected ceramic samples were polished and annealed at 1673 K (0.5 h) in Ar. TG studies (Setaram SetSys 16/18 instrument, sensitivity 0.4 μg, initial sample weight ~ 0.5 g) were performed in a flow of argon or dry air at 298 – 1373 K with constant heating/cooling rate of 2 K/min. Each TG procedure was repeated under identical conditions (temperature program and atmosphere) using a reference alumina sample and the obtained baseline was subtracted from experimental data in order to correct for buoyancy effects.

Thermal expansion of $(Fe, Al, Mg)_3O_4$ ceramics was measured on heating (3 K/min) up to 1350 K in argon and air atmospheres, using a vertical alumina dilatometer Linseis L75V/1250 with a gas system, including an yttria-stabilized zirconia (YSZ) oxygen sensor at the outlet. Total electrical conductivity (σ) was measured by 4-probe dc technique at 750 – 1773 K in the oxygen partial pressure $p(O_2)$ range from 10^{-5} to 0.21 atm in flowing air-Ar mixtures. The $p(O_2)$ in the gas flow was monitored using an YSZ

oxygen sensor.

Static lattice simulations were performed using GULP software [19, 20] in the way, similar to that previously described for $(Fe, Al)_3O_4$ spinels [13]. Simulations were based on 1004 supercells (2×2×2) with random distribution of cations in tetragonal and octahedral sublattices, including previously reported results for pure magnetite and $(Fe, Al)_3O_4$, [13]. The interatomic potentials, used for simulation, are given in Table 1.

The collected data of the lattice energy (in GULP formalism) E_{cell} were firstly fitted vs. total magnesium content [Mg^{2+}] and amounts of Mg^{2+} and Fe^{2+} in octahedral sites, [Mg_0^{2+}] and [Fe_0^{2+}], correspondingly, using formal linear regression model:

$$E_{cell} = E_o + a_{Mg}\left[Mg^{2+}\right] + b_{Mg}\left[Mg_o^{2+}\right] + b_{Fe}\left[Fe_o^{2+}\right] \quad (1)$$

where E_0 corresponds to the lattice energy for undoped and not inverted magnetite, a_{Mg} - impact of the substitution with Mg, b_{Mg} - impact of magnesium in octahedral positions, and b_{Fe} - impact of the spinel inversion (i.e. Fe^{2+} in octahedrally-coordinated sites).

Table 1 – Phenomenological potentials, used in simulation.

Atom	Core-shell		Interatomic (Buckingham)				References
	Y, e (shell charge)	*k*, eV/Å^2	Pair	A, eV	ρ, Å	C, eV/Å^2	
O^{2-}	-2.513	20.53	O^{2-}	22.41	0.6937	32.32	[21,22]
Fe_t^{3+}	1.029	10082.5	O^{2-}	1240.232	0.3069	0	[21,22]
Fe_o^{3+}	1.029	10082.5	O^{2-}	1342.754	0.3069	0	[21,22]
Fe^{2+}	2	n/a	O^{2-}	2763.945	0.2641	0	[21,23]
Al^{3+}	2.957	403.98	O^{2-}	2409.505	0.2649	0	[21,24]
Mg^{2+}	0.4200	349.95	O^{2-}	2457.243	0.261	0	[21,24]

Similar modelling was then performed for the ternary (Fe, Al, Mg)$_3$O$_4$ system, with introduction of the additional term c to achieve desirable quality of the model:

$$E_{cell} = E_o + a_{Mg}\left[Mg^{2+}\right] + b_{Mg}\left[Mg_o^{2+}\right] + a_{Al}\left[Al^{3+}\right] + b_{Al}\left[Al_o^{3+}\right] + b_{Fe}\left[Fe_o^{2+}\right] + c\left[Al_o^{3+}\right]\left[Fe_o^{2+}\right]\left[Mg_o^{2+}\right] \quad (2)$$

Factors a_{Al} and b_{Al} denote the same impacts for substitution with aluminium, as described above for magnesium. Fitting was performed in Wolfram Research Mathematica 6 software [25].

4.2.4 Results and Discussion

XRD analysis of as-prepared $Fe_{2.6}Al_{0.2}Mg_{0.2}O_4$ and $Fe_{2.3}Al_{0.2}Mg_{0.5}O_4$ samples obtained by sintering in Ar (Fig. 1) showed formation of single-phase spinel structure (space group Fd 3m).

Higher substitution leads to appearance of second periclase-based phase, containing aluminium, as confirmed by EDS analysis (Fig. 2). Noteworthy that, in the case of simultaneous presence of Mg and Al, formation of (Mg, Al)O is more favourable, than separation of wüstite, previously reported for (Fe, M)$_3$O$_4$ (M = Mg, Al) materials at high substitution levels [8,13].

Corresponding lattice parameters are given in Table 2, together with the identification of secondary phases. For the single-phase samples, the unit cell parameters decrease upon substitution, due to smaller ionic radii of Al^{3+} compared to Fe^{3+}, and Mg^{2+} compared to Fe^{2+} (assuming the same coordination numbers of considered cations [26]).

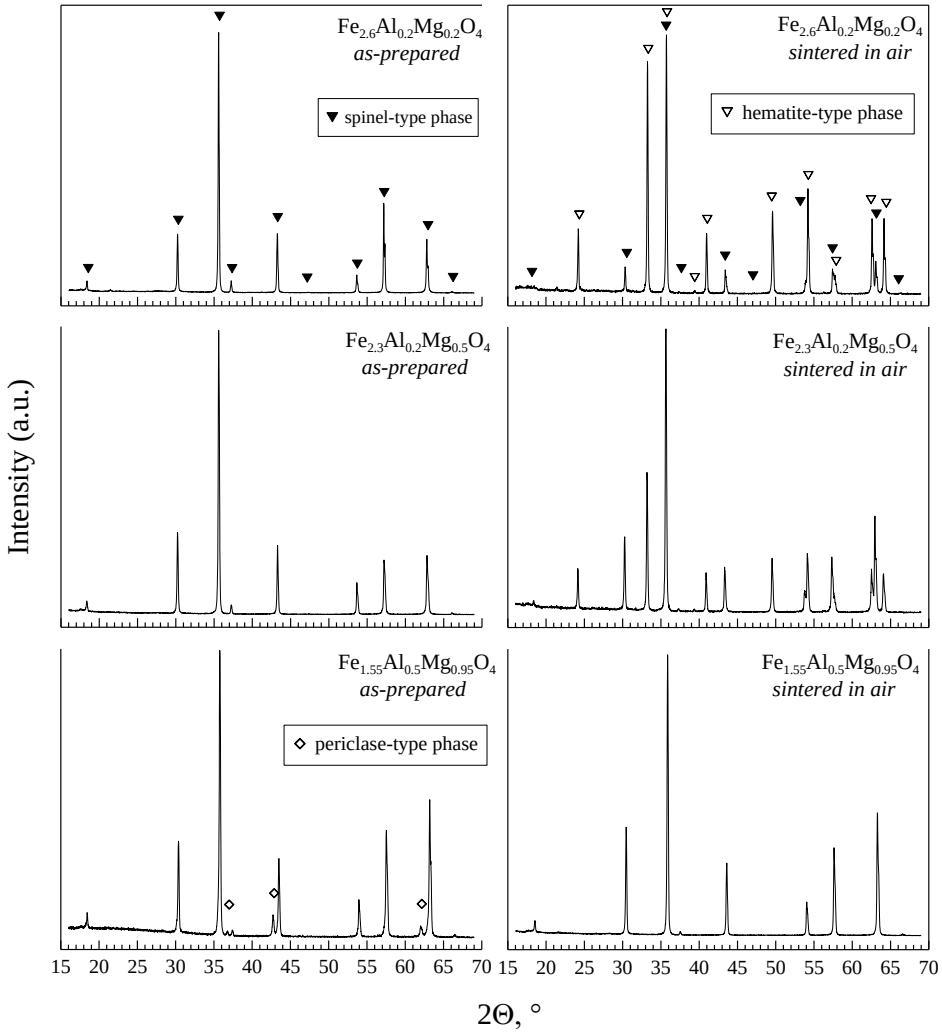

Figure 1 – Room-temperature XRD patterns of as-prepared and air-sintered (Fe, Al, Mg)$_3$O$_4$ samples.

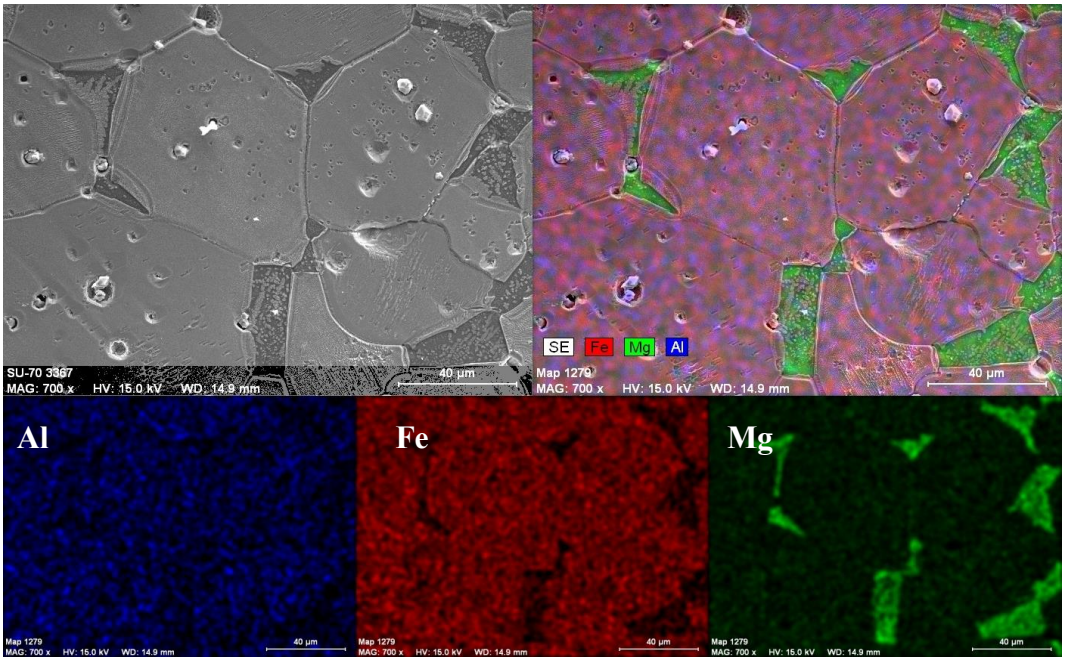

Figure 2 – Example of SEM/EDS mapping results for $Fe_{2.1}Al_{0.2}Mg_{0.7}O_4$ spinel sample.

Table 2 – Properties of as-prepared (Fe, Al, Mg)$_3$O$_4$ ceramic samples.

Chemical composition	Phase composition	Unit cell parameter of spinel-type phase, nm	Density, g/cm^3	Relative density, %
$Fe_{2.6}Al_{0.2}Mg_{0.2}O_4$	Spinel	0.83684(3)	4.67	93.9
$Fe_{2.3}Al_{0.2}Mg_{0.5}O_4$	Spinel	0.83615(3)	4.68	98.1
$Fe_{2.2}Al_{0.1}Mg_{0.7}O_4$	Spinel (major) + periclase (minor)	0.83767(3)	4.56	97.7*
$Fe_{2.1}Al_{0.2}Mg_{0.7}O_4$	Spinel (major) + periclase (minor)	0.83657(3)	4.48	96.9*
$Fe_{1.55}Al_{0.5}Mg_{0.95}O_4$	Spinel (major) + periclase (minor)	0.83136(3)	3.59	82.9*
$Fe_{1.55}Al_{0.95}Mg_{0.5}O_4$	spinel	0.82687(2)	4.06	91.8

* - was calculated assuming phase-pure spinel

According to the XRD results, the tolerance against oxidative decomposition for (Fe, Al, Mg)$_3$O$_4$ spinels appears to be largely determined by [Al^{3+}]:[Mg^{2+}] concentration ratio in substituted magnetite and total iron concentration. For the samples sintered in air, the relative intensities of hematite-type phase peaks decrease from $Fe_{2.6}Al_{0.2}Mg_{0.2}O_4$ to $Fe_{2.3}Al_{0.2}Mg_{0.5}O_4$ (Fig.1).

Higher magnesium content, apparently, lowers the Fe^{2+}:Fe^{3+} ratio in spinel lattice, while the total amount of cations, susceptible to oxidation, decreases. A possibility to obtain single-phase $Fe_{1.55}Al_{0.5}Mg_{0.95}O_4$ ceramics by sintering in air (Fig. 1) is another good illustration for the redox-stabilizing effect of magnesium. Indeed, $Fe_{3-x}Al_xO_4$ materials ($0.1 \leq x \leq 1.0$) undergo full oxidation under similar conditions [13], whilst single phase $Fe_{2.05}Mg_{0.95}O_4$ ceramics can be prepared in air [8]. Minor amounts of phase impurities, in fact, may not be crucial for application as consumable electrodes, implying that these materials can sustain the conditions of pyroelectrolysis in melts and provide sufficient power density.

The information, provided by XRD analysis, is in a good agreement with the results of static lattice simulation and fitting, which are given in Fig. 3 and Table 3. The linearity of the proposed models, described above, and proximity of the corresponding coefficient values for different compositions indicate that considered solid solutions are close to ideal. Comparison of the impacts of substitution with magnesium (a_{Mg}) (Eq.1, Table 3) and aluminium (a_{Al}) [13] confirms an increase in lattice stability in the case of Mg addition, while Al shows an opposite tendency. The values of the lattice energies for all simulated $(Fe, Mg)_3O_4$ compositions are fairly more negative that for pure magnetite (Fig. 3).

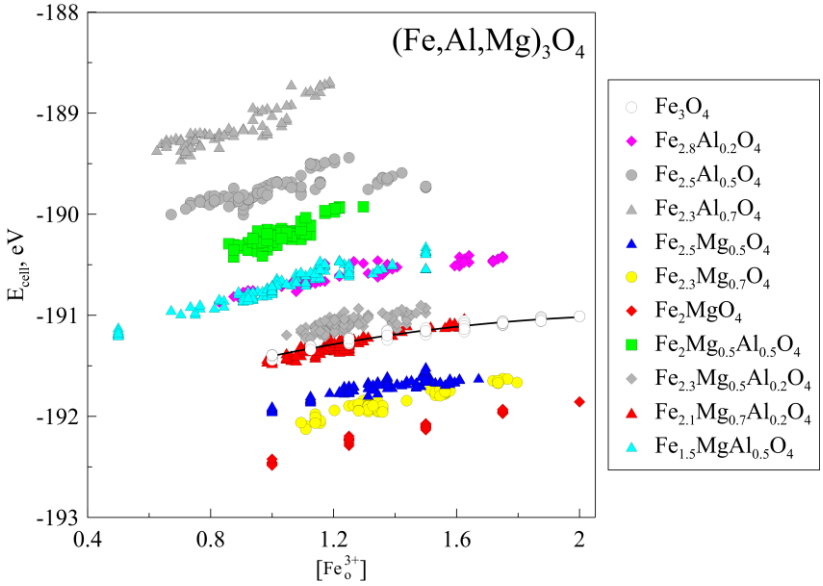

Figure 3 – Results of static lattice simulation: energy of the cell formation vs. concentration of Fe^{3+} in octahedral environment.

Table 3 – Parameters of the regression models (Eq.1 and 2) (95 % confidence).

Parameter	Value	
	$(Fe,Mg)_3O_4$, Eq.1	$(Fe,Al,Mg)_3O_4$, Eq.2
E_o	-190.99 ± 0.01	-190.99 ± 0.01
a_{Mg}	-0.84 ± 0.02	-0.97 ± 0.02
b_{Mg}	-1.27 ± 0.05	-1.14 ± 0.04
a_{Al}	–	3.53 ± 0.03
b_{Al}	–	-1.06 ± 0.04
b_{Fe}	-0.40 ± 0.02	-0.40 ± 0.02
c	–	-35 ± 1.5
R^2	0.990	0.996
N_{points}	293	1005

Cosubstitution appears to result in partial stabilization of the lattice compared to $(Fe, Al)_3O_4$, although the calculated energies predict slightly lower or similar stabilities for $(Fe, Al, Mg)_3O_4$, compared to Fe_3O_4. The latter, in particular, may indicate that the effect of magnesium is not enough to substantially improve the stability of aluminium substituted magnetite. However, confirmation of lattice stability should be addressed with the respect to actual decomposition process mechanism.

The analysis of fitting results (Eq. 2, Table 3) shows that substituting cations Mg^{2+} and Al^{3+} tend to reside in octahedral sites of spinel lattice, and their affinity to octahedral position is almost two times higher compared with Fe^{2+}. This prediction, in general, is in agreement with the results for cation distribution in $Fe_3O_4 – MgAl_2O_4$ system [14], obtained from thermopower and conductivity measurements, where substitution was found to lead to partial enrichment of the tetrahedral sites with both Fe^{2+} and Fe^{3+}.

At the same time, similar negative values of b_{Mg} and b_{Al} coefficients for $(Fe, Al, Mg)_3O_4$ system (Table 3) indicate, that these cations may have similar inherent affinity to occupy octahedral sites, which are responsible for the electronic conduction in ferrospinels (Refs. [8, 13] and references therein).

The results of thermogravimetric analysis of the powdered (Fe, Al, Mg)$_3$O$_4$ samples in Ar ($p(O_2) \sim 10^{-5}$ atm) (Fig. 4A), again, confirm an increase in redox stability upon substitution with magnesium. However, as for the case of $Fe_{3-x}Al_xO_4$ ($0.1 \leq x \leq 0.7$) [13], these results also demonstrated, that as-prepared (Fe, Al, Mg)$_3$O$_4$ ceramics are metastable at lower temperatures. One may notice that, even in air, the powdered samples of $Fe_{3-y}Mg_yO_4$ ($0.7 \leq y \leq 0.95$) ceramics show only an increase in weigh upon heating [8]. (Fe, Al, Mg)$_3$O$_4$ samples demonstrate lower oxygen uptake and X-ray peak intensities of secondary phases also decrease (Fig. 5), relative to (Fe,Al)$_3$O$_4$ spinels for the same iron content.

The same tendencies for the moderately substituted samples were observed in air (Fig. 4B), where oxidation proceeds to greater extent and results in almost complete spinel phase decomposition with the formation of hematite-based phase (Fig. 5). Although $Fe_{2.1}Al_{0.2}Mg_{0.7}O_4$ spinel, having only minor hematite impurities, can be sintered in air, the powder of this composition also oxidizes readily even in Ar (Fig. 4C).

On the contrary, heavily-substituted $Fe_{1.55}Al_{0.5}Mg_{0.95}O_4$ spinel, sintered in air, demonstrates oxygen release from the lattice on heating (Fig. 4C) and the same single-phase composition before and after TG (Fig. 5). High magnesium additions can significantly increase the redox stability of aluminium-substituted magnetite. However, a considerable decrease in electronic conductivity of (Fe, Al, Mg)$_3$O$_4$ spinels at this substitution level may be expected.

Concerning the target application, one may anticipate that spinel-based consumable anodes will be based on bulk ceramics. Thus, for discussed materials, the oxidation presumably will take place mainly at the surface, with less pronounced effect on the bulk, depending on composition.

For example, single phase metastable (Fe, Al, Mg)$_3$O$_4$ spinel ceramics can be prepared by sintering as described above, whereas powders of identical composition, in accordance with TG results, undergo oxidation when heated above 500 K. Depending on the rate, oxidation may cause excessive dimensional changes in spinel ceramics on heating, and, thus, limited tolerance to thermal cycling.

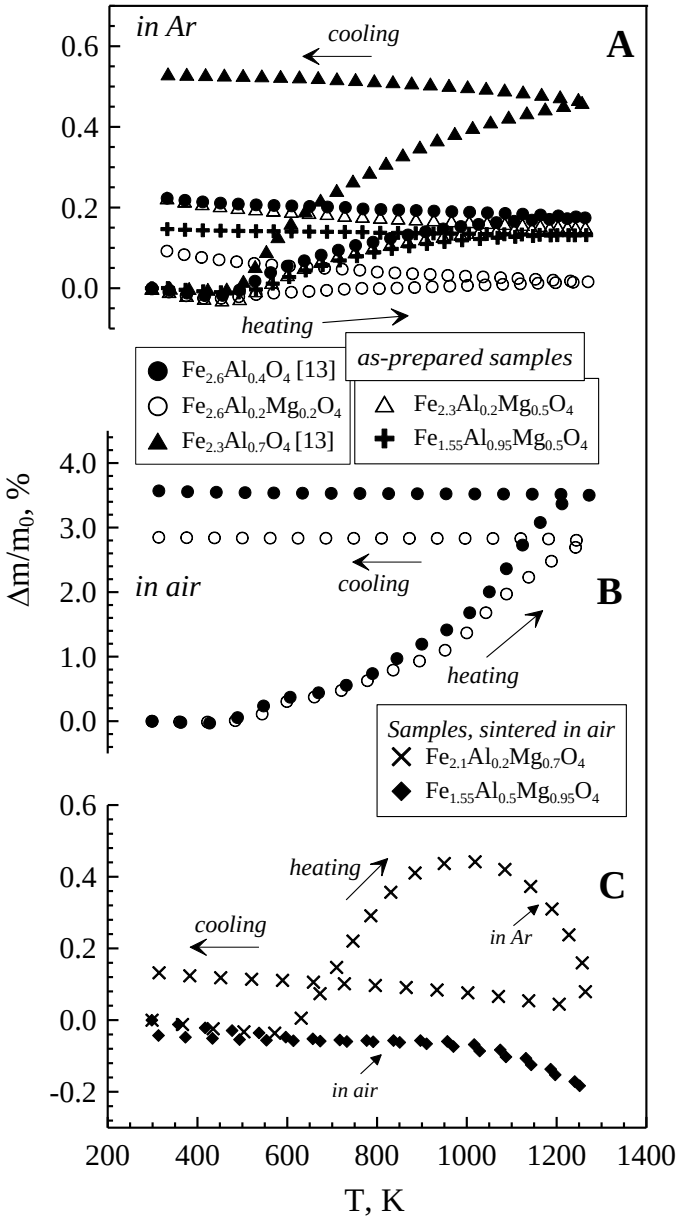

Figure 4 – Relative weight change of the powdered (Fe, Al, Mg)$_3$O$_4$ on heating and cooling: as-prepared samples in Ar (A), as-prepared samples in air (B) and air-sintered samples in Ar and air (C).

The results of dilatometric studies, performed on (Fe,Al,Mg)$_3$O$_4$ ceramic samples, are presented in Fig. 6. The dilatometric curves of moderately substituted materials exhibit non-linear behaviour above ~ 650 K, similar to that observed for Fe_3O_4 in the atmospheres with low oxygen content [8, 27, 28]. The phenomenon may be attributed to a chemical contribution to thermal expansion [8], or rearranging point defects in the cationic sublattice [27].

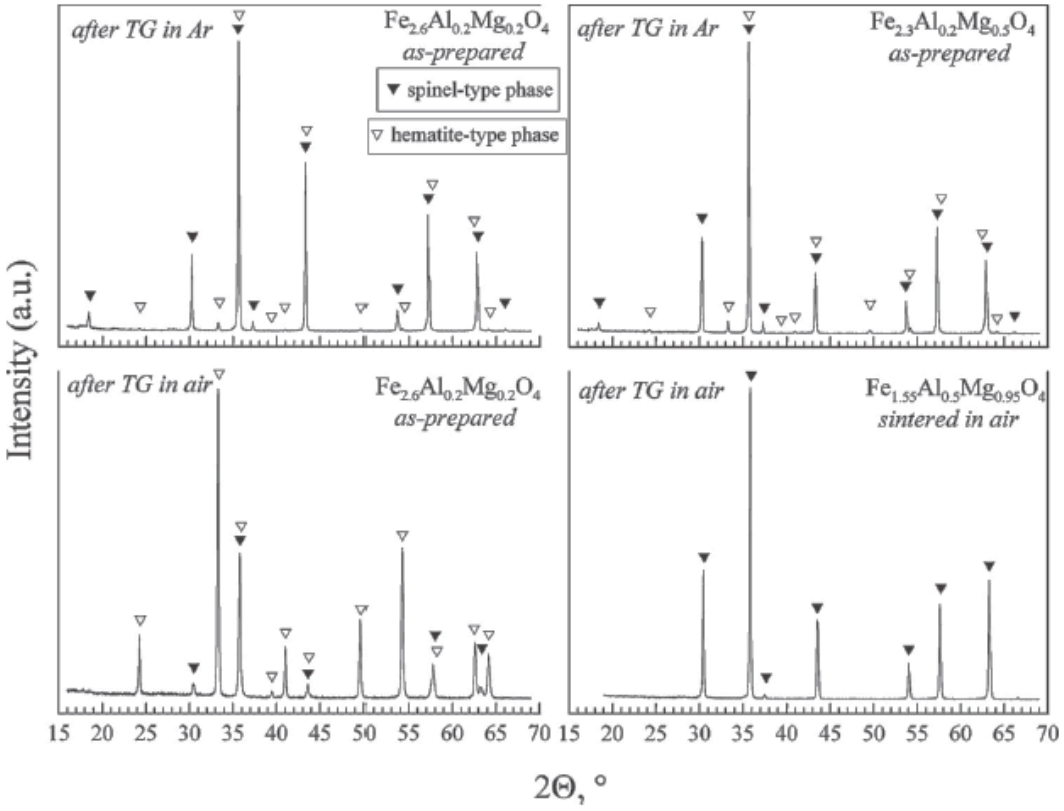

Figure 5 – XRD patterns of the samples after TG studies.

Although substitution with Mg and Al generally decreases the thermal expansion of magnetite, the variations in thermal expansion coefficient (TEC) of $(Fe, Al, Mg)_3O_4$ with composition are very small. At 300 – 650 K all studied materials show very similar expansion behaviour both in Ar and air, with thermal expansion coefficients in the range $(11.0 – 11.6) \times 10^{-6}$ K (Table 4).

For moderately substituted samples, at higher temperatures the thermal expansion coefficients increase and correspond to $(13.0 – 13.1) \times 10^{-6}$ K at 750 – 1370 K in Ar. Heavily substituted $Fe_{1.55}Al_{0.5}Mg_{0.95}O_4$ and $Fe_{1.55}Al_{0.95}Mg_{0.5}O_4$ demonstrate almost linear thermal expansion in Ar in the whole studied temperature range, with similar TEC values.

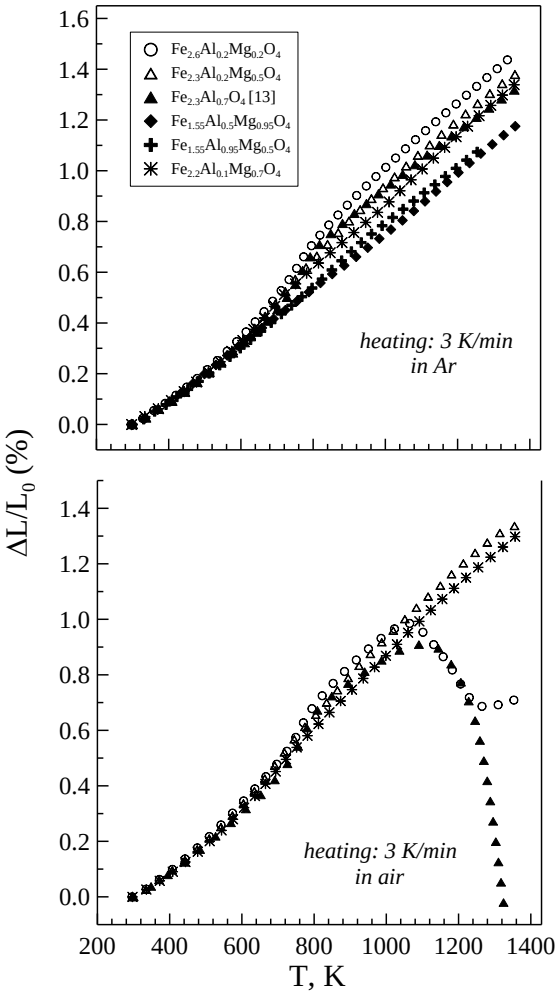

Figure 6 – Dilatometric curves for (Fe, Al, Mg)$_3$O$_4$ materials.

One may notice that, although powdered $Fe_{2.6}Al_{0.2}Mg_{0.2}O_4$, $Fe_{2.3}Al_{0.2}Mg_{0.5}O_4$ and $Fe_{2.3}Al_{0.7}O_4$ [13] samples oxidize in Ar at T > 500 K, the latter has no distinguishable effect on the thermal expansion of corresponding ceramic samples in similar conditions. However, in air, at temperatures above 1050 – 1100 K the behaviour becomes different and provides additional evidences for redox-stabilizing effect of Mg. Even contraction can occur, due to oxidation of Fe^{2+} to Fe^{3+}, as one may observe for $Fe_{2.6}Al_{0.2}Mg_{0.2}O_4$ and $Fe_{2.3}Al_{0.7}O_4$ (Fig. 6). The contraction is much more pronounced for aluminium substituted magnetite. Magnesium addition, on the contrary, reduces or eliminates unfavourable dimensional changes, caused by oxidation. Thus, for ceramic ferrospinel products, magnesium effectively improves the tolerance against oxidative decomposition even at relatively low substitution levels.

Table 4 – Thermal expansion coefficients and activation energies for the total conductivity.

Composition	Average thermal expansion coefficients			Activation energy for the total conductivity		
	$p(O_2)$, atm	T, K	$(\bar{\alpha} \times 10^6) \pm 0.1$, K^{-1}	$p(O_2)$, atm	T, K	E_a, kJ/mol
$Fe_{2.6}Al_{0.2}Mg_{0.2}O_4$	10^{-5}	300–650 800–1370	11.4 13.1	3.8×10^{-5}	1197–1772	15.2 ± 0.7
	0.21	300–600	11.4			
$Fe_{2.3}Al_{0.2}Mg_{0.5}O_4$	10^{-5}	300–650 800–1370	11.4 13.0	6.6×10^{-5}	1369–1773	19 ± 1
	0.21	300–650 800–1200	11.6 13.3			
$Fe_{2.2}Al_{0.1}Mg_{0.7}O_4$	10^{-5}	300–650 750–1370	11.3 13.1	2.4×10^{-4}	1372–1714	23 ± 1
	0.21	300–650 750–1000	11.0 12.6			
$Fe_{2.1}Al_{0.2}Mg_{0.7}O_4$	–	–	–	1.6×10^{-4}	1373–1764	23.2 ± 0.9
$Fe_{1.55}Al_{0.5}Mg_{0.95}O_4$	10^{-5}	300–1370	11.2	1.5×10^{-4}	1482–1772	129 ± 18
$Fe_{1.55}Al_{0.95}Mg_{0.5}O_4$	10^{-5}	300–900 900–1260	11.4 11.2	–	–	–

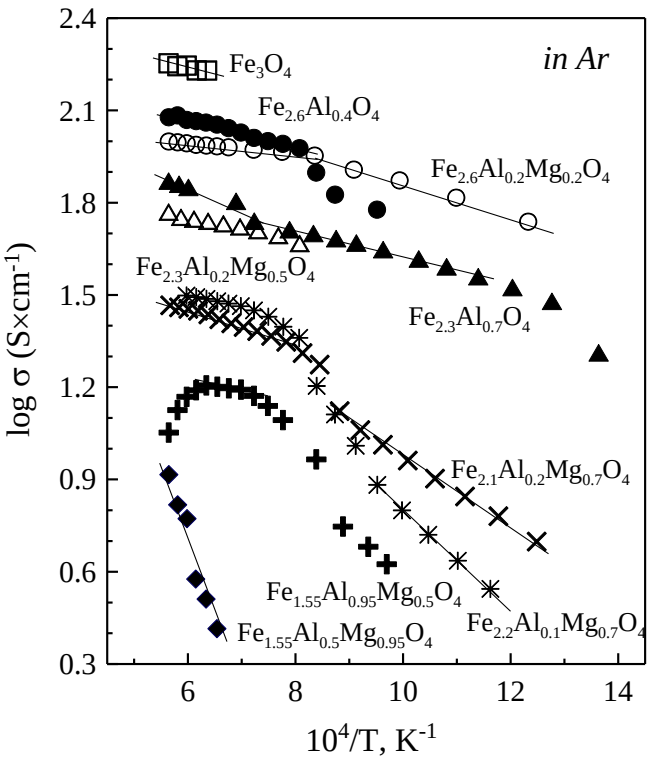

Figure 7 - Temperature dependence of the total conductivity of Mg- and Al- substituted magnetite.

Fig. 7 shows temperature dependence of the total conductivity for (Fe, Al, Mg)$_3$O$_4$ spinel materials; the data on $Fe_{3-x}Al_xO_4$ [13] system was added for comparison. Magnetite-based spinels are predominantly electronic conductors; as an example, the ion transference numbers in $Fe_{2.11}Mn_{0.54}Zn_{0.35}O_4$ were found to vary in the range 10^{-7} – 10^{-4} at 1370 – 1570 K [29]. The electronic transport occurs via smallpolaron mechanism by hopping between $Fe^{2+} \leftrightarrow Fe^{3+} + e^-$, and is restricted mainly to octahedral sites [7, 8, 14, 30].

Both magnesium and aluminium possess stable oxidation state and are, therefore, excluded from the electron hopping process. Effects exerted by additions of Mg and/or Al are, thus, mainly related to changes in the fraction of Fe^{2+}, and preference of Mg^{2+} and Al^{3+} to occupy octahedral positions (Table 3). Both contributions may affect the probability of hopping (i.e. the $[Fe^{2+}]$ $[Fe^{3+}]$ product in octahedral positions). Correspondingly, substitution of iron in spinel with Mg and Al results in systematic decrease of the electrical conductivity. For the same substitution level, the negative effect on conductivity is more pronounced for magnesium, while (Fe, Al)$_3$O$_4$ spinels show noticeably higher conductivity. Note that the $[Fe^{2+}][Fe^{3+}]$ product vanishes for $MgFe_2O_4$ to maintain charge neutrality. Thus, generation of extra amount of Fe^{2+} is beneficial for n-type electronic conduction in ferrospinels, in opposite to Fe^{3+}. This tendency is well-illustrated by the total conductivity dependence on the $[Fe^{2+}]_{oct}$ $[Fe^{3+}]_{oct}$ product (Fig. 8).

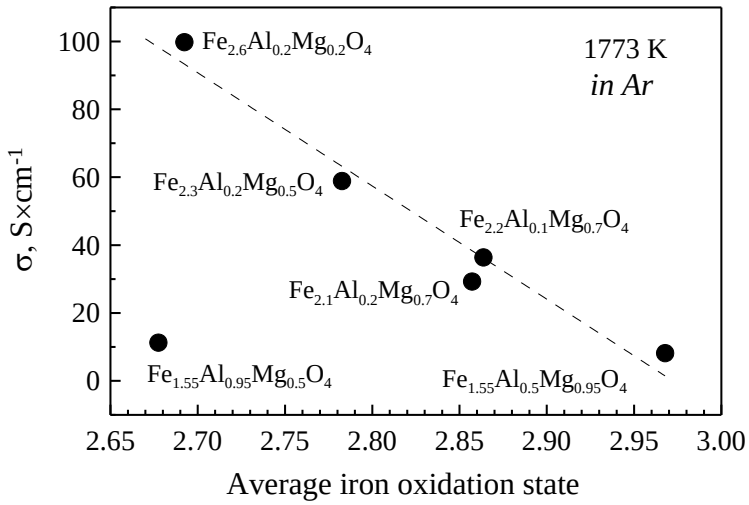

Figure 8 – Total conductivity *vs.* average iron oxidation state in (Fe, Al, Mg)$_3$O$_4$ spinels.

However, some uncertainties may still originate from calculations without accounting for other heating induced point defects in ferrospinels, such as cation vacancies or interstitials (Ref. [8] and references therein) and assumption, that all substituent cations and Fe^{2+} reside in octahedral sites. For all studied compositions the dependence shows almost linear behaviour, indicating that probability of hopping is the main factor, responsible for conductivity changes upon substitution in $(Fe, Al, Mg)_3O_4$ system. High additions of trivalent Al^{3+} with preferential octahedral occupancy may affect the probability of hopping by lowering $[Fe^{3+}]$ while maintaining $[Fe^{2+}]$; this is demonstrated by the behaviour of $Fe_{1.55}Al_{0.95}Mg_{0.5}O_4$ spinel, which shows a distinct conductivity variation with temperature in the high temperature range (Fig. 7). Apparently, at sufficiently high temperatures oxygen losses on heating may even result in further decrease of $[Fe^{2+}]_{oct}[Fe^{3+}]_{oct}$. In addition, one cannot exclude the possibility of changes in mobility, mainly for spinels with highest compositions changes, due to combined effects of structural changes and thermal collisions, leading to the conductivity drop. Additional explanation for the observed compositional dependence of the total conductivity of $(Fe, Al, Mg)_3O_4$, can rely on the different conditions for electron hopping in these materials, depending on Al and Mg content. In particular, the unit cell volume is smaller for aluminium-containing magnetite, if compared to $(Fe, Mg)_3O_4$ [8,13]; co-substitution is shown to demonstrate additive effect (Table 2). Thus, aluminium promotes smaller average Fe^{2+} – Fe^{3+} distance, facilitating electron hopping. Noteworthy, that small average Fe^{2+} – Fe^{3+} in spinels, in some cases, may even lead to appearance of band-like conductivity, as described in [15] and references therein. This mechanism may also, to a certain extent, contribute to the different conductivity behaviour of $Fe_{1.55}Al_{0.95}Mg_{0.5}O_4$ spinel, which has the smallest unit cell parameter among the studied materials.

The variations of the total conductivity of $(Fe, Al, Mg)_3O_4$ spinels with temperature are quite complex and, most likely, are determined by the changes in defect-chemistry from interstitial cation formation above 1300 K to generation of cation vacancies at lower temperatures (Ref. [8] and references therein), and partial decomposition of the spinel phase. Thus, the maghemite structure can be regarded as the extreme case of cation deficient $Fe_{3-\delta}O_4$ spinels.

Below 1200 K all studied samples demonstrated slow equilibration kinetics on cooling, resulting in gradual conductivity drift with time. Therefore, the values of activation energies (E_a) (Table 4) were calculated only for high temperature range, using the case of adiabatic hopping for small-polaron conductivity mechanism [7]:

$$\sigma = \frac{A}{T}\exp(-E_a / RT) \quad (3)$$

The activation energies of moderately substituted samples increases upon substitution and vary in the range from 15 to 23 kJ/mol at 1200 – 1773 K in Ar, being consistent with literature data [7, 13]. Compared to the (Fe, Al)$_3$O$_4$ binary system, addition of magnesium decreases the activation energy of the total conductivity in high temperature range; e.g., from 23 kJ/mol for $Fe_{2.3}Al_{0.7}O_4$ at 1451 – 1773 K [13] down to 19 kJ/mol for $Fe_{2.3}Al_{0.2}Mg_{0.5}O_4$ at 1369 – 1773 K (Table 4).

At 1773 K and p(O_2) from 10^{-5} to 0.21 atm, moderately substituted (Fe, Al, Mg)$_3$O$_4$ spinels show high and stable electrical performance, indicating their phase stability in these conditions (Fig. 9). An example of XRD pattern of $Fe_{2.1}Al_{0.2}Mg_{0.7}O_4$ at 1673 K in vacuum is given in Fig.10. In opposite to the as-prepared sample at room temperature, periclase impurity was not present in these conditions. Within the phase stability domain, the electrical conductivity of moderately substituted samples is essentially p(O_2)-independent at 1573 – 1773 K. A minor increase in total conductivity with reducing oxygen partial pressure is, probably, associated with increasing concentration of n-type charge carriers. The conductivity behaviour with p(O_2) for $Fe_{2.6}Al_{0.2}Mg_{0.2}O_4$ and $Fe_{2.3}Al_{0.2}Mg_{0.5}O_4$ materials is quite similar to that of (Fe, Al)$_3$O$_4$ analogues [13].

Redox induced phase decompositions and/or onset of secondary phases may also affect conductivity, in addition to effects on carrier concentration and mobility. For example, highly substituted $Fe_{1.55}Al_{0.5}Mg_{0.95}O_4$ demonstrates a substantial increase in conductivity on reducing oxygen partial pressure below a certain limit. The onset of this increase shifts to lower p(O_2) when decreasing the temperature. Such behaviour can be ascribed to phase decomposition and segregation of more conductive wüstite-based phase, as previously confirmed for $Fe_{1.55}Cr_{0.5}Mg_{0.95}O_4$ and $Fe_{2.1}Mg_{0.9}O_4$ spinels [8].

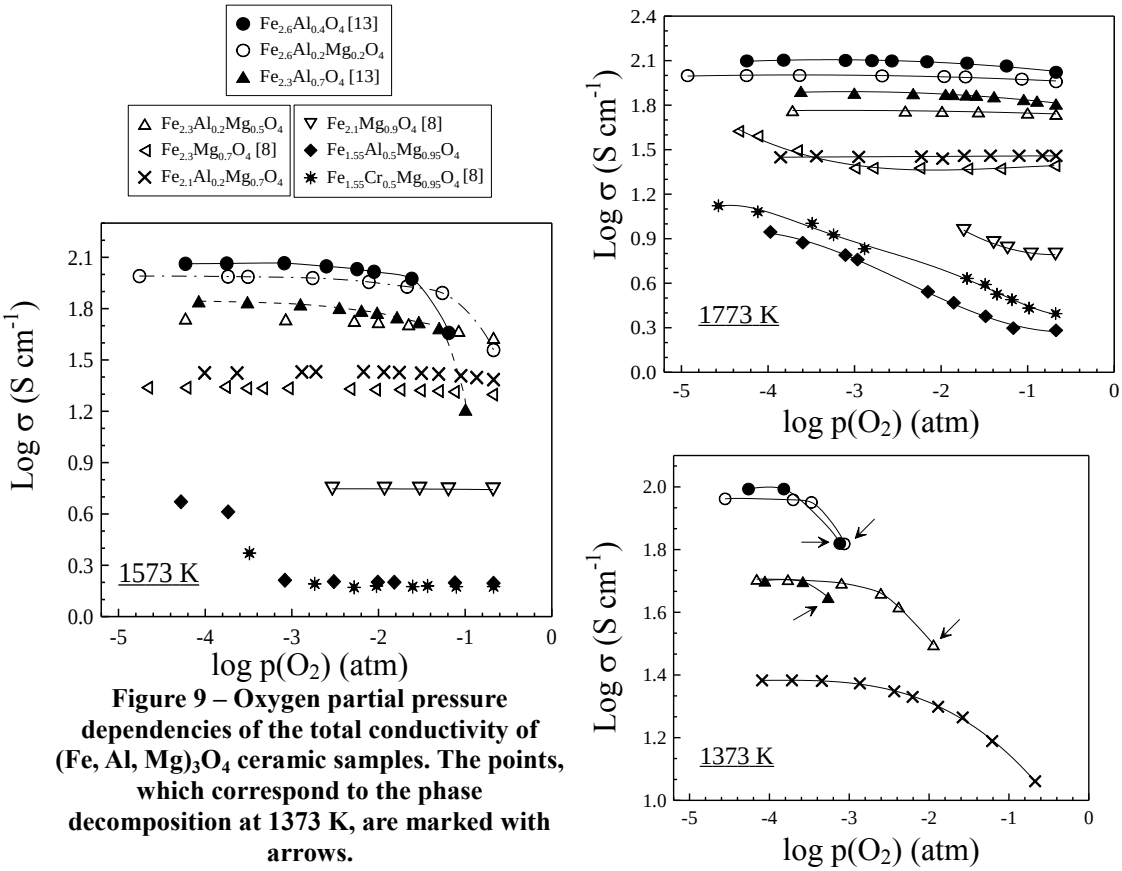

Figure 9 – Oxygen partial pressure dependencies of the total conductivity of (Fe, Al, Mg)$_3$O$_4$ ceramic samples. The points, which correspond to the phase decomposition at 1373 K, are marked with arrows.

The conductivity drop on increasing oxygen partial pressure above certain value at temperatures ≤ 1573 K (Fig. 9), in most cases, is also associated with phase decomposition, induced by oxidation. The inflection point, which corresponds to the onset of the decomposition, is quite obvious for $Fe_{2.6}Al_{0.4}O_4$, $Fe_{2.6}Al_{0.2}Mg_{0.2}O_4$ and $Fe_{2.3}Al_{0.7}O_4$ at 1573 K. Note that the values of conductivity after decomposition onset are not related to the equilibrium conditions, since this process is very slow in spinel ceramics. The arrows shown in Fig. 9 (at 1373 K) mark the sharp decrease of conductivity at onset of oxidative decomposition, to emphasize differences relative to more gradual changes in conductivity observed for $Fe_{2.1}Al_{0.2}Mg_{0.7}O_4$, when Fe^{2+} oxidation to Fe^{3+} causes decrease in $[Fe^{2+}][Fe^{3+}]$ in spinel lattice.

Although precise determination of $p(O_2)$-stability limits for the studied materials was not performed in present work, since it requires long-time equilibration, the effect of substitution on stability is quite obvious and confirms previous observations.

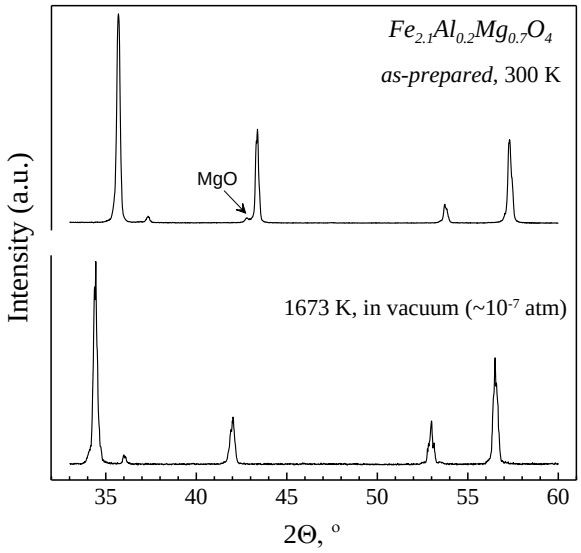

Figure 10 – Examples of XRD patterns for as-prepared $Fe_{2.1}Al_{0.2}Mg_{0.7}O_4$ at room temperature and at 1673 K in vacuum.

As an example, at 1573 K the onset of phase decomposition and conductivity drop for $Fe_{2.3}Al_{0.7}O_3$ corresponds to $p(O_2) \sim 0.05$ atm, whereas $Fe_{2.3}Al_{0.2}Mg_{0.5}O_4$ (Fig. 9) is stable even in air. Thus, for moderate substitution level, magnesium addition increases the $p(O_2)$ range, where $(Fe, Al, Mg)_3O_4$ show stable electrical performance and single-phase composition at 1373 – 1573 K.

Reasonably high performance is characteristic for $Fe_{2.6}Al_{0.2}Mg_{0.2}O_4$ and $Fe_{2.3}Al_{0.2}Mg_{0.5}O_4$ spinels; for the former the total conductivity in Ar is less than two times lower than for undoped magnetite at 1773 K.

4.2.5 Conclusions

Addition of magnesium was found to increase the tolerance of aluminium-containing magnetite against oxidative decomposition. The phase stability of $(Fe, Al, Mg)_3O_4$ spinels is mainly determined by $[Al^{3+}]$:$[Mg^{2+}]$ concentration ratio and iron content. XRD analysis and static lattice simulation studies revealed that the effect of moderate substitution with magnesium may be not sufficient to substantially improve the redox stability of $(Fe, Al)_3O_4$. However, due to relatively slow rate of exchange and diffusion controlled processes in ferrospinels, magnesium, even at relatively low substitution levels, effectively improves the dimensional stability of bulk ceramics.

For single-phase ceramics, thermal expansion coefficients of (Fe, Al, Mg)$_3$O$_4$ are weakly dependent on the composition and vary in the range (11.0 – 11.6) × 10^{-6} K at 300 – 650 K, and (13.0 – 13.1) × 10^{-6} K at 750 – 1370 K. Substitution with magnesium led to lower total conductivity, if compared to aluminium-substituted analogue. Weak p(O_2)-dependence of the conductivity and phase stability at 1673-1773 K suggest a broad range of conditions where (Fe,Al,Mg)$_3$O$_4$ –based anodes can be successfully used in the pyroelectrolysis.

4.2.6 References

[1] – Sadoway DR. New opportunities for metal extraction and waste treatment by electrochemical processing in molten salts. J Mater Res 1995; 10:487-92.

[2] – Wang DH, Gmitter AJ, Sadoway DR. Production of oxygen gas and liquid metal by electrochemicaldecomposition of molten iron oxide. J Electrochem Soc 2011; 158:E51-4.

[3] – Kim H, Paramore J, Allanore A, Sadoway DR. The influence of electrolyte basicity on the performance of an iridium anode for the electrolysis of molten iron oxide. J Electrochem Soc 2011; 158:E101-5.

[4] – Kofstad P. Nonstoichiometry, Diffusion and electrical conductivity in binary metal oxides. New York: Wiley-Interscience; 1972.

[5] – Maris G., Shklyarevskii O, Jdira L, Hermsen JGH. Speller S. One-dimensional structural and electronic properties of magnetite Fe3O4 (110). Surface Sci 2006; 600:5084-91.

[6] – Petric A, Ling H. Electrical conductivity and thermal expansion of spinels at elevated temperatures. J Am Ceram Soc 2007; 90:1515-20.

[7] – Mason TO, Bowen HK. Electronic conduction and thermopower of magnetite and iron-aluminate spinels. J Amer Ceram Soc 1981; 64:237-42.

[8] – Yaremchenko AA, Kovalevsky AV, Naumovich EN, Kharton VV, Frade J.R. High-temperature electrical properties of magnesiowustite Mg1-xFexO and spinel Fe3-x-yMgxCryO4 ceramics. Solid State Ionics 2011; 192:252-8.

[9] – Birat J, Borlee J. Carbon Dioxide Reduction Metallurgy. In: Neelameggham NR, Reddy RG, editors. The Minerals, Warrendale: Metals & Materials Soc; 2008, p.59.

[10] – Charette GG, Flengas SN. Thermodynamic properties of the oxides of Fe, Ni, Pb, Cu, and Mn, by EMF measurements, J Electrochem Soc 1968; 115:796-804.

[11] – Tretyakov YD. Thermodynamics of Ferrites, Leningrad: Khimiya, 1967.

[12] – Jung IH, Decterov SA, Pelton AD. Critical thermodynamic evaluation and optimization of the Fe-Mg-O system. J Phys Chem Solids 2004; 65:1683-95.

[13] – Kovalevsky AV, Naumovich EN, Yaremchenko AA, Frade JR. High-temperature conductivity, stability and redox properties of Fe3-xAlxO4 spinel-type materials. J Eur Ceram Soc 2012; 32:3255-63.

[14] – Nell J, Wood BJ, Mason, TO. High-temperature cation distributions in Fe3O4-MgAl2O4-MgFe2O4- FeAl2O4 spinels from thermopower and conductivity measurements. Amer Miner 1989; 74:339-51.

[15] – Modi KB, Joshi HH, Kulkarni RG. Magnetic and electrical properties of Al3+-substituted MgFe2O4. J Mater Sci 1996; 31:1311-7.

[16] – Marchant DD, Bates JL. Preparation and properties of iron-magnesium-aluminium spinel. Comm Amer Ceram Soc 1983; C99-102.

[17] – Weeks RA, Sonder E. Electrical conductivity of pure and Fe-doped magnesium-aluminium spinel. J Amer Ceram Soc 1980; 63: 92-5.

[18] – Rodríguez-Carvajal J. Recent advances in magnetic structure determination by neutron powder diffraction. Physica B 1993; 192: 55–69.

[19] – Gale JD. GULP - a computer program for the symmetry adapted simulation of solids. JCS Faraday Trans 1997; 93:629-37.

[20] – Gale JD, Rohl AL. The General Utility Lattice Program. Mol Simul 2003; 29:291-341.

[21] – http://www.ucl.ac.uk/klmc/Potentials/ , 2012.

[22] – Woodley SM, Catlow CRA, Piszora P, Stempin K, Wolska E. Computer modeling study of the lithium ion distribution in quaternary Li–Mn–Fe–O spinels. J Sol State Chem 2000; 153:310-6.

[23] – Woodley SM, Battle PD, Gale JD, Catlow CRA. The prediction of inorganic crystal structures using a genetic algorithm and energy minimization. Phys Chem Chem Phys 1999; 1:2535-42.

[24] – Bush TS, Gale JD, Catlow CRA, Battle PD. Self-consistent interatomic potentials for the simulation of binary and ternary oxides. J Mater Chem 1994; 4:831-7.

[25] – http://www.wolfram.com/mathematica/ , 2013.

[26] – Shannon RD. Revised effective ionic radii and systematic studies of interatomic distances in halides and chalcogenides. Acta Cryst 1976; A32:751-67.

[27] – Levy D, Artioli G, Dapiaggi M. The effect of oxidation and reduction on thermal expansion of magnetite from 298 to 1173 K at different vacuum conditions. J Solid State Chem 2004; 177:1713-6.

[28] – Okudera H, Kihara K, Matsumoto T. Temperature dependence of structure parameters in natural magnetite: single crystal X-ray studies from 126 to 773 K. Acta Crystallogr Sect B 1996; 52:450-7.

[29] – Jang YI, Yoo HI. Phase stability and ionic transference number of a ferrite spinel, Mn0.54Zn0.35Fe2.11O4. Solid State Ionics 1996; 84:77-88.

[30] – Carter DC, Mason TO. Electrical properties and site distribution of cations in (MnyCo1-y)0.4Fe2.6O4. J Am Ceram Soc 1988; 71:213-8.

4.3 Effects of transition metal additives on redox stability and high-temperature electrical conductivity of $(Fe, Mg)_3O_4$ spinels

N.M. Ferreira, A.V. Kovalevsky, E.N. Naumovich, A.A. Yaremchenko, K.V. Zakharchuk, F.M. Costa and J.R. Frade

(Journal of the European Ceramic Society 34 (2014) 2339–2350
http://dx.doi.org/10.1016/j.jeurceramsoc.2014.02.016)

4.3.1 Abstract

Magnetite-based spinels are considered as promising oxide materials to meet the requirements for ceramic consumable anodes in molten oxide pyroelectrolysis process, a breakthrough low-CO_2 steel technology aimed to overcome the environmental impact of classical extractive metallurgy. The present work focuses on the assessment of phase relationships, redox stability and electrical conductivity of $Fe_{2.6}Me_{0.2}Mg_{0.2}O_4$ (M = Ni, Cr, Al, Mn, Ti) spinel-type materials at 300 – 1773 K and $p(O_2)$ from 10^{-5} to 0.21 atm. The oxidation state of substituting transition metal cation, affecting the fraction of Fe^{2+} in spinel lattice, was found to be a key factor, which determines the electronic transport and tolerance against oxidative decomposition, while the impact of preferred coordination of additives on these properties was less pronounced. At T > 650 K thermal expansion of $Fe_{2.6}Me_{0.2}Mg_{0.2}O_4$ ceramics exhibited complex behaviour, and, in highly oxidizing conditions, resulted in significant volume changes, unfavourable for high-temperature electrochemical applications.

4.3.2 Introduction

Though molten oxide electrolysis was proposed for carbon-lean steelmaking [1,2], feasibility of this technology is far from being demonstrated, largely due to the highly corrosive nature of molten electrolytes. The concept itself is also far from being convincingly demonstrated even at laboratory scale. Highly corrosive nature of high-temperature molten electrolytes raises major questions about prospects to develop stable anode materials, able to withstand extreme operation conditions.

Noble metal oxygen electrodes (e.g., Ir) were proposed for small scale demonstration [2], but these are far from being truly inert in molten oxide electrodes, and their cost is not affordable for mass production. Similarly, although molybdenum shows good prospects for electric boosting in glass technology due to high corrosion resistance in glass melts under ac operation, one cannot consider dc anodic polarization of Mo electrodes in contact with molten oxide electrolytes, due to poor refractoriness of Mo oxide scales. Thus, one of the major challenges in steelmaking by molten oxide electrolysis is to seek alternative concepts of consumable oxygen electrodes, as currently used in aluminium production by electrolysis in melts.

Magnetite-based spinels have been considered as slowly consumable oxide electrodes to tackle this challenge. Pure magnetite combines low cost and occurrence as major components of natural raw materials with relatively good refractoriness, compatibility with molten silicates and high electronic conductivity [3-8]. Its chemical composition nicely fits the concept of consumable anode, since the dissolution of Fe_3O_4 does not lead to contamination of the system and may even account for a fraction of iron oxide raw materials. However, insufficient redox stability in air below 1667 K and even in inert gas ($p(O_2) \approx 10$ Pa) below 1300 – 1373 K [9] represents a serious drawback. In addition, the melting point of pure magnetite (1811 K) is only slightly above that for metallic iron (1808 K). Along with thermodynamic stability, further improvement of refractoriness is also desirable.

Our previous studies have demonstrated that redox stability of magnetite at high temperatures can be substantially enhanced by substitution with magnesium [6, 10, 11], which is also attractive due to the low cost, natural abundance and compatibility with molten silicate systems. At the same time, substitution of iron with Mg^{2+} shifts the melting point up to 2023 K for $MgFe_2O_4$, simultaneously improving the refractoriness. Phase diagrams [12, 13] also predict substantially large compositional ranges for stable $Fe_{3-x}Mg_xO_4$ spinels even in contact with pure oxygen atmosphere. However, partial iron substitution with magnesium significantly reduces the electrical conductivity at 1250 – 1773 K [6, 11] due to decrease in the concentration of n-type electronic charge carriers.

Substitution with redox stable cations of higher valency (e.g., Al^{3+}) was proved to have less negative effect on the electronic transport within the phase stability limits, whilst the impact on the stability is opposite to that from magnesium [11, 14].

Thus, the present work focuses on guidelines for further composition changes, seeking a reasonable compromise between redox stability and high-temperature electrical conductivity in magnetite-based spinel materials, considering the targets set by requirements for high-temperature electrolytic steelmaking. Taking into account the contribution of magnesia to redox stability, the selected compositions were $Fe_{2.6}Me_{0.2}Mg_{0.2}O_4$ spinels, with additions of transition metal cations differing in redox stability (i.e. Me = Ni, Mn, Cr, Ti). As an additional benefit for the pyroelectrolysis process, one should consider a possibility for co-reduction of those metals at the cathode and further alloying with iron. The obtained data on the electrical conductivity and stability is compared to that obtained previously for $Fe_{2.6}Al_{0.2}Mg_{0.2}O_4$ spinel [11]. The level of iron substitution is selected to retain reasonably high electrical conductivity, essential for ceramic anodes in high temperature electrolysis. As for previously studied $(Fe, Al, Mg)_3O_4$ system [6, 11, 14], particular attention is given to the relevant properties in the intermediate temperature range, aiming on guidelines for electrode integrity, which may depend largely on the operation regime of the electrolysis cell.

4.3.3 Methods

4.3.3.1 Experimental methods

The precursor powders of $Fe_{2.6}Me_{0.2}Mg_{0.2}O_4$ (M = Ni, Cr, Mn, Ti) spinels were prepared by solid state route from stoichiometric amounts of $FeC_2O_4{\cdot}2H_2O$ (99%, Sigma-Aldrich), $Ni(NO_3)_2{\cdot}6H_2O$ (≥ 98.5%, Sigma-Aldrich), $Cr(NO_3)_3{\cdot}9H_2O$ (99%, Sigma-Aldrich), $Mn(CH_3COO)_2{\cdot}4H_2O$ (≥ 99%, Aldrich) and TiO_2 (99.8%, Sigma-Aldrich). The conditions of powder processing and sintering were similar to those used for preparation of $(Fe, Al)_3O_4$ and $(Fe, Al, Mg)_3O_4$ spinels [11, 14]. The ceramic samples were sintered at 1753 – 1773 K for 10 h in argon atmosphere ($p(O_2) \sim 10^{-5} – 10^{-4}$ atm)) and cooled down to room temperature at 3 K/min; another set of the samples was prepared in air in similar conditions. X-ray diffraction (XRD) and thermogravimetry (TG) studies were performed on powders, after grinding corresponding ceramics in a mortar.

For the electrical conductivity and thermal expansion measurements, the obtained disk samples were cut into rectangular bars (~ 2 × 3 × 12 mm^3). The experimental density of the ceramics was determined via Archimedes´ method, using distilled water as a liquid medium and measuring the weights of dry, soaked and suspended sample. Thus obtained density was ~ 2 – 3 % higher than that calculated for the sake of comparison from dry weight and geometrical dimensions of the sample.

X-ray diffraction patterns were recorded using a Rigaku D/Max-B diffractometer (CuK_α, 2Θ=10-80°, step 0.02°, exposition 2 s). Unit cell parameters were calculated from the diffraction data using profile matching method in Fullprof software [18]. SEM analysis (Hitachi SU-70 model) was performed on fractured surface of the ceramic samples, sintered in Ar. Redox behaviour of the samples in the intermediate temperature range was studied by thermogravimetry (TG) (Setaram SetSys 16/18 instrument, sensitivity 0.4 μg, initial sample weight ~ 0.5 g), in a flow of argon or dry air at 298 – 1373 K with constant heating/cooling rate of 2 K/min. Thermal expansion studies were performed on heating (3 K/min) up to 1350 K in argon and air atmospheres, using a vertical alumina dilatometer Linseis L70/2001. Total electrical conductivity (σ) was measured by 4-probe dc technique at 750 – 1773 K in the oxygen partial pressure $p(O_2)$ range from 10^{-5} to 0.21 atm in flowing air-Ar mixtures. The $p(O_2)$ in the gas flow was monitored using an YSZ oxygen sensor.

4.3.3.2 Lattice simulations

Static lattice simulations were performed using GULP software [16,17], the procedure was similar to that previously described for $(Fe, Al)_3O_4$ [14] and $(Fe, Al, Mg)_3O_4$ spinels [11]. For simulation of the magnetite-based spinels, Bush/Woodley potentials sets (Table 1) were selected. A 2 x 2 x 2 supercell (64 formula units) with 18 Å cut-offs for Buckingham interatomic potentials was used to simulate a solid solution. A special technique of the random cells generation was elaborated to resolve possible issues with implicit cation ordering in hand-crafted supercells. For each composition a set of 70 – 100 supercells with random distribution of cations in tetragonal and octahedral sublattices was generated.

Each set had a fixed infill of the considered cation (Fe^{2+}, Al^{3+}, Ti^{4+} Cr^{3+}, Ni^{2+}, Mn^{2+} or Mn^{3+}) for the octahedral sublattice, while distribution of other cations between sublattices was random. Use of the fixed infill allows to decrease substantially the amount of trial lattices, necessary to cover desired region of the solid solutions. The generated supercells were analyzed in GULP to determine the influence of cation distribution in the lattice on the energy of the supercell.

Table 1 – Phenomenological potentials, used for static lattice simulation.

Atom	Core-shell		Interatomic (Buckingham)				References
	Y, e (shell charge)	*k*, eV/Å^2	Pair	A, eV	ρ, Å	C, eV/Å^2	
O^{2-}	-2.513	20.53	O^{2-}	22.41	0.6937	32.32	[18,19]
Fe_t^{3+}	1.029	10082.5	O^{2-}	1240.232	0.3069	0	[18,19]
Fe_o^{3+}	1.029	10082.5	O^{2-}	1342.754	0.3069	0	[18,19]
Fe^{2+}	2	n/a	O^{2-}	2763.945	0.2641	0	[18,20]
Al^{3+}	2.957	403.98	O^{2-}	2409.505	0.2649	0	[18,21]
Mg^{2+}	0.420	349.95	O^{2-}	2457.243	0.261	0	[18,21]
Ni^{2+}	n/a	n/a	O^{2-}	2057.230	0.267000	2.1980	[18,22]
Ti^{4+}	1.668	253.6	O^{2-}	2088.107	0.2888	0	[18,21]
Mn^{3+}	1.029	148.0	O^{2-}	1686.125	0.2962	0	[18,19]
Mn^{2+}	n/a	n/a	O^{2-}	426.8332	0.380836	0	present work
Cr^{3+}	2.541	261.9	O^{2-}	1760.1505	0.282958	0	present work

Since phenomenological potentials for Mn^{2+} and Cr^{3+} against Bush "oxygen-oxygen" potential could not be found in published literature, these were obtained by fitting experimental results in GULP software (Mn^{2+}) or simulated by DFT (Cr^{3+}) data sets. To fit the potential for Mn^{2+}, the experimental data on MnO compressibility in the range up to 8.09 GPa was used [23, 24], with 13 data points in a set. The sum of squares, obtained by simultaneous simplex fit, was 0.001783, indicating that the potentials almost precisely describe the rock-salt structure of the MnO. Attempts to reproduce similar technique for Cr_2O_3 using experimental compressibility data [25, 26] resulted in acceptable pair of the potentials for corundum-like structures, with error in lattice parameter below 3%.

However, verification of these potentials for the $MgCr_2O_4$ spinel structure failed, giving an error of around 25% in the cell volume, compared to the experimental data [24, 27]. Hence, the energy surface fit for $MgCr_2O_3$ structure was used. $MgCr_2O_4$ cell was simulated in ABINIT DFT software [28-32], using GTH pseudopotencials with PBE exchange-correlation functionals [33, 34]. These pseudopotentials resulted in up to 1.3% of the error in lattice parameters, when energy cutoff 90 Hartree and *tolvrs* 10^{-15} were used. For fitting procedure eight datasets with lattice parameters varying from 7.8 to 8.4 Å were simulated.

Obtained data set, comprising values of the lattice parameter, energy and pressure for each simulated cell, was used to fit the Buckhingham and core-shell potentials in GULP. As a result, Cr^{3+}-O^{2-} pair potential and core-shell parameters for Cr^{3+} were calculated. These interatomic potentials were tested with $MgCr_2O_4$ and Cr_2O_3 lattices, and simulation results demonstrated errors -1.7 % and -1.8 % (a, b)/-3.4% (c), relative to the experimental cell parameters of spinel ($MgCr_2O_4$) and corundum (Cr_2O_3) structures, correspondingly.

The obtained results were analysed in terms of energy of the structure formation (ΔE_{str}) from simple oxides, expressed as:

$$\Delta E_{str} = E_{cell} - \sum \gamma_i E_i^{cell} \quad (1)$$

where E_i^{cell} - energy of formation of the individual oxide, calculated in GULP, γ_i - stoichiometric coefficient. To assess the stability of the considered solid solutions against oxidative decomposition with the formation of Fe_2O_3 and simple oxides, corresponding energy ΔE_{ox} was calculated:

$$\Delta E_{ox} = \sum \gamma_i E_i^{cell} + \gamma\left(Fe^{2+}\right)\Delta E_{Fe}^{ox} - E_{cell} \quad (2)$$

where $\gamma\left(Fe^{2+}\right)$ is stoichiometric coefficient for Fe^{2+}, ΔE_{Fe}^{ox}=-1.45 eV- energy of the oxidation of Fe^{2+} to Fe^{3+} according to the reaction $2FeO + 1/2\ O_2 \rightarrow Fe_2O_3$, with corresponding formation enthalpies $\Delta_f H^0_{298}(FeO)$= –272.0 kJ/mol and $\Delta_f H^0_{298}(Fe_2O_3)$= –824.2 kJ/mol [35].

The collected data on the lattice energy (in GULP formalism) E_{cell} were also fitted using simple linear models, to reveal the coordination preference of the substituting cations by corresponding impact on the lattice stability. The fitting procedure was performed in Wolfram Research Mathematica 9 software [36]. The dataset on (Fe, Al, Mg)$_3$O$_4$ system was supplemented with our results [11], published earlier, to provide adequate comparison with similar transition-metal containing spinels. The sets for (Fe, Me, Mg)$_3$O$_4$ were extended by earlier collected data for Fe_3O_4 and $Fe_{2.5}Mg_{0.5}O_4$ [11,14]. The data for (Fe, Me, Mg)$_3$O$_4$ (Me=Al, Ni, Cr, Ti) was fitted using a regression model:

$$E_{cell} = E_o + a_{\mathrm{Mg}}\left[\mathrm{Mg}^{2+}\right] + b_{Mg}\left[\mathrm{Mg}_{\mathrm{o}}^{2+}\right] + a_{\mathrm{Me}}\left[\mathrm{Me}^{z+}\right] + b_{\mathrm{Me}}\left[\mathrm{Me}_{\mathrm{o}}^{z+}\right] + b_{Fe}\left[\mathrm{Fe}_{\mathrm{o}}^{2+}\right] \qquad (3)$$

where E_0 corresponds to the lattice energy for undoped and not inverted magnetite, $[Mg^{2+}]$ and $[Me^{z+}]$ are the total concentrations of Mg^{2+} and Me^{z+} cations, and $[Me_o^{z+}]$ and $[Fe_o^{2+}]$ represent concentration of respective cations in octahedral sites, while coefficients *a* and *b* with corresponding subscript symbols describe their impact on the lattice energy. For the reasons, described below in "Results and discussion" section, in the case of substitution with manganese, one considered coexistence of divalent Mn^{2+} and trivalent Mn^{3+} and the corresponding regression model was used:

$$\begin{aligned} E_{cell} = {} & E_o + a_{\mathrm{Mg}}\left[\mathrm{Mg}^{2+}\right] + b_{Mg}\left[\mathrm{Mg}_{\mathrm{o}}^{2+}\right] + a_2\left[\mathrm{Mn}^{2+}\right] + b_2\left[\mathrm{Mn}_{\mathrm{o}}^{2+}\right] + \\ & + a_3\left[\mathrm{Mn}^{3+}\right] + b_3\left[\mathrm{Mn}_{\mathrm{o}}^{3+}\right] + b_{Fe}\left[\mathrm{Fe}_{\mathrm{o}}^{2+}\right] \end{aligned} \qquad (4)$$

where, similarly, a_2 and a_3 are the impacts of total concentration of Mn^{2+} and Mn^{3+} cations on the lattice energy, and b_2 and b_3 – corresponding impacts of their concentrations in octahedral sites.

4.3.4 Results and Discussion

Fig. 1 shows XRD patterns of $Fe_{2.6}Me_{0.2}Mg_{0.2}O_4$ samples, sintered in Ar and air atmospheres. Sintering in Ar results in single-phase spinel materials (space group $Fd\bar{3}m$), the data for $Fe_{2.6}Al_{0.2}Mg_{0.2}O_4$ [11] are shown for comparison. The experimental densities of spinel ceramics, containing transition metals, are quite similar and amount to 88-90% from theoretical density, calculated from XRD data; $Fe_{2.6}Al_{0.2}Mg_{0.2}O_4$ shows slightly better sinterability than other compositions under the same conditions (Table 1).

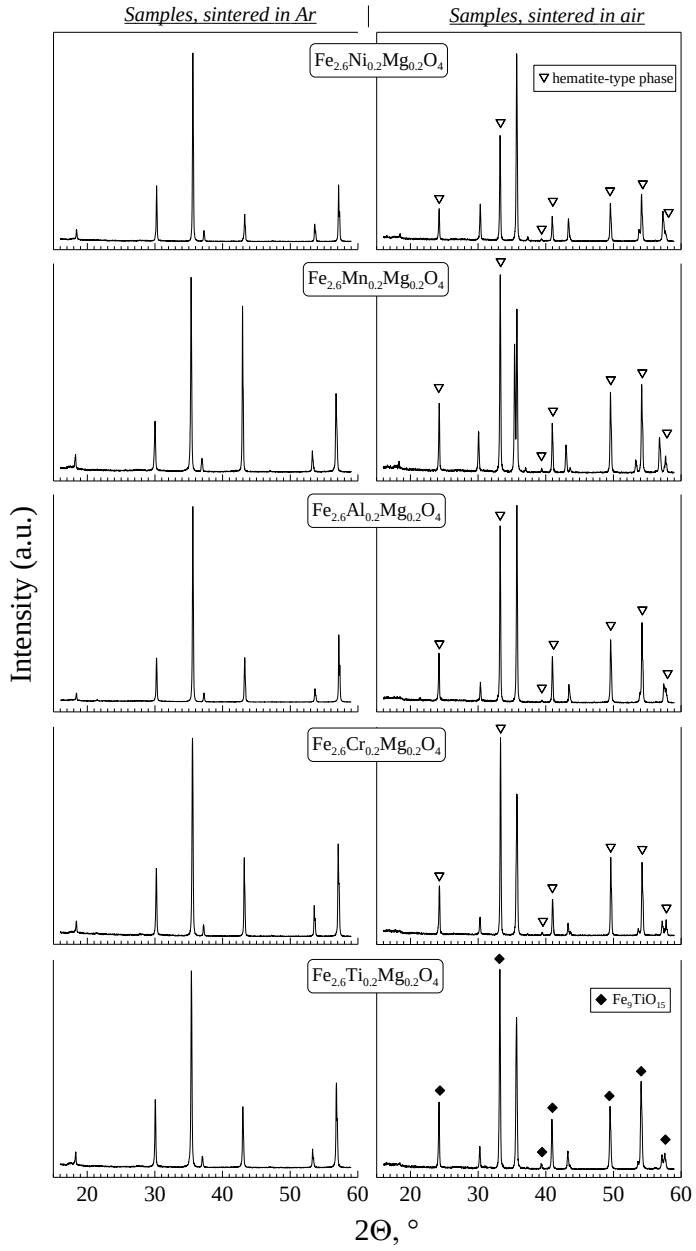

Figure 1 – XRD results for Ar- and air-sintered $Fe_{2.6}Me_{0.2}Mg_{0.2}O_4$ samples. Triangle symbols and diamonds indicate the individual peaks of hematite-type or Fe_9TiO_{15} phase, which are not present in pure spinel pattern.

Typical ceramics microstructure with grain size in the range 10-50 μm is shown in Fig.2 for $Fe_{2.6}Ni_{0.2}Mg_{0.2}O_4$ and $Fe_{2.6}Cr_{0.2}Mg_{0.2}O_4$ materials. Differences in unit cell parameters are determined not only by cation size, by also by preferred coordination of the transition metal cations, which can reside in octahedral and/or tetrahedral sites of the spinel structure, with corresponding impact on the bond length [37]. Due to significantly smaller ionic radius of Al^{3+} cation [38], $Fe_{2.6}Al_{0.2}Mg_{0.2}O_4$ has the lowest unit cell volume compared to other compositions.

As expected, sintering in air leads to oxidation and onset of hematite-type phases, containing transitional metal or aluminium; similar decomposition processes were observed for $(Fe, Al)_3O_4$ and $(Fe, Al, Mg)_3O_4$ spinel ceramics [11, 14]. Oxidative decomposition of $Fe_{2.6}Ti_{0.2}Mg_{0.2}O_4$ may include formation of hematite-type Fe_9TiO_{15} phase [39], as shown in Fig. 1.

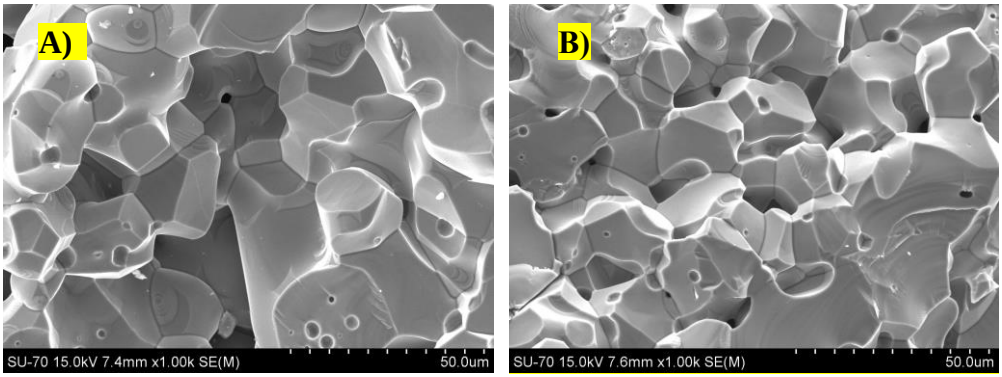

Figure 2 – SEM micrographs of the surface of fractured $Fe_{2.6}Ni_{0.2}Mg_{0.2}O_4$ (A) and $Fe_{2.6}Cr_{0.2}Mg_{0.2}O_4$ (B) samples.

The results of thermogravimetry studies suggest metastable phase composition of Ar-sintered $Fe_{2.6}Me_{0.2}Mg_{0.2}O_4$ (M=Cr, Mn, Ni, Ti) ceramic samples at low temperatures. Although phase-pure ceramics of the above compositions can be obtained in Ar, grinding to powders promotes faster oxygen exchange and perceptible weight increase upon heating even in argon atmosphere ($p(O_2) \sim 10^{-5}$ atm), due to oxygen uptake (Fig. 3A).

The oxidation is more pronounced for Mn and Ti -containing spinels. On the contrary, $Fe_{2.6}Ni_{0.2}Mg_{0.2}O_4$ shows almost negligible weight changes on heating in Ar, suggesting higher tolerance against oxidative decomposition for this material. Generally, one may anticipate that, for the same substitution level, cations with lower oxidation state (e.g, 2+) should improve the redox stability of magnetite by decreasing the Fe^{2+}:Fe^{3+} ratio in spinel lattice and reducing the total amount of cations, susceptible to oxidation. Substitution with cations possessing higher oxidation states (e.g, 4+), hence, can be expected to have an opposite effect on redox stability. The latter is in agreement with TG results upon heating in air (Fig. 3B). The maximum oxygen uptake increases in the sequence Me = $Ni^{2+} < Mn^{2+/3+} < Cr^{3+} \approx Al^{3+} < Ti^{4+}$, following the trends in changing the oxidation state of the substituting cation. The decomposition in air results in formation of hematite-type phases, as illustrated by Fig.4.

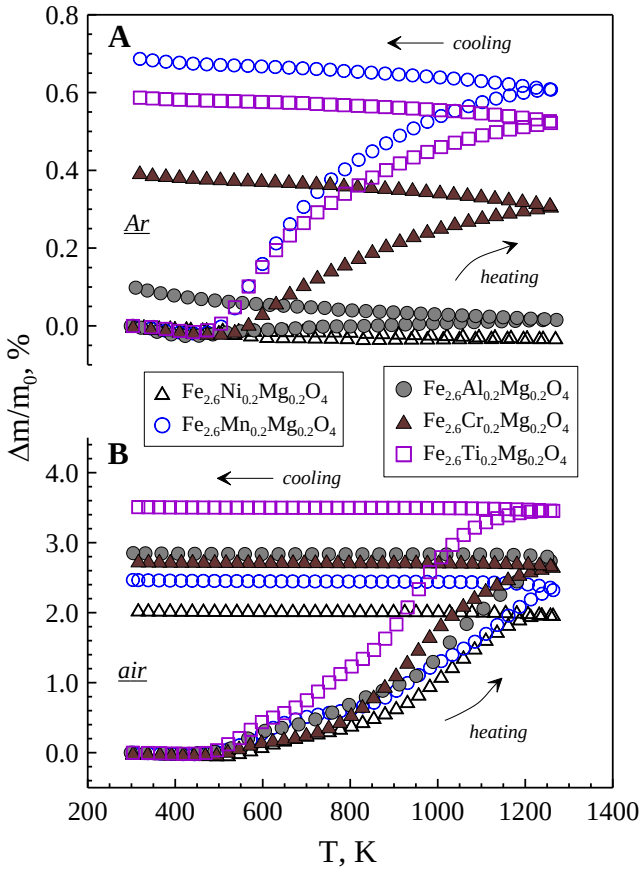

Figure 3 - Relative weight change of the powdered Ar-sintered $Fe_{2.6}Me_{0.2}Mg_{0.2}O_4$ spinel samples on heating and cooling (indicated with arrows) in Ar (A) and air (B).

Noteworthy, that oxygen content in the atmosphere may have a noticeable impact on the redox behaviour of the studied materials, as a result of different oxidation mechanisms. In nearly inert atmospheres (Ar) additional structural factors may be responsible for the observed difference in oxygen uptake, compared to the results obtained in air. In particular, distribution of Fe^{2+} cations between tetrahedral and octahedral sites determines their availability for oxidation, and, thus, may contribute to redox tolerance at least in low temperature range (450 – 750 K) [40]. Secondly, in atmospheres with low $p(O_2)$ the extent of oxidation may be also significantly affected by the thermodynamic stability of the spinel lattice itself, and its dependence on relevant parameters of substituting cations such as oxidation state and ionic radius.

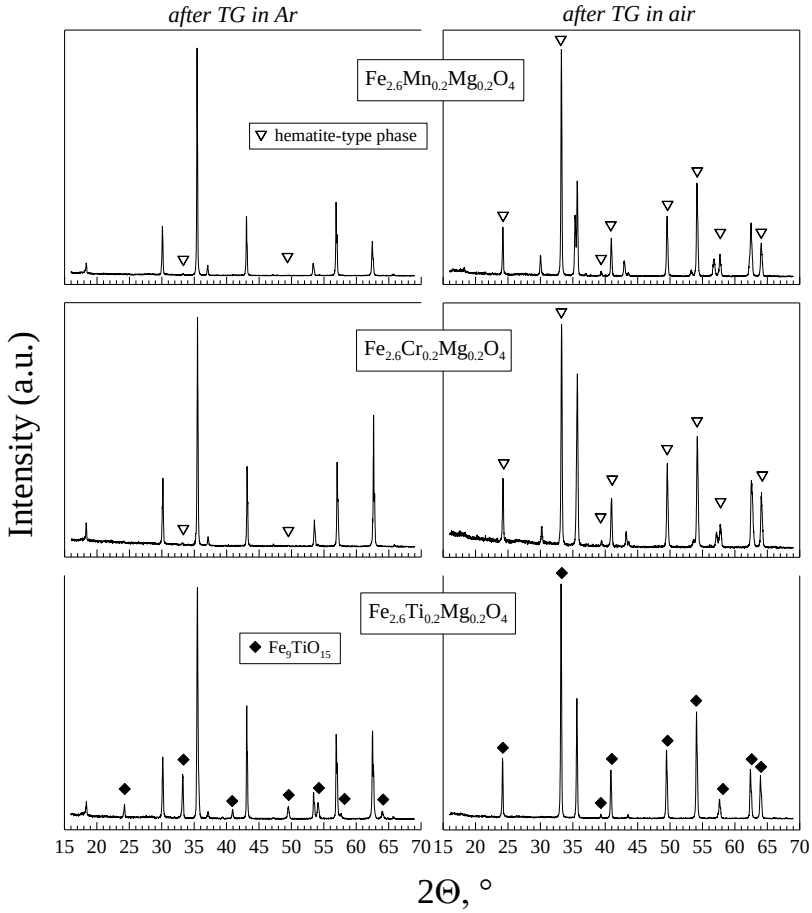

Figure 4 – XRD patterns of the samples, sintered in Ar, after TG studies. Triangle symbols and diamonds indicate the individual peaks of hematite-type or Fe_9TiO_{15} phase, which are not present in pure spinel pattern.

The mechanism has been ascribed to ionization of absorbed oxygen atoms by acquiring electrons from Fe^{2+}, followed by formation of Fe^{3+} cations and cation vacancies, which diffuse into the grain interior, whereas Fe^{2+} and Me^{z+} migrate in opposite direction [41]. Thus, for mild oxidizing conditions, the interdiffusion of cations is expected to partially accommodate the stress in the crystal lattice, exerted by incorporation of the oxygen ions, while at relatively high $p(O_2)$ massive formation of Fe^{3+} cations facilitates onset of hematite-type phase instead. As an example, in Ar $Fe_{2.6}Mn_{0.2}Mg_{0.2}O_4$ shows higher oxygen uptake than even $Fe_{2.6}Ti_{0.2}Mg_{0.2}O_4$ (Fig.3), at the same time having lower decomposition level (Fig.4).

Note that the prevailing ionic defects in magnetite and related spinels at moderately high temperatures, are cation vacancies in relatively oxidising conditions and cation interstitials for reduced $p(O_2)$, while the concentration of oxygen vacancies and interstitials is negligible [6,42,43].

Thus, the composition of studied materials can be expressed as $(Fe_{2.6/3}Me_{0.2/3}Mg_{0.2/3})_{3-\gamma}O_4$, where γ is cation nonstoichiometry. In spinel-type phases γ can be varied up to a maximum of γ = 0.333 in magnetite based materials, where $Fe_{2.667}O_4$ corresponds to the maghemite structure.

The estimated change in cation nonstoichiometry Δγ due to oxidation of $Fe_{2.6}Mn_{0.2}Mg_{0.2}O_4$ in Ar, calculated from TG data (Fig. 3B), does not exceed ~ 0.07 even without accounting for the partial phase decomposition (Fig. 4). This value is fairly in the range of acceptable changes in cation nonstoichiometry within spinel phase stability domain, reported for $(Fe_{1-z}Mn_z)_{3-\gamma}O_4$ and $(Fe_{1-x-y}Co_xMn_y)_{3-\gamma}O_4$ systems [44,45]. Apparent discrepancy between oxygen uptake and phase composition upon heating in Ar, found for $Fe_{2.6}Mn_{0.2}Mg_{0.2}O_4$ and $Fe_{2.6}Ti_{0.2}Mg_{0.2}O_4$ may be, therefore, related to different stability of the spinel lattice regarding the Fe^{2+} :Fe^{3+} ratio. The same lattice stability issues might be responsible for the difference in oxygen uptake observed for $Fe_{2.6}Mn_{0.2}Mg_{0.2}O_4$, $Fe_{2.6}Cr_{0.2}Mg_{0.2}O_4$ and $Fe_{2.6}Al_{0.2}Mg_{0.2}O_4$ spinels upon heating in Ar, while in highly-oxidizing air atmosphere these materials show similar redox behaviour, interrelated with the oxidation state of substituting cation.

Table 2 – Properties of $Fe_{2.6}Me_{0.2}Mg_{0.2}O_4$ samples, sintered in Ar: lattice parameters, densities and activation energy for the high-temperature total conductivity.

Chemical composition	a_o nm	ρ_{exp}, g/cm^3	Relative density, %	Activation energy for the total conductivity ($p(O_2)=10^{-5}-10^{-4}$ atm)	
				T, K	E_a, kJ/mol
$Fe_{2.6}Ni_{0.2}Mg_{0.2}O_4$	0.83812(3)	4.47	88	1385–1774	18.0 ± 0.2
$Fe_{2.6}Mn_{0.2}Mg_{0.2}O_4$	0.84186(4)	4.50	90	1347–1773	19.9 ± 0.9
$Fe_{2.6}Al_{0.2}Mg_{0.2}O_4$	0.83684(3)	4.67	94	1197–1772	15.2 ± 0.7
$Fe_{2.6}Cr_{0.2}Mg_{0.2}O_4$	0.83849(3)	4.49	89	–	–
$Fe_{2.6}Ti_{0.2}Mg_{0.2}O_4$	0.84160(3)	4.46	90	1527–1771	18.7 ± 0.8

The results of static lattice simulation further confirm the above assumptions regarding stability of spinel lattice in the case of various substituting cations. The obtained data on energy of the structure formation (ΔE_{str}, Eq. 1) for $Fe_{2.6}Me_{0.2}Mg_{0.2}O_4$, presented in Fig. 5, predict highest stability, comparable with that for pure magnetite, for Ni-containing spinel, while less negative values for $Fe_{2.6}Ti_{0.2}Mg_{0.2}O_4$ suggest that its stability is lowest among the studied compositions.

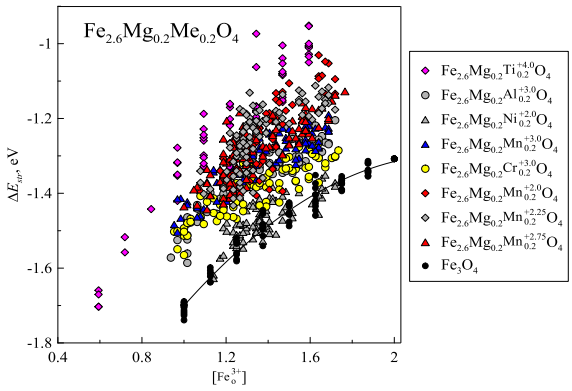

Figure 5 - Energy of the structure formation *vs.* concentration of Fe^{3+} in octahedral sites, calculated using static lattice simulation.

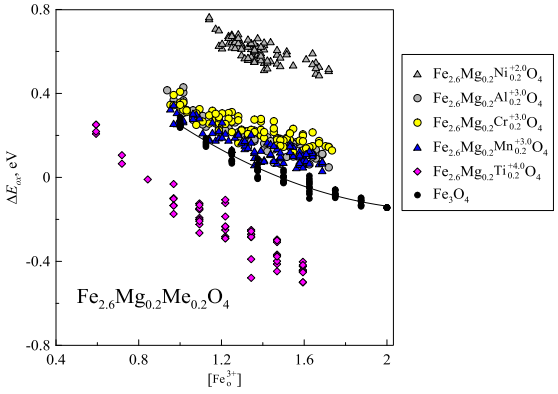

Figure 6 - Energy of the oxidative decomposition, calculated using static lattice simulation for the case of total Fe^{2+} to Fe^{3+} oxidation. (see text).

Furthermore, the latter is clearly emphasized by the obtained results on the energy of oxidative decomposition (ΔE_{ox}, Eq. 2), shown in Fig. 6. $Fe_{2.6}Ni_{0.2}Mg_{0.2}O_4$ and $Fe_{2.6}Ti_{0.2}Mg_{0.2}O_4$ spinels represent two extreme cases, while Mn-, Cr- and Al- containing spinels show comparable ΔE_{ox} values, in excellent agreement with the results of TG studies upon heating in air (Fig. 3B). Noteworthy, that the energies of the structure formation for $Fe_{2.6}Mn_{0.2}Mg_{0.2}O_4$, calculated assuming 2+, 3+ and mixed oxidation states for Mn, are close to each other. This suggests that, besides oxidations state, other factors may influence lattice stability of ferrospinels, even for quite similar substituting cations.

The redox behaviour of $Fe_{2.6}Me_{0.2}Mg_{0.2}O_4$ ceramics in various atmospheres may be even more complex, compared to the powder samples. Concerning conditions expected for pyroelectrolysis application, one may anticipate that spinel-based consumable anodes will be based on bulk ceramics, and oxidation presumably will take place mainly at the surface, with less pronounced effect on the bulk. However, if any, significant changes in redox state of iron cations and phase separation may cause excessive dimensional changes in spinel ceramics on heating, resulting in limited tolerance to thermal cycling.

The results of dilatometric studies in argon and air atmospheres, performed on $Fe_{2.6}Me_{0.2}Mg_{0.2}O_4$ ceramic samples, sintered in Ar, are presented in Fig. 7 (A and B). At relatively low temperatures (300 – 650 K) the studied materials show quite linear and similar expansion behaviour both in Ar and air, with thermal expansion coefficients in the range $(11.0 – 13.7)\times10^{-6}$ K (Table 3).

At temperatures above ~ 650 K in Ar the expansion curves show deviation from linearity, similar to that observed for Fe_3O_4 and $Fe_{3-x}Al_xO_4$ in the atmospheres with low oxygen content [6, 14, 46]. This may be attributed to changes in concentration of point defects, or their rearrangement in the tetrahedral and octahedral sublattices [46], possibly combined with onset of oxidative decomposition, as shown below.

Table 3 – Thermal expansion coefficients of $Fe_{2.6}Me_{0.2}Mg_{0.2}O_4$ spinels.

Composition	Average thermal expansion coefficients		
	p(O_2), atm	T, K	$(\bar{\alpha}\times10^6)\pm0.1, K^{-1}$
$Fe_{2.6}Ni_{0.2}Mg_{0.2}O_4$	10^{-5}	300–650	11.6
		800–1100	16.0
		1100–1369	21.5
	0.21	300–650	11.8
$Fe_{2.6}Mn_{0.2}Mg_{0.2}O_4$	10^{-5}	300–650	13.3
		800–1050	13.3
		1180–1369	13.2
	0.21	300–650	12.7
$Fe_{2.6}Al_{0.2}Mg_{0.2}O_4$	10^{-5}	300–650	11.4
		800–1370	13.1
	0.21	300–600	11.4
$Fe_{2.6}Cr_{0.2}Mg_{0.2}O_4$	10^{-5}	300–650	12.2
		800–1100	15.4
		1100–1369	17.9
	0.21	300–650	11.0
$Fe_{2.6}Ti_{0.2}Mg_{0.2}O_4$	10^{-5}	300–650	13.4
		800–1100	16.4
		1100–1369	21.6
	0.21	300–650	13.7

High temperature thermal expansion results in Ar atmosphere (≈ 10^{-5} atm) are highest for $Fe_{2.6}Ni_{0.2}Mg_{0.2}O_4$ and $Fe_{2.6}Ti_{0.2}Mg_{0.2}O_4$ (Table 3). These materials represent two extreme cases regarding oxidation energy, as predicted by static lattice simulation method (Fig. 6). Along with the highest stability, $Fe_{2.6}Ni_{0.2}Mg_{0.2}O_4$ is expected to have the lowest concentration of Fe^{2+} and, thus, smaller contraction due to oxidation of iron cations.

In opposite to other studied materials, the oxidative decomposition of $Fe_{2.6}Ti_{0.2}Mg_{0.2}O_4$ in Ar occurs via progressive separation of significant amount of the Fe_9TiO_{15} phase (Fig. 4), which may be responsible for the noticeable volume changes in ceramic samples. Thus, the reasons for variations in thermal expansion behaviour of $Fe_{2.6}Me_{0.2}Mg_{0.2}O_4$ at high temperatures may include distinct oxidation mechanisms.

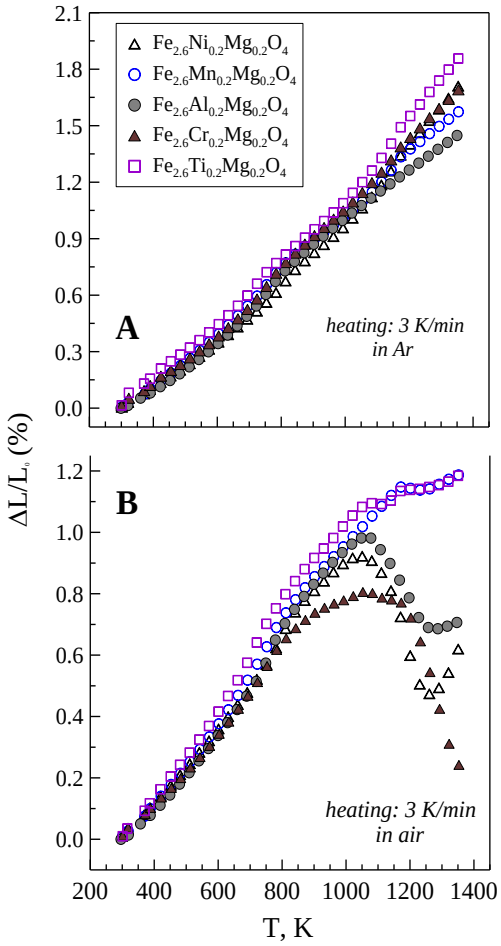

Figure 7 - Dilatometric curves for Ar-sintered $Fe_{2.6}Me_{0.2}Mg_{0.2}O_4$ materials in Ar (A) and air (B).

Whatever the microscopic mechanisms, the results demonstrate that some spinel materials may have relatively high thermochemical expansion, complicating their use in high-temperature electrochemical systems, except possibly for conditions when a suitable current collector is used to bridge the temperature gap from room temperature to very high temperatures, i.e., when the spinel anode is operating at very high temperatures, without significant temperature gradients.

On heating in air, massive transformation into hematite-type phases may result even in more severe volume changes, e.g., contraction due to oxidation of Fe^{2+} cation to smaller Fe^{3+} (Fig. 7B). This may cause large mechanical stresses and eventually provoke cracking of the ceramic anode. Again, for massive ceramics the oxidation is expected to affect mostly the surface, especially, under relatively fast heating/cooling rates during thermal cycling, thus preventing the problems with the whole electrode integrity. In particular, relatively fast heating/cooling may be essential in the intermediate temperature ranges, where contraction due to the partial oxidation occurs. Anyway, for ceramic anodes in pyroelectrolysis application, the tolerance against oxidative decomposition should be further improved by increasing Mg content, possibly combined with microstructural engineering to alter the interdiffusion paths of cations and, consequently, oxidation mechanisms in ferrospinel ceramics.

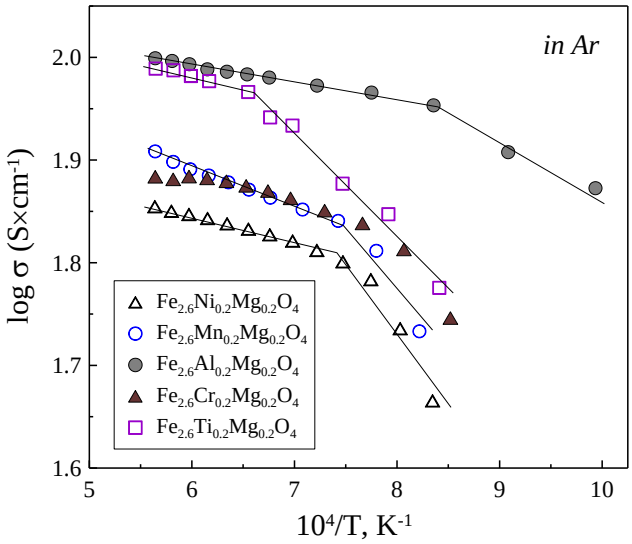

Figure 8 - Temperature dependence of the total conductivity of Ar-sintered samples in Ar.

The temperature dependence of the total conductivity of $Fe_{2.6}Me_{0.2}Mg_{0.2}O_4$ materials in Ar is shown in Fig. 8. The n-type electronic transport in magnetite-based materials occurs via small polaron mechanism, by hopping between Fe^{2+} and Fe^{3+} cations, and is restricted mainly to octahedral sites [4 – 8]. Substitution by the cations having stable oxidation states decreases the conductivity of magnetite; this can be ascribed to changes in concentrations of Fe^{2+} and Fe^{3+} cations. Note that the inverse spinel structure of magnetite corresponds to maximum $[Fe^{2+}][Fe^{3+}]$ concentration product in octahedral sublattice, yielding highest hopping probability.

For the modified compositions, one found highest total conductivity for $Fe_{2.6}Ti_{0.2}Mg_{0.2}O_4$ and $Fe_{2.6}Al_{0.2}Mg_{0.2}O_4$ spinel ceramics, while minimum corresponds to $Fe_{2.6}Ni_{0.2}Mg_{0.2}O_4$. The effects exerted by different additives are determined by the changes in fraction of Fe^{2+} cations, affecting the probability of hopping (i.e. the $[Fe^{2+}][Fe^{3+}]$ product in octahedral positions).

The mechanism considers the expected charge compensation in spinel lattice upon substitution. Charge compensation for co-additions of redox stable Ti^{4+} and Mg^{2+} cations should compensate each other, contributing to maintain the $[Fe^{2+}][Fe^{3+}]$ product close to its maximum. Thus, highest hopping probability is consistent with the highest conductivity observed for $Fe_{2.6}Ti_{0.2}Mg_{0.2}O_4$, among the studied materials, except $Fe_{2.6}Al_{0.2}Mg_{0.2}O_4$. Similarly to the redox behaviour in oxidizing atmosphere, the conductivity increases in the sequence $Ni^{2+} < Mn^{2+/3+} \approx Cr^{3+} < Ti^{4+}$, in line with the trend for oxidation state of transition metal cations.

For similar substitution level and same oxidation states, the preferred coordination of the substituting cations in spinel lattice may also have a noticeable impact on the conductivity. In present work, the affinity of those cations to reside in octahedral sublattice, where electronic charge transfer process takes place, was assessed by static lattice simulation; corresponding results on lattice energy fitting, based on Eqs. 3 and 4, are given in Tables 4 and 5. Additional terms in Eq. 4 compared to Eq. 3 account for $Mn^{2+} + Fe^{3+} \leftrightarrow Mn^{3+} + Fe^{3+}$ equilibrium, which may contribute by enhanced probability of hopping at high temperatures [47]. However, the quality of the model (Eq. 4) for $(Mg, Mn, Fe)_3O_4$ was still poorer, compared to other systems.

As an example, Fig. 9 shows the correlation between predicted response of the models Eqs. 3 and 4, (E_{cell}^{fit}) and lattice energy, calculated in GULP, for $(Mg, Mn, Fe)_3O_4$ and $(Mg,Ti,Fe)_3O_4$ solid solutions (E_{cell}). Although direct comparison between impacts of manganese (b_2 and b_3, Eq. 4) and Al^{3+}, Cr^{3+}, Ni^{2+} and Ti^{4+} cations (b_{Me}, Eq.3) on the lattice energy may not be correct in this case, the results still indicate that Mn^{3+} has a strong preference to reside in octahedral sites, while Mn^{2+} is prone to substitute iron mostly in tetrahedral sites. Al^{3+} shows lower affinity to octahedral sublattice than Cr^{3+} (Table 4) and, correspondingly, higher total conductivity.

Table 4 – Parameters of the regression models (Eq.3) (95% confidence).

Parameter	Value for $(Fe, Me, Mg)_3O_4$			
	Me=Al^{3+}	Me=Cr^{3+}	Me=Ni^{3+}	Me=Ti^{4+}
E_o	-190.96 ± 0.02	-190.99 ± 0.01	-190.98 ± 0.01	-190.97 ± 0.01
a_{Mg}	-0.98 ± 0.03	-0.66 ± 0.04	-0.63 ± 0.04	-0.66 ± 0.05
b_{Mg}	-1.06 ± 0.05	-0.78 ± 0.05	-0.82 ± 0.05	-0.81 ± 0.06
a_{Me}	3.40 ± 0.03	-1.82 ± 0.05	-0.81 ± 0.05	-11.8 ± 0.1
b_{Me}	-0.92 ± 0.05	-1.31 ± 0.07	-0.77 ± 0.07	-1.8 ± 0.1
b_{Fe}	-0.35 ± 0.03	-0.38 ± 0.01	-0.39 ± 0.01	-0.43 ± 0.02
R^2	0.996	0.995	0.99	0.9998
N_{points}	1084	396	460	380

Table 5 – Parameters of the regression models for $Fe_{2.6}Mg_{0.2}Mn_{0.2}O_4$ (Eq.4) (95% confidence).

Parameter	Value
E_o	-190.91 ± 0.03
a_{Mg}	-0.9 ± 0.1
b_{Mg}	-0.51 ± 0.2
a_2	1.4 ± 0.2
b_2	2.7 ± 0.3
a_3	2.8 ± 0.1
b_3	-3.6 ± 0.2
b_{Fe}	-0.56 ± 0.04
R^2	0.95
N_{points}	837

However, for $Fe_{2.6}Al_{0.2}Mg_{0.2}O_4$, smaller unit cell volume may also contribute, by promoting lower average Fe^{2+}–Fe^{3+} distance, thus facilitating electron hopping. Whatever the exact mechanism in this case, the results generally indicate, that the effect of substitution with transition metal cations on electrical conductivity of $(Fe, Mg)_3O_4$ is mostly determined by their oxidation states, rather than preferred coordination.

A quite good illustration of this fact is given by the observed difference in conductivity for $Fe_{2.6}Ti_{0.2}Mg_{0.2}O_4$ and $Fe_{2.6}Ni_{0.2}Mg_{0.2}O_4$ spinels (Fig. 8): although nickel is expected to have the lowest octahedral preference among the studied materials (Table 4), highest fraction of Fe^{2+} cations provides maximum conductivity for Ti-containing material.

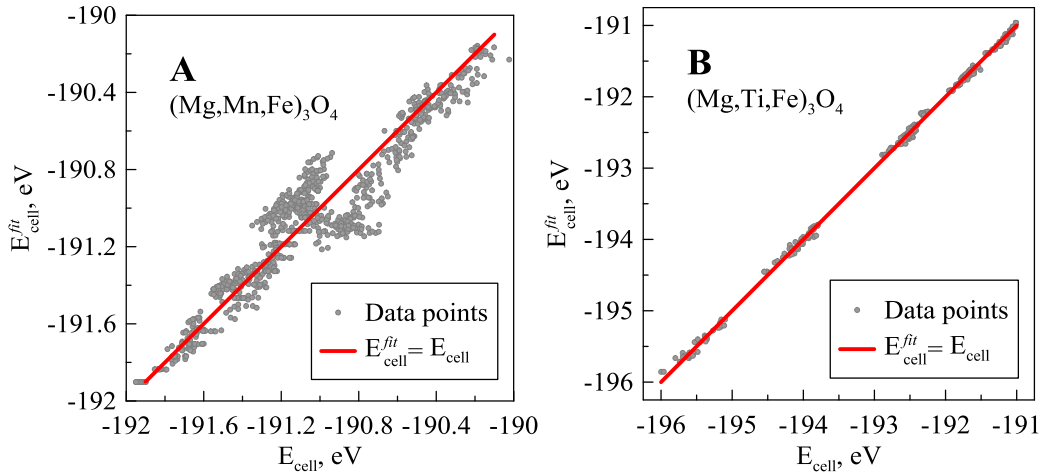

Figure 9 – Correlation of the predicted response of the models Eq.(3) and Eq.(4) and Ecell values, calculated in GULP, for (Mg,Mn,Fe)3O4 and (Mg,Ti,Fe)3O4 solid solutions.

Similar to that observed for $(Fe, Mg, Al)_3O_4$ spinels [6, 11, 14], the variations of the total conductivity of $Fe_{2.6}Me_{0.2}Mg_{0.2}O_4$ spinels with temperature exhibit a complex behaviour, determined by changes in defect-chemistry from interstitial cation formation to generation of cation vacancies at lower temperatures and partial decomposition of the spinel phase. The latter, in particular, is responsible for the conductivity drop observed for $Fe_{2.6}Ti_{0.2}Mg_{0.2}O_4$, which corresponds to higher temperatures compared to other materials.

The onset of this decomposition is in a good agreement with the above conclusions on the relative redox stability of $Fe_{2.6}Me_{0.2}Mg_{0.2}O_4$ spinel materials, drawn from the results of thermogravimetry, XRD and static lattice simulation studies. Below 1200 K all samples demonstrated slow equilibration kinetics on cooling and, correspondingly, a gradual conductivity drift with time.

The values of activation energies (E_a) (Table 2) were, therefore, calculated only for high temperature range, using the case of adiabatic hopping for small-polaron conductivity mechanism [5]:

$$\sigma = \frac{A}{T}\exp(-E_a / RT) \qquad (5)$$

The activation energies of $Fe_{2.6}Me_{0.2}Mg_{0.2}O_4$ (Me = Ni, Mn, Ti) spinels are quite similar and vary in the range 18.0 – 19.9 kJ/mol at 1347 – 1774 K. Previously observed E_a value for the total conductivity of $Fe_{2.6}Al_{0.2}Mg_{0.2}O_4$ in Ar at 1197 – 1772 K was noticeably lower, again suggesting more favourable conditions for electron hopping due to smaller unit cell volume and relatively low affinity of Al^{3+} to reside in octahedral sites. Noteworthy, that, among Ni-, Mn- and Ti- containing spinels, $Fe_{2.6}Ni_{0.2}Mg_{0.2}O_4$ also shows lowest E_a along with the lowest preference for six-fold coordination. High temperature variations of the total conductivity of $Fe_{2.6}Cr_{0.2}Mg_{0.2}O_4$ represent a specific case of charge transfer mechanism in ferrospinels. Similar behaviour was also observed for heavily-substituted $Fe_{1.55}Al_{0.95}Mg_{0.5}O_4$ spinel [11], and attributed to the condition, when no additional charge carriers are generated upon heating, while the probability of hopping $[Fe^{2+}]^{oct}[Fe^{3+}]^{oct}$ may even decrease.

Within the phase stability domain all studied materials demonstrate a minor increase in total conductivity with reducing oxygen partial pressure, possibly due to increasing concentration of n-type charge carriers (Fig. 10). The changes are more pronounced for $Fe_{2.6}Ti_{0.2}Mg_{0.2}O_4$ spinel, which should attain the highest concentration of Fe^{2+}. The conductivity drop on increasing oxygen partial pressure above certain value, marked by dashed line, is ascribed to phase decomposition, induced by oxidation. One should notice that the values of conductivity after onset of decomposition may deviate significantly from equilibrium conditions, since redox induced decomposition is slow in spinel ceramics (e.g., [14]).

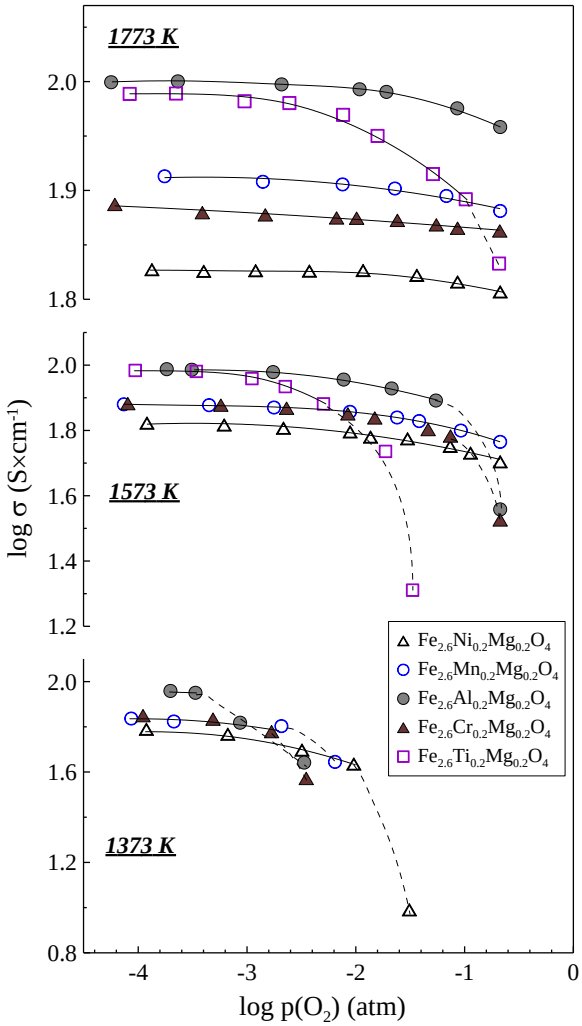

Figure 10 - Oxygen partial pressure dependencies of the total conductivity of $Fe_{2.6}Me_{0.2}Mg_{0.2}O_4$ ceramic samples. Dashed lines correspond to the $p(O_2)$ range with onset of oxidative decomposition.

Thus, precise determination of the $p(O_2)$-stability limits for the studied materials was not performed in present work, as it requires long-time equilibration. However, the obtained data on conductivity vs $p(O_2)$ dependence are in good agreement with experimental results obtained by TG/XRD (Figs. 3 and 4) and theoretical predictions (Fig. 6). The onset of oxidative decomposition for $Fe_{2.6}Ti_{0.2}Mg_{0.2}O_4$ corresponds to $p(O_2) \sim 0.10$ atm at 1773 K and ~ 0.03 atm at 1573 K, while $Fe_{2.6}Ni_{0.2}Mg_{0.2}O_4$ at these temperatures is stable within the whole measured $p(O_2)$ range. Al-, Mn- and Cr- containing spinels, in turn, demonstrate comparable redox stability at 1373 – 1773 K. Thus, trade-off relation between electrical conductivity and stability is the case for the studied materials. Regarding high-temperature electrochemical applications, $Fe_{2.6}Al_{0.2}Mg_{0.2}O_4$ represents a reasonable compromise between those two important properties.

Nevertheless, $Fe_{2.6}Ti_{0.2}Mg_{0.2}O_4$ ceramics do not collapse upon heating in air (Fig. 7B), at the same time possessing high level of electrical conductivity (Figs. 9 and 10). The latter also suggests this material as a possible candidate for consumable anodes in pyroelectrolysis, despite its lower redox stability and higher thermal expansion coefficient.

Considering the obtained trends for changing redox stability of $Fe_{2.6}Me_{0.2}Mg_{0.2}O_4$ with the oxidation state of transitional metal, one may anticipate the necessity for further adjusting the ratio between higher- and lower-valence substituting cations, as an important guideline for developing stable magnetite-based consumable anodes. In general, the obtained results showed that simultaneous substitution of iron with 2+ and 3+/4+ cations allows achieving high conductivity level with still acceptable redox stability, since the oxidation will proceed mostly at the surface of anode ceramics. From this perspective one promising approach may include substitution with silicon and zirconium in $(Fe, Mg)_3O_4$ spinel materials. Noteworthy that under the conditions of pyroelectrolysis process one should already expect the formation of Si-containing spinels at the anode surface, immersed into molten silicate electrolyte. The latter, along with the anticipated conductivity increase, may result in gradual deterioration of the redox stability, requiring certain optimization of the anode configuration (e.g., creating transversal gradient of magnesium concentration from the bulk to anode surface, etc.).

4.3.5 Conclusions

Single-phase spinel-type ceramic samples of $Fe_{2.6}Me_{0.2}Mg_{0.2}O_4$ (Me = Ni, Mn, Al, Cr, Ti) were prepared by conventional solid state route, followed by sintering at 1773 K for 10 h in Ar or air atmosphere. Combined TG/XRD studies showed metastable phase composition of Ar-prepared ceramic samples at low temperatures. Comparative analysis of the oxygen uptake in air and Ar ($p(O_2) \sim 10^{-4} – 10^{-5}$ atm) demonstrated that the extent of oxidative decomposition is determined by Fe^{2+} content in spinel, and the oxidation mechanism depends on the oxygen partial pressure. Static lattice simulation predicted highest tolerance against oxidative decomposition for $Fe_{2.6}Ni_{0.2}Mg_{0.2}O_4$ spinel, whilst the lowest stability was foreseen for $Fe_{2.6}Ti_{0.2}Mg_{0.2}O_4$, in agreement with TG/XRD results.

The high-temperature electrical conductivity was found to increase in the sequence $Ni^{2+} < Mn^{2+/3+} \approx Cr^{3+} < Ti^{4+}$, following the trend for oxidation state of transition metal cations and corresponding changes in Fe^{2+} : Fe^{3+} ratio, whereas additional contribution can be also expected from preferred coordination of transition metals cations, in accordance with the predictions from static lattice simulation. Although studied materials demonstrate a trade-off relation between electronic transport and redox stability, the results on thermal expansion and electrical conductivity still suggest good prospects for the application of $Fe_{2.6}Al_{0.2}Mg_{0.2}O_4$ and $Fe_{2.6}Ti_{0.2}Mg_{0.2}O_4$ spinels as potential materials for consumable ceramic anodes in high-temperature pyroelectrolysis.

4.3.6 References

[1] – Sadoway DR. New opportunities for metal extraction and waste treatment by electrochemical processing in molten salts. J Mater Res 1995; 10:487-92.

[2] – Kim H, Paramore J, Allanore A, Sadoway DR. The influence of electrolyte basicity on the performance of an iridium anode for the electrolysis of molten iron oxide. J Electrochem Soc 2011; 158:E101-5.

[3] – Kofstad P. Nonstoichiometry, Diffusion and electrical conductivity in binary metal oxides. New York: Wiley-Interscience; 1972.

[4] – Maris G., Shklyarevskii O, Jdira L, Hermsen JGH. Speller S. One-dimensional structural and electronic properties of magnetite Fe_3O_4 (110). Surface Sci 2006; 600:5084-91.

[5] – Mason TO, Bowen HK. Electronic conduction and thermopower of magnetite and iron-aluminate spinels. J Amer Ceram Soc 1981; 64:237-42.

[6] – Yaremchenko AA, Kovalevsky AV, Naumovich EN, Kharton VV, Frade J.R. High-temperature electrical properties of magnesiowustite $Mg_{1-x}Fe_xO$ and spinel $Fe_{3-x-y}Mg_xCr_yO_4$ ceramics. Solid State Ionics 2011; 192:252-8.

[7] – Nell J, Wood BJ. High-temperature electrical measurements and thermodynamic properties of Fe_3O_4-$FeCr_2O_4$-$MgCr_2O_4$-$FeAl_2O_4$ spinels, Amer Miner 1991; 76: 405-426.

[8] – Nell J, Wood BJ, Mason, TO. High-temperature cation distributions in Fe_3O_4-$MgAl_2O_4$-$MgFe_2O_4$-$FeAl_2O_4$ spinels from thermopower and conductivity measurements. Amer Miner 1989; 74:339-51.

[9] – Charette GG, Flengas SN. Thermodynamic properties of the oxides of Fe, Ni, Pb, Cu, and Mn, by EMF measurements, J Electrochem Soc 1968; 115:796-804.

[10] – Domingues EM, Tsipis EV, Yaremchenko AA, Figueiredo FM, Waerenborgh JC, Kovalevsky AV, Frade JR. Redox stability and electrical conductivity of $Fe_{2.3}Mg_{0.7}O_{4\pm\delta}$ spinel prepared by mechanochemical activation. J Eur Ceram Soc 2013; 33: 1307-1315.

[11] – Kovalevsky AV, Yaremchenko AA, Naumovich EN, Ferreira NM, Mikhalev SM, Costa FM, Frade JR. Redox stability and high-temperature electrical conductivity of magnesium- and aluminium- substituted magnetite. J Eur Ceram Soc, accepted for publication, 2013, doi: 10.1016/j.jeurceramsoc.2013.04.008.

[12] – Tretyakov YD. Thermodynamics of Ferrites, Leningrad: Khimiya, 1967.

[13] – Jung IH, Decterov SA, Pelton AD. Critical thermodynamic evaluation and optimization of the Fe-Mg-O system. J Phys Chem Solids 2004; 65:1683-95.

[14] – Kovalevsky AV, Naumovich EN, Yaremchenko AA, Frade JR. High-temperature conductivity, stability and redox properties of $Fe_{3-x}Al_xO_4$ spinel-type materials. J Eur Ceram Soc 2012; 32:3255-63.

[15] – Rodríguez-Carvajal J. Recent advances in magnetic structure determination by neutron powder diffraction. Physica B 1993; 192: 55–69.

[16] – Gale JD. GULP - a computer program for the symmetry adapted simulation of solids. JCS Faraday Trans 1997; 93:629-37.

[17] – Gale JD, Rohl AL. The General Utility Lattice Program. Mol Simul 2003; 29:291-341.

[18] – http://www.ucl.ac.uk/klmc/Potentials/ , 2012.

[19] – Woodley SM, Catlow CRA, Piszora P, Stempin K, Wolska E. Computer modeling study of the lithium ion distribution in quaternary Li–Mn–Fe–O spinels. J Sol State Chem 2000; 153:310-6.

[20] – Woodley SM, Battle PD, Gale JD, Catlow CRA. The prediction of inorganic crystal structures using a genetic algorithm and energy minimization. Phys Chem Chem Phys 1999; 1:2535-42.

[21] – Bush TS, Gale JD, Catlow CRA, Battle PD. Self-consistent interatomic potentials for the simulation of binary and ternary oxides. J Mater Chem 1994; 4:831-7.

[22] – Battle PD, Bush TS, Catlow CRA. Structures of quaternary Ru and Sb oxides by computer simulation. J Amer Chem Soc 1995; 117: 6292-96.

[23] – Zhang J. Room temperature compressibilities of MnO and CdO: further examination of the role of cation type in bulk modulus systematics. Phys Chem Miner 1999; 26: 644-8

[24] – http://www.crystallography.net Crystallography Open Database , 2012

[25] – Kantor A, Kantor I, Merlini M, Glazyrin K, Prescher C, Hanfland M, Dubrovinsky L. High-pressure structural studies of eskolaite by means of single-crystal X-ray diffraction. Amer Miner 2012; 97: 1764-70.

[26] – Downs RT, Hall-WallaceM. The American Mineralogist Crystal Structure Database. Amer Miner 2003; 88: 247-50.

[27] – O'Neill HSC; Dollase WA. Crystal structures and cation distributions in simple spinels from powder XRD structural refinements: $MgCr_2O_4$, $ZnCr_2O_4$, Fe_3O_4 and the temperature dependence of the cation distribution in $ZnAl_2O_4$ Phys Chem Miner 1994; 20: 541-55.

[28] – Gonze X, Amadon B, Anglade PM, Beuken JM, Bottin F, Boulanger P, Bruneval F, Caliste D, Caracas R, Cote M, Deutsch T, Genovese L, Ghosez P, Giantomassi M, Goedecker S, Hamann DR, Hermet P, Jollet F, Jomard G, Leroux S, Mancini M, Mazevet S, Oliveira MJT, Onida G, Pouillon Y, Rangel T, Rignanese GM, Sangalli D, Shaltaf R, Torrent M, Verstraete MJ, Zerah G, Zwanziger JW. ABINIT: First-principles approach to material and nanosystem properties. Computer Phys Comm 2009; 180: 2582-2615.

[29] – Gonze X, Rignanese GM, Verstraete M, Beuken JM, Pouillon Y, Caracas R, Jollet F, Torrent M, Zerah G, Mikami M, Ghosez P, Veithen M, Raty JY, Olevano V, Bruneval F, Reining L, Godby R, Onida G, Hamann DR, Allan DC. A brief introduction to the ABINIT software package. Zeit Kristallogr 2005; 220: 558-562.

[30] – The ABINIT code, a common project of the Université Catholique de Louvain, Corning Incorporated, and other contributors http://www.abinit.org 2012.

[31] – Goedecker S. Fast Radix 2, 3, 4, and 5 kernels for fast fourier transformations on computers with overlapping multiply --Add Instructions. SIAM J Sci Comput 1997; 18: 1605-11.

[32] – Bottin F, Leroux S, Knyazev A, Zerah G. Large-scale ab initio calculations based on three levels of parallelization. Comput. Mat. Science 2008; 42: 329-36.

[33] – Krack M. Pseudopotentials for H to Kr optimized for gradient-corrected exchange-correlation functionals. Theor Chem Acc 2005; 114: 145–152.

[34] – http://people.web.psi.ch/krack/potentials.html Personal Homepage of Matthias Krack 2012

[35] – Lide DR. CRC Handbook of Chemistry and Physics. 89th Edition (Internet Version 2009). Boca Raton: CRC Press/Taylor and Francis, 2009.

[36] – http://www.wolfram.com/mathematica/ , 2013.

[37] – Hill RJ, Craig JR, Gibbs GV. Systematics of the spinel structure type. Phys Chem Minerals 1979; 4:317-339.

[38] – Shannon RD. Revised effective ionic radii and systematic studies of interatomic distances in halides and chalcogenides. Acta Cryst 1976; A32:751-67.

[39] – Powder Diffraction File, PDF#00-054-1267.

[40] – Gillot B, Jemmali F, Chassagneux F, Salvaing C, Rousset A. Availability of Fe^{2+} ions in Cr- or Al- substituted magnetites with relevance to the process of oxidation in defect phase γ. J Solid State Chem 1982; 45:317-23.

[41] – Freer R, O´Reilly W. The diffusion of Fe2+ ions in spinels with relevance to the process of maghemitization. Miner. Magaz. 1980; 43:889-899.

[42] – Aggarwal S, Töpfer J, Tsai TL, Dieckmann R. Point defects and transport in binary and ternary, non-stoichiometric oxides. Solid State Ionics 1997; 101-103: 321-331.

[43] – Kang SH, Yoo HI. Nonstoichiometry (δ) of $(Mg_xFe_{1-x})_{3-\delta}O_4$ ferrite spinel. Solid State Ionics 1996; 86-88: 751-5.

[44] – Guillemet-Fritsch S, Viguié S, Rousset A. Structure of highly divided nonstoichiometric iron manganese oxide powders $Fe_{3-x}Mn_x\square_{3\delta/4}O_{4+\delta}$. J Solid State Chem 1999; 146: 245-252.

[45] – Lu FH, Dieckmann R. Point defects in oxide spinel solid solutions of the type $(Co,Fe,Mn)_{3-\delta}O_4$ at 1200ºC. J Phys Chem Solids 1995; 56: 725-733.

[46] – Levy D, Artioli G, Dapiaggi M. The effect of oxidation and reduction on thermal expansion of magnetite from 298 to 1173 K at different vacuum conditions. J Solid State Chem 2004; 177:1713-6.

[47] – Lotgering FK, Semiconduction and cation valencies in manganese ferrites. J Phys Chem Solids 1964; 95-103.

5 Spinel-based anode materials prepared by LFZ method

5.1 Introductory notes

Chapter 5 focuses on assessment of the relevant physical and redox properties of model magnetite-based samples, prepared by LFZ processing. The preparation route simulates the conditions, which would be present during pyroelectrolysis process, both in terms of extremely high temperatures and steep temperature gradients. The results are described in one published paper: 5.2 – Magnetite/Hematite core/shell fibres grown by laser floating zone method. This study establishes a link between the results on redox stability of spinel-type materials, obtained by conventional techniques, and related properties of the LFZ-processed samples, grown at various pulling rates to reproduce highly-non equilibrium conditions imposed by MOE.

5.2 Magnetite/Hematite core/shell fibres grown by laser floating zone method

N.M. Ferreira, A. Kovalevsky, M.A. Valente, F.M. Costa, J. Frade

(Applied Surface Science 278 (2013) 203–206
http://dx.doi.org/10.1016/j.apsusc.2013.01.108)

5.2.1 Abstract

Magnetite (Fe_3O_4) is a very important material due to its unique physical and chemical properties. However, the low redox stability and tendency towards oxidation impose certain limitations on the conditions, where Fe_3O_4 can be successfully used. A possibility to control and prevent oxidation of Fe_3O_4 thus represents an important challenge for materials engineering. In the present work, the laser floating zone (LFZ) method was employed to produce Fe_3O_4 fibres using hematite (Fe_2O_3) as a precursor material. Different growth conditions, namely pulling rate in the range 10 to 400 mm/h, were studied. The prepared fibres showed a core/shell structure, where the core is isolated by a shell of Fe_2O_3. The pulling rate was found to be a crucial growth parameter to control the crystalline nature of the fibres, particularly, the thickness of the shell. Increasing the pulling rate favours the formation Fe_2O_3 phase and, thus, decreases the width of shell isolating phase. X-ray diffraction (XRD) analysis was performed to identify the presence of Fe_3O_4 and Fe_2O_3 phases. The morphology and phase distribution of the grown fibres was analysed by optical microscopy. Electrical properties of the fibres were measured at various temperatures, to understand the influence of pulling rate on the fibres shell. Vibrating Sample Magnetometer (VSM) measurements were used to study the dc magnetic susceptibility and hysteresis curves behaviour of Fe_3O_4 phase in the temperature range 5 K – 300 K.

5.2.2 Introduction

Iron oxides are important in many industrial applications, including pigments, magnetic materials, electrical materials, catalysts and sensors [1-3]. Potential applications of the most stable phase in air (Fe_2O_3) are mainly related to its semiconducting behaviour and/or its band gap in the visible range (e.g. [4]), and differ markedly from those of magnetite (Fe_3O_4), with superior magnetic properties and significant electronic conductivity.

However, magnetite/hematite composites might also raise opportunities to seek novel applications or different combinations of relevant properties (e.g. [5]). The phase transformation from hematite (Fe_2O_3) to magnetite (Fe_3O_4) and oxidation states of iron was, thus, widely studied by different methods and techniques [1 – 3, 6, 7].

The present work relies on the laser floating zone (LFZ) method to obtain core-shell magnetite-hematite fibres, and to adjust their characteristics and properties, based on the flexibility of the method to obtain materials with unique features such as high quality single crystals of a variety of oxides [8 – 9], eutectic structures [10], highly oriented polycrystalline materials [11], etc. Different approaches for the floating zone technique have been used to grow crystals of intermetallic systems, where heating and melting are achieved using conducting properties of the metal, e.g., an induction furnace or an electron-beam system [8, 12, 13]. Following the series of discoveries of interesting correlated electron phenomena in complex ceramic oxides such as cuprates, manganites, ruthenates, titanates and ferrites, there has been an increased interest among materials scientists within the condensed matter community in studying single crystals of these systems [8].

In this paper, we report the successful growth of magnetite/hematite - core/shell by the floating zone method, using Fe_2O_3 as a precursor. Fibres were grown using different pulling rates, examined by X-ray diffraction, optical microscopy, VSM and electrical measurements, to observe the effect of growth conditions on physical properties.

5.2.3 Experimental procedure

Fe_2O_3 powder (Aldrich +99%) with addition of a binder (PVA - Polyvinyl alcohol) was extruded as precursor rods [8], which were used as feed in the LFZ method, equipped with a continuous CO_2 Spectron SLC laser (λ = 10.6 μm; 200 W) to grow dense fibres. The growth rate was varied between 10 and 400 mm/h, and the seed and feed rod precursors rotated in opposite directions to provide better homogeneity of the target fibres.

The phase composition and crystalline structure were investigated at room temperature by X-ray diffraction (XRD) analysis, using a PANalytical X'Pert PRO system; the obtained spectra were analysed using the JCPDS database. Phase distribution in the samples was examined by Raman spectra (SPEX, Jobin Yvon T64000) at room temperature in backscattering configuration, using the 532 nm exciting line, from 100 to 2100 cm^{-1}.

The samples morphology at polished cross-section and transversal regions was characterized by optical microscopy (Olympus BH-2). The results were used for the determination of Fe_2O_3 shell thickness. Scanning electron microscopy (Hitachi SU 70) was unable to reveal relevant microstructural features of the magnetite-based core or its orientation.

The electrical response of core-shell fibres was monitored by dc and ac measurements in a suitable home-made cryogenic system, comprising a Keithley 617 Programmable Electrometer for dc measurements, an Agilent 4292A Precision Impedance Analyser (40 Hz - 2 MHz) for ac resistivity and capacity studies, and an Oxford ITC4-Inteligent Temperature Controller for variation of temperature from 80 to 360 K.

One of the electrodes was applied with Ag paste onto one top of the fibre, to provide electrical contact to the magnetite-based core, and the second electrode was applied to the external cylindrical surface of the hematite shell. One attempted to confirm the core-shell microstructure by the prevailing effect of the conductivity hematite shell; this should be accounted by $X/(R\pi DL)$, where the geometric factor thickness/area ratio was based on the diameter of the fibre (D), the length of the external electrode (L), and thickness of the hematite shell (X).

The dc magnetic measurements were performed on fibre samples (50 – 100 mg) using a vibrating sample magnetometer-VSM, (Cryogenic – Cryofree). The dc magnetization was recorded on field-cooled (FC) under 0.1 T, between 5 and 300 K. Typical hysteresis curves were obtained at several temperatures (5 – 300 K), for all samples in magnetic field up to 10 T. The magnetic parameters such as saturation magnetization (Ms), coercivity (Hc) and magnetic moment are obtained from the VSM results.

5.2.4 Results and discussion

XRD patterns of crushed fibres showed the presence of magnetite (Fe_3O_4) and hematite (Fe_2O_3) phases for all powder samples (Fig. 1). However, the intensity of hematite peaks is rather residual for fibres grown at the highest pulling rates, and are most obvious for <100 mm/h.

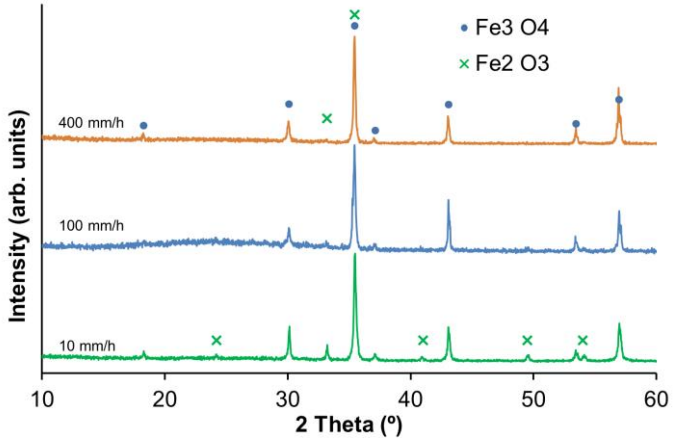

Figure 1 – XRD pattern of powdered samples for different pulling rate.

Optical observations (Fig. 2a) revealed the presence of two different contrast regions in samples, and Raman spectra confirm the presence of two distinct phases, as indicated by the shell signed to Fe_2O_3 phase (612 cm^{-1}), whilst the middle/bulk component can be signed to Fe_3O_4 phase (668cm^{-1}), in accordance with literature data [14, 15].

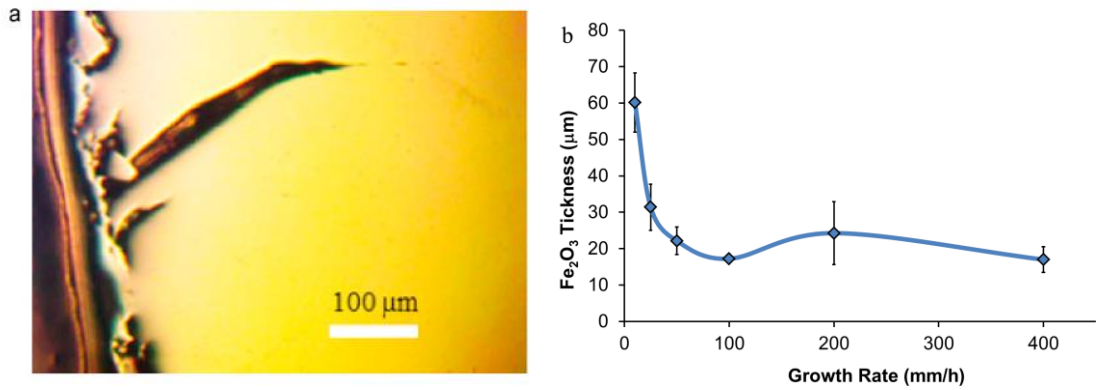

Figure 2 – a) Optical microscopy of longitudinal section for sample grown at 50 mm/h, b) evolution of Fe2O3 thickness layer with pulling rate.

The presence of a core/shell structure can be due to thermal gradients in the radial and longitudinal directions, and possibly also by transient redox changes [9]. Note that hematite may be transformed into magnetite: 3 $Fe_2O_3 \rightarrow 2Fe_3O_4 + ½ O_2$ at sufficiently high temperatures, probably before melting. Thus, one expects transformation to magnetite before melting, at the front of the hot zone, and magnetite should also be the primary solidified phase at the rear of the molten zone.

Onset of the outer hematite shell may, thus, be due to reoxidation of previously solidified magnetite, or delayed solidification occurring under significant undercooling. The melting temperatures of magnetite (≈ 1597 ºC) and hematite (≈ 1565 ºC) are similar. Note also that microcracks were observed for the lowest pulling rates (< 100 mm/h), possibly due to thermal stresses and slightly expansive transformation of magnetite to hematite.

The thickness of shell layer (Fig. 2b) shows a decrease with an increase in growth rate up to ~ 100 mm/h. High pulling rates (> 100 mm/h) may yield porosity instead, possibly because heat transfer limitations in the radial direction may delay solidification of the inner core at the rear of the molten zone. The impervious outer shell may still hinder oxidation of the inner magnetite-based core.

The high conductivity of the magnetite-based core should imply a prevailing effect of the hematite shell on resistance; this is confirmed by the order of magnitude of results in Fig. 3, which is much lower than expected for magnetite (≈ $2x10^4$ S/m at room temperature [2, 16]. Still, the results at 100 K may include a contribution of the magnetite core due to the Verwey transition, implying decrease in conductivity by about 2 orders of magnitude [16]. The order of magnitude of capacitance values is also within the expected range for the hematite shell [17].

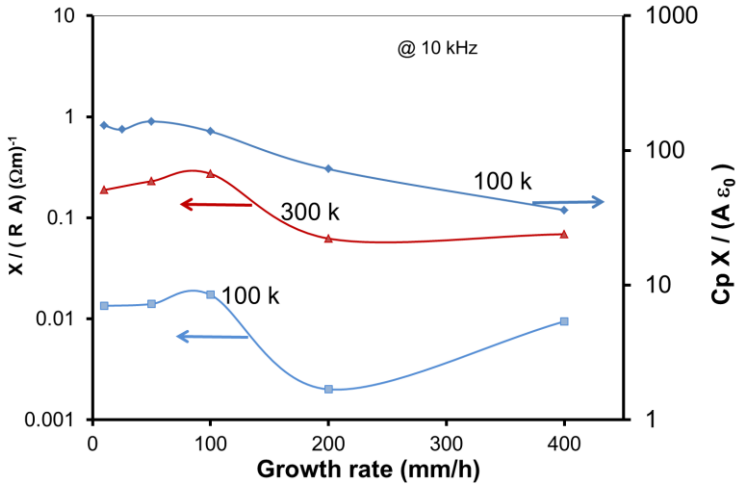

Figure 3 – Electrical characterization (X/RA and CX/Aε$_0$) as a function of pulling rate where R is the measured resistance, C the capacity measured, X is thickness of the hematite shell and A is the area of the external electrode, and ε$_0$ is the permittivity of vacuum.

From the field cooled (FC) measurements for B = 0.1 T (Fig. 4a) a transition behaviour on values of magnetic moment was observed near 90 K for all samples, in accordance with the results for system with similar composition [2]. The behaviour of samples in FC condition is in agreement with that observed previously [18]. The effect of Fe_3O_4 phase amount on the magnetic moment and transition temperature follows the same trend as it was found for structural and electrical properties, with highest value of magnetic moment observed for the growth rate of 100 mm/h (Fig. 4b).

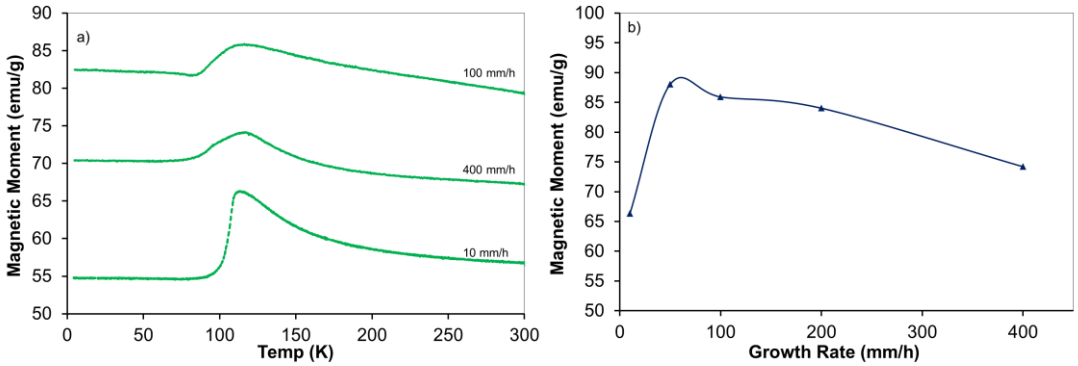

Figure 4 – a) Magnetic moment as function of temperature (5 to 300 K) of FC measurement for B = 0.1 Tesla, b) magnetic moment at the transition temperature as a function of pulling rate.

Figure 5a) shows the isothermal magnetic moment vs. applied field and Fig. 5b the maximum magnetization, measured at 300 K for the samples grown with different pulling rate. The values obtained in hysteresis cycle (Fig. 5a) are in agreement with those measured for Fe_3O_4 bulk material ~ 88,65 emu/g at 300 K, and 98.18 emu/g at 5 K [19].

The fibres exhibit higher magnetic moment than that for magnetite and hematite precursor's powders. This may be a result of densification of the fibres, if compared with the precursors, and the effect of boundaries, as reported when comparing films and single crystal values [14].

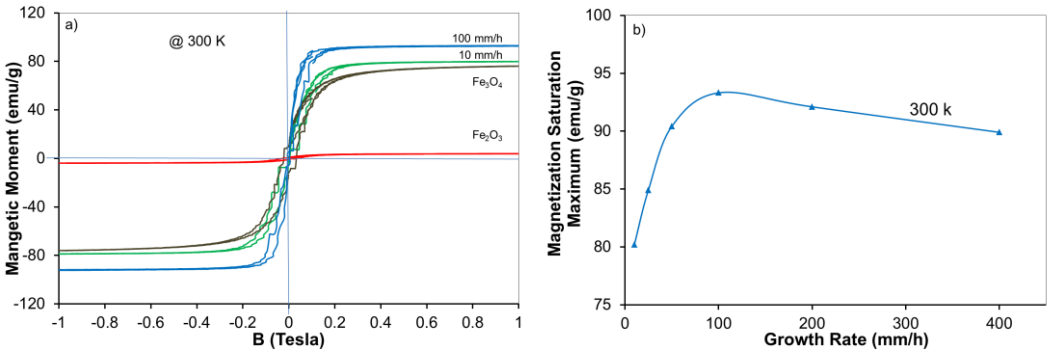

Figure 5 – a) Hysteresis loop vs. B at 300K and b) Magnetization saturation maximum for T = 300K as a function of pulling rate.

An increase of maximum magnetization saturation at room temperature was observed with growth rate, which reaches the maximum for a growth rate of 100 mm/h (Fig. 5b). For the sample grown at 10 mm/h we obtain the minimum value of the magnetization at 300K for the studied samples. This behaviour correlates the amount of magnetite phase, detected by XRD analysis.

From the results it was observed that the coercive magnetic field was near 0 Tesla for all measured samples. From the results is possible to observe that the moment magnetic increase with the growth rate until 100 mm/h, suggesting that the Fe_3O_4 phase increase.

5.2.5 Conclusions

LFZ was found a suitable method to obtain Fe_3O_4/Fe_2O_3 core/shell fibres with an isolating shell, from hematite precursor. The growth rate was found to be a crucial parameter for adjusting the phase proportions in fibres and shell thickness. Increasing pulling rate favours retention of high contents of Fe_3O_4. The thickness of Fe_2O_3 shell decreases with the growth rate. For high pulling rates one observed appearance of porosity in the magnetite-based core. The electrical measurements revealed the influence of pulling rate on the fibres shell (Fe_2O_3 layer). Magnetic measurements show the influence of the pulling rate on the magnetic moment, with impact on the values of maximum magnetization saturation, magnetic moment and transition temperature of samples.

5.2.6 References

[1] – V. A. Hiremath, A. Venkataraman; Dielectric, electrical and infrared studies of g-Fe2O3 prepared by, combustion method; Bull. Mater. Sci., 26 (2003), 391–396.

[2] – P. Brahma, S. Dutta, D. Dutta, Sourish Banerjee, A. Ghosh, D. Chakravorty, Electrical properties of nanocrystalline magnetite with large non-stoichiometry, near Verwey transition, Journal of Magnetism and Magnetic Materials 321 (2009) 1045–1051.

[3] – M. Ziese, P. D. Esquinazi, D. Pantel, M. Alexe, N. M. Nemes and M. Garcia-Hernandez, Magnetite (Fe3O4): a new variant of relaxor multiferroic, J. Phys.: Condens. Matter 24 (2012) 086007 (8pp) doi:10.1088/0953-8984/24/8/086007

[4] – A. Mao, N.G. Park, G.Y Han, J.H. Park, Controlled growth of vertically oriented hematite/Pt composite nanorod arrays: use for photoelectrochemical water splitting, Nanotechnology 22 (2011) 175703.

[5] – S. Dutta, S.K. Manik, M. Pal, S.K. Pradhan, P. Brahma, D. Chakravorty, Electrical conductivity in nanostructured magnetite-hematite composites produced by mechanical milling, J. Mag. Mag. Mat., 288 (2005) 301-306

[6] – T. Otake, D.J. Wesolowski, M.Lawrence, Experimental evidence for non-redox transformations between magnetite and hematite under H2-rich hydrothermal conditions, Earth and Planetary Science Letters 257 (2007) 60–70.

[7] – C. Pérez León, L. Kador, M. Zhang, A.H.E. Muller; In situ laser-induced formation of α-Fe2O3 from Fe^{3+} ions in a cylindrical core-shell polymer brush; Journal of Raman Spectroscopy 35 (2004) 165-169, doi: 10.1002/jrs.1125

[8] – F. Ritzert and L. Westfall, Laser-Heated Floating Zone Production of Single-Crystal Fibers, NASA Technical Memorandum 4732, National Aeronautics and Space Administration, Office of Management, Scientific and Technical Information Program, 1996.

[9] – P. Guptasarma, M. S. Williamsen and S. K. Ray, Floating Zone Growth of Bulk Single Crystals of Complex Oxides, Mater. Res. Soc. Symp. Proc. Vol. 848 (2005) Materials Research Society.

[10] – J.r LLorca, V. M. Orera, Directionally solidified eutectic ceramic oxides, Progress in Materials Science 51 (2006) 711–809.

[11] – M. F. Carrasco, R. F. Silva, J. M. Vieira, F. M. Costa, Electrical field freezing effect on laser floating zone (LFZ)-grown Bi2Sr2Ca2Cu4O11 superconducting fibres, Supercond. Sci. Technol. 17 (2004) 612-619. http://dx.doi.org/10.1088/0953-2048/17/4/008

[12] – N.M. Ferreira, F.M. Costa, R.N. Nogueira, M.P.F. Graça, Lithium niobate bulk crystallization promoted by CO2 laser radiation, Journal Applied Surface Science 258 (2012) 9457– 9460, doi:10.1016/j.apsusc.2011.08.050

[13] – N.M. Ferreira, Sh. Rasekh, F.M. Costa, M.A. Madre, A. Sotelo, J.C. Diez, M. A.Torres, New method to improve the grain alignment and performance of thermoelectric ceramics, Materials Letters 83 (2012) 144–147, doi:10.1016/j.matlet.2012.05.131

[14] – J. Ding, D. Zhang, M. Arita, Y. Ikoma, K. Nakamura, K. Saito, Q. Guo, Growth and characterization of Fe3O4 films, Materials Research Bulletin 46 (2011) 2212–2216

[15] – O. N. Shebanova and P. Lazor, Raman study of magnetite (Fe3O4): laser-induced thermal effects and oxidation, J. Raman Spectrosc. 34 (2003) 845-852, DOI: 10.1002/jrs.1056

[16] – J. Garcıa and G. Subıas, The Verwey transition—a new perspective J. Phys.: Condens. Matter 16 (2004) R145–R178.

[17] – J.C. Papaioannoua, G. S. Patermarakisb, H. S. Karayianni, Electron hopping mechanism in hematite (a-Fe2O3), Journal of Physics and Chemistry of Solids 66 (2005) 839–844.

[18] – A. Shavel, B. Rodríguez-González, M. Spasova, M. Farle, L. M. Liz-Marzán, Synthesis and Characterization of Iron/Iron Oxide Core/Shell Nanocubes, Volume 17, Issue 18 (2007) 3870–3876, DOI: 10.1002/adfm.200700494

[19] – D. Caruntu, G. Caruntu and C. J O'Connor, Magnetic properties of variable-sized Fe3O4 nanoparticles synthesized from non-aqueous homogeneous solutions of polyols, J. Phys. D: Appl. Phys. 40 (2007) 5801–5809 doi:10.1088/0022-3727/40/19/001

6 Pyroelectrolysis studies

6.1 Introductory notes

The content of this chapter is based on a manuscript submitted for publication (6.2) and shows the results of studies aimed at assessment of the relevant mechanisms and limitations of iron pyroelectrolysis, performed using laboratory-scale electrochemical cells. The results demonstrate the feasibility of the pyroelectrolysis process, in particular in electron-blocking cell concept, and underline future challenges to be overcome. Regarding the inherent experimental difficulties and interpretation of the obtained results, the work described in this chapter can be considered as a most complicated part of the thesis. The main conclusions refer to the electron blocking conditions and are based on post-mortem analysis and in-situ monitoring of current-time dependencies and capacitive effects. Transient responses on re-establishing anodic or cathodic polarization allowed one to evaluate the dependence of conductivity on redox changes. Moreover, experiments performed under direct electrolysis regime allowed to estimate the residual electronic current and to predict the impact on faradaic efficiency.

6.2 Prospects and challenges of iron pyroelectrolysis in aluminosilicate melts

N.M. Ferreira, A.V. Kovalevsky, F.M. Costa and J.R. Frade

(submitted to Energy & Environmental Science journal
November 2014)

6.2.1 Abstract

Although steel production by molten oxide electrolysis offers potential economic and environmental advantages over classic extractive metallurgy, its feasibility is far from being convincingly demonstrated, mainly due to inherent experimental difficulties exerted by harsh process conditions. The present work was intended to demonstrate the concept of pyroelectrolysis at very high temperature, conducted under electron-blocking conditions using yttria-stabilized zirconia cells. The results of electrochemical measurements and post-mortem SEM/EDS analyses indicate that significant current yields are possible for pyroelectrolysis performed in electron-blocking mode using solid electrolyte membrane to separate the anode and molten electrolyte. However, metallic Fe readily alloys with the platinum cathode, and leads to disintegration of the Pt cathode, probably by onset of low melting liquid phase in the ternary system Pt-Fe-Si. Parasitic electrochemical processes rise gradually as the concentration of iron oxide dissolved in the molten electrolytes is depleted, impairing faradaic efficiency. Reduction of silica to metallic silicon was identified as a significant contribution to those parasitic currents, among other plausible processes. Direct pyroelectrolysis without electron blocking was found much less plausible, due to major limitations on faradaic efficiency. This was ascribed to a combination of electronic leakage and insufficient ionic conductivity of the aluminosilicate melt. Ohmic losses may consume an excessive fraction of the applied voltage, thus failing to sustain the Nernst potential required for reduction to metallic Fe.

6.2.2 Introduction

Steel is essential in huge quantities in the modern world, and its extractive metallurgy is one of the largest industrial contributors to greenhouse emissions, due to extensive use of coal as reducing agent and other fossil fuels to operate at very high temperatures. Thus, the development of alternative CO_2-lean and highly efficient technologies is critical for sustainable steelmaking [1, 2].

Although classical extractive metallurgy is well-established, and energy consumption per tonne of produced steel has been reduced by 50 % in recent years, this sector is now facing stronger pressure to lower greenhouse gas emissions, and to comply with stricter international regulations. A carbon-free alternative for steelmaking based on the use of hydrogen for reduction of iron oxide ore also raises concerns about safety and poor volume/time yield (Ref. [3] and references therein). Thus, from a broad environmental prospective, one seeks new strategies for carbon-lean iron extraction, with emphasis on electrolysis.

Pyroelectrolysis has been proposed for direct extraction of liquid iron from the oxide feedstock in molten oxides [3 – 7]. Operation at very high temperatures is expected to yield potential decrease in energy consumption compared to classical extractive metallurgy [3, 7], based on expectations of enhanced electrode kinetics, and mainly if one seeks nearly auto-thermal conditions. In this case, direct use of waste heat generated by electrode overpotentials and ohmic losses may account for endothermic reduction of hematite to magnetite. It has even been claimed that pyroelectrolysis opens perspectives for extraterrestrial production of oxygen, iron and silicon [8]. Although the idea itself is established, technical feasibility is far from demonstrated, mainly due to the very corrosive nature of molten electrolytes, critical issues concerning development of suitable anode materials, and inherent difficulties in monitoring electrochemical processes at very high temperatures. Faradaic efficiency reported for iron reduction from silicate melts by direct electrolysis using $Cr_{90}Fe_{10}$ anode did not exceed 35 % [7], showing a strong need for deeper understanding of mechanisms and further optimization of the concept to attain acceptable current yields.

Other recent approaches for less common metal electrolysis are based on solid oxide membranes (SOM) to achieve electrochemical oxygen pumping from melts [9 – 13]. This process was demonstrated for electrochemical extraction of calcium and magnesium from oxide/chloride or fluoride melts at intermediate temperatures. These metals are important as reducing agents for metallothermic production of titanium and other metals from their oxides. SOM technology is based on a solid electrolyte membrane with high ionic conductivity between the anode and liquid electrolyte, allowing selective transport of the oxygen ions, and blocking the oxidation of electrochemically active species in the anode compartment.

Benefits of electrochemical pumping with SOM are expected to be reached at the highest feasible temperatures to ensure high current densities [11], provided that this does not cause reducibility of the solid electrolyte membrane and electrochemical leakage. The most common electrolyte material is yttria-stabilized zirconia (YSZ), which possesses high ionic conductivity and appropriate stability under the harsh conditions imposed by molten electrolytes. Zirconia-based solid electrolytes also maintain reasonably wide electrolytic domains up to very high temperature. Using literature sources for temperatures in the range 1673 – 1873 K [14, 15] one estimated values of average electronic transport below 0.01 S/cm for up to about 1827 K, under a typical oxygen partial pressure range ~ 10^{-13} – 0.21 atm. This corresponds to a Nernst potential of about 1.11 V, which is within the expected range required to reduce iron oxide to metallic Fe, as shown below. Actually, reduction to metallic iron was reported on the basis of oxygen permeation across the YSZ membrane [16], i.e., with the YSZ membrane separating the anolyte and catholyte compartments without direct contact with electrodes. The high applied cell voltage used in that work (4 V) was much wider than the electrochemical stability of the YSZ, causing its reducibility, onset of mixed conduction and electrochemical permeation.

In the present work, the electron-blocking ability of the solid electrolyte membrane was retained by keeping the applied voltage in the range 1.5 – 2 V, to demonstrate the concept of Fe electrolysis under oxygen pumping conditions, using the type of cell represented in Figs. 1. This study is intended to attain better understanding of relevant mechanisms and limitations of high temperature electrochemical iron extraction. Results obtained in electron-blocking operation mode are also compared with corresponding results under direct electrolysis mode, without employing the solid electrolyte membrane.

Pyroelectrolysis of iron at very high temperatures is poorly understood in what concerns electrode kinetics in molten oxides, their ionic and electronic transport properties, and dependence on composition and temperature. This includes uncertainties concerning valence states of Fe^{nx} ions dissolved in the molten oxide electrolyte, and cell voltage required for electrochemical reduction to metallic Fe without exceeding the electrochemical stability of the solid electrolyte.

One of the main issues is related to coexistence of divalent: Fe^{2+} and trivalent: Fe^{3+} in the molten silicate used as electrolyte [17], and its expected impact on the ionic and electronic transport numbers. The Fe^{2+}:Fe^{3+} ratio is likely to depend on glass composition [18], with emphasis on basicity [19].

One also expects strong correlation between redox kinetics and basicity, based on the contributions of alkaline and alkaline earth components to transport properties with obvious impact on reoxidation [20]. Humidity may also play relevant effects on the activities of divalent and trivalent Fe^{n+} species [21], oxygen migration [22, 23] and conductivity [24].

Compilation of literature data relative to the dependence of (Fe^{2+}:Fe^{3+}) ratio on optical basicity of silicate melts at temperatures of about 1400 ºC and in air has been described by a typical dependence [18, 25]:

$$\log\left(\frac{Fe^{2+}}{Fe^{3+}}\right)^2 \approx 1.29 - 3.34x \qquad (1)$$

where x accounts for summation of oxide optical basicities. For composition $Al_{0.374}Mg_{0.203}Si_{0.423}O_{1.61}$ with 2 mol% FeO_x one expects x ~ 0.56 and (Fe^{2+}:Fe^{3+}) ~ 0.52, suggesting that trivalent Fe^{3+} may still prevail under oxidising conditions, mainly because the basicity of the actual composition is low. Other relevant information can be extracted from literature data for the solubility of divalent $X_{FeO_{(s.m.)}}$ and trivalent oxides $X_{FeO_{1.5-\delta((s.m.)}}$ in natural silicate melts ([26-28] and quoted references). Indeed, redox changes may occur on cooling, and one found evidence that divalent Fe^{2+} may still prevail in the actual composition, at least for samples cooled in air at least for high pulling rates [29]. Still, one considered the dependence on temperature (T), oxygen fugacity (f_{O2}) and contents of basic components (X_i) proposed elsewhere [26]:

$$\ln\left(\frac{X_{FeO_{1.5-\delta((s.m.)}}}{X_{FeO_{(s.m.)}}}\right) \approx 0.232\ln(f_{O_2}) + \frac{48.3x10^3}{T} - 23.2 - \frac{\sum_i X_i \Delta\mu_i}{RT} \qquad (2)$$

with chemical potential contributions $\Delta\mu_i$=49.04 kJ for Al_2O_3, - 48.87 kJ for CaO and - 106.05 kJ for Na_2O.

The dependence on redox conditions in Eq. 2 is close to the expected dependence for nearly ideal or regular behaviour in dilute conditions:

$$FeO_{(s.m.)} + 0.25O_2 \Leftrightarrow FeO_{1.5(s.m.)} \quad (3)$$

Thus, one also expects depletion of oxygen fugacity for representative conditions of SOM operation, i.e., when the inner electrode (1) in the YSZ-based cell (Fig. 1) is polarized cathodically, and the outer electrode (3) is polarized anodically. The highest oxygen fugacity in the silicate melt is expected at the melt/YSZ interfaces and, on assuming that the YSZ membrane is a pure oxygen ion conductor, with the external electrode in air, this may be given by the Nernst equation:

$$P_{O_2,i} \approx 0.21 \exp\left\{-\frac{4F(\eta_i + R_{YSZ}I + \eta_3)}{RT}\right\} atm \quad (4)$$

Note that total losses relative to the external reference (0.21 atm) combine ohmic losses in the YSZ electrolyte ($R_{YSZ}I$), overpotential of the outer electrode (η_3) and probably also interfacial losses at the melt/YSZ interface (η_i).

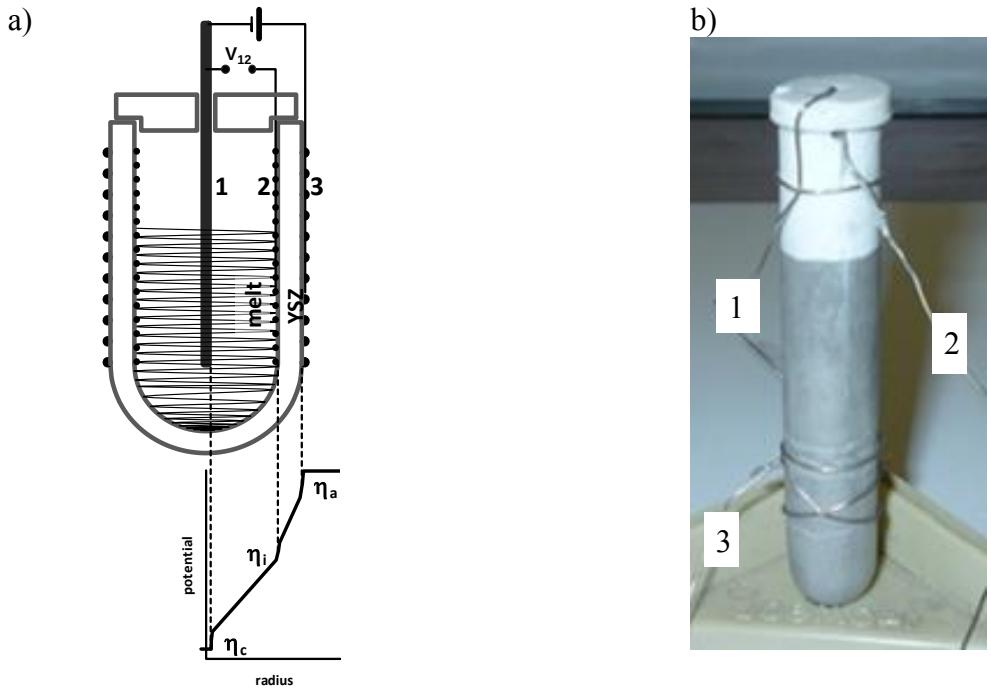

Figure 1 – a) Schemmatic representation and b) phtotograph of the electronic blocking cell used for iron pyroelectrolysis.

The activity of divalent iron in the silicate melt $a_{FeO}^{sil.m.}$ and its dependence on basicity may also affect redox conditions required for the onset of metallic Fe, at the inner cathode.

Equilibrium conditions for co-existence of metallic Fe with the melt can be described by:

$$2Fe + O_2 \Leftrightarrow 2FeO_{\ sil.melt} \tag{5}$$

and

$$f_{O_2,c} = \left(X_{FeO}\gamma_{FeO}^{sil.m.}\right)^2 \exp\left(\frac{\Delta G^o}{RT}\right) \tag{6}$$

where ΔG^o=-488.24-(0.01695 x ln(T) – 0.2311), ΔG^o is the free energy of reaction: $2Fe + O_2 \Leftrightarrow 2FeO_{liq.}$, and the activity coefficient of FeO in the silicate melt may be described by the empirical dependence [30]:

$$\gamma_{FeO}^{sil.m.} = \sum_{j=1}^{4}\sum_{k=1}^{j} a_{jk} X_j X_k \tag{7}$$

For the actual composition $Al_{0.374}Mg_{0.203}Si_{0.423}O_{1.61}$ with 2 mol% FeO one obtain $\gamma_{FeO}^{sil.m.} = 1.20$ at ≈ 1400 ºC, and on inserting this in Eq. 6 one predicts $f_{O_2} \approx 10^{-13} atm$. This also yields the corresponding Nernst potential relative to air (1.02 V). Further additions of iron oxide yield $f_{O_2} \approx 3.8x10^{-13} atm$ for 4 mol% FeO, $f_{O_2} \approx 1.42x10^{-12} atm$ for 8 mol% FeO, etc.

The contents of iron oxide and (Fe^{2+} : Fe^{3+}) ratio may determine the ionic and electronic transport properties. However, the relative contributions also depend on mobility of these cationic species in silicate glasses, which is determined by their prevailing structural incorporation as network formers or modifiers. Migration of glass former cations form structural tetrahedral units ($[SiO_4]^{4-}$, $[AlO_4]^{5-}$,…..) with very low mobility. This also applies partially to Fe^{3+}, with mixed character between network former $[FeO_4]^{5-}$ and modifier [31, 32]. Thus Fe^{2+} should have a prevailing contribution to ionic conductivity, due to its network modifier character, probably combined with the additional contribution of Mg^{2+}, at least if one considers ac electrical response. Otherwise, dc electrical behavior should be mainly dependence on migration of Fe^{2+} if the applied voltage exceeds the Nernst potential for reduction to metallic Fe, possibly combined with an additional electronic contribution by small polaron hopping between ferric and ferrous ions [33]. Redox stable mobile cations (e.g. Mg^{2+}) are likely to give rise to space charge effects.

6.2.3 Experimental

Powders of MgO (Merck, 99+ %), Al_2O_3 (Merck, 99.5 %), SiO_2 (Sigma Aldrich, 99.6 %) were mixed in required proportion to obtain the nominal composition $Mg_{0.203}Al_{0.374}Si_{0.423}O_{1.61}$ (MAS – Magnesium Aluminosilicate) with minimum liquidus temperature. The required amounts of Fe_3O_4 (Aldrich, 99 %) was added to prepare the corresponding composition with 2 mol% of Fe (MAS-2Fe). After addition of a binder (PVA) the prepared mixtures were extruded as feed and seed precursor rods to prepare the intended glasses by laser floating zone (LFZ) method. Amorphous samples were grown at 100 mm/h using a continuous CO_2 Spectron SLC laser (λ = 10.6 μm; 200 W). During the process the seed and feed rod precursors were rotated in opposite directions to enhance the homogeneity of the target samples. Obtained samples were then crashed and ball-milled in ethanol to produce a fine glass powder, which was further used as the molten electrolyte in pyroelectrolysis. Preliminary experiments showed that the obtained glass composition can be melted at temperatures above 1700 K.

Pyroelectrolysis was studied using an electrochemical cell made of yttria-stabilized zirconia (YSZ) shown schematically in Fig. 1. The cell comprised an YSZ closed-end tube and three Pt electrodes (1 to 3) to perform electrolysis studies in various regimes and to evaluate the resistance of molten electrolyte by impedance spectroscopy. The cells were loaded with 3.6 to 4.8 g of the glass electrolyte powder, prepared as described above. After filling the internal compartment with electrolyte and centering the electrode (1) wire (∅ 0.5 mm), the cell was closed by an YSZ lid and vertically aligned in an external alumina crucible and held vertically with alumina powder. The distance between electrode (1) and bottom of the cell was circa 5 to 7 mm. Thus assembled cell was heated up to 1728 K at a rate of 5 K/min. Onset of melting was monitored by rapid drop in resistance between electrodes 1 and 2, measured under open-circuit condition by electrochemical impedance spectroscopy (Autolab PGSTAT302 instrument, frequency range 0.01 to 10^6 Hz and 0.5 V of amplitude AC signal). Fig. 2 shows corresponding Nyquist plots during electrolysis process. Above 1700 K the shape of the impedance spectra significantly changes, while the resistance of the cell dramatically decreases.

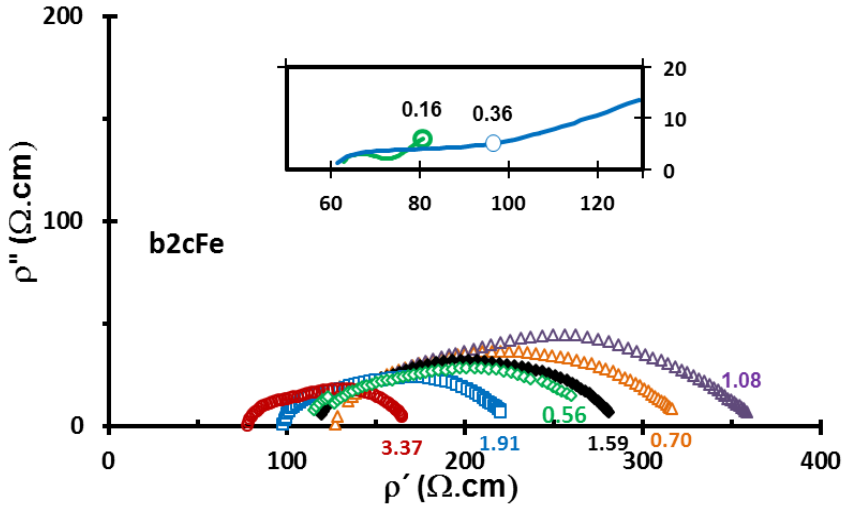

Figure 2 – Complex resistivity spectra: $\rho^* = [2\pi L \ln(r_e / r_i)]Z^*$ **(see Eq.12) for cell b2cFe, obtained after different relative charging, i.e., Q/Q_{Fe} = 0.16, 0.36, 0.56, 0.70, 1.59, 1.91 and 3.37, where Q_{Fe} denotes the charge required to reduce the actual content of iron oxide to metallic Fe, assuming that Fe^{2+} prevails, based in eqs 1.12 and 1.13.**

Table 1 shows the relevant experimental conditions of pyroelectrolysis experiments. These studies were preceded by preliminary experiments which were required to screen appropriate procedures for the preparation of cells, conditions for high-temperature electrochemical measurements, risks of short-circuiting in the cell, caused by displacement of the central electrode wire (1), etc. In electron-blocking cell experiments, a constant dc voltage was applied between the Pt wire cathode (1) and the external counter electrode (3). Other experiments were performed in direct electrolysis mode between cathode (2) and anode (1), i.e., without electron blocking. The changes in electrochemical properties of the cell components were also monitored by impedance spectroscopy, between electrodes (1) and (2). These spectra (see Fig. 2) were acquired without dc bias, by temporarily disconnecting the applied dc voltage, for 2 to 3 min, to ensure sufficient signal to noise ratio.

Table 1 – Operating regimes and other relevant experimental conditions of electrochemical cells.

Notation	Regime	Cathode	Anode	V_{appl} (V)	FeOx additions
b2cFe	Electron-blocking	(1)	(3)	2.0	2 mol%
b1.5cFe	Electron-blocking	(1)	(3)	1.5	2 mol%
b1.5c	Electron-blocking	(1)	(3)	1.5	Fe-free
d1.5aFe	Direct-electrolysis	(2)	(1)	-1.5	2 mol%

After the pyroelectrolysis experiments the cells were cooled down to room temperature at 5 K/min, for subsequent post-mortem analysis. The bottom part of the cell, containing solidified electrolyte, was cut transversely by a diamond wafering blade into 3 to 5 pieces, to analyse the cation distribution in the cathodic compartment and to assess the approximate liquid electrolyte level during the pyroelectrolysis process. The cut pieces were polished and examined by combined SEM/EDS studies (Hitachi SU-70 model equipped with Brucker silicon drift EDS detector).

The element distribution in the samples polished were examined also by Raman spectra (SPEX, Jobin Yvon T64000) at room temperature in backscattering configuration, using the 532 nm exciting line, from 100 to 1000 cm^{-1}.

6.2.4 Results and Discussion

6.2.4.1 Proposed equivalent circuit

Under electron-blocking operation mode, the YSZ membrane separates the cathodic and anodic compartments, and is expected to block electronic transport. This allows selective transport of oxygen ions and should prevent iron reoxidation at the anode. Iron cations migrate in the molten silicate under the applied electric field and are expected to be reduced to metallic Fe at the cathode, when the applied voltage exceeds the minimum Nernst cell voltage, while oxygen ions are likely to be transferred across the molten silicate/YSZ interface, migrate through the YSZ solid electrolyte by a vacancy mechanism, and feed the oxygen evolution reaction at the outer electrode. Thus, the actual concept of pyroelectrolysis with electron blocking provided by YSZ can be approximately described on assuming the following half-cell cathodic (electrode 1) and anodic (electrode 3) reactions, coupled with partial conversion of non-bridging to bridging oxygens in the molten silicate and ion transfer across the silicate melt/YSZ interface:

$$Fe^{2+} + 2e^{-} \rightarrow Fe^{0}(Pt) \tag{8}$$

$$2(\equiv Si - O^{-} ... M^{2+} ...^{-} O - Si \equiv)_{melt} + V_O^{\bullet\bullet}(YSZ) \rightarrow (\equiv Si - O - Si \equiv)_{melt} + M_{melt}^{2+} + O_O^{\times}(YSZ) \tag{9}$$

$$O_O^{\times}(YSZ) - 2e^{-} \rightarrow 1/2 O_2(g) + V_O^{\bullet\bullet}(YSZ) \tag{10}$$

Note that divalent Fe^{2+} is expected to prevail in the molten silicate glass electrolyte under conditions of electrochemical oxygen pumping, which depresses O_2 fugacity, at least near the Pt cathode. Thus, one can assume that pyroelectrolysis with electronic blocking involves partial transfer of non-bridging oxygen ions from the melt to the solid electrolyte, according to reaction of Eq. 9, with simultaneous migration of the modifier cations in opposite direction, towards the inner cathode.

A schematic representation of a proposed equivalent circuit for the overall behaviour is presented in Fig. 3. Equivalent circuits have been proposed to analyse mixed conduction in solids [34]. Though this is arguable in the present case, due to scarce information and excessive experimental scattering, one may still assume association of a prevailing contribution of ionic transport and a parallel contribution of electronic transport, with series associations of components in the molten electrolyte and in the YSZ solid electrolyte, i.e., $R_{I,m}$+ $R_{I,s}$, respectively.

The equivalent circuit in Fig. 3 also includes expected electrode overpotential contributions, and an interfacial contribution, based on the intermediate frequency arc revealed by impedance spectra (Fig. 2). This may be nearly accounted for by the $R_{int}C_{int}$ component in the equivalent circuit, or a corresponding constant phase element (CPE) taking into account that interfacial arcs are usually depressed (e.g. Fig. 2). In addition, the YSZ solid electrolyte allows selective oxygen ion transport and should be nearly blocking to the electronic conductivity and to contributions of redox stable cations (e.g. Mg^{2+}), this was accounted for by inserting a capacitor in the equivalent circuit (C_{tr}).

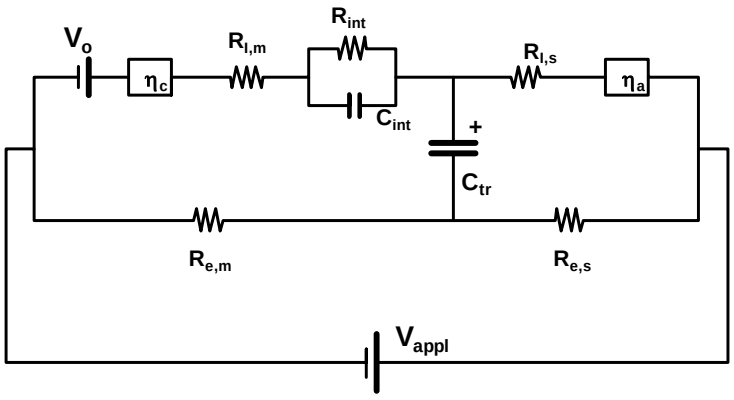

Figure 3 – Proposed equivalent circuits for electron-blocking cells.

The cell voltage must exceed a lower limit corresponding to the Nernst potential generated by oxygen fugacity ratio between the surrounding atmosphere (0.21 atm), and the silicate melt in the presence of metallic Fe. For a typical temperature of about 1728 K and based on Eq. 6, with a typical activity coefficient $\gamma_{FeO}^{sil.m.} = 1.20$ (for 2 mol% iron oxide), one estimated $f_{O_2} \approx 2.7x10^{-13} atm$, and the corresponding value of Nernst potential:

$$E_o = \frac{RT}{4F} \ln\left(\frac{0.21}{2.7x10^{-13}}\right) \approx 1.02\,V \tag{11}$$

Ohmic losses are likely to be one of the main limitations in energy efficiency due to insufficiency ionic conductivity. One expects major dependence on the inner electrode under the actual nearly cylindrical geometry, due to major differences between the inner (r_i) and outer electrode (r_e) radii, with corresponding impact on electric field, current density differences, and gradient of ohmic losses. This gradient is much steeper near the central electrode, as derived on assuming a steady state regime with nearly cylindrical geometry and without radial changes in conductivity, i.e., $\sigma(dV/dr) \approx I/(2\pi rL)$, where I is current, L is length and r is radial distance. On integrating one obtains the relevant solutions for ohmic resistance and electric field:

$$R = \frac{\Delta V_{ohmic}}{I} \approx \left[2\pi L \sigma \ln\left(\frac{r_e}{r_i}\right)\right]^{-1} \tag{12}$$

and

$$\frac{dV}{dr} \approx \frac{\Delta V_{ohmic}}{r \ln(r_e / r_i)} \tag{13}$$

where ΔV_{ohmic} is the overall ohmic drop. Thus, the actual geometry is suitable to identify differences between specific electrode limitations under cathodic and anodic polarization, even for conditions when the use of a reference electrode is impaired by very harsh operating conditions.

Faradaic efficiency may also be affected by onset of electronic conductivity, as shown in the proposed equivalent circuit in Fig. 3, except possibly for conditions when the electronic conductivity of YSZ is negligible and provides almost perfect blocking for electronic leakage.

This condition may be assessed by combining the dependence of n-type and p-type contributions in YSZ [35], including high temperature results [14]:

$$\sigma_n = 1.65x10^6 \exp\left(-\frac{3.85\text{eV}}{\text{kT}}\right)(\text{pO}_2)^{-1/4} = \sigma_{n,o}\,(\text{pO}_2)^{-1/4}\ \text{S/cm} \tag{14}$$

$$\sigma_p = 27\exp\left(-\frac{1.40\text{eV}}{\text{kT}}\right)(\text{pO}_2)^{1/4} = \sigma_{p,o}\,(\text{pO}_2)^{1/4}\ \text{S/cm} \tag{15}$$

The corresponding average value can be computed for the relevant boundary conditions pO_2' and pO_2'':

$$\begin{aligned}\sigma_{e,av} &= \frac{4}{\ln\left(\frac{pO_2''}{pO_2'}\right)}\int_{pO_2'}^{pO_2''}(\sigma_n + \sigma_p)\,d\ln(pO_2) = \\ &= \frac{4}{\ln\left(\frac{pO_2''}{pO_2'}\right)}\left\{\sigma_{n,o}\left[(pO_2')^{-1/4} - (pO_2'')^{-1/4}\right] + \sigma_{p,o}\left[(pO_2'')^{1/4} - (pO_2')^{1/4}\right]\right\}\end{aligned} \tag{16}$$

yielding a typical value for electronic conductivity of YSZ ($\sigma_{e,av}$ ~2.8 × 10^{-3} S/cm) under the actual working conditions, i.e., at 1728 K, and on assuming limiting conditions for air (pO_2 = 0.21 atm), and equilibrium between metallic Fe and molten electrolyte (≈ 2.7x 10^{-13} atm).

The ionic resistance in the YSZ solid electrolyte may also be estimated by considering literature data for ionic conductivity of YSZ at very high temperatures [15].

$$\sigma_I = 1.95x10^5\,T^{-1}\exp\left(-\frac{0.74\text{eV}}{\text{kT}}\right)\text{S/cm} \tag{17}$$

with a typical value of 0.79 S/cm at 1728 K. This is more than 2 order of magnitude higher than the electronic conductivity, which confirms that YSZ should provide electronic blocking.

In addition, the ionic conductivity of YSZ is close to 2 orders of magnitude higher than the actual order of magnitude of conductivity of the molten electrolyte, extracted from impedance spectra (e.g. Fig. 2). These impedance spectra are shown as complex resistivity plots for cylindrical symmetry (Eq. 12), i.e.:

$$\rho_{I,m} \approx \frac{2\pi\,\text{L}\,\text{R}_{I,m}}{\ln\left(\text{d}_i/\text{d}_o\right)} \tag{18}$$

where d_i is the inner diameter and d_o the outer diameter of the YSZ cell.

Results in Fig. 2 are in the order of 10^2 Ωcm, which is a significant limitation for pyroelectrolysis with the actual molten electrolyte. Note that basaltic melts attain similar conductivity values at significantly lower temperatures (≈ 1573 K) [36]. This can be understood by taking into account that the mobility of prevailing carriers in the actual aluminosilicate melts (Fe^{2+} and Mg^{2+}) may be much smaller than the mobility of alkali carriers in basaltic melts, as revealed by corresponding diffusivity ranges [20]. The structure of molten silicates can be described as three-dimensional interconnected network of $[SiO_4]^{4-}$ tetrahedra, where the silicon atoms are mostly joined by bridging oxygen atoms $(\equiv Si-O-Si\equiv)_{melt}$ [37], whereas alkaline (Na^+, ...), alkaline earth (Mg^{2+},...) and other cations (Fe^{2+},...) provide charge compensation for non-bridging oxygens and may act as ionic charge carriers.

6.2.4.2 Post-morten analyses

Although one attempted to estimate Faradaic efficiency by direct weighing the cathode after iron extraction and quantifying the volume of gaseous species, evolved at the anode, such measurements have particular difficulties under the extremely harsh experimental conditions of pyroelectrolysis, with emphasis on disintegration of the Pt cathode and changes in morphology (Fig. 4). In addition, estimates of Faradaic efficiency are affected by uncertainties concerning the initial distribution Fe^{2+} and Fe^{3+} in the aluminosilicate melt and their changes on lowering the oxygen fugacity by electrochemical pumping. Therefore, in the present work one relied mostly on post-mortem analysis of the cell by combining SEM (Fig. 4) and EDS analyses (Fig. 5), and results of electrochemical measurements, to confirm electroreduction to metallic Fe.

Somewhat surprisingly Fig. 4 shows drastic degradation of the Pt cathode, in contrast with the reference Pt electrode. The Pt cathode disintegrated in isolated segment in the cross section, including small spots organized in ring-like distribution. Smaller dispersed fragments are also found in the surrounding area, as shown in the expanded SEM image.

Still, the total cross section of the remaining Pt fragments is significantly smaller than the initial cross section of the Pt wire.

The circular area traced by Pt fragments is also surrounded by the Al-rich and Si-deficient ring. In addition, high Fe-concentrations are found both inside this ring, mostly overlapping with the Pt elemental map, and in the surrounding area. One may speculate that dispersed Fe-rich fragments correspond to metallic Fe, based on their spatial distribution.

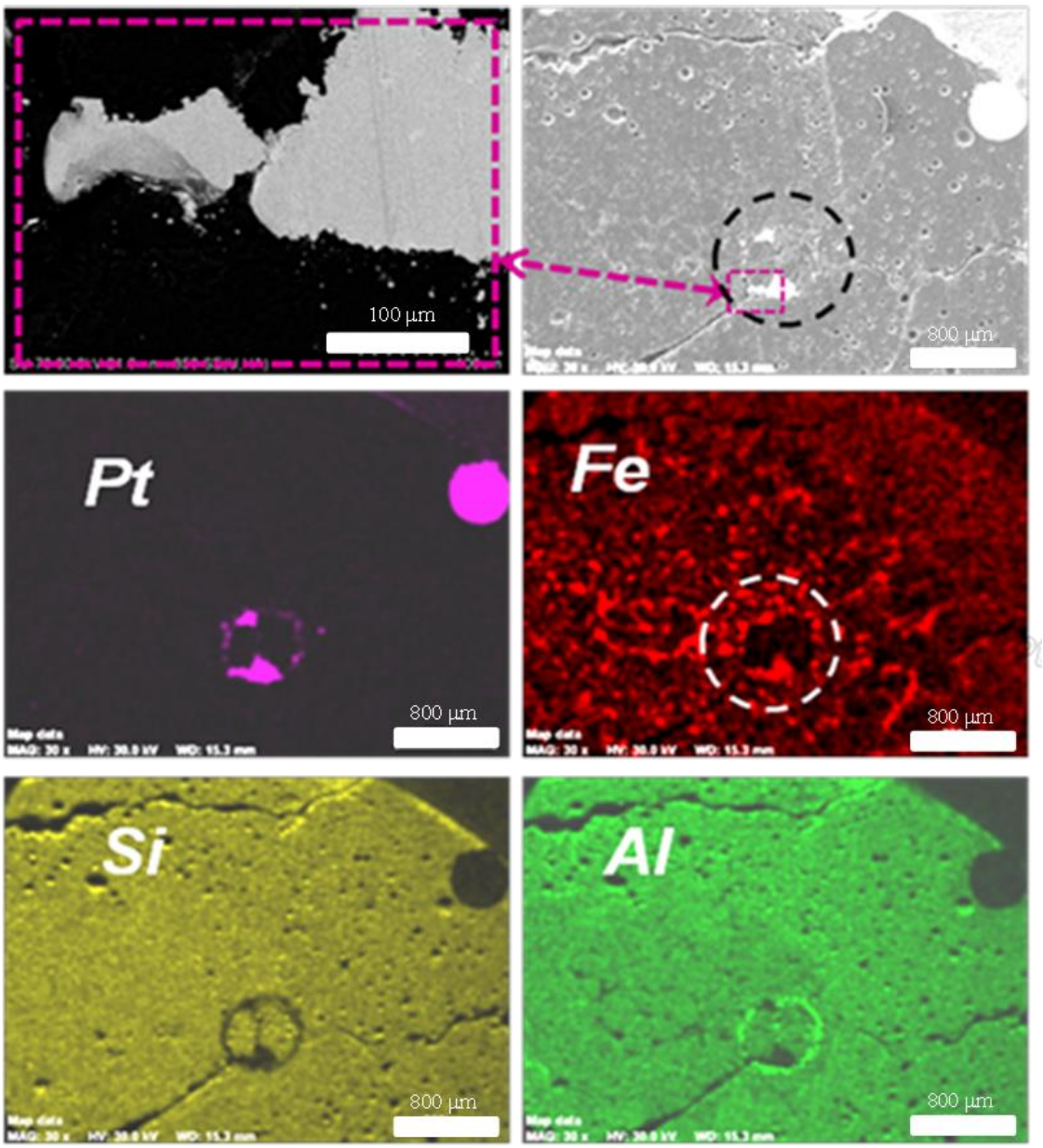

Figure 4 – Post-mortem SEM microstructures and elemental maps of the pyroelectrolysis cell b2cFe tested with applied cell voltage 2 V.

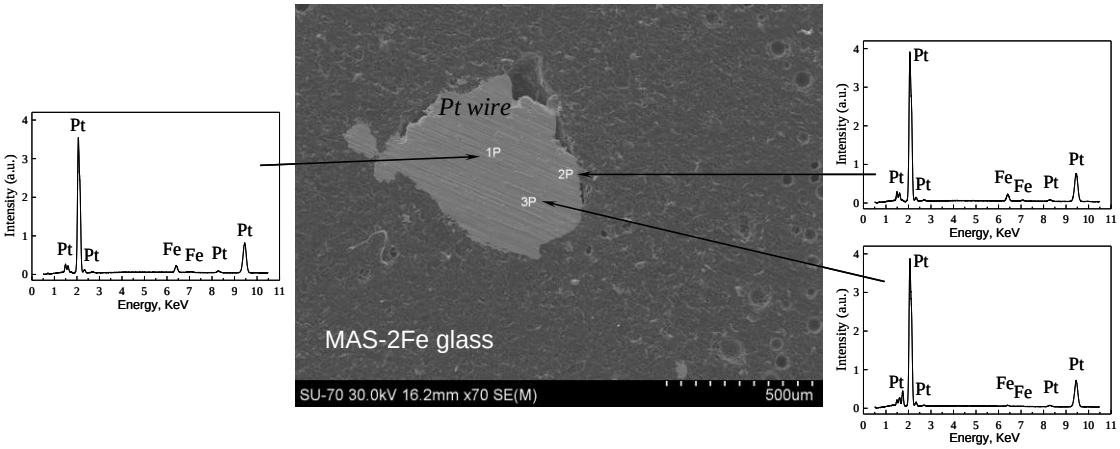

Figure 5 – EDS analysis by post-mortem analysis of Cell b2cFe.

Note that the expected cross section of metallic Fe deposit should be in the order of 0.3 mm^2, if one considers complete reduction of the iron oxide content in the melt. Though one could not confirm the nature of these Fe-rich spots the surrounding area, they resemble onset of metallic Fe inclusions reported for aluminosilicate melts exposed to reducing atmospheres [38, 39]. Dispersed metallic inclusions are also found in basaltic rocks [40].

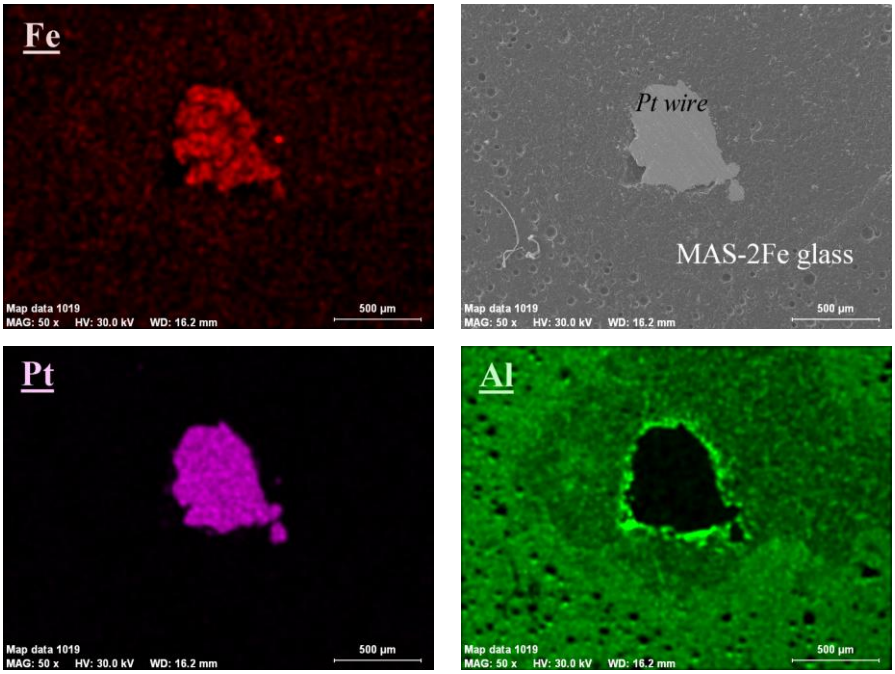

Figure 6 – SEM and elemental maps obtained by post-mortem analysis of a Pt cathode after testing cell b1.5cFe, with applied cell voltage 1.5 V.

Less drastic degradation of the Pt cathode, and clearer evidence of Pt-Fe alloying is demonstrated by postmorten analysis of cell b1.5cFe, after pyroelectrolysis with applied voltage 1.5 V (Fig. 6). The Al-rich boundary is also shown in this case, and EDS spectra (Fig. 6) confirm alloying of Pt with Fe. Alloying of Pt with Fe extended to the bulk of the original Pt wire, with atomic Pt : Fe ratio of about 6.3:1, preserving the metallic appearance (color, luster, etc.), as expected for metallic alloys. Formation of Pt-Fe alloys was also reported for electrodeposition of Fe^{2+} on Pt electrodes in chloride melts at 973 – 1023 K [17]. In addition Pt-Fe alloys have been proposed as containers for silicate melts, to avoid losses of iron [41, 42].

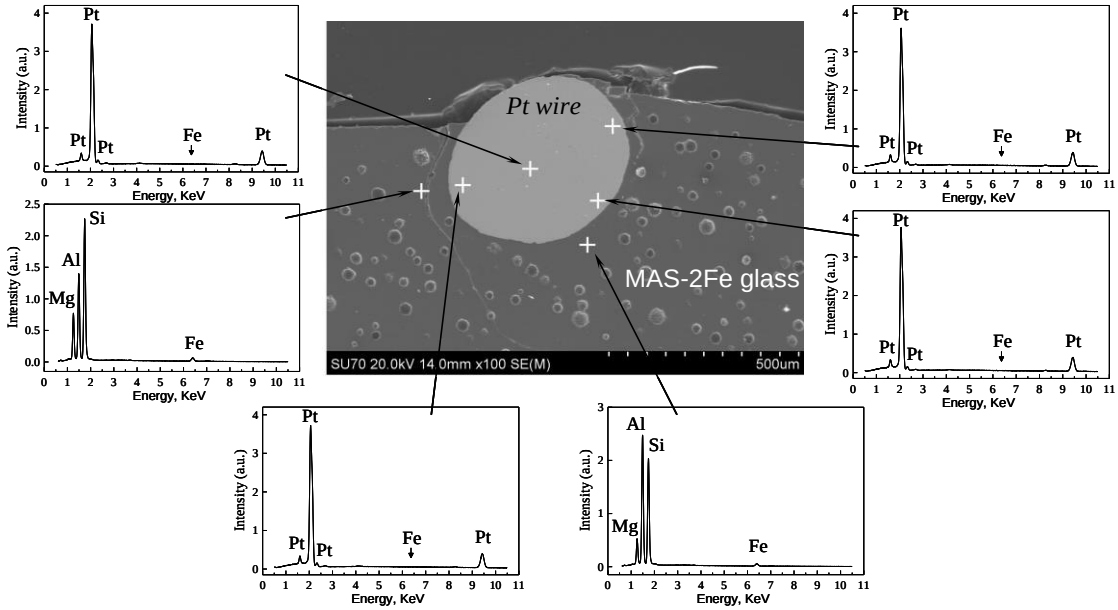

Figure 7 – ***Post-mortem EDS analysis at representative locations in the Pt wire, after contacting with molten MAS-2Fe glass at 1728 K for 5 h without electrical polarization.***

Indeed, allowing with Fe and disintegration of Pt electrodes requires cathodic polarization to induce reduction to metallic Fe, being hindered without application of electric field (Fig 7), and also under anodic polarization. Thus, the physical or electrochemical nature of actual disintegration of Pt electrodes cannot be ascribed to oxidation of Pt, and is more consistent with incorporation of Pt on metallic inclusions in silicate melts under reducing conditions [40]. Post-mortem analyses are also more consistent with formation of low melting liquid phase in the ternary system Pt-Fe-Si. Note also that the actual temperature (1728 K) is lower than required for liquid phase formation in the binary Pt-Fe system.

Though reduction of silica to metallic Si and diffusion into the metallic phase might seem somewhat surprising, under a relatively low applied cell voltage (1.5 V), one finds evidence in the literature for alloying of metallic Fe with Si on exposing aluminosilicate melts to reducing atmospheres such as CO-CO_2 [39] or H_2-Ar [43].

Partitioning of Si between the Fe-based earth´s core and silicate melts on earth´s mantle is also known [44]. In addition, SiO_2 can be reduced to metallic silicon by pyroelectrolysis in chloride halide melts [45]. However, the solubility of Si in solid Pt is only about 1 atm% [46] thus explaining why the EDS signal of Si remains very weak in Pt-rich spots (Fig. 7). On the contrary, one may expect a wide range of compositions for liquid phase formation in the Pt-Si system at the actual temperatures (≈ 14 – 100 mol% Si) [46].

Thus, onset of liquid phase is expected on increasing the contents of reduced Si, and this may explain disintegration of the Pt cathode and its dispersion as small droplets in the surrounding aluminosilicate melt. This may also explain onset of dispersed metallic particles shown in Fig. 4, at sufficiently high magnification. The relevant literature also showed evidence for the dynamic behaviour of Pt-Si liquid phases [47, 48].

Simultaneous reduction of Si and Fe may also explain the Al-rich ring in Figs. 4 and 6, possibly yielding liquid phase at the actual high temperatures, as predicted by the binary Fe-Si phase diagram [49, 50], and also contributing to dispersion of metallic inclusions in the area surrounding the Pt cathode. Thus, disintegration of the Pt cathode may be ascribed to liquid phase formation in the ternary system Fe-Si-Pt, and its dispersion in the surrounding area, mainly for cell b2cFe, when the applied voltage is highest and most likely to reach conditions for reduction to metallic Si. The enhanced wetting of metallic surfaces (Fe, Pt,...) by aluminosilicate melts [43] may also contribute to ready dispersion of liquid metallic drops.

Thermodynamic and electrochemical conditions for reduction of silicon dioxide to metallic silicon or silicon monoxide can also be estimated based on relevant thermodynamic data [51]. This has been summarized in Table 2 which shows the Gibbs free energy ΔG_R of plausible reactions at 1728 K, and corresponding Nernst $\Delta G_R/(nF)$ potential relative to standard conditions, i.e, for $pO_2 \approx 1$ atm and considering unit activity ratio $a_{SiO2} : a_{Si}$, a_{SiO2} for silicon dioxide and a_{Si} for silicon.

Thus, reduction of silica to SiO or Si is likely to occur when the pyroelectrolysis cell is operated atV_{appl} = 2 V. Indeed, this is unlikely for redox stable trivalent aluminium Al^{3+}, with prevailing glass former character, and also for redox stable Mg^{2+}, with prevailing modifier-character. The mobility of modifier cations may contribute to minimize the concentration gradient of magnesium. Reduction of silicon dioxide to metallic Si may still occur on lowering the applied voltage to V_{appl} = 1.5 V, mainly if one considers a relatively low activity ratio $a_{Si}/a_{SiO2} << 1$, a_{Si} being the activity of Si in the metallic liquid phase, and a_{SiO2}, the activity of silica in the MAS melt, i.e.:

$$(SiO_2)_{MAS} \rightarrow (Si)_{lm} + (O_2)_{MAS} \quad (19)$$

$$V_o' = V_o + \frac{RT}{4F} \ln\left\{\left(\frac{a_{Si,lm}}{a_{SiO2,MAS}}\right) pO_2\right\} < V_o \quad (20)$$

EDS spectra in Fig. 6 even suggest the presence of Al in the postmortem analysis of the Pt-cathode, possibly as an artifact resulting from polishing. In fact, the redox stability of alumina should prevent reduction to metallic Al, except possibly for relatively high applied cell voltage, as emphasized by the Gibbs free energy of the relevant reaction and corresponding Nernst potential (Table 2). Still, one cannot rule out the possibility of reduction of alumina for cell b2cFe, operated under applied of 2 V. Note that the presence of Al in ternary Pt-Si-Fe would also contribute to suppress the liquidus temperatures of metallic inclusions [50]. Prospects for reduction of aluminium oxide to metallic Al were demonstrated for redox conditions corresponding to very dry hydrogen ($H_2 : H_2O > 10^5$), possibly assisted by volatile intermediate species (AlH or Al_2O) [52].

Table 2 – Gibbs free energies of reduction of silica to silicon oxide or silicon.

Reaction	ΔG (kJ)	V_o=ΔG/(nF) (V)
$2SiO_2$ (l) = O_2 (g) + 2SiO (l)	540	1.34
$2SiO_2$ (l) = O_2 (g) + 2SiO (g)	709	1.78
SiO_2 (l) = O_2 (g) + Si (l)	586	1.46
SiO_2 (s) = O_2 (g) + Si (l)	601	1.50
$2/3Al_2O_3$ (s) = O_2 (g) + 4/3Al (l)	750	1.88

Evidence that disintegration of the Pt cathode may be induced by reduction to elemental Si and formation of Si-Pt liquid phase may also be inferred from micro-Raman spectra (Fig. 8). Spectra localised on residual fragments of the Pt cathode show a main peak at ≈ 480 cm^{-1}, which is close to the characteristic transverse optical band of amorphous silicon [53], and is absent in the Raman spectrum of the MAS matrix. Though one cannot exclude the presence of this peak in the Raman spectrum obtained for original Pt wire, this is close to the background noise.

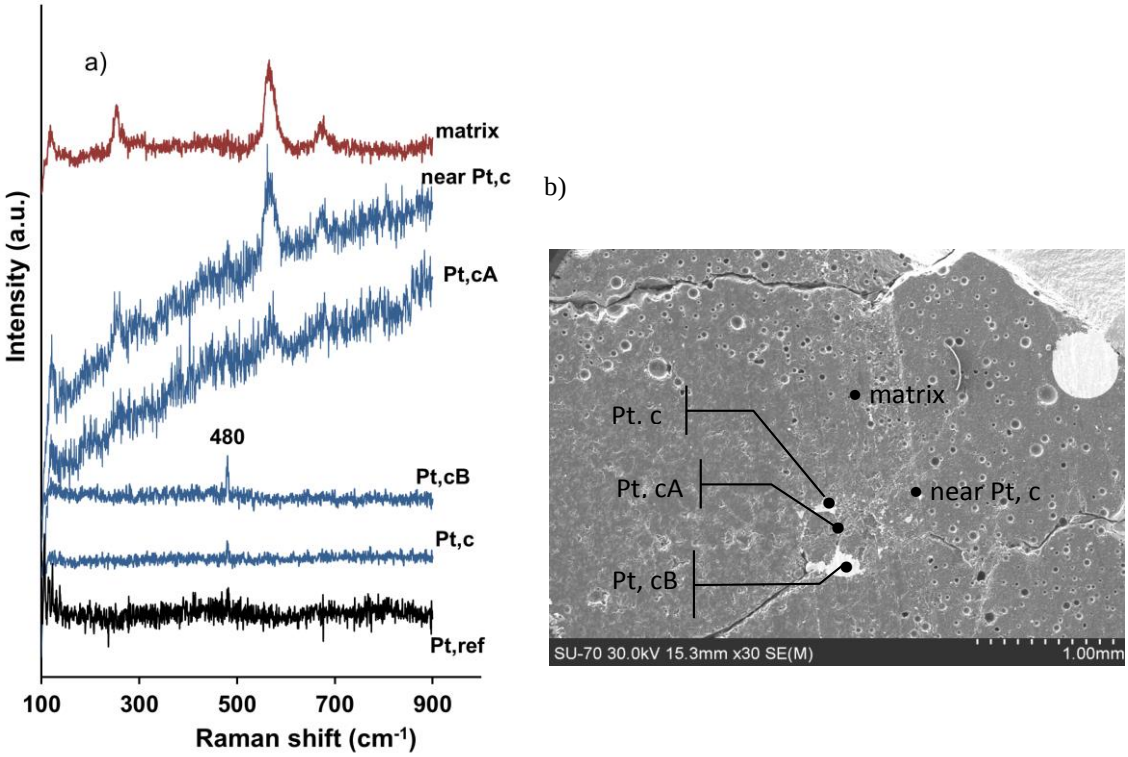

Figure 8 – a)Raman spectra and b) SEM microstructure of cell b2cFe, located at the MAS matrix, reference Pt wire (Pt,ref), major spot of the Pt cathode (Pt,c), smaller Pt spots (Pt,cA and Pt,cB), and a nearby location (near PT,c).

Thus, this does not contradict the evidence that disintegration of the Pt cathode may be induced by alloying and formation of liquid phases, probably in the ternary Pt-Fe-Si system. Note also that the active Raman bands of the MAS matrix (≈ 253 cm^{-1}, 567 cm^{-1} and 673 cm^{-1}) vanish in the proximity of the remaining spots of the Pt cathode.

Cell (b1.5c) was operated in blocking-electron configuration with Fe-free MAS glass electrolyte, while keeping the remaining conditions similar to cell b1.5cFe (Table 1). In this case, the Pt cathode remains relatively immune to disintegration, as shown in Fig. 9.

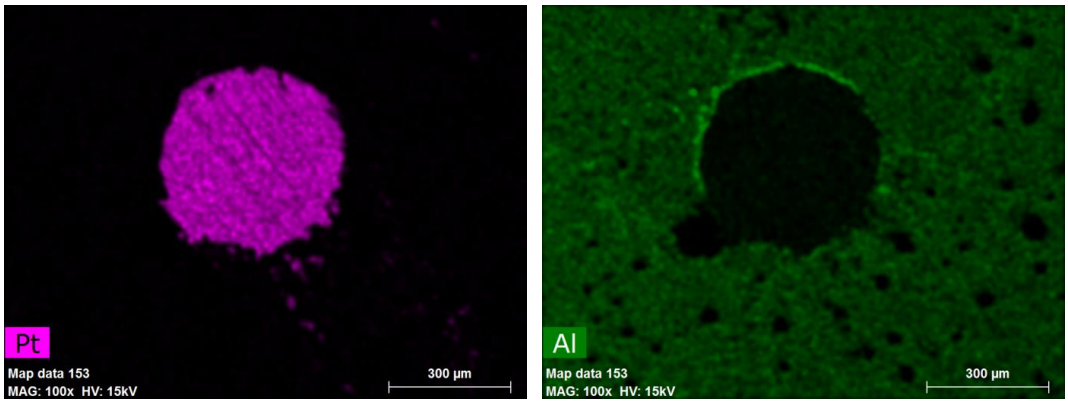

Figure 9 – Pt and Al elemental maps of cell b1.5c.

Note that traces of Pt towards the bottom-right of this map are an artefact due to cutting of the sample. Thus, the presence of Fe in Pt-based alloys play a key role in the disintegration of the Pt cathode observed for the previous cells (b2cFe and b1.5cFe). In addition, enhanced wetting of cathode by the aluminosilicate melt is expected upon incorporation of Fe in the metallic phase [43], possibly contributing to assist incorporation of Si and formation of liquid phase in the ternary system Pt-Fe-Si, responsible for the disintegration of the cathode in cells b2cFe and b1.5cFe.

Additional evidence that disintegration of the Pt electrode is specific of cathodic polarization was provided by reversing the polarization of the central Pt electrode to anodic in cell d1.5aFe (Table 1). In this case, anodic polarization also prevents disintegration, as shown in Fig. 10.

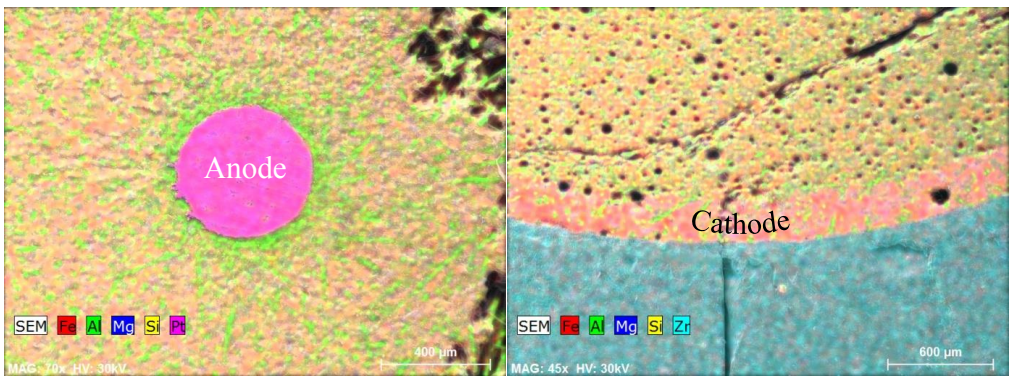

Figure 10 – *Post-mortem* elemental maps of cell d1.5aFe.

Note also that the surrounding aluminosilicate melt still becomes Al-rich, probably by migration of Fe^{2+} ions towards the cathode (i.e., the outer electrode (2)), yielding a Fe-enriched layer next to the YSZ container. Note that electrode (2) had been applied by painting with Pt past on the internal surface of the YSZ container. Still, the Fe-rich layer lacks metallic luster and its thickness is excessive to assume reduction to metallic Fe. Thus, one may assume enhanced concentration of Fe^{2+} and/or Fe^{3+} ions instead.

6.2.4.3 Transient electrochemical response

The time dependence of current under constant applied cell voltage may reveal changes related to exhaustion of iron oxide in the aluminosilicate melts, and the corresponding accumulated charge may be a guideline to estimate the Faradaic efficiency, this is shown in Fig. 11. Except for current spikes due to periodic switching off of the applied voltage for impedance studies, one may identify a minimal in average current, and this is close to conditions when the accumulated charge should correspond to full reduction of iron, considering predominant Fe^{2+} oxidation state in the melt and ~ 100 % faradaic efficiency. This transition is also revealed by the decrease in the slope of cumulative charge. The latter is more evident for cell b1.5cFe, operated at lower applied voltage (1.5 V), possibly because this cell was less affected by side electrochemical reactions and parasitic effects, such as reduction of silicon dioxide, as shown above. Though a significant fraction of Fe^{3+} would require greater cumulative charge, this may only account for up to 1/3 of the total charge required to reduce Fe^{n+} ions.

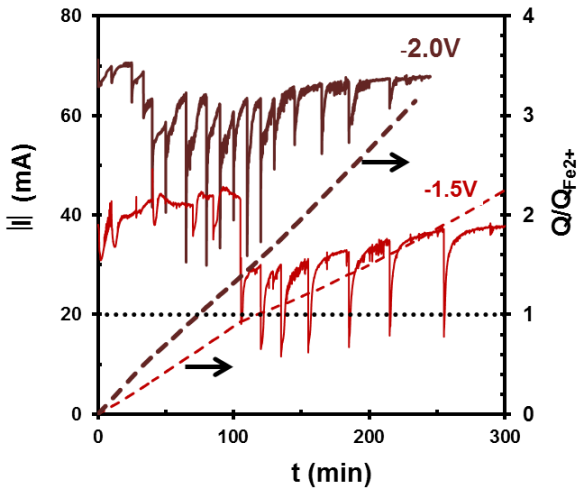

Figure 11 – Time dependence of current (solid lines) under applied voltage of -2V (cell b2cFe in Table 1) and -1.5 V (cell b1.5cFe). Cumulative charge was computed by integration, and its relative range refers to complete reduction of divalent iron oxide $QrefFe^{2+}$ (dashed lines).

Thus, cumulative charge shows that the final stage is determined by parasitic effects, after depletion of the initial contents of iron oxide in the molten silicate, with corresponding decrease in overall Faradaic efficiency.

Cell b1.5c was also tested with blocking-electron configuration but in Fe-free MAS electrolyte. Thus, the time dependence of current (Fig. 12) should be ascribed exclusively to parasitic electrochemical reactions. This parasitic current increases gradually, approaching the last stage of cell b1.5cFe with 2 mol% iron oxide This confirms that parasitic contributions predominate as the contents of iron oxide in the molten electrolyte is depleted. Still, the cathode in cell b1.5c retains its morphologic stability. Thus parasitic current should not be exclusively related to disintegration of Pt cathode.

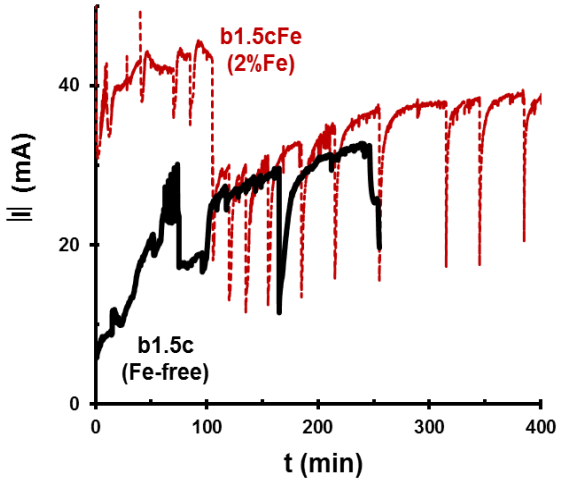

Figure 12 – Comparison of time dependence of current for cells operating with applied cell voltage -1.5V, for the MAS melts with 2 mol% Fe (cell b1.5cFe in Table 1) and the Fe-free melt (cell b1.5c).

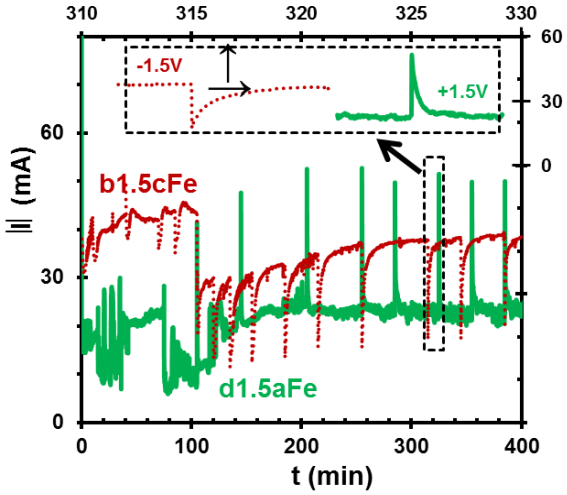

Figure 13 – Comparison of time dependence of current for cells d1.5aFe and b1.5cFe.

Cell d1.5aFe was operated without electron blocking, i.e., using the central Pt electrode (1) as anode and electrode (2) as cathode (Fig. 13). This cell was also modified to include a stopper at the bottom of the inner Pt electrode to maintain its vertical alignment, thus preventing its drift. Note that long term drift of the central Pt cathode, towards the inner surface of the YSZ container, may cause decrease in resistance due to changes in effective geometry. This may account, at least partly, to long term increase in current recorded for cells b2cFe, b1.5cFe and b1.5c, whereas cell d1.5aFe shows long term stability.

Another significant difference between cells d1.5aFe and b1.5cFe is the reversed transient response after temporary interruptions to monitor electrical properties by impedance spectroscopy, i.e., decrease in current on re-establishing anodic polarization of the central Pt electrode, after the initial peak (cell d1.5aFe), and increase in current on re-establishing cathodic polarization, after an initial minimum (cell b1.5cFe). This can be ascribed to redox changes induced by cathodic or anodic polarization and corresponding changes in conductivity, as expected on changing the fugacity of O_2 [36]. In addition, the concentration of positively charged carriers may drop close to the positive electrode, as revealed by EDS maps (Fig. 10).

6.2.4.4 Transient changes in conductivity

Impedance spectra recorded on disconnecting the applied voltage during operation of different cells (Figs. 2, 14, 15) were used to extract corresponding changes in conductivity (Fig. 16).

The spectra reveal mainly the intermediate frequency arc, ascribed to an interfacial contribution (Fig. 17), whereas the upper limit of frequency range (10^6 Hz) is insufficient to resolve the contribution at higher frequencies, this was ascribed to the ohmic resistance of the molten MAS (Fig. 16). In addition, the spectra obtained for cell d1.5aFe shows onset of a low frequency contribution and its nearly linear Z" vs Z' dependence resemble the Warburg impedance of diffusion controlled limitations. However, its slope is significantly lower than expected, and suggests anomalous diffusion [54], possibly because the concentration of charged species is time dependent, as emphasized also by the transient response on re-establishing the applied potential (Fig. 13).

This is more likely to occur when the central Pt electrode is under anodic polarization (cell d1.5aFe), thus causing local depletion of positively charged carriers (Fe2+). Indeed, the transient response time shown in Fig. 13 (in the order of 1 min) is several orders of magnitude longer than the reciprocal frequency range of the equipment (≤ 0.05 s), thus preventing a clear impedance analysis of the diffusion controlled processes. The impedance spectra for cell b1.5cFe (Fig. 14) are not conclusive about diffusion limitations at lower frequencies.

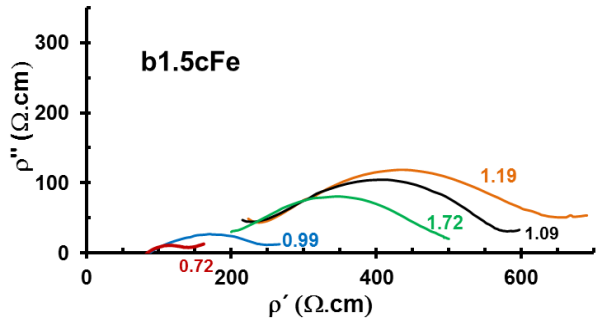

Figure 14 – Complex resistivity spectra $\rho^* = [2\pi L \ln(r_e / r)]Z^*$ for b1.5cFe cell, obtained after relative charging Q/Q_{Fe}=0.72, 0.99, 1.09, 1.19 and 1.72, where Q_{Fe} denotes the charge required to reduce the actual content of iron oxide to metallic Fe, assuming that Fe^{2+} prevails.

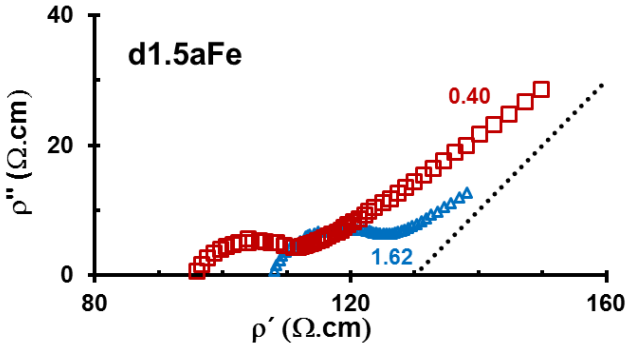

Figure 15 – Complex resistivity spectra $\rho^* = [2\pi L \ln(r_e / r)]Z^*$ for cell d1.5aFe, obtained at relative charging Q/QFe=0.40 and 1.62, where QFe denotes the charge required to reduce the actual content of iron oxide to metallic Fe, assuming that Fe^{2+} prevails.

Fig. 16 confirms sharp increase in ohmic resistance for cells b2cFe and b1.5cFe, on approaching the cumulative charge expected for reduction of Fe^{2+} to metallic Fe, and corresponding depletion of charge carriers. This trend is reverted for greater charging, which is also indicative that parasitic currents increase gradually as the actual concentration of Fe^{n+} vanishes. On the contrary, the direct electrolysis cell d1.5aFe, with central anode, only shows slight increase in ohmic resistance, without any evidence that this will go through a maximum.

This confirms that depletion of charge carriers is less effective in this case, consistent with the EDS maps showing accumulation of Fe^{2+} next to the cathode (Fig. 10), and indicating that reduction to metallic Fe is marginal. Thus, Faradaic efficiency is very low in this case.

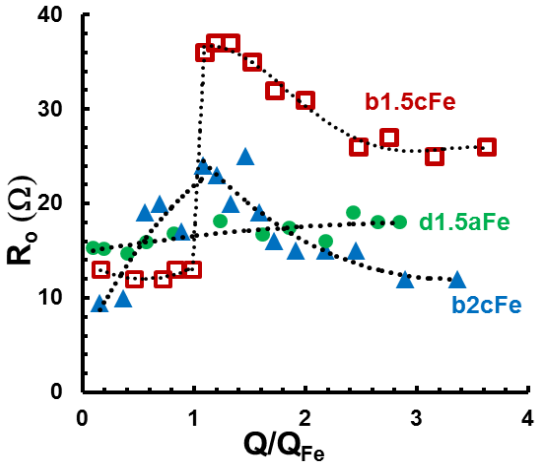

Figure 16 – Dependence of ohmic resistance on relative charging Q/Q_{Fe}, where Q_{Fe} denotes the charge required to reduce the actual content of iron oxide to metallic Fe, assuming that Fe^{2+} prevails.

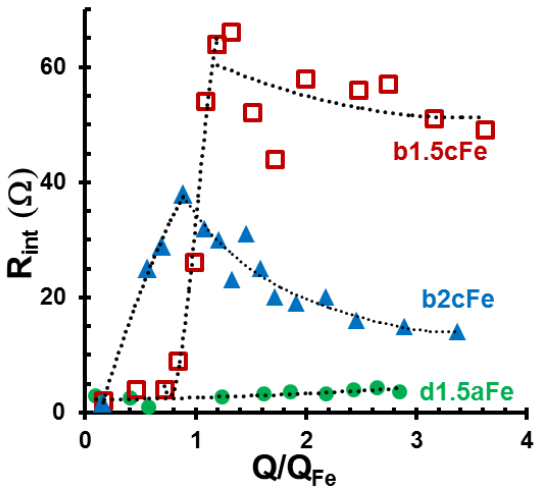

Figure 17 – Dependence of interfacial resistance on relative charging Q/Q_{Fe}, where Q_{Fe} denotes the charge required to reduce the actual content of iron oxide to metallic Fe, assuming that Fe^{2+} prevails.

The dependence of interfacial resistance on relative charging also confirms major differences between direct electron blocking cells (b2cFe and b1.5cFe) and the electrolysis cell d1.5aFe. Depletion of Fe^{2+}, upon reduction to metallic Fe, also causes drastic increase in interfacial resistance and clearly different trends on exceeding the nominal charge required for reduction.

On the contrary, the interfacial resistance remains low in the case of cell d1.5aFe, possibly due to a significant contribution of electronic transport, and without significant decay. This behavior also confirms that faradaic efficiency is marginal in this case.

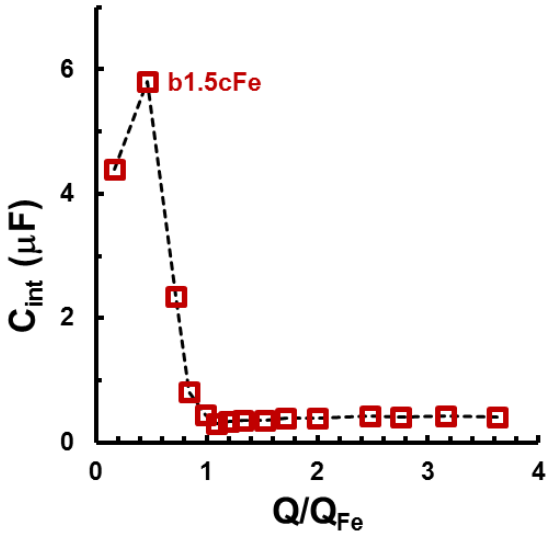

Figure 18 – Dependence of interfacial capacitance of cell b1.5cFe on relative charging Q/Q_{Fe}, where Q_{Fe} denotes the charge required to reduce the actual content of iron oxide to metallic Fe, assuming that Fe^{2+} prevails.

Changes in interfacial capacitance for cell b1.5cFe (Fig. 18) also reveal the main differences between the electrochemical behaviour at relatively low charging, and after exceeding the nominal charging required for reduction of Fe^{2+} to Fe. The initial stages may comprise increase in effective interfacial area by deposition of metallic Fe, the opposite trend at the onset of disintegration of the Pt cathode, and then a major drop in capacitance as the overall behavior becomes controlled by parasitic currents. This is also consistent with evidence that disintegration of the Pt cathode involves alloying with Fe, as shown above.

6.2.4.5 Concluding remarks on long term parasitic current

Post-morten analysis of cell d1.5aFe does no show evidence of reduction to metallic Fe and in situ monitoring by impedance spectroscopy also failed to show evidence of significant changes upon exceeding the cumulative charge required for complete reduction to metallic Fe.

Thus, the behaviour of this cell should be mainly due to a combination of parasitic effects or electronic leakage, combined with accumulation of carriers next to the outer electrode (cathode) and depletion next to the central electrode (anode), as revealed in Fig. 10. The most likely hypothesis is electron hopping between Fe^{2+} and Fe^{3+}, combined with corresponding charge transfer reactions at cathode ($Fe^{3+} + e' \rightarrow Fe^{2+}$) and at the anode ($Fe^{2+} \rightarrow Fe^{3+} + e'$). Dependence of conductivity on redox conditions or anodic polarization may also cause excessive increase in ohmic losses, near the central electrode (anode), lowering the actual difference between applied voltage (1.5 V) and ohmic losses ($V_{appl} - I\,R_O$).

Thus, reduction to metallic Fe will be halted if this drops below the required Nernst potential (≈ 1.02V). In fact, ohmic resistance extracted from impedance spectra under open circuit conditions (Fig. 16) are clearly underestimated in the case of cell d1.5aFe, due to dependence of resistivity on O_2 fugacity or anodic polarization. The transient response in Fig. 13 suggests that resistance under anodic polarization increases by a factor greater than 2, implying that the ohmic resistance in Fig. 15 may increase to values above 30 Ω when current attains a nearly steady value of about 25 mA. This yields ohmic losses exceeding 0.75 V, and V_{appl}-IR_O < 0.75 V, except possibly at short times or during the transient responses (Fig. 13). In this case, faradaic efficiency should be very low and the long term current may be ascribed to electronic leakage.

The impact of ohmic losses should be much lower for cells b2cFe and b1.5cFe, due to the positive effect of cathodic polarization on conductivity, near the central electrode, as revealed by the transient spikes in Fig. 13. Thus, one still expects conditions required for reduction to metallic Fe ($V_{appl} - IR_O > 1.02$ V), and high faradaic efficiency is expected by hindering electronic leakage via the electron blocking YSZ membranes. Still this cannot explain the long term current when the cumulative charge exceeds largely the nominal charge required for complete reduction to metallic Fe. A plausible explanation was proposed above, based on reduction of silica to metallic Si, mainly for cell b2cFe, yielding low melting liquid phases in the ternary system Fe-Si-Pt. Disintegration of the Pt cathode may also be taken as a footprint of this parasitic effect. Still, this cannot explain parasitic effects observed also for cells operating in Fe-free molten MAS (cell b1.5c).

Thus, one should also consider other parasitic contributions for the long term current in electron-blocking cells, mainly as the aluminosilicate melt approaches Fe-lean conditions. Plausible additional parasitic effects may be related to contributions of atmospheric gases such as O_2 and humidity, which are known to dissolve in basaltic melts, depending on temperature (T), total pressure (P), water vapour partial pressure (pH_2O) and non-bridging oxygen per unit oxygen (NBO/O) [55]:

$$\ln\{wt\%H_2O\} = 0.54\ln(pH_2O) + 1.24[NBO/O] - 2.95 + 0.02(P/T) \tag{21}$$

where

$$\ln(\mathrm{NBO/O}) = \frac{2\{X_{K2O} + X_{Na2O} + X_{CaO} + X_{MgO} + X_{FeO} - X_{Al2O3}\}}{\{2X_{SiO2} + 2X_{TiO2} + 3X_{Al2O3} + X_{K2O} + X_{Na2O} + X_{CaO} + X_{MgO} + X_{FeO}\}} \tag{22}$$

If one assumes this dependence for the actual MAS compositions and for typical conditions T = 1728 K, P = 1 atm and $pH_2O \approx 0.03$ atm one predicts ≈ 0.0083 wt% H_2O. This is, indeed, a very low concentration. Still, the corresponding OH groups represent a significant fraction of non-bridging oxygen (0.086). Dissolved water is also known for its impact on the electrical conductivity of aluminosilicate melts [24] and on diffusivity of oxygen, as emphasized by major differences in O^{18} diffusivity for hydrous and anhydrous conditions [22].

Water dissolution in silicate melts may occur in a variety of forms, including molecular H_2O, hydroxyl groups and even molecular H_2 under reducing conditions [22, 23, 56]. Still, hydroxyl groups ($\equiv Si-OH$) are likely to prevail for relatively low water contents and for high alumina contents [57], thus contributing to break bonding oxygens:

$$\equiv Si-O-Si\equiv + H_2O \rightarrow 2\equiv Si-OH \tag{23}$$

There is also evidence that H_2 can evolve from aluminosilicate melts, and the fugacity of H_2 is expected to increase under reducing conditions [56, 58], mainly in the presence of Pt, this may account also for a plausible alternative cathodic reaction:

$$2\equiv Si-OH + 2e^- \rightarrow H_2(g) + 2\equiv Si-O^- \tag{24}$$

Thus, humidity uptake may sustain alternative cathodic reactions while providing also non-bridging oxygens to sustain oxygen ion transfer at the melt/YSZ interface.

6.2.5 Conclusions

High-temperature iron extraction from the molten magnesium aluminosilicate-based electrolyte was studied in solid electrolyte cells by electrochemical methods, combined with post-mortem SEM/EDS techniques.

The cell comprised an YSZ closed-end tube and three platinum electrodes for conducting pyroelectrolysis experiments, and impedance spectroscopy allows in-situ monitoring of changes in ohmic resistance and relevant interfacial process. Various experiments under potentiostatic conditions were performed at 1728 K in electron-blocking cell regime and using direct electrolysis mode. The results of post-mortem microstructural analysis and EDS mapping for the transverse sections of the cell confirmed iron deposition at the cathode, followed by alloying with platinum. The observed trends for changing of the electrolysis current and electrolyte resistance with time suggest high faradaic efficiency under electron-blocking conditions until depletion of the Fe-contents in the aluminosilicate melts.

Still, a conclusive proof of concept for pyroelectrolysis with electron blocking requires alternative electrode materials, to overcome the observed disintegration of the Pt cathode, Pt-Fe alloying, and to sustain high faradaic efficiency as the contents of iron oxide decreases. Efficiency is likely to depend on the actual contents of iron oxide in the aluminosilicate melt, applied voltage and relative cumulative charging. A significant limitation on faradaic efficiency was ascribed to onset of reduction of silica to metallic Si. Its inclusion in low melting Fe-Si-Pt liquid phase is also a plausible explanation for disintegration of the Pt cathode. Other plausible parasitic limitations on faradaic efficiency may be related to uptake of atmospheric gases such as humidity or oxygen. These may also sustain alternative cathodic reaction and transfer of oxygen ions across the melt/YSZ interface.

The efficiency of the iron separation from the melt by direct electrolysis process was found very poor, probably due to onset of electronic leakage, and also because the applied voltage is insufficient to account for the combined contributions of ohmic losses and Nernst potential required for reduction to metallic Fe.

6.2.6 References

[1] – C.H.P. Lupis, Greenhouse gases and the metallurgical process industry, Metallurg. Mat. Trans. B 30B (1999) 841-856, doi:10.1007/s11663-999-0089-3.

[2] – M. Barati, Energy intensity and greenhouse gases footprint of metallurgical processes: a continuous steelmaking case study, Energy 35 (2010)3731-3737, doi:10.1016/j.energy.2010.05.022.

[3] – D.R. Sadoway, New opportunities for metals extraction and waste treatment by electrochemical processing in molten salts, J. Mater. Res. 10 (1995) 487-492.

[4] – R.H. Aiken, Process of making iron from the ore, US Patent 816142 (1906).

[5] – H. Kim, J. Paramore, A. Allanore, D.R. Sadoway, The influence of electrolyte basicity on the performance of an iridium anode for the electrolysis of molten iron oxide, J Electrochem Soc 158 (2011) E101-5.

[6] – D. Wang, A.J. Gmitter, D.R. Sadoway, Production of oxygen gas and liquid metal by electrochemical decomposition of molten iron oxide; J. Electrochem. Soc. 158 (2011) E51-E54.

[7] – A. Allanore, L. Yin, D.R. Sadoway, A new anode material for oxygen evolution in molten oxide electrolysis, Nature 497 (2013) 353-356.

[8] – L.A. Haskin, R.O. Colson, D.J. Lindstrom, R.H. Lewis, K.W. Semkow, Electrolytic smelting of lunar rock for oxygen, iron, and silicon, in: The Second Conference on Lunar Bases and Space Activities of the 21st Century, Houston, Texas, USA, 5-7 April 1988, Vol. 1, NASA Conference Publication, 1992, p. 411.

[9] – A. Martin, J.C. Poignet, J. Fouletier, M. Allibert, D. Lambertin, G. Bourgès, Yttria-stabilized zirconia as membrane material for electrolytic deoxidation of CaO-$CaCl_2$ melts, J. Appl. Electrochem. 40 (2010) 533-542, doi:10.1007/s10800-009-0025-x.

[10] – U.B. Pal, A.C. Powell, The use of solid-oxide-membrane technology for electrometallurgy, JOM 59 (2007) 44-49, doi: 10.1007/s11837-007-0064-x.

[11] – U.B. Pal, D.E. Woolley, G.B. Kenney, Emerging SOM technology for the green synthesis of metals from oxides, JOM 53 (2001) 32-35, , doi: 10.1007/s11837-001-0053-4.

[12] – A. Martin, D. Lambertin, J.C. Poignet, M. Allibert, G. Bourges, L. Pescayre, J. Fouletier, The electrochemical deoxidation of metal oxides by calcium using a solid electrolyte membrane, JOM 55 (2003) 52-54, doi:10.1007/s11837-003-0177-9.

[13] – A. Krishnan, X.G. Lu, U.B. Pal, Solid oxide membrane (SOM) technology for environmentally sound production of tantalum metal and alloys from their oxide sources, Scand. J. Metallurgy 34 (2005) 293-301, doi: 10.1111/j.1600-0692.2005.00749.x.

[14] – H.J. Park, G.M. Choi, The effect of surface coating on the oxygen permeation characteristics of zirconia, J. Eur. Ceram. Soc. 25 (2005) 2577-2581, doi:10.1016/j.jeurceramsoc.2005.03.105.

[15] – H.W. Koo, H.J. Park, G.M. Choi, H.G. Lee, Electrochemical deoxidation of molten steel with application of oxygen permeable membrane, ISIJ International, 47 (2007) 689-698.

[16] – Y.M. Gao, B. Wang, S.B. Wang, S. Peng, Study on electrolytic reduction with controlled oxygen flow for iron from molten oxide slag containing FeO, J. Min. Metall. Sect. B-Metall. 49B (2013) 49 – 55.

[17] – A. Lugovskoy, M. Zinigrad, D. Aurbach, Z. Unger, Electrodeposition of iron (II) on platinum in chloride melts at 700-750ºC, Electrochim. Acta 54 (2009) 1904-1908, doi:10.1016/j.electacta.2008.10.016.

[18] – G. Ottonello, R. Moretti, L. Marini, M.V. Zuccolini, Oxidation state of iron in silicate glasses and melts: a thermochemical model, Chemical Geology, 174 (2001) 157–179, doi:10.1016/S0009-2541(00)00314-4.

[19] – J.A. Duffy, A review of optical basicity and its applications to oxidic systems, Geochimica et Cosmochimica Acta, 57 (1993) 3961-3970, doi:10.1016/0016-7037(93)90346-X.

[20] – V. Magnien, D.R. Neuville, L. Cormier, J. Roux, J.-L. Hazemann, D. de Ligny, S. Pascarelli, I. Vickridge, O. Pinet, P. Richet, Kinetics and mechanisms of iron redox reactions in silicate melts: The effects of temperature and alkali cations, Geochimica et Cosmochimica Acta 72 (2008) 2157–2168, doi:10.1016/j.gca.2008.02.007.

[21] – F. Gaillard, M. Pichavant, B. Scaillet, Experimental determination of activities of FeO and Fe2O3 components in hydrous silicic melts under oxidizing conditions, Geochimica et Cosmochimica Acta 67 (2003) 4389-4409, DOI:10.1016/S00167037(03)00376-4.

[22] – H. Behrens, Y. Zhang, M. Leschik, M. Wiedenbeck, G. Heide, G.H. Frischat, Molecular H2O as carrier for oxygen diffusion in hydrous silicate melts, Earth and Planetary Science Letters 254 (2007) 69–76, doi:10.1016/j.epsl.2006.11.021.

[23] – H. Behrens,Y. Zhang, H2O diffusion in peralkaline to peraluminous rhyolitic melts, Contrib Mineral Petrol 157 (2009) 765–780, doi:10.1007/s00410-008-0363-4.

[24] – A. Pommier, F. Gaillard, M. Pichavant, B. Scaillet, Laboratory measurements of electrical conductivities of hydrous and dry Mt. Vesuvius melts under pressure, Journal Geophysical Research 113 (2008) 41, doi:10.1029/2007JB005269.

[25] – R. Morelli, Polymerisation, basicity, oxidation state and their role in ionic modelling of silicate melts, Annals of Geophysics, 48 (2005), 583-608.

[26] – V.C. Kress, I.S.E. Carmichael, Stoichiometry of the iron oxidation reaction in silicate melts, Amer. Mineralogist, 73 (1988) 1267-1274.

[27] – G. S. Nikolaev, A. A. Borisov, and A. A. Ariskin, Calculation of the Ferric–Ferrous Ratio in Magmatic Melts: Testing and Additional Calibration of Empirical Equations for Various Magmatic Series, Geochemistry International 34 (1996) 641–649.

[28] – A. Berry, H.S.C. ONeill, K.D. Jayasuriya, S.J. Campbell, G.J. Foran, XANES calibrations for the oxidation state of iron in a silicate glass, American Mineralogist 88 (2003) 967–977.

[29] – N.M. Ferreira, A.V. Kovalevsky, J.C. Waerenborgh, M. Quevedo-Reyes, A.A. Timopheev, F.M. Costa, J.R. Frade, Crystallization of iron-containing Mg-Al-Si-O glasses under laser floating zone conditions, J. Alloys & Compounds 611 (2014) 57–64.

[30] – H.S.C. O´Neill, S.M. Eggins, The effect of melt composition on trace element partitioning: An experimental investigation of the activity coefficient of FeO, NiO, CoO, MoO2 and MoO3 in silicate melts, Chemical Geology 186 (2002) 151-181, doi: doi:10.1016/S0009-2541(01)00414-4.

[31] – B.O. Mysen, D. Virgo, C.M. Scarfe, D.J. Cronin, Viscosity and structure of iron- and aluminium-bearing calcium silicate melts at 1 atm, American Mineralogist 70 (1985) 487-498.

[32] – C. Weigel, L.Cormier, G. Calas, L. Galoisy, D.T. Bowron, Nature and distribution of iron sites in a sodium silicate glass investigated by neutron diffraction and EPSR simulation, J.Non Cryst. Solids 354 (2008) 52-54, doi:10.1016/j.jnoncrysol.2008.09.030.

[33] – L. Murawski, Review: Electrical conductivity in iron-containing oxide glasses J. Mat. Sci. 17 (1982) 2155-2163, doi:10.1007/BF00543723.

[34] – N.S. Choudhury, J.W. Patterson, Performance characteristics of solid electrolytes under steady-state conditions, J. Electrochem. Soc. 118 (1971) 1398-1403.

[35] – T.H. Etsell, S.N. Flengas, N-type conductivity in stabilized zirconia solid electrolytes, J. Electrochem. Soc. 119 (1972) 1-7.

[36] – A. Pommier, F. Gaillard, M. Pichavant, Time-dependent changes of the electrical conductivity of basaltic melts with redox state, Geochimica et Cosmochimica Acta 74 (2010) 1653-1671, doi:10.1016/j.gca.2009.12.005.

[37] – W.M. White, Geochemistry, Wiley-Blackwell, 2013.

[38] – R.L.A. Everman, R.F. Cooper, Internal Reduction of an Iron-Doped Magnesium Aluminosilicate Melt, J. Amer. Ceram. Soc. 86 (2003) 487–494.

[39] – R.F. Cooper, R.L.A. Everman, J.W. Hustoft, S.H.D. Shim, Mechanism and kinetics of reduction of a FeO-Fe2O3-CaO-MgO aluminosilicate melt in a high CO-activity environment, Amer. Miner. 95 (2010) 810-824.

[40] – N.R. Bennett, J.M. Brenan, K.T. Koga, The solubility of platinum in silicate melt under reducing conditions: Results from experiments without metal inclusions, Geochimica et Cosmochimica Acta, 133 (2014) 422-442.

[41] – C.E. Ford, Platinum-iron alloy sample containers for melting experiments on iron-bearing rocks, minerals, and related systems, Miner. Magaz. 42 (1978) 271-275.

[42] – T.L. Grove, Use of FePt alloys to eliminate the iron loss problem in 1 atmosphere gas mixing experiments: theoretical and practical considerations, Contrib. Mineral. Petrology 78 (1981) 298-304, doi:10.1007/BF00398924.

[43] – G. Parry, O. Ostrovski, Wettability of Solid Metals by Molten CaO-SiO2-Al2O3 Slag, Met. Mat. Trans.B, 39B (2008) 681-689, doi: 10.1007/s11663-008-9181-3.

[44] – A. Ricolleau, Y.Fei, A.Corgne, J.Siebert, J.Badro, Oxygen and silicon contents of Earth's core from high pressure metal–silicate partitioning experiments, Earth and Planetary Sci. Lett. 310 (2011) 409-421, doi:10.1016/j.epsl.2011.08.004.

[45] – S.K. Cho, F. Ren, F. Fan, A.J. Bard, Formation of a silicon layer by electroreduction of SiO2 nanoparticles in CaCl2 molten salt, Electrochimica Acta 65 (2012) 57– 63, doi:10.1016/j.electacta.2012.01.008.

[46] – L.L. Xu, J. Wang, H.S. Liu, Z.P. Jin, Thermodynamic assessment of the Pt-Si binary system, CALPHAD 32 (2008) 101-105, doi:10.1016/j.calphad.2007.07.010.

[47] – W.C. Yang, H. Ade, R. J. Nemanich, Stability and dynamics of Pt-Si liquid microdroplets on Si (001), Phys. Rev. B69 (2004) 045421, doi:10.1103/PhysRevB.69.045421.

[48] – H. Jeong, T.E. Park, H.K. Seong, M. Kim, U. Kim, H.J. Choi, Growth kinetics of silicon nanowires by platinum assisted vapour–liquid–solid mechanism, Chem. Phys,. Lett. 467 (2009) 331-334, doi:10.1016/j.cplett.2008.11.022.

[49] – J. Lacaze, B. Sundman, An assessment of the Fe-C-Si system, Metall. Trans.A, 22A (1991) 2211-2223, doi:10.1007/BF02664987.

[50] – Z.K. Liu, Y.A. Chang, Thermodynamic assessment of the Al-Fe-Si system, Metall. Mat. Trans. 30A (1999) 1081-1095, doi:10.1007/s11661-999-0160-3.

[51] – M. Nagamori, I. Malinski, A. Claveau, Thermodynamics of the Si-C-O system for the production of silicon carbide and metallic silicon, Met. Trans. B 17B (1986) 503-514, 503-514, doi:10.1007/BF02670216.

[52] – O. Braaten, A. Kjekshus, H. Kvande, The possible reduction of alumina to aluminum using hydrogen, JOM- J. Min. Met. Mat. Soc. 52 (2000) 47-53, 10.1007/s11837-000-0047-7.

[53] – C. Smit, R. A. C. M. M. van Swaaij, H. Donker, A. M. H. N. Petit, W. M. M. Kessels, M. C. M. van de Sanden, Determining the material structure of microcrystalline silicon from Raman spectra J. Appl. Phys. 94 (2003) 3582-3588, doi:10.1063/1.1596364.

[54] – J. Bisquet, A. Compte, Theory of the electrochemical impedance of anomalous diffusion, J. Electroanal. Chem. 499 (2001) 112-120, doi:10.1016/S0022-0728(00)00497-6.

[55] – G.Iacono-Marziano, Y.Morizet, E.Le Trong, F.Gaillard, New experimental data and semi-empirical parameterization of H2O–CO2 solubility in mafic melts, Geochimica et Cosmochimica Acta 97 (2012) 1–23, doi:10.1016/j.gca.2012.08.035.

[56] – A. Kadik, F. Pineau, Y. Litvin, N. Jendrzejewski, I. Martinez, M. Javoy, Formation of Carbon and Hydrogen Species in Magmas at Low Oxygen Fugacity, J. Petrology 45 (2004) 1297–1310, doi:10.1093/petrology/egh007.

[57] – W.J. Malfait, The nearly complete dissociation of water in glasses with strong aluminum avoidance, Amer. Miner. 99 (2014) 1648-1652.

[58] – A.A. Kadik, N.A. Kurovskaya, Yu.A. Ignat'ev, E.B. Kryukova, V.V. Koltashev, N.N. Kononkova , Use of platinum capsules in the study of the carbon and hydrogen solubility in silicate melts in equilibrium with liquid iron alloys at high pressures and temperatures, Geochem. Int. 51 (2013) 1019–1024, doi:10.1134/S0016702913120045.

7 Conclusions and remarks

This thesis contributed to clarify some of the most critical and debatable issues concerning demonstration of pyroelectrolysis as a prospective breakthrough technology for steelmaking, and challenges ahead. One confirmed the relevance of important parameters concerning the molten oxide electrolyte, and promising electrode concepts, to overcome overwhelming stability limitations. Inert electrodes are unlikely concepts, even if one considers noble metals such as platinum, because cost is unaffordable and also because their claimed inertness is not maintained in the actual prospective operating conditions. Thus, one must consider alternative concepts such as:

i) Fe-based cathodes, probably in the form of a liquid/solid concept, with suitable thermal gradients to adjust freeze lining and to ensure compatibility with refractory materials;

ii) Consumable oxide anodes, with sufficient properties to meet the requirements of anode materials, and possessing compositions with minimum long term impact on the molten electrolyte composition and intended product (Fe or its alloys), for long term operation.

The thermochemical and electrochemical processes in molten silicates are still far from being properly understood, due to the inherent harsh conditions of pyroelectrolysis, and also by difficulties in tracing relevant literature from quite disperse technical and scientific fields (glass technology, extractive metallurgy, volcanic and earth mantle studies, geology,...).

One established important guidelines for relevant conditions such as temperature gradients and their impact on de-vitrification, crystallization of iron oxides on lowering the temperature of silicate melts, and their redox changes on varying the thermochemical conditions. One also obtained convincing evidence that divalent Fe^{2+} is the prevailing dissolved cation in the selected melt, even in air.

This information on the thermochemistry of silicate melts also provides guidelines to predict interactions between the intended consumable anodes with magnetite-based spinel compositions, and silicate melts. Yet, the anode/melt compatibility could not be assessed within this PhD project, due to time limitations and also for other insufficient conditions (equipment, funding and related resources).

Due to experimental difficulties and limitations one restricted the pyroelectrolysis tests to temperatures below melting of metallic Fe. Under these conditions, one found that the relevant transport properties of studied melt composition are clearly insufficient for an efficient concept of pyroelectrolysis. The ionic conductivity is much below the range required to suppress ohmic losses to an acceptable range, and onset of electronic leakage raises strong doubts about direct electrolysis with both cathode and anode in contact with the molten electrolyte. Thus, much additional work and effort is needed to design alternative silicate melt compositions with greatly increased ionic conductivity and suppressed electronic conductivity. This must include detained studies of their dependence on the contents of iron oxide dissolved in the molten silicate, as well as temperature dependence, mainly if one seeks direct electroreduction to liquid metal.

Still one found sufficient evidence that pyroelectrolysis can be achieved by an alternative concept of pyroelectrolysis with electron blocking membrane. Indeed, it is also debatable whether this approach may ever reach a stage of technological development for mass production. Pyroelectrolysis with electron-blocking membrane also emphasized unexpected side electrochemical reactions and parasitic effects, imposing additional challenges and (possibly) also raising doubts on prospects for successful development of pyroelectrolysis as a viable technology. One of the most striking findings is the possibility of electrochemical reduction of silica to metallic Si, and possibly even reduction of alumina to Al, under relatively low applied voltages. Thus, one may consider quite contradicting conclusions, from a pessimistic view that pyroelecrolysis is invalid by fundamental restrictions, to alternative optimistic prospects for production of alloys by simultaneous electroreduction of different metallic components. One must also consider risks of other parasitic effects, with emphasis on side electrochemical reactions involving dissolved gases (humidity, carbon dioxide, etc.).

The study of prospective compositions for consumable anodes indicates that one must seek a compromise between redox stability and electrical conductivity at high temperature. Additions of magnesia enhance the tolerance of alumina-containing magnetite against oxidative decomposition, where the phase stability of (Fe, Al, Mg)$_3$O$_4$ spinels is determined mainly by the [Al^{3+}]/[Mg^{2+}] ratio. However, substitution of iron oxide with magnesia lowered the conductivity, if compared to the alumina-substituted analogue. Nevertheless, the impacts on conductivity and phase stability at required temperatures suggest a broad range of compositions for (Fe,Al,Mg)$_3$O$_4$ –based anodes and conditions for their successful testing in pyroelectrolysis.

Additions of other metallic cations (e.g. Me = Ni, Mn, Cr, Ti in $Fe_{2.6}Me_{0.2}Mg_{0.2}O_4$ based spinels) yield changes in high-temperature electrical conductivity in the sequence Ni^{2+} < $Mn^{2+/3+}$ ~ Cr^{3+} < Ti^{4+}; this follows the corresponding trend for oxidation state of transition metal cations and can be ascribed to effects on Fe^{2+}:Fe^{3+} ratio. Reasonable trade-off between electronic transport, redox stability and tolerance to thermal cycling may also be claimed. These results suggest good prospects for spinels with compositions $Fe_{2.6}Al_{0.2}Mg_{0.2}O_4$ and $Fe_{2.6}Ti_{0.2}Mg_{0.2}O_4$ as potential materials for consumable ceramic anodes in high-temperature pyroelectrolysis. One may also consider additions of other redox stable oxides (SiO_2, ZrO_2,...) to seek enhanced trade-off between electrical conductivity and other requirements of redox and thermomechanical stability, etc.

Guidelines for the design of consumable anodes also included propects for direct in-situ conversion of poorly conducting hematite or derived phases to conducting magnetite or derived spinel compositions, at sufficiently high temperatures. In addition, one considered prospects for two-phase materials with ability to retain sufficient conductivity, by extending their redox stability or retaining metastable conditions. A core-shell concept was proposed based on laser floating zone (LFZ) experiments with hematite percursors. Dependence on pulling rate allowed one to emphasize the time dependence of redox changes.

The results here obtained had shown the necessity to perform several assessments to understand the process. However, to reach an industial application still many studies are necessary, as it has been reported.